



UNIVERSITY OF
BIRMINGHAM

**TOWARDS SIMULATION-BASED DIGITAL TWINS:
SENSOR PLACEMENT STUDIES FOR STRUCTURAL
HEALTH MONITORING OF RAILWAY SWITCHES BY
IMPLEMENTING NUMERICAL SIMULATIONS WITH
CALIBRATED TRACK MODELS.**

by

NIKHIL RAJESH PILLAI

A thesis submitted to
The University of Birmingham
for the degree of
DOCTOR OF PHILOSOPHY

Birmingham Centre for Railway Research and Education
School of Electronic, Electrical and Systems Engineering
College of Engineering and Physical Sciences
University of Birmingham
December 2022

UNIVERSITY OF
BIRMINGHAM

University of Birmingham Research Archive

e-theses repository

This unpublished thesis/dissertation is copyright of the author and/or third parties. The intellectual property rights of the author or third parties in respect of this work are as defined by The Copyright Designs and Patents Act 1988 or as modified by any successor legislation.

Any use made of information contained in this thesis/dissertation must be in accordance with that legislation and must be properly acknowledged. Further distribution or reproduction in any format is prohibited without the permission of the copyright holder.

ABSTRACT

This thesis contributes to the knowledge of how train-switch interaction models can be developed and calibrated against reference assets or models in order to support the predictive maintenance of switches. The modelling approach that has been suggested within this thesis could be further developed for implementation as part of a live Digital Twin. The key research that will be demonstrated through this thesis includes: (i) the selection, development and evaluation of numerical simulation approaches to address a range of different research questions; (ii) calibration of the track dynamics for the developed FE model against the reference model, (iii) rolling contact simulations for the wheel and the switch, as well as the validation of the model against the reference model, and (iv) an approach to determine sensor placement in order to implement effective fault detection.

At first, the existing examples of S&C modelling to simulate train-turnout interactions, wheel-rail contact and damage prediction were reviewed. A number of the results from this evaluation have been implemented in order to determine which modelling approaches will be suitable to determine the appropriate locations in switches that are susceptible to surface rail damage, the placement of sensors for fault detection and the testing of the potential for condition monitoring.

Based on the results from the evaluation of the numerical simulation approaches, a combined MBS-FE numerical approach has been implemented for modelling the switch. A 3D solid FE model for a railway switch assembly has been calibrated for representing the dynamic properties for a reference track model that is based on the properties shared in the S&C benchmark project, where 20 research institutions achieved consensus for the results from the dynamic vehicle-turnout interaction simulations whilst implementing different software packages. Furthermore, numerical simulations have been carried out after introducing the rail and substructure defects such as wear, Rolling Contact Fatigue (RCF) and voiding.

The results from the numerical simulations have been used to assess the best locations on the switch rail for the placement of strain sensors for monitoring the health of the switch. The characteristics

(range, data acquisition rate, etc.) have also been discussed. Strain sensitivity analysis has been carried out for determining the direction of the strain measurement that is sensitive to the defects that have been introduced.

The correlation analysis between the rail strain and wheel/rail impact forces has been carried out and it has been discovered that a good correlation between the strains and the impact forces is conditional on the sensor placement location. The measurement of the vertical strains on the rail web is more sensitive to the lateral position of the wheel than the measurement of longitudinal strains on the rail foot. The measurement of the strains in the sleeper spacing has shown potential for the detection of the specific defects that have been introduced into the model. The surface defects have been introduced on sleeper-supported rail as well as the section of the rail in the sleeper spacing. The ability of the sensor to detect the faults whilst being installed at the proposed locations has also been numerically verified.

To conclude, an approach has been demonstrated for taking decisions on structural health monitoring of switches through this research. The requirements for sensor specification and the best sensor locations for detecting faults can be assessed digitally, which reduces the need for field experimentation. The knowledge from this research can be taken further for developing Digital Twins of track infrastructure. Real-time data from the measurement can be integrated with the numerical data developed in the present research to obtain a better insight of the switch dynamic behaviour as well as damage prediction.

ACKNOWLEDGEMENTS

First and foremost, I would like to express my immense gratitude to my PhD supervisors for taking me on as their student and presenting me with the opportunities to flourish as a professional researcher. I would like to thank Professor Clive Roberts for providing me with numerous professional development opportunities including attendance to conferences, training programmes, teaching, encouraging me to publish as well as providing me with responsibility for co-ordinating student projects in the centre. I would like to thank Dr Jou-Yi Shih for her constant encouragement, invaluable advice and feedback that helped shape the overall direction of this research. Your mentorship, feedback and advice have been instrumental in helping me grow as a professional researcher.

I would like to thank Dr Ramakrishnan Ambur for sharing his work on Multi-Body Simulations and the results from his reference model. They were very useful for verifying the results from my simulations.

I am also immensely grateful for the full scholarship I had received through the School of Engineering Doctoral Scholarship and the Birmingham Centre for Railway Research and Education through the S-CODE project. I would like to thank all other colleagues in the Birmingham Centre for Railway Research and Education at the University of Birmingham, the peer reviewers for my publications and conference attendees from around the world who have supported me with the feedback on my work.

I am immensely thankful to my entire family, especially my parents, Rajesh and Srividya Pillai for their attention and sacrifice so that their children could get a good head start in life. I have been away for many years now but the values and work ethic that I imbibed because of you have remained intact. And to my siblings Neha and Nihar Pillai for ensuring that my absence was seldom felt and their unwavering support. I am also grateful to my grandparents and extended family for all the help and support they have provided over the years. Thank you Sameeksha Pavaskar for your love, understanding, support, encouragement and being my home away from home.

Thank you Mohamed Samra, Rabee Jibrin and Dhruv Joshi for being excellent flatmates, companions, as well as for your motivation and intellectually stimulating conversations. Thank you to all my friends from Birmingham and elsewhere in the world for your company and bringing joy to my life. Finally, thank you to all my mentors, be it at Atkins, University of Birmingham, Knorr-Bremse, Cardiff University, college or school for your belief in me and bringing out the best in me.

LIST OF RELEVANT PEER-REVIEWED JOURNAL AND CONFERENCE PUBLICATIONS

The publications and the Chapters that they represent (specific portions) have been linked below:

CHAPTER 1: Shih, J.-Y., Weston, P., Pillai, N., Entezami, M., Stewart, E., & Roberts, C. (2019).

Potential Condition Monitoring System for Switch and Crossings Using Accelerometers. Proceedings of the 13th International Workshop on Railway Noise.

https://www.researchgate.net/publication/336363520_Potential_condition_monitoring_system_for_switch_and_crossings_using_accelerometers

CHAPTER 2: Pillai, N., Shih, J.-Y., & Roberts, C. (2021). Evaluation of Numerical Simulation

Approaches for Simulating Train–track Interactions and Predicting Rail Damage in Railway Switches and Crossings (S&Cs). *Infrastructures*, 6(5). <https://doi.org/10.3390/infrastructures6050063>

CHAPTER 3: Pillai, N., Shih, J.-Y., Ambur, R., & Roberts, C. (2022). Replicating the Vehicle and Track Dynamics in Combined Multi-Body System and Finite Element Simulations for the Appropriate Analysis of Subsurface Rail Behaviour. Proceedings of the Fifth International Conference on Railway Technology: Research, Development and Maintenance. Accepted. In Press.

CHAPTER 3: Pillai, N., Shih, J.-Y., & Roberts, C. (2021). Enabling Data-driven Predictive

Maintenance for Switch and Crossing (S&C) Through Digital Twin Models and Condition Monitoring Systems. *Journal of the Permanent Way Institution*, 139(4), 14–20.

https://www.researchgate.net/publication/355476166_Enabling_Data-driven_Predictive_Maintenance_for_SC_Through_Digital_Twin_Models_and_Condition_Monitoring_Systems

CHAPTER 4: Pillai, N., Shih, J.-Y., Ambur, R., & Roberts, C. (2021). A Combined Multi-body System and Finite Element Analysis Approach to Simulating Train-track Switch Interaction Dynamics. Proceedings of the Fifth Australasian Conference on Computational Mechanics. <https://doi.org/10.26183/t5jn-8y77>

CHAPTER 5: Pillai, N., Shih, J.-Y., & Roberts, C. (2022). Numerical Simulation of Train-Track Switch Interactions in the Presence of Surface Rail Defects for Determining Physical Sensor Placement for Structural Health Monitoring. Proceedings of the ASME 2022 Joint Rail Conference. <https://doi.org/10.1115/JRC2022-79455>

CHAPTER 5 and CHAPTER 6: Pillai, N., Shih, J.-Y., & Roberts, C. (2021). Sensor Selection and Placement for Track Switch Condition Monitoring through Validated Structural Digital Twin Models of Train–Track Interactions. Engineering Proceedings, 10(1), 49. <https://doi.org/10.3390/ecsa-8-11297>

CHAPTER 5 and CHAPTER 6: Pillai, N., Shih, J.-Y., & Roberts, C. (2022). Smarter Health Monitoring of Track Switches through Digital Twin Models of Train-Track interactions. Proceedings of the 13th World Congress on Railway Research. <https://www.rssb.co.uk/spark/sparkitem/pb029351>

Table of Contents

ABSTRACT	i
ACKNOWLEDGEMENTS	iii
LIST OF RELEVANT PEER-REVIEWED JOURNAL AND CONFERENCE PUBLICATIONS	v
LIST OF FIGURES	x
LIST OF TABLES	xv
CHAPTER 1. INTRODUCTION	1
1.1 Switches and Crossings	1
1.2 Failures in S&C and associated defects	7
1.2.1 FMS records from Network Rail	8
1.2.2 Analysis of the RDMS data	13
1.2.3 Rectification and total cost for the dominant failure mechanisms in switches	15
1.2.4 Dominant failure mechanisms and the resulting rail defects	16
1.3 Inspection, monitoring and maintenance procedures	20
1.3.1 An overview of the existing requirements for inspection of S&C rail in the UK	20
1.3.2 An overview of some of the common approaches to instrumented rail inspection	23
1.3.3 Evaluating the potential for detecting defects in S&C rails by implementing physical sensors for continuous condition monitoring	24
1.4 Research questions	29
1.5 Original contributions from the research	30
1.6 Conclusions from the chapter	32
CHAPTER 2. REVIEWING THE NUMERICAL SIMULATION APPROACHES AND SETTING OUT THE MODELLING METHODOLOGY FOR TRAIN-SWITCH INTERACTIONS.	34
2.1 A review of numerical simulation approaches, wheel-rail contact models and damage prediction models for Wear, RCF and Plastic deformation.	35
2.1.1 Numerical simulation approaches for modelling the interaction between trains and S&C.	35
2.1.2 Wheel/Rail contact modelling	45
2.1.3 Damage prediction models	53
2.1.4 Discussion of factors that would impact the choice of a modelling approach	62
2.2 Modelling methodology and assessment criteria	69
2.3 Digital Twin and selection of the reference model in the context of this thesis.	73
2.4 Conclusions	76

CHAPTER 3. DEVELOPING SOLID MODELS AND SIMULATING THE APPROPRIATE TRACK DYNAMICS FOR THE RAILWAY SWITCH IN TWO-STEP MBS-FE SIMULATIONS 77

3.1	Determining the sections of the switch track to monitor for the development of surface-initiated rail damage. _____	79
3.1.1	Different track models for vehicle-track interaction dynamics using MBS. _____	79
3.1.2	Description of the damage prediction model, the Wear number - ($T\gamma$). _____	97
3.1.3	Discussion of the results obtained for the Wear number ($T\gamma$) on the stock rail for simulations in the through route. _____	102
3.1.4	Discussion of the results obtained for the Wear number ($T\gamma$) on the switch rail for simulations in the through route. _____	103
3.1.5	Discussion of the results obtained for the Wear number ($T\gamma$) on the stock and switch rails for simulations in the through route _____	107
3.2	Developing a 3D, solid Finite Element Model of a railway track switch _____	108
3.3	Introducing rail receptance and determining the length of sleeper, longitudinal length of the track for the 3D FE model. _____	118
3.3.1	Determining the length of the sleeper _____	122
3.3.2	Investigating the effect of the length of a track model on the results for the rail receptance. _____	125
3.4	Derivation of the track properties and comparing the rail receptance against the reference _____	131
3.4.1	The stiffness for the pads and the baseplate _____	132
3.4.2	Modelling the effect of damping of the pads _____	135
3.4.3	The track properties for the ballast layer _____	143
3.5	Conclusions from the chapter _____	147
CHAPTER 4. FINITE ELEMENT ANALYSIS FOR THE ROLLING CONTACT INTERACTION BETWEEN THE TRAIN AND THE SWITCH. _____		149
4.1	Description of the FE model for the wheel-rail interactions _____	149
4.1.1	Steps in the simulation _____	150
4.1.2	Wheel-rail Contact model _____	151
4.1.3	Loading and the boundary conditions for the wheel _____	152
4.2	Meshing approach and mesh sensitivity analysis _____	156
4.2.1	Determining the ideal element size at the contacting surfaces _____	156
4.2.2	Assessment of the stress distributions at a specific cross-section of the rail for different mesh sizes _____	158
4.2.3	Effect of the mesh size on the strain time series on the rail head _____	163
4.3	Simulations for the wheel-switch contact interactions and comparing the outputs against the reference _____	166
4.3.1	Comparison of the wheel-rail interaction outputs between the MBS reference and the FE simulations _____	168

4.3.2	Influence of modelling the substructure dynamics on the results for the vertical contact forces	176
4.3.3	Influence of the substructure dynamics on subsurface rail strains	177
4.4	Conclusions	183
CHAPTER 5. WHEEL-RAIL ROLLING CONTACT ANALYSIS AFTER THE INTRODUCTION OF TRACK DEFECTS		185
5.1	Introduction of the defects in the track model	185
5.2	Effect of modelling track defects on the rail strains	189
5.3	Effect of modelling the different vehicle loads on the results for the wheel-rail interaction and subsurface rail strains	193
5.4	Conclusions from Chapter 5	198
CHAPTER 6. DETERMINING THE SENSOR PLACEMENT AND TESTING THE ABILITY OF FAULT DETECTION		200
6.1	Approach to determining sensor placement	200
6.2	Results from the Screening step when the wheel-rail contact results are captured where the surface rail defects are introduced in the sleeper spacing	206
6.3	Ranking the locations for determining the placement of sensors for the detection of the defect when the wheel-rail contact results are captured in the sleeper spacing	211
6.4	Determining sensor placement for monitoring the development of the defect at the sleeper-supported rail section	218
6.5	Results from the cross-section of the rail that shows the highest potential for fault detection	221
6.6	Testing the ability of the sensors installed at the proposed locations to detect the defects.	229
6.6.1	Occurrence of the rail defect between sleeper spacing and sensor installed on the rail in sleeper spacing.	232
6.6.2	Occurrence of the rail defect over supported sleeper and sensor installed on sleeper supported rail.	237
6.6.3	Occurrence of the rail defect between the sleeper spacing and sensor installed on sleeper supported rail.	242
6.6.4	Occurrence of the rail defect over sleeper supported rail and sensor installed on the rail in sleeper spacing.	244
6.7	Summary and Conclusions from Chapter 6	248
CHAPTER 7. CONCLUSIONS AND FUTURE WORK		251
7.1	Contributions from the thesis	251
7.2	Further work	255
LIST OF REFERENCES		258

LIST OF FIGURES

FIGURE 1: COMPONENTS OF A TURNOUT, REPRODUCED FROM [2].	2
FIGURE 2: TURNOUT AND DIAMOND, REPRODUCED FROM [2].	3
FIGURE 3: FACING AND TRAILING ROUTES IN A TURNOUT, REPRODUCED FROM [2].	4
FIGURE 4: APPEARANCE OF A RAILWAY TURNOUT, REPRODUCED FROM [5].	5
FIGURE 5: DIFFERENT APPROACHES FOR MACHINING THE SWITCH; (A) UNDERCUT AND FULL DEPTH SWITCH; (B) STRAIGHT CUT AND FULL DEPTH SWITCH; (C) CHAMFERED AND SHALLOW DEPTH SWITCH, REPRODUCED FROM [6].	7
FIGURE 6: DISTRIBUTION OF DELAY COST DUE TO S&C PWAY DEFECTS (NOT INCLUDING THE POINTS OPERATING EQUIPMENT (POE))	9
FIGURE 7: DISTRIBUTION OF DELAY COST DUE TO S&C TRACK COMPONENT DEFECTS (S&C CATEGORIES BROKEN DOWN)	10
FIGURE 8: POINTS (S&C) – CROSSING - COMPONENT LEVEL 2 CATEGORIES	10
FIGURE 9: POINTS (S&C) – SWITCH RAIL- COMPONENT LEVEL 2 CATEGORIES	11
FIGURE 10: POINTS (S&C) – STOCK RAIL- COMPONENT LEVEL 2 CATEGORIES	12
FIGURE 11: DISTRIBUTION OF DELAY COST DUE TO DEFECTS IN THE SUBSTRUCTURE AND FASTENING COMPONENTS	13
FIGURE 12: RDMS S&C DEFECT CATEGORIES	14
FIGURE 13: NR4 SIDEWEAR GAUGE MEASUREMENTS (A) NEW RAIL; (B) SIDEWORN RAIL, REPRODUCED FROM [26].	22
FIGURE 14: CO-RUNNING TRACK MODEL WITH TRACK FLEXIBILITY (ADAPTED FROM [43]).	36
FIGURE 15: CO-RUNNING TRACK WITH MULTIPLE DOFs (ADAPTED FROM [45]).	36
FIGURE 16: SOLID ELEMENT HALF-TRACK SWITCH MODEL WITH A SINGLE WHEEL	63
FIGURE 17: SOLID ELEMENT FULL TRACK SWITCH MODEL WITH ONE WHEELSET	63
FIGURE 18: SIMULATION APPROACH FOR THE INTERACTION BETWEEN RAILWAY VEHICLES AND TRACK SWITCHES	70
FIGURE 19: MEASURED AND SIMULATED VERTICAL CONTACT FORCES IN THE THROUGH ROUTE WITH SOFT RAILPADS, REPRODUCED FROM [68].	75
FIGURE 20: (A) SCHEMATIC OF THE TURNOUT; (B) STATIC TRACK STIFFNESS OF THE TURNOUT IN VERTICAL; (C) LATERAL DIRECTIONS; REPRODUCED FROM [41].	83
FIGURE 21: TRACK SCHEMATIC FOR THE THREE-LAYER MBS MODEL, REPRODUCED FROM SHIH ET AL. [41].	85
FIGURE 22: 3D SCHEMATIC OF THE RAILS OF THE 60E1-760-1:15 SWITCH LAYOUT WITH THE KEY LONGITUDINAL POSITIONS.	88
FIGURE 23: SCHEMATIC OF THE BOGIE FOR THE MANCHESTER BENCHMARK PASSENGER VEHICLE, REPRODUCED FROM [153].	89
FIGURE 24: LATERAL DISTANCES ALONG THE SWITCH AND STOCK RAILS.	94
FIGURE 25: SIMULATION RESULTS FROM MODEL 4: LATERAL AND LONGITUDINAL POSITIONS FOR THE CONTACT POINTS.	95
FIGURE 26: VERTICAL WHEEL-RAIL CONTACT FORCES FOR THE SWITCH RAIL IN THE THROUGH ROUTE, ADAPTED FROM [41].	95
FIGURE 27: TOTAL VERTICAL WHEEL-RAIL CONTACT FORCE- MODEL 4.	96
FIGURE 28: BILINEAR RCF DAMAGE FUNCTION [134].	98
FIGURE 29: WEAR NUMBER (Tt) ON CONTACT BETWEEN THE RIGHT-HAND STOCK RAIL AND THE LEADING, TRAILING WHEELS OF THE FIRST BOGIE.	102
FIGURE 30: WEAR NUMBER (Tt) ON CONTACT BETWEEN THE SWITCH RAIL AND THE WHEEL FOR A. WHEELSET 1 OF BOGIE 1; B. WHEELSET 2 OF BOGIE 1; C. WHEELSET 1 OF BOGIE 2; D. WHEELSET 2 OF BOGIE 2	104
FIGURE 31: LATERAL AND LONGITUDINAL CREEP FORCES FOR CONTACT POINT 1, WHEELSET 1 OF BOGIE 1.	105
FIGURE 32: LATERAL AND LONGITUDINAL CREEPAGES FOR CONTACT POINT 2, WHEELSET 1 OF BOGIE 1.	106

FIGURE 33: CREEP PARAMETERS FOR CONTACT POINT 2, WHEELSET 1 OF BOGIE 1; (A). LATERAL AND LONGITUDINAL CREEP FORCES; (B). LATERAL AND LONGITUDINAL CREEPAGES. _____	107
FIGURE 34: Tt NUMBER FOR THE CONTACT BETWEEN THE LEADING WHEEL OF THE LEADING BOGIE AND THE STOCK AND SWITCH RAILS FOR TRACK MODEL 4. _____	108
FIGURE 35: SCHEMATIC FOR THE MBS TRACK MODEL [12]. _____	109
FIGURE 36: ASSEMBLY OF THE TRACK MODEL ALONG WITH THE WHEEL; (A) FRONT VIEW; (B) ISOMETRIC VIEW. _____	109
FIGURE 37: (A) NOMINAL 60E1A1 SWITCH RAIL PROFILE; (B) SWEPT MATERIAL REMOVAL ON THE FIELD SIDE; (C) SWEPT MATERIAL REMOVAL ON THE TRACK-SIDE WHILST IMPLEMENTING THE MILLING TOOL PROFILE _____	111
FIGURE 38: MBS RAIL PROFILES- SWITCH ASSEMBLY AFTER MILLING, REPRODUCED FROM [65]. _____	111
FIGURE 39: RAIL CROSS-SECTION FROM THE SOLID MODEL AT A LONGITUDINAL DISTANCE OF 9.13 M FROM THE SWITCH TOE. _____	112
FIGURE 40: RAIL PROFILES AT A LONGITUDINAL DISTANCE OF 9.13 M FROM THE SWITCH TOE; A. MBS RAIL PROFILE; B. PROFILE FROM FE MODEL (UP TO A DEPTH OF 35 MM). _____	113
FIGURE 41: SWITCH RAIL SOLID GEOMETRY USED FOR ANALYSIS; (A) PERSPECTIVE FRONT VIEW; (B) 3D PLAN VIEW _____	113
FIGURE 42: SOLID GEOMETRY OF THE STOCK RAIL; (A) PERSPECTIVE FRONT VIEW; (B) 3D PLAN VIEW _____	114
FIGURE 43: GEOMETRY OF THE BASEPLATE THAT HOLDS THE STOCK AND THE SWITCH RAILS _____	114
FIGURE 44: BOUNDARY CONDITION FOR THE BOTTOM SURFACE OF THE SLEEPER WHEN IMPLEMENTING SIMPLIFIED BEDDING _____	117
FIGURE 45: VERTICAL POINT MOBILITY OF TRACK WITH DISCRETE AND CONTINUOUS SUPPORT, ADAPTED FROM THOMPSON [162]. _____	118
FIGURE 46: COMPARISON OF THE RAIL RECEPTANCE BETWEEN MODELS 2, 3 AND 4; A. VERTICAL RECEPTANCE; B. LATERAL RECEPTANCE, ADAPTED FROM [41]. _____	119
FIGURE 47: A. MEASURED MAXIMUM VERTICAL CONTACT FORCES IN THE CROSSING PANEL; B. MEASURED MAXIMUM LATERAL WHEEL-RAIL CONTACT FORCES IN THE SWITCH PANEL. _____	121
FIGURE 48: (A) THE HALF-SLEEPER, HALF-TRACK MODEL; (B) THE FULL-SLEEPER, HALF-TRACK MODEL _____	123
FIGURE 49: COMPARISON OF THE RAIL RECEPTANCE AGAINST THE REFERENCE MBS MODEL FOR DETERMINING THE LENGTH OF THE SLEEPER MODEL; (A) VERTICAL RAIL RECEPTANCE; (B) LATERAL RAIL RECEPTANCE _____	124
FIGURE 50: REGION OF INTEREST- 7.8 TO 10.5 M FROM THE TOE _____	125
FIGURE 51: REGION OF INTEREST WITH FOUR ADDITIONAL SLEEPERS- 6.6 TO 12.274 M FROM THE TOE _____	126
FIGURE 52: COMPARISON OF THE VERTICAL AND LATERAL RAIL RECEPTANCE AGAINST THE REFERENCE FOR DIFFERENT TRACK LENGTHS; (A) VERTICAL RECEPTANCE AT 7.9 M; (B) LATERAL RECEPTANCE AT 7.9 M; (C) VERTICAL RECEPTANCE AT 9.1 M; (D) LATERAL RECEPTANCE AT 9.1 M; (E) VERTICAL RECEPTANCE AT 10.3 M; (F) LATERAL RECEPTANCE AT 10.3 M. _____	129
FIGURE 53: COMPARISON OF THE APPROACHES TO INCLUDING PAD DAMPING IN FE; (A) COMPARISON OF VERTICAL RECEPTANCE AGAINST THE REFERENCE; (B) COMPARISON OF THE LATERAL RECEPTANCE AGAINST THE REFERENCE _____	137
FIGURE 54: COMPARISON OF THE DIFFERENT APPROACHES FOR INCLUDING THE STIFFNESS-PROPORTIONAL RAYLEIGH DAMPING COEFFICIENT; (A) COMPARISON OF THE VERTICAL RECEPTANCE AGAINST THE REFERENCE; (B) COMPARISON OF THE LATERAL RECEPTANCE AGAINST THE REFERENCE _____	139
FIGURE 55: SENSITIVITY STUDIES FOR THE LOSS FACTOR TO OBTAIN THE APPROPRIATE STIFFNESS-PROPORTIONAL RAYLEIGH DAMPING COEFFICIENTS; (A) COMPARISON OF THE VERTICAL RECEPTANCE AGAINST THE REFERENCE; (B) COMPARISON OF THE LATERAL RECEPTANCE AGAINST THE REFERENCE. _____	141
FIGURE 56: 3D FE MODEL FOR THE ANALYSIS OF WHEEL-RAIL ROLLING CONTACT _____	150
FIGURE 57: VERTICAL WHEEL SUSPENSION FORCE _____	154
FIGURE 58: VERTICAL SUSPENSION FORCES ON THE WHEEL AND WHEEL-SWITCH CONTACT FORCE. _____	154
FIGURE 59: RELATIONSHIP BETWEEN THE PEAK CONTACT PRESSURE, NUMBER OF ELEMENTS AND COMPUTATIONAL TIME, REPRODUCED FROM [77]. _____	158
FIGURE 60: MESH SENSITIVITY ANALYSIS FOR CAPTURING ACCURATE CROSS-SECTIONAL DISTRIBUTIONS FOR THE DIFFERENT MESH STRATEGIES; A TO E. VON MISES STRESS DISTRIBUTIONS; F. KEY FOR THE PLOTS WITH VON MISES STRESS VALUES IN PASCALS. _____	160

FIGURE 61: MIXED TETRAHEDRAL AND HEXAHEDRAL MESHING FOR CAPTURING THE APPROPRIATE CROSS-SECTIONAL STRESS DISTRIBUTIONS; A, B. VON MISES STRESS DISTRIBUTIONS FOR THE DIFFERENT MESH STRATEGIES; F. KEY FOR THE PLOTS WITH VON MISES STRESS VALUES IN PASCALS. _____	161
FIGURE 62: DIFFERENT POSITIONS ON THE RAIL HEAD AND WEB FOR PLOTTING THE VERTICAL STRAINS. _____	164
FIGURE 63: PLOT FOR THE VERTICAL STRAINS AT DIFFERENT LOCATIONS ALONG THE RAIL HEAD IN THE WEB IN THE TIME DOMAIN. _____	165
FIGURE 64: AMPLITUDE FOR THE LATERAL WHEEL DISPLACEMENT FROM THE MBS SIMULATION _____	169
FIGURE 65: COMPARISON OF THE VERTICAL CONTACT FORCE AGAINST THE REFERENCE MBS MODEL FOR DYNAMIC AND STATIC LOADING IN FE. _____	170
FIGURE 66: COMPARISON OF THE VERTICAL DISPLACEMENT OF THE WHEEL; A. COMPARISON OF THE AMPLITUDE OF THE WHEEL RAISE FROM THE POINT WHERE THE FE SIMULATION WOULD BEGIN; B. INFLUENCE OF THE STATIC AND DYNAMIC WHEEL LOADING ON THE OVERALL AMPLITUDE OF THE VERTICAL WHEEL DISPLACEMENT. _____	172
FIGURE 67: COMPARISON OF THE CONTACT POINT LOCATIONS BETWEEN MBS (CP1- SWITCH RAIL) AND FEA _____	173
FIGURE 68: OVERLAP BETWEEN THE MBS AND THE FEA CONTACT POINTS AT THE KEY LOCATIONS. _____	174
FIGURE 69: COMPARISON OF VERTICAL WHEEL-RAIL CONTACT FORCES FOR THE MODELS WITH AND WITHOUT THE SUPPORT STIFFNESS. _____	177
FIGURE 70: INFLUENCE OF MODELLING THE SUBSTRUCTURE DYNAMICS ON THE LONGITUDINAL STRAINS FOR THE SWITCH RAIL. CROSS-SECTIONAL STRAINS: (A) MODEL WITH FIXED RAIL; (B) MODEL WITH DETAILED SUBSTRUCTURE. VISUALISED FOR A LONGER LENGTH OF THE RAIL IN 3D: (C) MODEL WITH FIXED RAIL; (D) MODEL WITH DETAILED SUBSTRUCTURE. _____	179
FIGURE 71: INFLUENCE OF MODELLING THE SUBSTRUCTURE DYNAMICS; VERTICAL STRAINS FOR THE CROSS-SECTION OF WHEEL-RAIL CONTACT: (A) MODEL WITH FIXED RAIL; (B) MODEL WITH DETAILED SUBSTRUCTURE; VERTICAL STRAINS FOR THE SWITCH RAIL IN 3D: (C) MODEL WITH FIXED RAIL; (D) MODEL WITH DETAILED SUBSTRUCTURE. _____	181
FIGURE 72: EFFECT OF CONSIDERING THE DETAILED SUBSTRUCTURE; LATERAL STRAINS FOR THE CROSS-SECTION OF WHEEL-RAIL CONTACT: (A) MODEL WITH FIXED RAIL; (B) MODEL WITH DETAILED SUBSTRUCTURE; LATERAL STRAINS FOR THE 3D SWITCH RAIL: (C) MODEL WITH FIXED RAIL; (D) MODEL WITH DETAILED SUBSTRUCTURE. _____	182
FIGURE 73: INTRODUCTION OF THE RCF FAULT INTO THE MODEL; (A) REFERENCE DRAWING [166]; (B) THE FAULT INTRODUCED TO THE FE MODEL; (C) OCCURRENCE OF SQUATS ON A SWITCH. _____	187
FIGURE 74: MEASURED WEAR ALONG THE LENGTH OF THE CN60-350-1:12 TURNOUT, REPRODUCED FROM [43]. _____	187
FIGURE 75: MODELLING THE RAIL WEAR: (A) MODIFIED RAIL PROFILE WITH THE RAIL WEAR (ONLY A FINITE LENGTH HAS BEEN SHOWN); (B) DEPTH OF WEAR THAT WAS INTRODUCED ON THE RAIL SECTION _____	188
FIGURE 76: LOCATIONS FOR INTRODUCING WEAR, RCF AND VOIDING IN THE MODEL _____	189
FIGURE 77: CHANGE IN THE VERTICAL STRAINS DUE TO FAULT INTRODUCTION; (A) RCF DAMAGE; (B) WEAR DAMAGE; (C) VOIDING _____	191
FIGURE 78: CHANGE IN THE LONGITUDINAL STRAINS DUE TO FAULT INTRODUCTION; (A) RCF DAMAGE; (B) WEAR DAMAGE; (C) VOIDING _____	192
FIGURE 79: INFLUENCE OF THE INCREASE IN THE VEHICLE LOAD ON THE RESULTS FOR (A) VERTICAL WHEEL-RAIL CONTACT FORCE; (B) LONGITUDINAL STRAINS; (C) VERTICAL STRAINS. _____	194
FIGURE 80: INFLUENCE OF THE INCREASE IN THE VEHICLE LOAD ON THE RESULTS FOR (A) VERTICAL WHEEL-RAIL CONTACT FORCE; (B) LONGITUDINAL STRAINS; (C) VERTICAL STRAINS. _____	195
FIGURE 81: INFLUENCE OF THE INCREASE IN THE VEHICLE LOAD ON THE RESULTS FOR (A) VERTICAL WHEEL-RAIL CONTACT FORCE ON THE SWITCH RAIL; (B) CHANGE IN LONGITUDINAL STRAINS; (C) CHANGE IN VERTICAL STRAINS; (D) CONTACT POINT POSITIONS- NOMINAL LOAD _____	197
FIGURE 82: INFLUENCE OF THE INCREASE IN THE VEHICLE LOAD ON THE RESULTS FOR (A) VERTICAL WHEEL-RAIL CONTACT FORCE; (B) VERTICAL WHEEL DISPLACEMENT; (C) CHANGE IN THE SUBSURFACE RAIL STRAINS FOR THE MODEL WITH THE VOIDING DEFECT. _____	198
FIGURE 83: LOCATIONS THAT MEET THE SCREENING CONSTRAINTS FOR DETECTING THE PRESENCE OF THE MODELLED RCF DEFECT; (A) LATERAL STRAINS AND TARE LOAD; (B) LATERAL STRAINS AND HEAVIER	

LOAD; (C) VERTICAL STRAINS AND TARE LOAD; (D) VERTICAL STRAINS AND LADEN LOAD; (E) LONGITUDINAL STRAINS AND TARE LOAD; (F) LONGITUDINAL STRAINS AND LADEN LOAD. _____	207
FIGURE 84: LOCATIONS THAT MEET THE SCREENING CONSTRAINTS FOR DETECTING THE PRESENCE OF THE MODELLED WEAR DEFECT; (A) LATERAL STRAINS AND TARE LOAD; (B) LATERAL STRAINS AND HEAVIER LOAD; (C) VERTICAL STRAINS AND TARE LOAD; (D) VERTICAL STRAINS AND LADEN LOAD; (E) LONGITUDINAL STRAINS AND TARE LOAD; (F) LONGITUDINAL STRAINS AND LADEN LOAD. _____	209
FIGURE 85: LOCATIONS THAT MEET THE SCREENING CONSTRAINTS FOR DETECTING THE PRESENCE OF THE MODELLED VOIDING DEFECT; (A) LATERAL STRAINS AND TARE LOAD; (B) LATERAL STRAINS AND HEAVIER LOAD; (C) VERTICAL STRAINS AND TARE LOAD; (D) VERTICAL STRAINS AND LADEN LOAD; (E) LONGITUDINAL STRAINS AND TARE LOAD; (F) LONGITUDINAL STRAINS AND LADEN LOAD. _____	211
FIGURE 86: INTERSECTION OF THE LOCATIONS FROM ALL SIMULATIONS FOR DETECTING THE RCF DEFECT; (A) LATERAL STRAINS; (B) VERTICAL STRAINS; (C) LONGITUDINAL STRAINS. _____	213
FIGURE 87: INTERSECTION OF THE LOCATIONS FROM ALL SIMULATIONS FOR DETECTING THE WEAR DEFECT; (A) LONGITUDINAL STRAINS; (B) VERTICAL STRAINS; (C) LATERAL STRAINS. _____	214
FIGURE 88: INTERSECTION OF THE LOCATIONS FROM ALL SIMULATIONS FOR DETECTING THE VOIDING DEFECT; (A) LONGITUDINAL STRAINS; (B) VERTICAL STRAINS; (C) LATERAL STRAINS. _____	215
FIGURE 89: INTERSECTION OF THE LOCATIONS FROM ALL SIMULATIONS FOR DETECTING THE SURFACE DEFECTS; (A) LONGITUDINAL STRAINS; (B) VERTICAL STRAINS; (C) LATERAL STRAINS. _____	216
FIGURE 90: INTERSECTION OF THE LOCATIONS FROM ALL SIMULATIONS FOR DETECTING ALL THE SIMULATED DEFECTS; (A) LONGITUDINAL STRAINS; (B) VERTICAL STRAINS; (C) LATERAL STRAINS. _____	217
FIGURE 91: INTERSECTION OF THE LOCATIONS FROM ALL SIMULATIONS FOR DETECTING THE WEAR DEFECT ON THE SLEEPER; (A) VERTICAL STRAINS; (B) LONGITUDINAL STRAINS _____	218
FIGURE 92: INTERSECTION OF THE LOCATIONS FROM ALL SIMULATIONS FOR DETECTING THE RCF DEFECT ON THE SLEEPER; (A) VERTICAL STRAINS; (B) LONGITUDINAL STRAINS _____	219
FIGURE 93: INTERSECTION OF THE LOCATIONS FROM ALL SIMULATIONS FOR DETECTING THE VOIDING DEFECT ON THE SLEEPER; (A) VERTICAL STRAINS; (B) LONGITUDINAL STRAINS _____	219
FIGURE 94: INTERSECTION OF THE LOCATIONS FROM ALL SIMULATIONS FOR DETECTING THE SURFACE DEFECTS ON THE SLEEPER; (A) VERTICAL STRAINS; (B) LONGITUDINAL STRAINS _____	220
FIGURE 95: INTERSECTION OF THE LOCATIONS FROM ALL SIMULATIONS FOR DETECTING ALL DEFECTS ON THE SLEEPER; (A) VERTICAL STRAINS; (B) LONGITUDINAL STRAINS _____	221
FIGURE 96: RESULTS FOR THE CROSS-SECTIONAL STRAINS FROM THE WEAR SIMULATIONS- WHEEL-RAIL CONTACT ON THE SLEEPER; (A) VERTICAL STRAINS; (B) LONGITUDINAL STRAINS. _____	222
FIGURE 97: RESULTS FOR THE CROSS-SECTIONAL STRAINS FROM THE WEAR SIMULATIONS- WHEEL-RAIL CONTACT IN BETWEEN THE SLEEPER SPACING; (A) VERTICAL STRAINS; (B) LONGITUDINAL STRAINS. _____	223
FIGURE 98: RESULTS FOR THE CROSS-SECTIONAL STRAINS FROM THE RCF SIMULATIONS- WHEEL-RAIL CONTACT IN BETWEEN THE SLEEPER SPACING; (A) VERTICAL STRAINS; (B) LONGITUDINAL STRAINS. _____	224
FIGURE 99: RESULTS FOR THE CROSS-SECTIONAL STRAINS FROM THE RCF SIMULATIONS- WHEEL-RAIL CONTACT ON THE SLEEPER. (A) VERTICAL STRAINS; (B) LONGITUDINAL STRAINS. _____	224
FIGURE 100: RESULTS FOR THE CROSS-SECTIONAL STRAINS FROM THE VOIDING SIMULATIONS- WHEEL-RAIL CONTACT ON THE SLEEPER; (A) VERTICAL STRAINS; (B) LONGITUDINAL STRAINS. _____	225
FIGURE 101: RESULTS FOR THE CROSS-SECTIONAL STRAINS FROM THE VOIDING SIMULATIONS- WHEEL-RAIL CONTACT IN BETWEEN THE SLEEPER SPACING; (A) VERTICAL STRAINS; (B) LONGITUDINAL STRAINS. _____	226
FIGURE 102: RESULTS FOR THE CROSS-SECTIONAL STRAINS FROM ALL SIMULATIONS WITH THE SURFACE DEFECTS- WHEEL-RAIL CONTACT ON THE SLEEPER; (A) VERTICAL STRAINS; (B) LONGITUDINAL STRAINS. _____	226
FIGURE 103: RESULTS FOR THE CROSS-SECTIONAL STRAINS FROM ALL SIMULATIONS WITH THE SURFACE DEFECTS- WHEEL-RAIL CONTACT IN BETWEEN THE SLEEPER SPACING; (A) VERTICAL STRAINS; (B) LONGITUDINAL STRAINS. _____	227
FIGURE 104: RESULTS FOR THE CROSS-SECTIONAL STRAINS FROM THE SIMULATIONS WITH ALL DEFECTS- WHEEL-RAIL CONTACT ON THE SLEEPER; (A) VERTICAL STRAINS; (B) LONGITUDINAL STRAINS. _____	228
FIGURE 105: RESULTS FOR THE CROSS-SECTIONAL STRAINS FROM THE SIMULATIONS WITH ALL DEFECTS- WHEEL-RAIL CONTACT IN BETWEEN THE SLEEPER SPACING; (A) VERTICAL STRAINS; (B) LONGITUDINAL STRAINS. _____	228

FIGURE 106: OCCURRENCE OF THE RAIL DEFECT BETWEEN SLEEPER SPACING AND SENSOR INSTALLED ON THE RAIL IN SLEEPER SPACING. _____	229
FIGURE 107: OCCURRENCE OF THE RAIL DEFECT BETWEEN SLEEPER SPACING AND SENSOR INSTALLED ON THE RAIL IN SLEEPER SPACING. _____	230
FIGURE 108: OCCURRENCE OF THE RAIL DEFECT BETWEEN THE SLEEPER SPACING AND SENSOR INSTALLED ON SLEEPER SUPPORTED RAIL. _____	230
FIGURE 109: OCCURRENCE OF THE RAIL DEFECT OVER SLEEPER SUPPORTED RAIL AND SENSOR INSTALLED ON THE RAIL IN SLEEPER SPACING. _____	231
FIGURE 110: CORRELATION BETWEEN THE IMPACT FORCE AND THE VERTICAL RAIL STRAINS WHEN BOTH THE SENSOR AND THE DEFECT ARE IN THE SLEEPER SPACING; (A) TARE LOAD; (B) LADEN/HEAVIER LOAD. ____	233
FIGURE 111: HISTOGRAM FOR THE VERTICAL STRAIN VALUES FOR DETERMINING THE MEASUREMENT RANGE OF THE SENSOR WHEN BOTH THE SENSOR AND THE DEFECT ARE IN THE SLEEPER SPACING. _____	235
FIGURE 112: CORRELATION BETWEEN THE IMPACT FORCE AND THE LONGITUDINAL RAIL STRAINS WHEN BOTH THE SENSOR AND THE DEFECT ARE IN THE SLEEPER SPACING; (A) TARE LOAD; (B) LADEN/HEAVIER LOAD. ____	236
FIGURE 113: HISTOGRAM FOR THE LONGITUDINAL STRAIN VALUES FOR DETERMINING THE MEASUREMENT RANGE OF THE SENSOR WHEN BOTH THE SENSOR AND THE DEFECT ARE IN THE SLEEPER SPACING. _____	237
FIGURE 114: CORRELATION BETWEEN THE IMPACT FORCE AND THE VERTICAL RAIL STRAINS WHEN BOTH THE SENSOR AND THE DEFECT ARE ON THE SLEEPER-SUPPORTED RAIL SECTION; (A) TARE LOAD; (B) LADEN/HEAVIER LOAD. _____	238
FIGURE 115: HISTOGRAM FOR THE VERTICAL STRAIN VALUES FOR DETERMINING THE MEASUREMENT RANGE OF THE SENSOR WHEN BOTH THE SENSOR AND THE DEFECT ARE ON THE SLEEPER-SUPPORTED RAIL SECTION _	240
FIGURE 116: CORRELATION BETWEEN THE IMPACT FORCE AND THE LONGITUDINAL RAIL STRAINS WHEN BOTH THE SENSOR AND THE DEFECT ARE ON THE SLEEPER-SUPPORTED RAIL SECTION; (A) TARE LOAD; (B) LADEN/HEAVIER LOAD. _____	241
FIGURE 117: HISTOGRAM FOR THE LONGITUDINAL STRAIN VALUES FOR DETERMINING THE MEASUREMENT RANGE OF THE SENSOR WHEN BOTH THE SENSOR AND THE DEFECT ARE ON THE SLEEPER-SUPPORTED RAIL SECTION _____	242
FIGURE 118: CORRELATION BETWEEN THE IMPACT FORCE AND THE VERTICAL RAIL STRAINS WHEN THE SENSOR IS PLACED ON THE SLEEPER AND THE WHEEL PASSES OVER THE DEFECT BETWEEN THE SLEEPERS; (A) TARE LOAD; (B) LADEN/HEAVIER LOAD. _____	243
FIGURE 119: CORRELATION BETWEEN THE IMPACT FORCE AND THE LONGITUDINAL RAIL STRAINS WHEN THE SENSOR IS PLACED ON THE SLEEPER AND THE WHEEL PASSES OVER THE DEFECT BETWEEN THE SLEEPERS; (A) TARE LOAD; (B) LADEN/HEAVIER LOAD. _____	243
FIGURE 120: CORRELATION BETWEEN THE IMPACT FORCE AND THE VERTICAL RAIL STRAINS WHEN THE SENSOR IS PLACED BETWEEN THE SLEEPERS AND THE WHEEL PASSES OVER THE DEFECT ON THE SLEEPER; (A) TARE LOAD; (B) LADEN/HEAVIER LOAD. _____	244
FIGURE 121: CORRELATION BETWEEN THE IMPACT FORCE AND THE LONGITUDINAL RAIL STRAINS WHEN THE SENSOR IS PLACED BETWEEN THE SLEEPERS AND THE WHEEL PASSES OVER THE DEFECT ON THE SLEEPER; (A) TARE LOAD; (B) LADEN/HEAVIER LOAD. _____	246
FIGURE 122: HISTOGRAM FOR THE VERTICAL STRAIN VALUES FOR DETERMINING THE MEASUREMENT RANGE OF THE SENSOR WHEN THE SENSOR IS PLACED BETWEEN THE SLEEPERS AND THE WHEEL PASSES OVER THE DEFECT ON THE SLEEPER _____	247

LIST OF TABLES

TABLE 1: RELATIONSHIP BETWEEN S&C RAIL DEFECTS AND THE FAILURE MECHANISM, ADAPTED FROM [12].	19
TABLE 2. SUMMARY OF THE MBS NUMERICAL APPROACH	37
TABLE 3. SUMMARY OF FE NUMERICAL APPROACH FOR S&Cs	39
TABLE 4. SUMMARY OF COMBINED INDEPENDENT MODELLING APPROACH FOR S&Cs	43
TABLE 5. NORMAL CONTACT MODELLING APPROACHES	47
TABLE 6. TANGENTIAL CONTACT MODELLING APPROACHES	50
TABLE 7. SUMMARY OF DIFFERENT WEAR MODELS USED WITH S&C NUMERICAL SIMULATION	54
TABLE 8. SUMMARY OF DIFFERENT RCF MODELS USED WITH S&C NUMERICAL SIMULATION	57
TABLE 9. SUMMARY OF DIFFERENT MODELS FOR PLASTIC DEFORMATION USED WITH S&C NUMERICAL SIMULATION	60
TABLE 10: MODELLING ASSESSMENT CRITERIA	71
TABLE 11: TRACK CHARACTERISTICS OF THE MODELS THAT WERE VALIDATED AND THE FIELD MEASUREMENTS.	74
TABLE 12: TRACK PROPERTIES- BEAM ELEMENT FE MODEL (MODEL 2)	81
TABLE 13: TRACK PROPERTIES- THREE LAYER MBS MODEL (MODEL 4), ADAPTED FROM SHIH ET AL. [41].	86
TABLE 14: MASSES AND INERTIA FOR THE MANCHESTER BENCHMARK PASSENGER VEHICLE	89
TABLE 15: VEHICLE DIMENSIONS AND DISTANCES, ADAPTED FROM [153].	90
TABLE 16: VEHICLE SUSPENSION PROPERTIES, ADAPTED FROM [153].	91
TABLE 17: CASE STUDIES TO DETERMINE THE APPROPRIATE LENGTH FOR MODELLING	127
TABLE 18: QUANTITATIVE DIFFERENCES FOR THE RECEPTANCE RESULTS BETWEEN THE MODELS WITH THE SHORTEST AND LONGEST LENGTHS.	130
TABLE 19: GEOMETRY AND MATERIAL DETAILS FOR THE MODELLED COMPONENTS	132
TABLE 20: VARIABLES IN EQUATION 4 AND THEIR MEANING	134
TABLE 21: STIFFNESS AND EQUIVALENT YOUNG'S MODULUS FOR THE RAILPAD, BASEPLATE AND BASEPLATE PAD LAYERS.	135
TABLE 22: QUANTITATIVE COMPARISONS FOR THE RAIL RECEPTANCE- MASS AND STIFFNESS PROPORTIONAL DAMPING.	137
TABLE 23: QUANTITATIVE COMPARISONS FOR THE RAIL RECEPTANCE- DIFFERENT APPROACHES TO OBTAINING THE STIFFNESS-PROPORTIONAL DAMPING.	140
TABLE 24: RESULTS FROM THE SENSITIVITY STUDIES FOR THE LOSS FACTOR FOR IMPLEMENTING STIFFNESS- PROPORTIONAL DAMPING.	142
TABLE 25: FINAL DAMPING VALUES FOR THE RAILPAD AND BASEPLATE PAD	143
TABLE 26: CALCULATIONS FOR CAPTURING THE VERTICAL STIFFNESS OF THE BALLAST LAYER IN FE	144
TABLE 27: CALCULATIONS FOR CAPTURING THE VERTICAL DAMPING PROPERTIES OF THE BALLAST LAYER IN FE	145
TABLE 28: CALCULATIONS FOR CAPTURING THE LATERAL STIFFNESS OF THE BALLAST LAYER IN FE	145
TABLE 29: CALCULATIONS FOR CAPTURING THE LATERAL STIFFNESS OF THE BALLAST LAYER IN FE	146
TABLE 30: FINAL TRACK PROPERTIES FOR IMPLEMENTATION IN FE	147
TABLE 31: MASS AND STATIC LOADING PROPERTIES FOR THE VEHICLE	152
TABLE 32: RAIL SURFACE ELEMENT SIZES IMPLEMENTED IN THE FEA OF S&Cs.	157
TABLE 33: QUANTITATIVE COMPARISON OF THE RESULTS FOR THE VON-MISES STRESS FROM THE DIFFERENT MESHING STRATEGIES.	162
TABLE 34: COMPARISON OF THE VERTICAL WHEEL-RAIL CONTACT FORCE	170
TABLE 35: COMPARISON OF THE CONTACT PATCH DIMENSION BETWEEN THE MBS AND THE FEA MODELS AT 9.3 M.	175
TABLE 36: COMPARISON OF THE LONGITUDINAL STRAINS ON THE RAIL WEB AND FOOT DURING WHEEL-RAIL CONTACT IN THE SLEEPER SPACING.	178

TABLE 37: LIST OF THE PARAMETRIC STUDIES THAT HAVE BEEN IMPLEMENTED FOR DETERMINING SENSOR PLACEMENT _____	201
TABLE 38: DIFFERENT VARIABLES IN THE SIMULATIONS _____	203
TABLE 39: AVERAGE CHANGE IN THE VERTICAL STRAINS WHEN THE SENSOR AND THE SURFACE DEFECT ARE IN THE SLEEPER SPACING. _____	234
TABLE 40: AVERAGE CHANGE IN THE LONGITUDINAL STRAINS WHEN THE SENSOR AND THE SURFACE DEFECT ARE IN THE SLEEPER SPACING. _____	236
TABLE 41: AVERAGE CHANGE IN THE VERTICAL STRAINS WHEN THE SENSOR AND THE SURFACE DEFECT ARE ON THE SLEEPER-SUPPORTED RAIL SECTION. _____	239
TABLE 42: AVERAGE CHANGE IN THE VERTICAL STRAINS WHEN THE SENSOR AND THE SURFACE DEFECT ARE ON THE SLEEPER-SUPPORTED RAIL SECTION. _____	241
TABLE 43: AVERAGE CHANGE IN THE VERTICAL STRAINS WHEN THE SENSOR IS PLACED BETWEEN THE SLEEPERS AND THE WHEEL PASSES OVER THE DEFECT ON THE SLEEPER. _____	245
TABLE 44: AVERAGE CHANGE IN THE LONGITUDINAL STRAINS WHEN THE SENSOR IS PLACED BETWEEN THE SLEEPERS AND THE WHEEL PASSES OVER THE DEFECT ON THE SLEEPER. _____	247

CHAPTER 1. INTRODUCTION

This chapter will introduce the basic concepts and motivations behind the research topic as well as the hypotheses that have driven the research approach. In Section 1.1, a high-level explanation of Switches and Crossings (S&C) will be carried out whilst focusing on the layout design and the main components of S&C that are relevant to this thesis. In Section 1.2, the main conclusions from the literature reviewed in the area of S&C failure analysis will be discussed which has aided in narrowing down the focus of this research to the crucial failure mechanisms of the S&C permanent way (PWay) that would affect their safe and cost-effective operation. The existing and potential approaches to inspecting and monitoring the S&C PWay will be explained in Section 1.3 whilst building a case around the potential benefits of continuously monitoring the structural health of the S&C PWay. In Section 1.5, the contributions of this research by implementing a numerical simulation approach for carrying out structural health monitoring studies and the hypotheses that have driven the research approach will be explained. Section 1.6 will summarise the key topics that will be discussed in this chapter and how they will influence the research that will be discussed in the following chapter.

1.1 Switches and Crossings

The operation of conventional railways relies on the interaction between two main railway subsystems, the train and the track, also known as the permanent way. Permanent Way infrastructure limits the Degrees of Freedom (DOF) of travel for trains. Switches and Crossings play an important role in permanent way infrastructure by facilitating the changing of direction and the connection of different routes for trains.

A turnout essentially facilitates the diversion of a railway vehicle from one track to another and it comprises a pair of switch rails and a crossing that are connected by closure rails [1]. A common turnout and its components can be observed in Figure 1. It consists of a switch, crossing and a closure panel for connecting the first two.

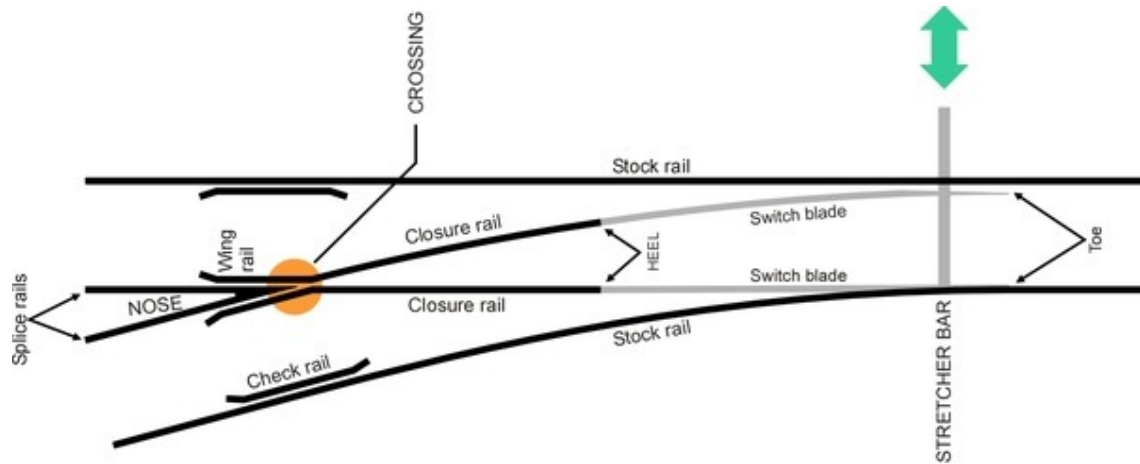


Figure 1: Components of a turnout, reproduced from [2].

Regardless of their complexity, every S&C layout is developed from the combinations of the switch, common crossing or obtuse crossing [3].

As shown in Figure 1, a set of switches comprises four rails, two fixed stock rails and the associated moveable switch rails.

Common crossings provide a point for the intersection of the two routes and include a crossing nose of 'V' shape as shown in Figure 1. As opposed to diamonds that have obtuse crossings, the crossing in a turnout generally has an acute angle. Since the population of acute crossings is higher than obtuse crossings, they are mainly referred to as 'common' crossings.

Obtuse crossings have been shown in Figure 2 and play a part in layouts such as diamonds for ensuring the "intersection of two corresponding gauge lines of intersecting tracks" whilst including two crossing noses [1].

Common or obtuse crossings can be fixed or moveable. Movable common and obtuse crossings are known as swing nose and switch diamonds respectively. An assembly of S&C in either turnouts or diamonds is known as a layout.

Regardless of their complexity, switch and crossing layouts are constructed to meet two main objectives. The first objective is to allow tracks to cross one another and the second is to ensure the ability of one track to diverge from or merge with another [1].

The first objective can be performed by a diamond and the second one can be performed by a turnout. It can be seen in Figure 2 that a turnout consists of both a switch and a crossing whereas a diamond could only consist of the crossing part for enabling the intersection between two lines.

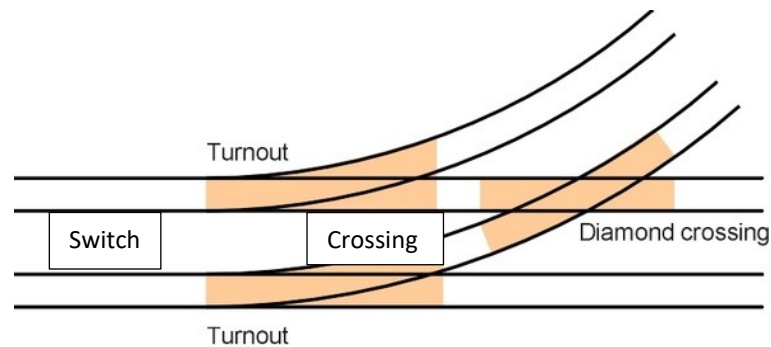


Figure 2: Turnout and Diamond, reproduced from [2].

Turnouts can be categorised on the basis of the predominating traffic direction as well as right or left handedness. Depending on the predominating traffic direction, the flow of traffic over turnout would be in the facing or the trailing route. As shown in Figure 3, if the tracks of a turnout diverge in the prevailing direction of the traffic, then the turnout is known as a facing turnout. If the flow of traffic is such that the two lines merge, then the turnout direction is known as the trailing route.

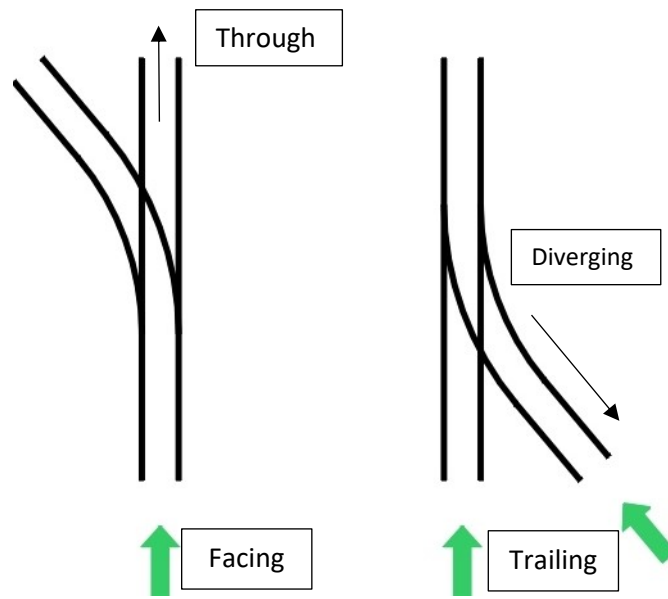


Figure 3: Facing and trailing routes in a turnout, reproduced from [2].

If the vehicle continues to move in the direction in which it entered the turnout, i.e. it passes straight through then the track over which it passes is known as the through track and the vehicles passes in the through route. On the contrary, if the direction of travel must change, then it would pass the turnout in the diverging route.

Based on the divergence of turnouts, they can be classified as right hand and left hand turnouts. As the name implies, the turnout diverges in the right and left directions respectively in right and left hand turnouts. Based on this definition, the turnout shown in Figure 3 is a left hand turnout.

There are various configurations in which S&Cs can be built and the reader is referred to the literature for understanding the various layouts that can be implemented [3]. For simplicity and relevance to this thesis, the content that will be discussed would be related to a common turnout.

The designation of turnouts, which is based on the geometry of the rail, includes the switch radius and the crossing angle. For example, a 60E1-R760-1:15 turnout would include rails with 60E1 profile, a switch radius of 760 m and a crossing angle of 1:15.

The geometry of the turnout would influence the speed of the train that would pass over it. A switch radius of 760 m and a crossing angle of 1:15 or 3.732 degrees would allude to the long length of the turnout as well as its long length of diversion. This implies that trains can pass through the turnout at relatively high speeds. In fact, the line speed of the 60E1-R760-1:15 turnout is 160 km/hr [4].

The appearance of a common turnout, which was schematically presented and discussed through Figure 1 has been shown in Figure 4. The stock and the switch rails were defined earlier by referring to the schematic in Figure 1. The role of a crossing in a turnout was discussed and explained through the schematic in Figure 2 and the crucial impact-bearing component in the crossing panel, i.e. the crossing nose can be observed in Figure 4.

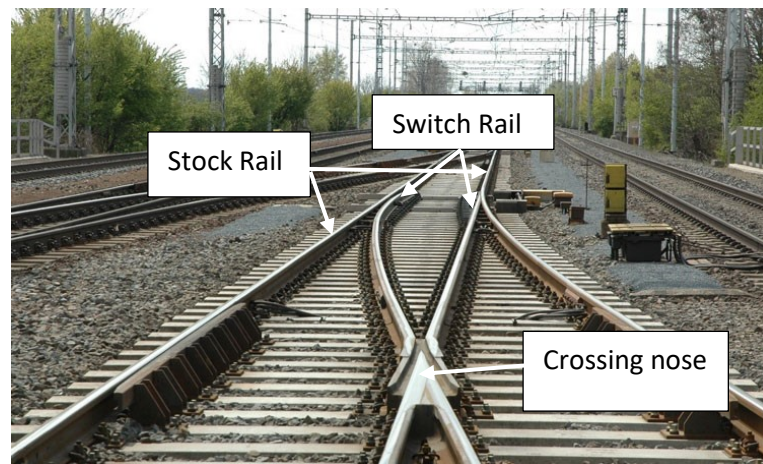


Figure 4: Appearance of a railway turnout, reproduced from [5].

Since the research that has been discussed through this thesis mostly concerns the switch panel, a quick overview of the important components of the permanent way in the switch panel that will be frequently discussed in this thesis has been provided.

As shown in Figure 4, the rail profile of the stock rail is the same as the section of the singular rail section preceding the S&C that it is connected to. The stock rail is machined to accommodate the switch which rests against it for the transition of the wheel-rail contact patch between the two rails. In the facing route, the wheel-rail contact patch for one side always stays on the stock rail and moves from the stock to the switch rail for the other side. The switch rail is machined to a point at one end

and the portion of the rail that is tapered is known as the switch tongue, which is designed to fit closely against the stock rail. The end of the switch tongue is also known as the toe or the tip of the switch. The switch tongue is the movable portion of the switch and is connected to a driving mechanism for moving it away from the stock rail so that the wheel can pass over the stock rail and in between the two rails.

From the switch toe up to the point where the switch is moveable, the switch is supported by slide baseplates. As shown in Figure 5C, the baseplate supports both the switch and the stock rails and allows the switch to slide horizontally with minimum friction. Just as the beginning of the switch is known as the switch toe/tip, the portion that is the end of the switch is known as the switch heel.

The rail sections can be broadly classified as plain line/full depth and shallow depth. As shown in Figure 5, the three profiles for machining the rail are undercut, straight cut and chamfered [1].

As shown in Figure 5A, undercut switch railhead machining would result in the formation of a very thin portion of the switch as the stock rail is not machined. This thin portion can be chipped and worn off easily and therefore this design has been obsolete in the UK since the 1970s [1].

On the contrary, a straight-cut switch would leave a larger portion of the thickness of the switch intact than an undercut switch and thus exceeds its gauge. For straight-cut, full-depth switches such as the one shown in Figure 5B, the rail foot of both the stock and the switch rails are vertically machined. This is beneficial when the switch is closed but would result in reduced structural support on the rail foot when the switch is open [1].

In chamfered switches, the railhead for both the switch and the stock rails are machined as shown in Figure 5C. The side of the head on the stock rail is machined to 1:4 or 14° [1]. This design improves the continuity of the transition of the wheel between the stock and the switch rails. For shallow-depth switches, the rail web is thick, and the foot is long which results in improved load-bearing capacity for the switch.

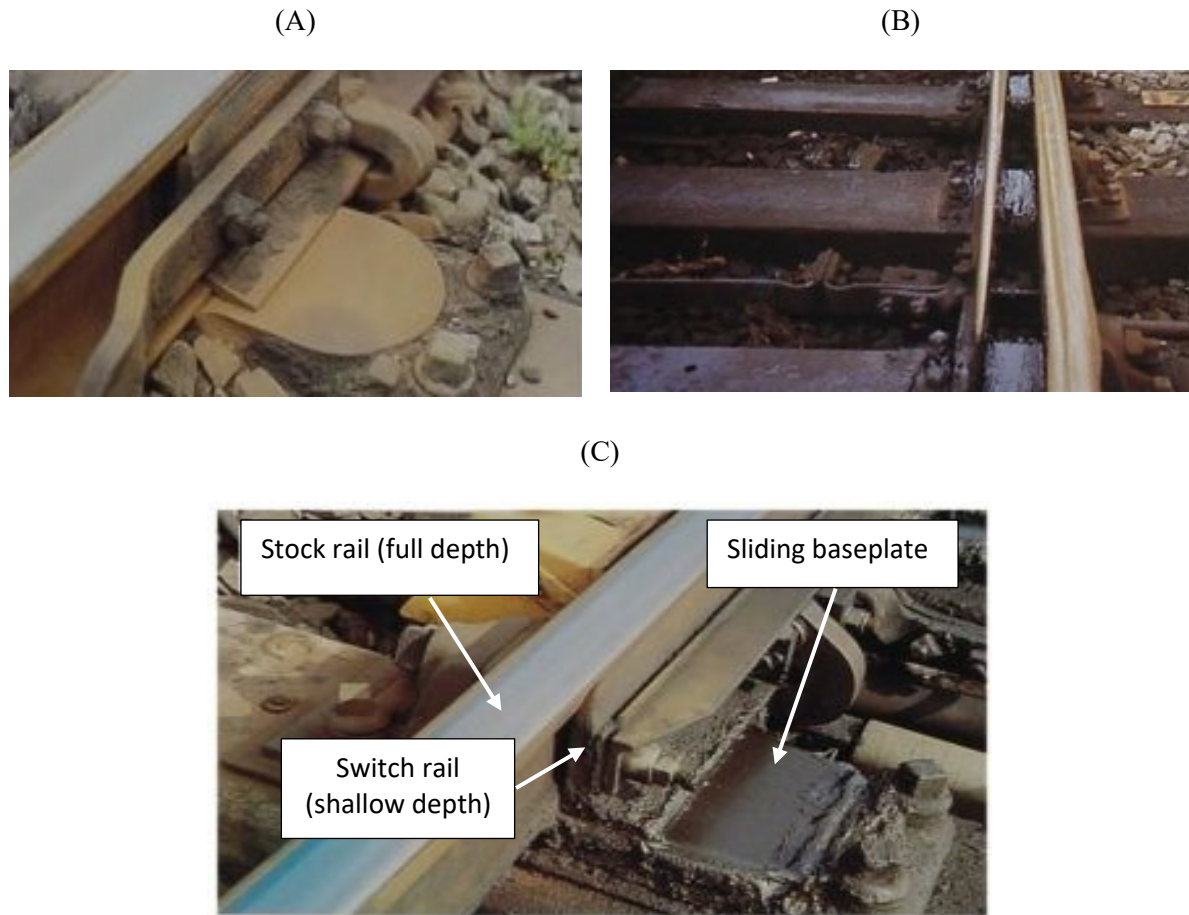


Figure 5: Different approaches for machining the switch; (A) Undercut and full depth switch; (B) Straight cut and full depth switch; (C) Chamfered and shallow depth switch, reproduced from [6].

1.2 Failures in S&C and associated defects

Although S&C made up just 5% of the total track miles in Britain between 2009 and 2011, they contributed to 23% of the renewal and 24% of the maintenance budgets for Network Rail [7]. This makes S&C one of the most expensive assets to maintain among the different subsystems of railway infrastructure.

The different defects that would result in the failure of S&C will be discussed in this section. Fault records that were provided to the University of Birmingham by Network Rail were analysed as part of a research project for determining the dominant causes of failure in S&C [8]. Fault records were obtained from three Network Rail databases. The first database is the Network Rail Fault Management System (FMS) records that include faults affecting service and delay minutes between April 2013 and

June 2018. The second database is the Network Rail Defect Management System (RDMS) which included rail defects occurring in the vicinity of plain line and S&C rail between April 2016 and June 2018. The third database, Ellipse, provides a snapshot of all the S&C on Network Rail infrastructure along with significant amounts of metadata. Crossing cracks and breaks were analysed from Ellipse data.

In addition, other data on the failure of S&C that has been published in the literature will be considered. Data from Network Rail that was gathered between 2009 and 2012 were analysed by Cornish [9]. The data was obtained from 3 main databases, namely GEOGIS (Geography and infrastructure system), TRUST (Train running system TOPS (total operation processing system)) and FMS. The failures in S&C that were captured by Network Rail's RDMS records database between 2011 and 2017 were statistically analysed by Grossoni et al. [10].

1.2.1 FMS records from Network Rail

The delay costs, i.e. the cost to Network Rail due to train delays have been analysed using data from the FMS database. Costs attributed to delays are assigned once the delay has stopped affecting the resumption of services [9]. Some factors that influence the cost of delay include the train operator, the number of trains that were cancelled because of the disruption and the amount of time the delay lasted. If the delay is due to the failure of infrastructure then the train operator would fine the infrastructure owner. The fine ranges from “£7 for a minute delay on a suburban service” up to “£25,000 for the cancellation of a train on a high-speed service” [9]. This data excludes the maintenance and repair costs.

According to Network Rail's delay attribution data from 2013-2014, S&C contributed 11% of the total delay minutes in 2013-14. This figure can be dissected for the different S&C subsystems.

A top-down analysis of the FMS data between April 2013 and June 2018 for the various S&C subsystems has been discussed. Among the various S&C subsystems, 72% of the delay costs could be attributed to the failure of Points Operating Equipment. A significant 27%, amounting to almost £20

million in fines per annum is spent on delay minutes that occur due to the failure of S&C permanent way (PWay) components. 1% of the delay costs are the results of the failure of points heating. This observation shows a good agreement with the analysis by Cornish that a higher percentage of failures occurred for the Points Operating Equipment than the S&C Permanent Way between 2009 and 2012 [9].

The contribution of the different S&C PWay assets to the delay costs can be observed in Figure 6. S&C PWay track components accounted for 66% of all the delay costs resulting from S&C PWay assets. 21% of the delay costs attributed to S&C PWay assets were the result of the substructure. 5% of the delay cost due to S&C PWay failure could be attributed to staff error and the other miscellaneous costs would result in the remaining expenditure.

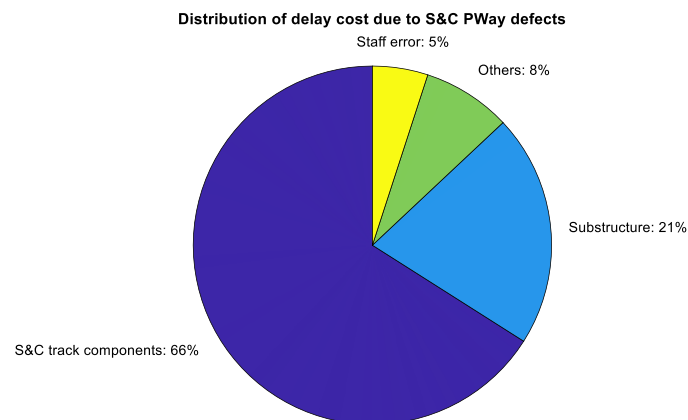


Figure 6: Distribution of delay cost due to S&C PWay defects (not including the Points Operating Equipment (POE))

As shown in Figure 7, the crossing rail failures contribute to half of the total delay costs among the main S&C PWay components. 46% of the costs could be attributed to the switch and stock rail assembly. The other rails accounted for less than 2% of the delay costs. Despite being a safety-critical component whose failure has resulted in accidents such as the one near Grayrigg in England [11], stretcher bar failures accounted for just 1% of the total delay cost due to S&C track components.

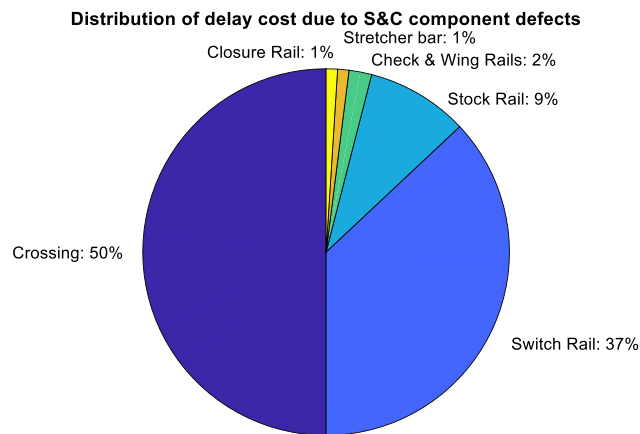


Figure 7: Distribution of delay cost due to S&C track component defects (S&C categories broken down)

Among the three S&C panels, the crossing panel contributes a little more than the switch panel to the delay costs. Among the different factors for the delay cost of the crossing, the cracking of cast crossings contributed to 68% of the total delay costs due to crossing failure. Along with the cracking of crossings that occurs due to fatigue, surface wear/damage of crossings is another major contributor that made up 8% of the total delay costs. Essentially, the different types of failure modes that can be observed in Figure 8 manifest themselves in the form of the degradation of the crossing rail.

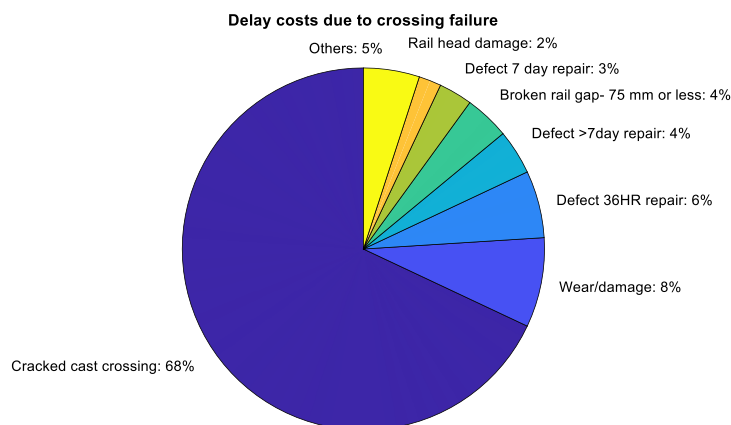


Figure 8: Points (S&C) – crossing - component level 2 categories

The breakdown of the switch rail failures that would result in high delay costs has been provided in Figure 9 and the same has been provided for the stock rail in Figure 10. The obstruction of the rails resulted in 30% of the delay costs for the switch rails.

The defects on the rail contributed to the rest of the delay costs in switch rails. Almost 22% of the total delay cost due to switches was due to Wear/Surface-initiated damage of switches. For the switch and the stock rails together, over £6 million of delay costs are a result of wear and rail damage.

Additionally, other rail defects and obstructions contribute to the total delay cost in switches.

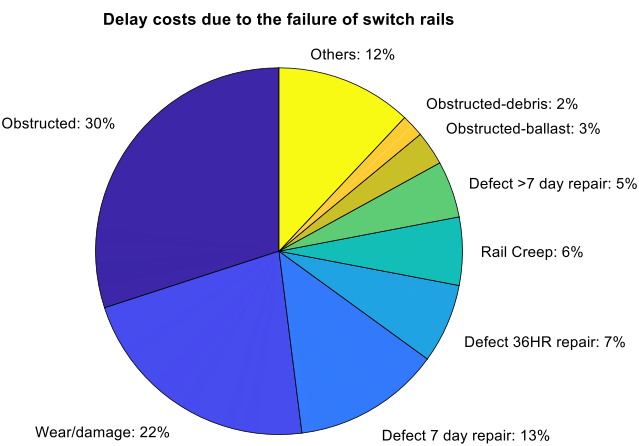


Figure 9: Points (S&C) – switch rail- component level 2 categories

As shown in Figure 7, the stock rail does experience degradation but not to the same extent as the switch rail. The variable and discontinuous cross-sectional geometry of the switch rail means that it is more susceptible to damage. The causes of stock rail failure resulting in the delay costs have been shown in Figure 10. The overall delay costs resulting from the stock rail are lower than those for the switch rail.

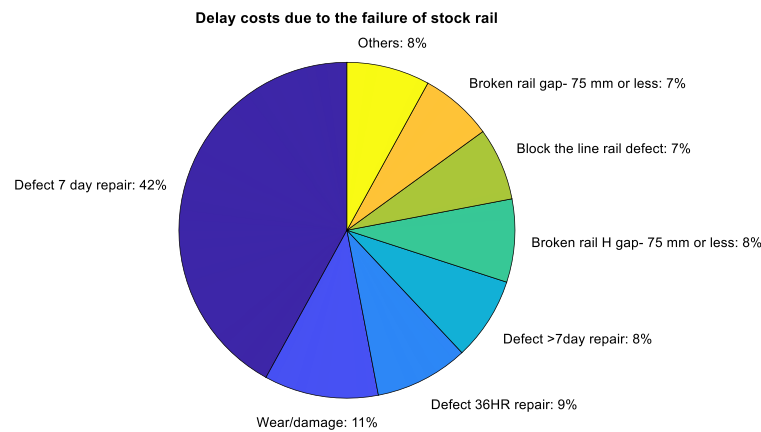


Figure 10: Points (S&C) – stock rail- component level 2 categories

Apart from the rails, other PWay-related damage costs can be attributed to the failure of the fastening system and the substructure. The results for the delay costs resulting from these components have been presented together in Figure 11. Baseplates, chairs and roller defects account for 46% of the total fastening and substructure-related defects. Ballast-related failure takes the second spot with 23% of the delay costs. The failure of connectors such as blocks, pins, bolts and studs results in 12% of the delay costs in this segment. Track geometry failures, including gauge, top and alignment failures contribute to 14% of the delay costs resulting from this segment. It is also worth noting that voiding contributes to 71% of the total costs resulting from the failure of the ballast. Insufficient ballast, poor ballast profile and contamination of the ballast are some of the other causes of failure of the ballast layer that result in delay costs.

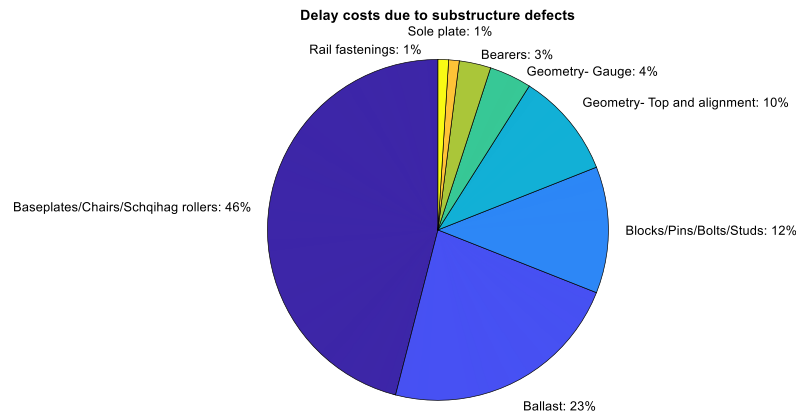


Figure 11: Distribution of delay cost due to defects in the substructure and fastening components

1.2.2 Analysis of the RDMS data

In the RDMS database, the failure information has been mapped against the location such as the operating route, location, type of permanent way e.g. switch, crossing, plain line etc., rail profile, assembly and track category, code, and the grade of material.

In the RDMS database, the defects are laid out against groups that are listed as 3-digit codes. Failures occurring at switches have a group code of 500 and the group code for crossing failures is 700. Rail ends are labelled as code 100, code 300 for mid-rail damage, 400 for weld-related failures and 600 is used to represent machined rails.

Network Rail's FMS database includes the delay cost for different S&C components. On the other hand, the RDMS data provided by Network Rail helps determine the dominant modes of failure of S&C rail. 75% of the faults that have been reported in the RDMS database include 504 (Switch blade damage); 727 (squat on crossing); 502 (Switch blade and stock rail both sideworn); 701 (Misshaped nose or wear/damage in wheel transfer area > 3 mm deep); 709 (lipping on crossing); 209 (lipping); 721 (shelling/flaking of wheel contact surface); 609 (lipping on reduced section rail). These defects occur over all S&C rails and the split obtained from the RDMS data has been shown in Figure 12. Faults in crossing and switch panel rails account for 39 and 40% of the rail-related defects respectively.

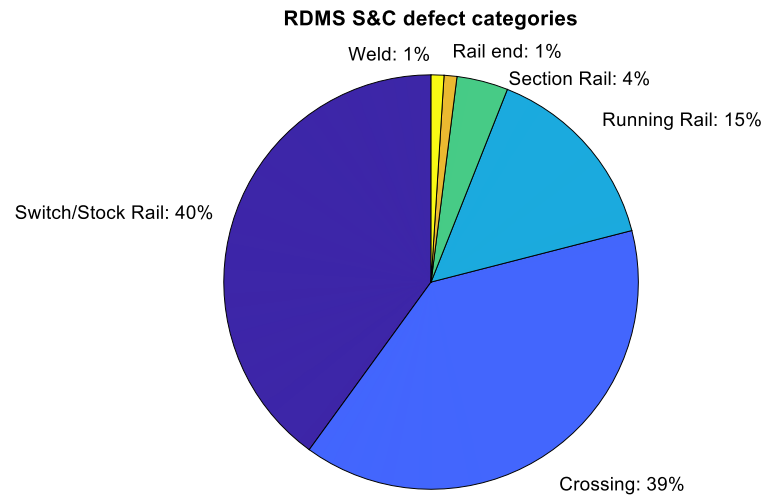


Figure 12: RDMS S&C defect categories

According to the analysis of the RDMS data by Grossoni [10], one-fifth of all reported failures occurred on the switch blade over a seven-year period. It is one of the least durable sections of S&C due to its tapered geometry. Although material grades with higher strength such as “HP335” have been experimented with for switches, their deployment has not been successful [10].

53% of the faults occur in the crossing panel as opposed to 44% in the switch panel [10]. 5 main types of failure categories account for all the faults in the switch panel. In contrast, 80% of the failures in the crossings result from just 6 main failure types. Overall, the majority of the causes resulting in the failure of S&C can be traced to the formation of surface defects. For the different types of S&C assemblies, most of the failures occur on the common S&C assembly whilst failure in obtuse crossings/diamonds accounts for just 5% of the total failures, which is also influenced by their numerical inferiority.

In the switch panel, the damage of the switch blade damage (504) accounts for 62% of all faults. The wear of the switch and stock rail together account for the next largest contributor (22%) [10]. The damage of the switch blade could occur for various reasons, with lipping being the dominant reason for switch blade damage (47%). Cracks and breaks result in 7% and 5% of the damage in the switch blade respectively. Excessive damage of the stock rail is another fault category in the RDMS database,

which can be expected when the predominant direction of travel is the through route and the superelevation of the track is substantial [10]. Lipping is one of the most important factors that would lead to the damage of the switch blade and occurs mostly on fast lines [10].

One third of all the faults in the crossing panel manifest themselves in the form of a squat on casting. Essentially crossing materials are hard, which improves their wear resistance but makes them more susceptible to crack formation and rolling contact fatigue (RCF). In reduced section rails such as switch rails, wing rails and check rails, plastic deformation and RCF are the dominant failure mode and account for 90% of observed failures.

It has also been stated that the loss of support stiffness and the presence of voiding in the switch panel would significantly increase the chance of switch blade failure [10]. Similarly, the rail defects that would result from voiding in the crossing panel include squats, plastic deformation and transverse cracking [10].

To summarise, one-fifth of all rail faults occur on the switch blade, which makes it an important subsystem to monitor. The majority of the switch blade damage takes the form of lipping, which predominantly occurs due to the passage of the vehicles in the through-route on high-speed lines. Similarly, wear is the second most prevalent failure mechanism in the rails of the switch panel and is more dominant in switches than crossings since the strength of the rail material is less in the switches than in crossings [10].

1.2.3 Rectification and total cost for the dominant failure mechanisms in switches

A significant portion of the budget is spent on the cost for maintenance and renewals occurring due to wear, fracture and plastic deformation of S&C rails. Cornish [9] calculated the total failure cost which is the sum of the total delay cost and the estimated cost for rectifying the defects. It was determined that wear, fracture and plastic deformation of rails are the failure mechanisms that would contribute the most to the total failure cost of switches and can be rectified by implementing various methods.

For rectifying failures resulting from plastic deformation such as lipping and switch rail damage, grinding is carried out, thus extending the time to replace the rail. Therefore, the failure cost due to plastic deformation in the rails of the switch panels was estimated to be the lowest [9].

The rectification for the fracture failure varies depending on the root cause of the fault that would result in the failure. Fracture of the rail can be rectified through either welding or the complete replacement of the S&C unit, depending on the severity of the failure. Cracks appearing at the top of the railhead due to rolling contact fatigue can be treated by removal through grinding. The portion of the rail that is broken off is either welded or the complete S&C unit is replaced.

Several alternate rectification approaches are implemented for treating worn rail. The rectification approach depends on the individual fault that is experienced by the rail. A damaged rail can either be welded or replaced. 89% of fractures take place within a weld and the rectification would only require the weld to be replaced and not the complete S&C unit. Under these circumstances, the total failure cost does not increase as much as it would if the components had to be replaced.

It was also estimated that 50% of the wear in rails can be repaired by welding but the other 50% would require the replacement of a unit. The total failure cost resulting from these individual defects was obtained and it has been determined that wear of the rails would contribute the most to the total failure cost. High-speed switches are more likely to experience wear damage than ones that are subject to lower line speeds [9], as the creep forces that would remove surface rail material would be higher. Among the different S&C failure mechanisms, the failure of the switch blade accounted for 53% of the total failures [9], which also quantifies the benefit of monitoring switches in order to improve safety and reduce costs.

1.2.4 Dominant failure mechanisms and the resulting rail defects

The various forms of defects observed in rails can be classified into two distinct categories [9,12]. Category 1 encompasses localised imperfections originating from mechanisms near the wheel-rail contact zone. Category 2 encompasses failure mechanisms that take place away from the contact point,

induced by broader system conditions like track quality, manufacturing flaws, and abnormal loading [9]. The primary Category 1 failure mechanisms that lead to a range of defects on S&C rails comprise of wear, rolling contact fatigue (RCF), and plastic deformation [12].

In the interaction between the surfaces of the wheel and rail, bonding takes place at specific points or junctions due to surface irregularities. When these junctions break as the surfaces move in relation to each other, the tip detaches from the softer surface and sticks to the harder surface, causing the subsequent layer of the surface tip to become loose, leading to the generation of wear debris [13]. In switch panel rails, wear primarily occurs when there is high creepage or differential velocity [10], coupled with elevated tangential forces, particularly on the diverging route, affecting both the switch and stock rails.

Repetitive loading and passage of vehicles over S&C rails, particularly at locations with discontinuities and significant wheel impact, result in RCF. This usually manifests as either material removal from the rail surface or the formation of subsurface cracks. RCF damage in S&Cs progresses through three stages: crack initiation, crack propagation, and eventual fracture or collapse of the structure. Surface RCF cracks, identified by material removal from the rail surface, are initiated due to ratcheting caused by the accumulation of plastic deformation on the rail head [14]. This is influenced by high contact stresses and forces affected by steering and traction [14]. Subsurface-initiated RCF occurs beneath the running rail surface, particularly pronounced at the rail gauge corner. It is more likely to happen under operational conditions with high normal wheel–rail contact forces and smaller contact patches, compounded by the presence of material defects [14].

Plastic deformation or permanent alteration of S&C rail material occurs when the rails are subjected to significant loads, causing stresses that surpass their elastic limit. This leads to residual stresses altering the internal microstructure of the material. The extent of deformation is influenced by both the applied load and the material condition, resulting in varying rates of deformation observed in the elastic shakedown, plastic shakedown, and ratcheting regimes [10]. After the initial cycle of permanent deformation in the internal structure, the material enters the elastic shakedown phase where very low

residual stresses allow it to carry the same load elastically without incurring permanent plastic deformation. Upon surpassing the elastic shakedown limit, the material transitions into cyclic plasticity or the plastic shakedown phase. Here, the material undergoes microstructural deformation with each loading cycle. Once the plastic shakedown limit is exceeded, each loading cycle induces significant permanent deformation and plastic strains, ultimately leading to the collapse of the structure [10].

Defects in S&C rails, where the primary mechanism of failure is RCF, include spalling, shelling, rail fissures, head checks, and squats. Spalling is identifiable by hollow areas and subsequent fracturing on the railhead, originating from repeated extrusion due to intense wheel–rail contact stresses, resulting in the onset and spread of minuscule cracks [15]. Shelling is discernible as material detaching from the rail surface, commencing with a minor crack on the rail surface, compromising structural integrity upon subsequent multiplication and merging [15]. Head checks manifest as parallel cracks on the rail gauge corner, initiated by RCF on the surface rail [16]. Squats result from the longitudinal displacement of railhead cracks, followed by propagation into the subsurface rail and subsequent lateral spread [17].

The occurrence of rail imperfections such as lipping, wheel burns, and rail corrugations is influenced by either individual or combined effects of plastic deformation and rail wear. Lipping, noticeable by the resettlement of material in the lower rail gauge corner, arises from plastic ratcheting [18]. Wheel burns, characterised by the erosion of railhead material, stem from plastic deformation due to wheel slip and high thermal stresses [19]. Corrugation, distinguished by irregularities and bands on the railhead, begins when a 'wavelength fixing mechanism' is activated during the dynamic interaction between the vehicle and the track. This is triggered by the nominal rail profile encountering roughness at different wavelengths [20,21]. Subsequent rail wear and plastic deformation alter the rail profile and activate the wavelength fixing mechanism, intensifying the corrugation [21]. Progressive transverse cracking, a subtype of lateral internal cracks within the railhead subsurface, is a result of a combination of material defects and significant gauge corner shelling [19].

An important fault falling under Category 2 and occurring away from the wheel–rail interface is rail fracture, with its main failure mechanisms being RCF and plastic deformation. Rail foot fracture, identified as a major issue in crossings from 2009 to 2012 as per the FMS database of Network Rail, is caused by wheel–rail contact forces concentrating bending stresses on weak areas of the rail foot. The presence of rail irregularities at the crossing amplifies dynamic loading on the rail, resulting in rail foot fractures when repeated high loading surpasses the material's ultimate tensile strength [14,19]. An increase in operational loading over time, resulting in fatigue and inappropriate mechanical handling of rails have also been listed as potential reasons [14]. Table 1 relates the defects in S&C to the main failure mechanisms and has been reproduced from the published article based on this research [12].

Table 1: Relationship between S&C rail defects and the failure mechanism, adapted from [12].

Fault in S&C	Damage Mechanism
Spalling	RCF [22].
Lipping	Plastic deformation [18,23].
Shelling	Subsurface RCF, plastic deformation due to cyclic loading [24].
Cracks in Rail	RCF [24].
Head checks	Surface-initiated RCF [16].
Squats	Surface-initiated RCF [17].
Progressive transverse cracking	Shelling in gauge corner [19].
Wheel burns	Plastic deformation due to wheel slip and rail head wear [19].
Corrugations	Wear because of longitudinal wheel slip [25], cyclic plastic deformation [25], wear and plastic deformation [19–21].
Rail fracture	RCF, plastic deformation [9,14]

1.3 Inspection, monitoring and maintenance procedures

In section 1.2, the costs attributing to the maintenance and failure of S&C were discussed. Although digital technologies have the potential to tremendously reduce these high costs, it is also important to state the potential benefit they could bring in terms of safety.

The Grayrigg derailment that resulted in a fatality due to switch failure occurred due to the fact that the fastenings for the switch rails were not inspected [11]. Several rail accidents have occurred because of the inappropriate shape and position of the switch rails [11,26–28]. In another instance, the crack growth in a crossing resulted in failure due to the cracking of the rail [29]. A derailment in the northwest of London was the result of a track twist in S&C [30]. Inadequate inspection of point machines would result in their malfunctioning, essentially risking derailment due to inappropriate switch positioning.

The existing approaches to the detection of defects in switches have been discussed in Section 1.3.1. Some examples of instrumented rail inspection have been discussed in 1.3.2. Finally, the examples in the literature where physical sensors were implemented for the condition monitoring of S&C rails have been discussed in Section 1.3.3.

1.3.1 An overview of the existing requirements for inspection of S&C rail in the UK

The standards for inspection and existing maintenance practices were evaluated in [31], where the research project aimed at digitalising manual switch inspection procedures in Great Britain.

According to [31], the S&C inspection requirements in the following areas can be digitalised.

1. “Visual inspection tasks.”
2. “Inspection of shape, size and position of switch rails, stock rails, crossing, wing rails and check rails.”
3. “Geometry measurements (gauge, cant, twist, alignment and levelling).”
4. “Measurement of cracks in rails and crossing.”
5. “Tightness checks.”

6. “Point machine inspections.”
7. Other inspection tasks such as the inspection of vegetation along a walking patch and inspecting rail isolation.

This overlaps with the requirements in various standards where it has been specified that the condition of the following S&C components would need to be assessed:

1. “Condition of switch/stock rails for wear, damage, lipping, RCF, false flange damage and residual switch opening.”
2. “Condition of switch rail fittings: stretcher bars, lock stretcher bars, driving rod and their fastenings for bent, damage, dents, missing and cracks.”
3. “Condition of crossing, wing rails, check rails and flangeways for wear, batter, lipping and cracks.”
4. “Condition of rail fastenings, soleplates, baseplates, blocks, welds, ballast, rail joints.”

Maintenance standards define the periods between track inspection; the visual inspection of rails must be carried out to scrutinise the presence of cracks and other defects.

Corrugations can be identified from increased wheel noise or “roaring” and the loss of rail head profile is detected by visual observation and rail profile measurement. The poor ride quality of vehicles on the track which is otherwise within maintenance tolerances can also highlight the presence of track defects. Visual inspection can also highlight flaws such as squats, wheel burns, gauge corner cracking and micro-cracks on the rail head which can be removed with rail rectification machines.

The wear of the rail that would occur because of the contact between the wheel flange and the rail gauge corner, i.e. the side wear is usually inspected with a side wear gauge.

The NR4 Stepped Sidewear Gauge was created specifically for gauging sidewear on stock rails as specified in the NR/L2/TRK/0053 inspection standard [32]. As shown in Figure 13, the gauging process entails ensuring the gauge makes contact with the rail at three specific points: the field side for alignment, and the gauge corner and top for actual measurement. If inadvertently used in the wrong

orientation (i.e., employing the gauge side for alignment), the measurements obtained would be inaccurate. The gauge comprises two distinct components: one tailored for measuring rail heads of 72 mm, identifiable by the presence of two small holes, and another for rail heads of 70 mm, recognisable by the absence of these holes. Therefore, Figure 13A showcases the measurement of a rail head with a width of 70 mm [31,32].

In summary, the gauge determines sidewear by comparing the loss in height of the gauge corner to the top of the rail. This disparity is gauged using a stepped tool with intervals of 0.78 mm. The stepped gauge is labelled with numbers ranging from 0 (representing a thickness of 10 mm, indicating the highest sidewear) to 18 (representing a thickness of 24.04 mm, signifying a new rail). As specified by Network Rail [32], sidewear measurements should be taken at a minimum of 4 locations per quarter mile along a curve, selected based on visual examination where sidewear is most prominent. It is mentioned that the maximum permitted lateral head loss in plain rail and rails with full head section is 9 mm [32].

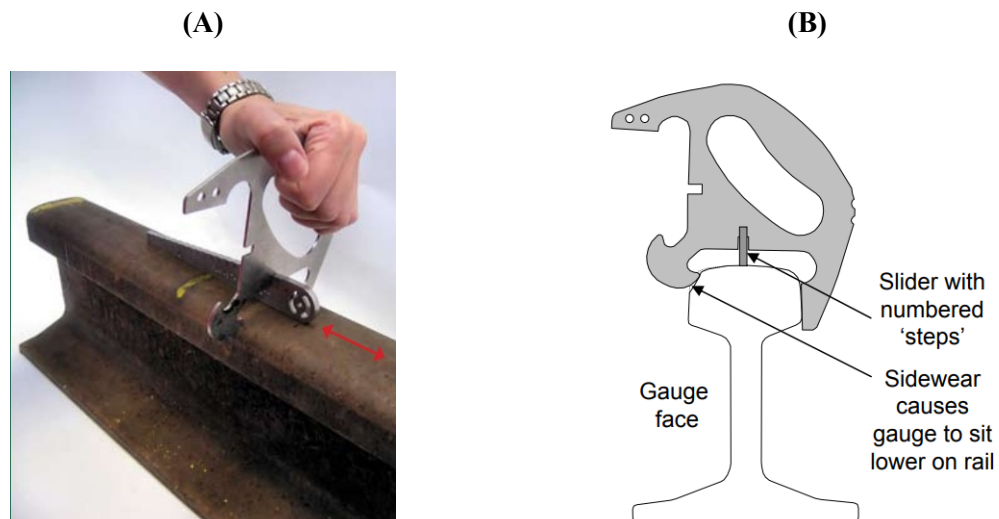


Figure 13: NR4 sidewear gauge measurements (A) New Rail; (B) Sideworn rail, reproduced from [26].

1.3.2 An overview of some of the common approaches to instrumented rail inspection

In railways around the world, the rails are subject to regular and frequent visual inspection for detecting the development of gross defects depending on the track category. Various types of NDT testing such as ultrasonic testing are also employed. One approach is ultrasonic detection regularly by either pedestrian operators or rail-borne ultrasonic testing units. The flaw detection equipment produces a short electric pulse which is applied to the piezoelectric transducer. “The piezo-electric transducer can convert an electrical pulse to an acoustic pulse” and vice-versa. A defect “such as a bolt hole or a crack in the rail” would return the pulse “at a shorter time and hence at a shorter range from the rail foot”. For S&C, these manual inspection units are generally employed by pedestrian operators since they can reach access such areas more efficiently [1].

Ultrasonic test units can be installed on railway vehicles and implemented for testing the development of subsurface faults on plain line continuously welded track by capturing data accurately whilst travelling at speeds up to 70 km/hr [1]. The vehicle has several “small wheels with ultrasonic transducers fitted to their axles which are enclosed by polypropylene tyres.” “The tyres are filled with a water-glycerol mixture and a water couplant is used between the tyre and the rail. The ultrasound travels from the transducer, through the internal fluid, the tyre-water couplant and into the rail to the rail foot and then returns back to the transducer. Non-contacting eddy current probes are also used for detecting surface defects [1].”

Other forms of rail inspection procedures include visual inspection, magnetic particle inspection, dye penetrant testing and eddy current testing. Visual inspection has been described as an initial step that can be used to indicate damage. This is generally followed up by a non-destructive testing procedure for indicating the severity of a visible defect. For example, ultrasonic testing is required to indicate the severity of subsurface defects such as squats. Another limitation of visual inspection is the misinterpretation of visual indicators, e.g. the interpretation of “fusion lines at the weld boundary as a defect [1].”

The defects that are detected are fed into a database and corrective actions are proposed based on the severity of the defect [1]. These range from retesting to speed restrictions, implementation of “emergency clamped fishplates or removing/replacing the section of the defective rail within a specified period [1].”

1.3.3 Evaluating the potential for detecting defects in S&C rails by implementing physical sensors for continuous condition monitoring

Inspection and condition monitoring are two approaches for detecting the presence of faults in the infrastructure. A periodic inspection would involve inspecting the asset manually or by carrying out an instrumented inspection at set time intervals. On the contrary, condition monitoring would involve a continuous check of the state of health of the asset and flagging up potential threats as and when they occur [33]. An ideal condition monitoring system should be able to detect, diagnose (determine the root cause) and predict faults in the infrastructure through the analysis of the measured data.

It has been argued that the limited accuracy, precision and reliability of existing condition monitoring systems can be insufficient for making them replace more traditional inspection processes. This is especially true when an asset is safety critical and its failure could lead to loss of life and injuries. However, they have the potential to gather data for understanding the behaviour of the asset and reduce costs. The benefits can be direct or indirect. One of the direct benefits would be knowing the real-time state of health of the asset at crucial locations. An indirect benefit would be the collection of long-term data for informing improvements in design, manufacturing and assembly.

It was described in Section 1.2 that the switch and crossing panels would contribute immensely and almost equally to the delay cost as well as the total number of failures. Therefore, it is proposed that the weakest sections of the rail should be continuously monitored for the development of rail defects. In a project that was carried out at the University of Birmingham [31], a feasibility study was carried out for digitalising S&C inspection procedures. The different recommendations included detecting the obstruction of the switch rail by implementing lasers and cameras. Similarly, it was recommended that

the contamination of baseplates can be detected by measuring the current or the force of POE. The locking mechanism of switches can also be assessed by monitoring the force and the current of the POE. Implementing physical sensors such as strain gauges and accelerometers were recommended for monitoring the development of wear/damage in switches and the cracking of crossings.

Field experiment studies by implementing sensor measurements for monitoring the health of S&C have already been carried out as evidenced by the amount of literature on this topic. However, most of the publications have focused on the crossing rather than the switch. Moreover, most studies have focused on field experimentation for the validation of numerical models rather than for developing condition monitoring systems.

Many examples of experimental condition monitoring studies that have been carried out in literature have focused on collecting data about the structural health of S&C by implementing inductive sensors, accelerometers, geophones and strain measurement sensors including strain gauges and fibre-optic sensors. Most of these studies have focused on the crossing nose and some have focused on switches.

The installation of Fibre Bragg Grating (FBG) strain sensors was carried out on the fishplates, switch blades and stretcher bars of a tram track system [34]. The sensors were installed in the axial direction at the side of the rail head and at 45 degrees at the rail web. The sensors were bonded to the rail with adhesive and coated with a sealant for protection. The changes in the track condition were reflected in the measurement data in the time series that were carried out for the switch blade.

Strain gauges were installed on the stock rail of the switch panel on the neutral axis at the location between the sleeper spacing [7]. The vertical shear strain on the rail was recorded whilst reducing the influence of structural bending on the measurement. Four sites for the same switch layout were chosen for experimentation and among them, three were straight switches. The sites experienced different vehicle speeds and tonnage. At all four sites, the sensor was installed at a distance of 1.2 m from the switch toe/tip. In one of the sites, the sensor was installed at a distance of 4.5 m from the switch tip for analysing the transition of the wheel-rail contact patch from one wheel to another. It was observed that

the strains are higher for the closed switch than for the opened switch. Most importantly the influence of the contact position on the strain measurement was analysed after implementing quasi-static FEA simulations, where it was found that a variation in the contact position of 5 mm can increase the value for the strain in rails by approximately 50 $\mu\epsilon$. Although the potential for strain measurements was analysed in this research, a detailed discussion about the monitoring of switches has not been carried out [7].

Strain gauges were installed at the bottom of the fixed crossing for measuring the bending strains in the longitudinal direction [35]. It could be inferred from the data that was gathered from the passage of multiple vehicles that they passed over the crossing at similar speeds. Along with the history of the strain measurements, the quantitative measurement of the change in the profile of the crossing nose was measured at predefined intervals by implementing laser profilometry and the influence of crossing deterioration on the change in the strain measurements could be observed. The authors proposed a model-based condition monitoring approach that is based on geometry, strain measurements and Finite Element Models to contribute to the planning of repair and visual inspection intervals [35].

Similarly, laboratory experimentation was carried out to check the potential for monitoring excessive wear for a metallic slab that was manufactured for simulating a crossing nose profile [36]. The strain profile of the crossing of the S&C was implemented for determining the size of the wear that was introduced into the test specimen. A 3D FE model was developed for defining the loading as well as the testing conditions so that it could be compared with the experimental tests. Sensors were installed in the longitudinal direction of the sides of the crossing nose. Two cuts were introduced on the side of the crossing nose for analysing the effect of the fault on the strain values. It was shown that the results of the experimental and numerical studies were in good agreement. Sensors were placed at two locations, one near the head of the rail and another near the foot of the rail. It was confirmed from the simulations that the positioning of the sensor near the rail head would provide more detail for the variation of the strain profile due to wear [36].

Field experimentation was carried for understanding the effect of the passage of a vehicle over the crossing nose [37]. As a part of the experimentation procedure, a triaxial accelerometer was installed 0.3 m away from the theoretical crossing nose point. For the measurement of speed, a pair of inductive sensors were installed in the closure panel. The range of the acceleration sensor that was implemented was 500 m/s^2 and the sampling frequency was 10 kHz. Along with the results from an FE model, the results for the measured acceleration were implemented for validating the MBS model. The transition region, wheel impact acceleration and the impact location were compared between the simulations and the experiments for validating the wheel-crossing dynamic analysis. However, the potential for monitoring the various faults in crossings has not been analysed.

In a similar experimental analysis [38], a tri-axial accelerometer, inductive sensor and Digital Image Correlation (DIC)-based video gauge system was implemented to provide a qualitative indication of impact locations for determining the development of fatigue in crossings. The impact locations were obtained by implementing the speed obtained from the inductive sensors in order to determine the position of the wheel along the crossing. The percentage occurrence for the values of the acceleration under worn and repaired conditions was analysed. Moreover, the locations where the impact would occur were compared against observations for fatigue development. It was demonstrated from this study that together acceleration measurements and inductive sensors would be able to support the qualitative detection of impact locations and the development of fatigue in crossings.

On the other hand, instrumentation with accelerometers, strain gauges and geophones was carried out on the rails and the sleeper at the University of Birmingham [39] and the potential for monitoring the health of both switches and crossings from the data gathered by the different sensors was analysed. In the switch panel, 2 Integrated Electronics Piezoelectric (IEPE) accelerometers were placed on either side of the rail web of one stock rail. 10 vertically mounted geophones were installed over 5 sleepers, i.e. two geophones per sleeper. The geophones were placed on the field side of the half-set of left and right switches.

Similarly, in the crossing, 10 vertically sensing geophones were placed on 5 sleepers. 8 IEPE accelerometers were installed on the crossing nose, where 4 were set vertically on the rail web between the sleeper spacing and the other 4 were set horizontally (either under the rails in the sleeper spacing or over the sleeper).

Three strain gauge bridges were installed in the spacing between two bearers and attached to the crossing nose. Two strain gauge bridges were installed on both sides of the crossing nose assembly for measuring the shear strain [39]. One strain gauge bridge was installed under the crossing for measuring the bending strain. In [39], it suggested the appropriate frequency bandwidth for capturing impact forces and bending at the crossing nose. It was suggested to have at least 300 Hz for capturing bending strains, and at least 2 kHz for capturing the impact forces, P1 and P2 that usually occur at a discontinuous wheel-rail interface. The first impact force (P1), which generally results in rail surface defect, is usually larger and can be captured at a higher frequency than the second (P2). The P2 forces occur at a lower frequency than the P1 force and influence the degradation of the ballast. A limit of 322 kN for the value of the P2 force has been prescribed by the Rail Safety Standards board [40].

In terms of usable data, the study showed that the data obtained from the different sensors can be implemented for the detection of different faults. The implementation of geophones showed potential for measuring peak-to-peak displacements for detecting defects such as voiding. However, they were unable to capture the influence of the wheel-rail interaction and are inadequate for determining the state of health of rails. It was discussed that the measurement of the bending/longitudinal strains at the rail foot had shown the potential for monitoring the condition of the track support. The data that was obtained from the accelerometers installed on the rails showed a poor correlation with the estimated impact forces. Although a 1 kHz filter was implemented in the study for removing unwanted noise in the sensor measurements, it also removed the crucial dynamic information that is needed for providing meaningful insights. On the other hand, a good correlation between the strain measurements and the impact forces was obtained for the crossing. An RCF monitoring index that can provide data for faulty trains, train speeds and train types was implemented to demonstrate the potential for fault detection.

The aforementioned examples of data acquisition from physical sensors show potential for monitoring the rail for the development of various kinds of defects.

1.4 Research questions

As introduced earlier in the chapter, railway switches are crucial to the safe and cost-effective functioning of the track infrastructure. As shown from the analysis of the FMS data from Network Rail in Section 1.2, the defects in the rails of the switch panel and the substructure have traditionally resulted in significant delays and maintenance costs. The RDMS data from Network Rail has shown that the defects on the rails of the switch panel are 40% of all the S&C rail defects. Moreover, the switch blade has accounted for one-fifth of all the defects that would occur in the S&C rails. In addition, the failure of switch components has resulted in fatal accidents in the past. As discussed in Section 1.3, switches have traditionally been visually inspected and can also be subject to intermittent instrumented inspection. There is a case for continuously monitoring the structural health of the switch rail because of its high maintenance cost and safety-critical nature.

A review of the studies involving field experimentation with physical sensors has highlighted the possibility of monitoring the rail strains for detecting the defects in railway switches. Many studies of field experimentation have also been implemented for validating numerical simulation models. The numerical simulations of the interaction between trains and S&C have predominantly been implemented for predicting S&C track damage. Since field experimentation is subject to time and cost constraints, it is proposed that Digital Twin simulation models can be implemented for taking important preliminary decisions for the structural health monitoring of switches. The approach to developing such a model and implementing the model for testing sensor placement for detecting the crucial rail and substructure defects that would occur in switches has been explored through this thesis. In particular, the following questions have been answered:

- What numerical simulation approach can be implemented for predicting the locations in switches that are prone to the occurrence of the dominant surface and substructure defects and those for installing the strain sensors on the rail for detecting them?
- How can the track dynamics of the switch model be calibrated against a reference model or asset?
- How can the model of a switch be developed whilst balancing the tradeoff between accuracy and computational efficiency?
- How can the track defects in switches be modelled?
- How can the results from numerical simulations be implemented for determining the placement of sensors in switches?
- How will the sleeper support influence sensor placement and what is the potential for predicting the wheel-rail contact force from the strain measurements for implementation in damage prediction models?

1.5 Original contributions from the research

The following are the original contributions from the research that are based on the aforementioned research questions:

1. Demonstrating the implementation of numerical simulation for studies related to the structural health monitoring of a railway switch. Traditionally, the two fields of MBS/FEA numerical simulations and instrumented experimentation have been implemented separately for studying switches, the former for studying mechanical degradation and the latter for detecting mechanical degradation. A concept for a Digital Twin is defined and explored within the thesis, with the aim of developing a 3D FEA model capable of considering both aspects that can be calibrated to the track properties of a reference model for studying the structural health monitoring of switches.
2. An evaluation of previous S&C numerical simulation approaches in literature will show that outputs from MBS train-track dynamic interactions have been implemented in independent

- FEA simulations without essentially ensuring compatibility for the vehicle and track dynamics between the two models. An attempt will be shown in reducing the differences between these models, which will be essential when developing Digital Twins of switches. An approach to modelling a switch track in FEA, whose track dynamics are compatible with a reference model that it is based on, will be shown in Chapter 3. This will be shown by comparing the results for the vertical and lateral rail receptance between the reference model and the FEA model that has been developed [41]. The compatibility between the two models will also be ascertained based on the results from the wheel-rail interaction and discussed in Chapter 4. Incorporating appropriate vehicle and track dynamics in the FE simulations would improve result accuracy for subsurface rail mechanical behaviour, as it will be shown in Chapter 4.
3. Specific geometry of defects that approximately seek to replicate the key failure mechanisms of wear, RCF and voiding will be modelled into the track for determining the placement of sensors in Chapter 5.
 4. The results from the FEA simulations will be implemented for determining the possibility of measuring the strains of the switch rail for fault detection. The results for the rail strains will be implemented for determining the locations and orientations in which the strain could be measured for detecting the defects and will be shown in Chapter 6. The contribution of aspects such as sensor placement at the longitudinal position (sleeper-supported or not), vertical position (proximity to the rail head) and the type of rail strain measurement (vertical/shear or longitudinal/bending) to the detection of the different defects (wear, squat and voiding) will be discussed in Chapter 6. Moreover, there will be a discussion on corroboration of the simulation results with existing examples of field experimentation [39].
 5. Whether the amplitude of the wheel-rail contact force, which is implemented in various mechanical damage prediction models can be determined from the rail strain will also be explored. The results for the vertical and the longitudinal strains at the proposed sensor placement locations will be implemented for studying their correlation with the vertical wheel-rail contact force for testing whether the contact force can be derived from the strains and thus

be implemented in damage prediction models. The difference between the results for the strains that will be obtained from the simulations carried out in the presence and absence of the defects will be implemented for studying the potential for fault detection. The results from the model will be assessed against the range and resolution of a reference sensor. Since the track and the vehicle dynamics of the model have essentially been calibrated against a reference model, this research will also demonstrate how physics-based Digital Twin models of switches could be implemented for virtually evaluating structural health monitoring systems.

1.6 Conclusions from the chapter

The benefits of implementing the condition monitoring of the rails of switches for improving the safety and reducing the maintenance costs for the railway were explained in this chapter. The discussion around the S&C layout as well as the failure statistics for them can help the reader understand the challenges surrounding their design and maintenance. Some of the approaches to traditionally inspecting the switch were highlighted and it has been proposed that such procedures can be replaced by continuously monitoring the condition of the crucial rail sections along the length of the switch by gathering and analysing data from physical sensors.

A review of previous field experimentation studies has shown the potential for measuring the rail strains for detecting the defects in the rails of the switch panel. It has been proposed that prior to carrying out field experimentation, numerical simulation can be implemented for answering the crucial questions on the locations for monitoring and installing the sensors on the switch rail.

Therefore, in the next chapter, an evaluation of the numerical simulation approaches for determining a suitable modelling approach for answering the research questions that have been posed in this chapter will be carried out. In the subsequent chapters, an approach for modelling the switch whilst calibrating the track dynamics against a reference track model will be shown. The model will be subject to wheel-rail interaction simulations in the absence and presence of track defects for determining the locations

for measuring the rail strains for condition monitoring. Moreover, the modelling results will be implemented for discussing the potential for successfully detecting the defects by either examining the strain results directly or through the derivation of the impact force.

CHAPTER 2. REVIEWING THE NUMERICAL SIMULATION APPROACHES AND SETTING OUT THE MODELLING METHODOLOGY FOR TRAIN-SWITCH INTERACTIONS.

This chapter will present the literature around the existing approaches to modelling switches and set out the modelling objectives that will be achieved through this thesis. The definition of a Digital Twin will be provided and how that fits within the context of the research objectives will be set out. The literature around the numerical simulation approaches, wheel-rail contact models and damage prediction models that have been applied to S&Cs will be discussed. Finally, the requirements for the modelling work and its assessment will be defined.

As described in Chapter 1, this thesis will demonstrate an approach for implementing numerical simulations for taking key decisions on the structural health monitoring of switches. Implementing numerical simulations for representing a reference system would be a step towards achieving Digital Twins. As defined by Ansys [42], a simulation based digital twin is a “Connected, virtual replica of an in-service physical asset, in the form of an integrated multi-domain system simulation that mirrors the life and experience of the asset.” For achieving a simulation-based Digital Twin according to this definition, the first essential step will be to demonstrate the process of building a model that represents the system that the twin seeks to replicate.

Therefore, the two key aims of the modelling work will be:

- Demonstrating the process of building a wheel-switch interaction model in 3D whose track properties will be modelled for representing a reference system, as a step towards showing how simulation based digital twins can be developed.
- Implementing the model in preliminary investigations for assessing the possibility of measuring rail strains for monitoring the health of the switch structure.

To this end, a review of the approaches to S&C modelling will be presented in Section 2.1 and the modelling methodology and the assessment criteria will be set out in Section 2.2. Section 2.3 will set a constraint on the definition of digital twins for this thesis whilst setting out the reference switch model for replication and Section 2.4 will present the conclusions from the chapter.

2.1. A review of numerical simulation approaches, wheel-rail contact models and damage prediction models for Wear, RCF and Plastic deformation.

This section will present a discussion on the numerical simulation approaches, wheel-rail contact models and damage prediction models for the main failure mechanisms of wear, RCF and plastic deformation in switches that were defined in Chapter 1.2.4. The content provided here was previously published as a journal article [12] and is paraphrased to give important background to the work that will be presented in the subsequent chapters.

2.1.1 Numerical simulation approaches for modelling the interaction between trains and S&C.

In this section, the different numerical simulation approaches for modelling the dynamic interaction between railway vehicles and S&Cs will be described whilst providing context to their benefits, constraints, and the S&C research attention they have garnered in the literature.

2.1.1.1 *Multi-Body System (MBS) Simulation*

The interaction between the vehicle and track dynamics can be simulated in MBS, where both the vehicle and track are represented as rigid components. The interaction between trains and S&Cs can be modelled within MBS using rigid elements, such as mass-spring-damper systems, with each wheelset having an associated moving rigid track system, commonly referred to as a co-running track [22].

Track flexibility is incorporated by adjusting the characteristics of the spring-dashpot component in both vertical and lateral directions, as depicted in Figure 14. In the example of the single-layer track system that has been depicted in Figure 14, the dynamic attributes of the railpad and substructure were

merged, and the entire track system was coupled to the vehicle model [43]. A notable limitation of the single-layer MBS track model is its inability to adequately represent high-frequency track dynamics, which makes it more suitable for purposes such as the analysis of vehicle ride dynamics [44].

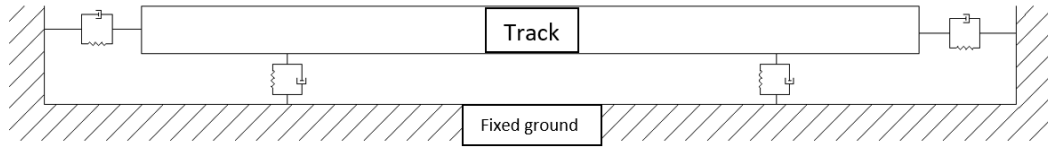


Figure 14. Co-running track model with track flexibility (adapted from [43]).

To enhance track flexibility and account for high-frequency dynamics, various track layer configurations can be employed. In multi-layer track systems, multiple rigid masses are utilised to represent the degrees of freedom (DOF) associated with the rails, sleepers, and potentially the ballast. For instance, as illustrated in Figure 15, a three-layer track system incorporates multiple masses and DOFs [45]. While the inclusion of multiple DOFs may extend computational processing time, it affords greater flexibility and facilitates the consideration of higher frequencies, thereby enhancing the accuracy of model results.

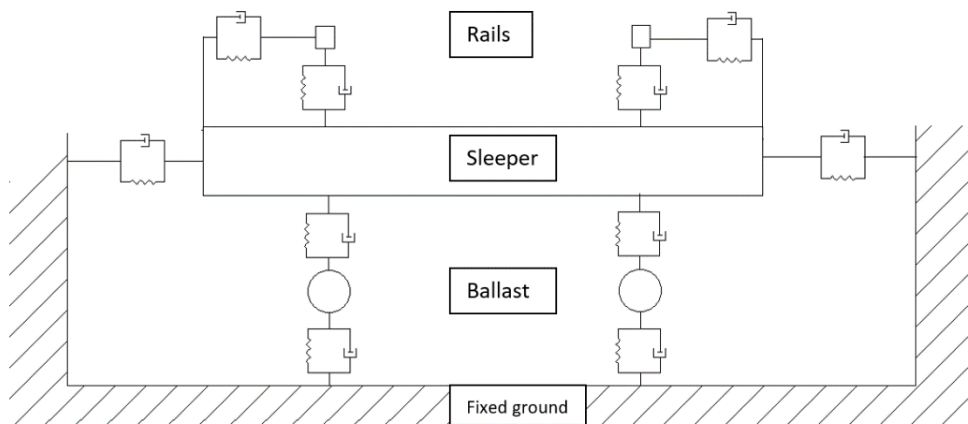


Figure 15. Co-running track with multiple DOFs (adapted from [45]).

MBS simulations are most suitable for scenarios requiring the examination of vehicle dynamics and rapid simulations, particularly when conducting parametric studies involving adjustments in wheel and track geometry, variations in speed, and changes in friction coefficients. However, MBS simulations

cannot be implemented for studying aspects such as the mechanical behaviour in the rail subsurface.

The benefits, drawbacks, and research focus related to MBS modelling of S&Cs, as documented in the reviewed literature, are condensed and presented in Table 2.

Table 2. Summary of the MBS numerical approach

Advantages	Limitations	Research interest
Single layer co-running track		Switch wear prediction [22,46–51].
High efficiency [52].	Only captures low frequency content [44].	Crossing wear prediction [45,48,49].
Detailed consideration of vehicle dynamics [52].	Less representative substructure mechanical behaviour [18].	Switch surface RCF prediction [22,47,49,52,53].
Acceptable results for low frequency applications [44,52].	Poor consideration of S&C rail cross-section variation [22].	Crossing surface RCF prediction [49].
Representative surface damage predictions based on the contact model [22].		Vehicle/turnout dynamics [37,54–59].
		New switch concept [60].
		Vehicle performance [61] .
Multi-layer co-running track		Wheel damage [62,63] .
Independent consideration of S&C component dynamics [45,68] .	Accurate results limited to frequencies up to 200 Hz [73].	S&C geometry optimisation [64–67].
Captures higher frequency content than single layer track [45].	Reduced efficiency [45].	Field calibration [68].
		Contact model validation [54].
		Flexible track model validation [44,55,69].

Advantages	Limitations	Research interest
		FE model validation [70–72].

2.1.1.2 Finite Element (FE) simulation approach

In FE analyses employing beam and solid element models, the analysis takes into account high-frequency dynamics and various non-linearities arising during the interaction between the vehicle and track. This is achieved by incorporating the 3D geometry of S&C rails, which considers details such as rail profile machining and milling thickness [65], and importing this representation as solid elements into the FE analysis. Additionally, for scenarios requiring precise information about the wheel/rail contact patch, the FE model includes a representation with solid elements for either an unsprung wheel or a complete wheelset. The modelling of the substructure can vary, with some approaches using solid elements while others option for simplified rigid elements.

The primary methodologies in S&C numerical simulation via FEA involve three main approaches: one is the half-track model focusing on a single wheel and track side (Figure 16), another is the full-track model with a complete wheelset and track (Figure 17), and the third involves applying concentrated loads on the rails within a detailed solid element turnout model encompassing full geometry. Section 2.1.4.1 of the thesis will discuss how these modelling approaches impact the consideration of vehicle dynamics.

The necessity for efficient FE models in cyclic analyses has prompted various simplification techniques. Some models simplify rail geometry to enhance efficiency in cyclic simulations [74,75], while others employ a plane strain assumption for certain rail cross-sections [52,76]. Alternatively, some models achieve accuracy by using a highly detailed FE model for a single run and then applying the resulting data to empirical models for cyclic predictions [24]. Examples in literature have also shown that a coarsely meshed global FE model of a larger area can provide initial dynamic response results to serve as boundary conditions for a subsequently developed finely meshed local sub-model,

which can be used for damage prediction on a smaller scale [77–79]. Section 2.1.4.3 underscores the significance of considering non-linear plastic material behaviour made possible through FE models. Table 3 offers a summary of the advantages, limitations, and research interests pertaining to various types of FE turnout models.

Table 3. Summary of FE numerical approach for S&Cs

Advantages	Limitations	Research interest
Solid element FE half-track model.		
<p>Reduced number of elements, higher efficiency.</p> <p>Non-linear elastic-plastic material behaviour for better prediction of contact stress/damage [71].</p> <p>Implementation of cyclic degradation [75].</p> <p>Consideration of a solid sleeper [80].</p>	<p>Poor efficiency</p> <p>Simplified vehicle dynamics [71].</p> <p>Constant yaw angle used for the wheel in the diverging route [71].</p> <p>Underestimation of slip, lateral and longitudinal tangential contact forces [81].</p> <p>Assumptions in substructure simplification/property assignment [71].</p>	<p>Crossing wear [71,72,80,82].</p> <p>Crossing RCF [72,74,75]</p> <p>Crossing plastic deformation[71,75,80–84].</p> <p>Wheel/crossing impact behaviour [83–88]</p> <p>Incorporation of RCF damage in Rail [89].</p>

Advantages	Limitations	Research interest
Solid element FE model for full track, including the opposite stock rail.		
<p>Non-linear elastic-plastic material behaviour for better contact stress/damage prediction [24].</p> <p>Implementation of cyclic degradation [90].</p> <p>Representative wheelset displacement [24].</p> <p>Sleeper and substructure material behaviour and vehicle dynamics [24,90,91].</p> <p>Sleeper and substructure stress distribution outputs [24,90,91].</p>	<p>Poor efficiency[24].</p> <p>Simplified vehicle dynamics [70].</p> <p>Poor efficiency [24].</p>	<p>Crossing wear [92–94].</p> <p>Crossing surface RCF [92].</p> <p>Crossing fatigue life [24,78].</p> <p>Switch component plastic deformation in special case run-through [95].</p> <p>Crossing plastic deformation [92–94].</p> <p>Bearer and ballast mechanical behaviour [96].</p> <p>Wheel/crossing contact behaviour [91].</p>
Direct application of axle load in absence of wheel geometry		Wheel/switch contact behaviour [70].
<p>Complete turnout substructure modelled [96].</p> <p>Stress distributions in all turnout components [96].</p> <p>Input loads for a complete train [96].</p>	<p>Poor efficiency [96].</p> <p>Wheel/rail contact ignored [96].</p> <p>Point loading rather than through a contact patch [96].</p>	<p>Dynamic behaviour of all S&C components [97].</p>

2.1.1.3 Combined MBS and FE modelling approaches

A comprehensive approach to addressing vehicle dynamics, material behaviour, rail subsurface, and substructure mechanics is achievable through a combined MBS and FE simulation strategy [43,52]. The MBS and FE simulation approaches can be utilised together through either substitution or co-simulation. In the substitution approach, the results that are obtained from the first numerical tool are manually output to the second tool after a vehicle has traversed the entire track. For example, there can be two separate models that are implemented in two separate tools but there is no automatic feedback or exchange of information between these two models in the substitution approach. Therefore, this particular approach will be referred to as a two-step or multi-step simulation approach, depending on the number of independent models.

In contrast, co-simulation can be executed in parallel, sequentially, or iteratively [98]. Parallel co-simulation entails running both numerical tools concurrently, sharing data to update their respective solutions at predefined coupling times, offering efficiency but with the risk of potential instability. In sequential co-simulation, the analysis in the first numerical tool guides the second, and information is exchanged at specific coupling points while the same vehicle's passage over the track occurs. Similar to the sequential approach, co-simulation through iterative coupling also involves the first tool leading the second, but it involves more intricate exchanges at defined coupling points, repeating them until termination criteria are satisfied [98].

In the study of S&Cs, several combined simulation approaches based on substitution have been applied. One approach that was reviewed involved using MBS model outputs, which include relevant wheel-S&C contact loads, positions, and radii of curvature, to generate a simplified 3D solid element FE model. This FE model was substituted for an empirical wheel-rail contact model for obtaining precise contact patch results, especially under elastic-plastic material conditions [52].

Another approach that was reviewed combined the use of an MBS model, a wheel/rail contact meta-model that considers elastic-plastic hardening material behaviour, and a 2D plane strain FE model for predicting plastic deformation. In this method, the MBS model provided the outputs for contact

positions and forces, which were used in the wheel-rail contact meta-model to calculate contact patch sizes and pressures. These results then served as inputs for the 2D plane strain FE model, which predicted the subsurface rail stress distribution related to plastic deformation [45]. It will be essential to ensure compatibility between MBS and FE models, particularly concerning contact point locations, bedding properties, and result stability when combining these methods.

MBS models can be enhanced for improved computational efficiency and the consideration of higher frequencies by coupling them with reduced-order models. This integration involves translating FE components into a set of representative Eigen-frequencies and mode shapes, accurately representing their behaviour under dynamic conditions [99]. Modal reduction methods simplify the flexible body problem by expressing it as a combination of its mode shapes. These methods utilise outputs related to node locations, connectivity, nodal mass, inertia, mode shapes, and generalized mass and stiffness matrices for the mode shapes to describe the flexible body [99].

To create flexible track models capable of capturing higher-frequency characteristics, FE models can be imported into MBS packages using modal reduction methods. While flexible track models employing beam elements are less efficient than MBS models, they can account for high-frequency impacts and longitudinal variations in S&C track properties, including track geometry. However, when detailed outputs of subsurface stress and strain distributions are required, modal reduction of solid element FE models becomes a more desirable approach. In contrast to combined simulation approaches involving multiple solver packages, this simulation method integrates an FE model through modal reduction within a single solver. This means that the substructure properties of the flexible track are directly incorporated into the simulation, eliminating the need for calibration between multiple models.

After preprocessing the wheel-rail contact locations using 2D cross-sections, the dynamic interaction between the rigid vehicle and the flexible components of the track can be conducted. It will be crucial to ensure good alignment between the rail profiles used in the preprocessor and the FE flexible track geometry if this approach is implemented [100]. However, post-processing of results from the flexible

track model is constrained by computational efficiency and requires selecting specific nodes of interest. Furthermore, this method applies concentrated forces to contact points, rather than distributing loading or pressure through a 3D contact patch. Additionally, analyses conducted using flexible track models are restricted to linear systems.

Section 2.1.4.2 will discuss the significance of calibrating substructure properties among models when employing co-simulation techniques. Furthermore, Table 4 provides a comprehensive overview, including advantages, limitations, and examples from existing literature, regarding the modelling process through combined approaches.

Table 4. Summary of combined independent modelling approach for S&Cs

Advantage	Disadvantage	Research interest
Combined multi-step and co-simulation approaches		
MBS/Solid Element FE		Switch wear [47,52].
Representative wheelset displacements and vehicle dynamics [43,52].	Less efficient than pure MBS models [52]. Effects of substructure ignored during FE wheel/rail contact [43,52].	Switch RCF [43,47].
Efficient analysis with simplified geometry [45,52].		Switch plastic deformation [52,101].
Track non-linearity considered [43].		Crossing wear [45].
Cyclic material degradation considered [45,52].		Crossing RCF [43].
		Crossing deformation [45] .
		Substructure dynamics/S&C settlement [102–107].

Advantage	Disadvantage	Research interest
Cyclic rail profile updated [52].		Vehicle/turnout dynamics [40,43,56,108–110]. Wheel-rail contact model comparison [111]. Crossing model validation [112].
MBS/Beam Element FE		Wheel behaviour [113].
High efficiency[40,102]. Substructure dynamics considered [102]. Very high efficiency of 2D models [104].	Subsurface outputs cannot be analysed [102]. Many calibrated inputs needed for 2D FEA [104].	
Combined MBS-FE simulation with modal reduction		
More efficient than FE [69]. Reducing number of modes/DOF improve efficiency [44]. Captures higher frequency content [69]. Substructure dynamics considered [69].	Poorer efficiency than MBS [69]. Linear track model [114].	S&C Wear [115,116]. S&C surface RCF [115]. Vehicle/Crossing dynamics [117] . Vehicle/ turnout dynamics [44,55,69,99,117,118]. Substructure dynamics [119]. Impact loads on crossing [114,119,120].

2.1.2 Wheel/Rail contact modelling

The approach to addressing wheel/rail contact problems is different for MBS and FEA. In MBS modelling, contact locations are typically updated based on wheel/rail movements to enhance efficiency. Subsequently, contact forces are determined by considering material stiffness and deformation. The calculation of contact pressure and contact patch in MBS can be handled analytically or numerically, depending on the applied contact models. In some instances, empirical equations may be employed to improve the numerical efficiency for solving contact-related issues.

On the other hand, FE modelling takes a different approach. In FE models, the wheel-rail contact conditions are not predefined. Instead, the calculation of contact geometry, forces, and pressures occurs at each time step through the application of a normal and tangential contact algorithm. Sections 2.1.2.1 and 2.1.2.2 in this thesis will provide some context to the normal and tangential wheel/rail contact models used in S&C modelling as found in the literature.

2.1.2.1 Normal contact modelling

In the context of modelling normal wheel/rail contact in S&Cs, various contact approaches, both Hertzian and non-Hertzian, have been applied. Notably, the Hertzian contact model, as described by Hertz [121], is the most commonly used contact model in MBS simulations. This model assumes an elliptical point contact between the wheel and rail and is highly accurate under specific criteria, as outlined in Table 5. However, it is important to note that these criteria are often not always met in the rail change/transitional regions of S&Cs. Moreover, only elastic material behaviour is taken into account. Recently, an elastic-plastic hardening material behaviour was integrated into a Hertzian-based metamodel to enhance the consideration of cyclic material behaviour within the contact model [45,76]. Nonetheless, it was stated that further research would be required to validate the results from this implementation.

An enhancement to the traditional Hertzian method is the Multi-Hertzian approach, which refines the contact patch shape by dividing it into multiple ellipses and incorporates a penetration function based

on the wheel/rail shape geometry [117]. However, it is important to note that this model still retains certain Hertzian assumptions [117].

Another improvement over the Hertzian method is the Semi-Hertzian approach, which enhances accuracy by considering virtual penetration between the wheel and rail. Initially developed by Piotrowski and Kik [122], this approach had limitations due to assumptions made in calculating the depth of penetration. These limitations were addressed by Ayasse and Chollet [123] through the introduction of curvature correction measures and the discretisation of the contact patch into strips. Further refinement was achieved by the Semi-Hertzian approach known as ANALYN, which improved accuracy by considering an approximate surface deformation parameter (ASD) [124]. To summarise, the Semi-Hertzian method enhances contact patch estimation by accounting for wheel/rail penetration but remains restricted to the assumption of purely elastic contact.

The CONTACT algorithm developed by Kalker [125] is a widely used and versatile approach for modelling wheel/S&C contact, not constrained by specific contact geometries, making it a benchmark in this field. Kalker's CONTACT model was further refined to provide more precise results for conformal contact through the WEAR algorithm [54].

In Finite Element (FE) analyses, the normal contact problem is addressed in real-time using the 'Hard Contact' algorithm. This algorithm is applied when there is no clearance between two surfaces and removed when the contact pressure reaches zero, indicating surface separation [98]. To simulate hard contact, three constraint enforcement methods are available: the direct method, penalty method, and augmented Lagrange method [98]. FE modelling also accommodates various types of material behaviours, enhancing the accuracy of normal contact simulations and yielding more realistic contact patches and pressures [111]. For a comprehensive overview of the advantages, limitations, and applications of normal contact models in S&Cs, refer to Table 5.

Table 5. Normal contact modelling approaches

Advantage	Limitation/ Assumptions	Reference examples
Hertz [121]		
<p>High efficiency and accuracy when assumptions are met [18].</p> <p>Introduction of a meta-model with Elastic-plastic hardening and non-linear cyclic material behaviour [45,76].</p>	<p>Assumes small strains, elastic half spaces, no irregularities, non-conformal contact, no friction/tangential contact [18].</p> <p>Poor for conformal, asymmetric multi-point contact [18].</p>	<p>Switch: Wear [22,47,52]; RCF [22,47,52]; Plastic deformation [52,101]</p> <p>Crossing: Wear [45]; Plastic deformation [45]</p> <p>Complete turnout: Wear [48,49,116]; RCF [49]</p>
Multi-Hertzian [117]		
<p>Better contact patch geometry [18].</p> <p>Good efficiency [18].</p>	<p>Hertzian assumptions remain valid [18].</p> <p>Elastic material behaviour [18].</p>	<p>Complete turnout: Vehicle/turnout dynamics [117,118]</p>
Semi- Hertzian approaches [122][123][124]		

Advantage	Limitation/ Assumptions	Reference examples
Improved accuracy of contact geometry through contact patch discretisation and penetration [47].	Poorer efficiency than Hertzian/multi-Hertzian [126] . Penetration value based on assumptions [47]. Elastic material [126]. Accuracy limited to symmetric contact patch. [18].	Switch: Wear [46,47,50]; RCF [47,53]
Kalker- CONTACT [125]		
Considers a variety of contact patch shapes [18,125]. Benchmark for other contact models[47].	Poor efficiency [18,47] Pure elasticity [18,125]	Switch: Wear [47]; RCF [47]; Vehicle/turnout dynamics/ New contact model [54] Complete turnout: Wear [115]; RCF [115]
Modified Kalker- WEAR [54]		
Accurate conformal contact modelling [54] Developed for S&C [54]	Ignores influence of traction [54]	

Advantage	Limitation/ Assumptions	Reference examples
FE normal contact (Direct/penalty/Augmented lagrange) [98]		
Real time solution whilst considering deformation/dynamics [127]. Gives subsurface stress distributions [18]. Potential to consider non-linear material behaviour [24,52].	Poor efficiency [18]. Effect of vehicle dynamics on contact is generally ignored/simplified in FE.	Switch: Wear [47,52]; RCF [52]; Plastic deformation [47,52,95] Crossing: Wear [71,72,80,82,92–94]; RCF [24,72,74,78,92]; Plastic deformation [71,75,80–84,92–94]

2.1.2.2 Tangential contact models

To achieve representative results for surface damage prediction, accurate load propagation to the rail subsurface, and to address stick/slip regions, sliding velocity, and creep parameters, an appropriate tangential contact algorithm is crucial.

Among the different approaches, Kalker's CONTACT algorithm [125] which is based on Haines and Ollerton's strip theory [128], is considered the benchmark for wheel/rail contact. However, it has limitations for S&C contact, including convergence issues and efficiency concerns [54]. The FASTSIM algorithm, a simplified version of Kalker's theory, is widely used for S&Cs, offering efficient creep estimations under usual conditions but with shortcomings for certain contact patch geometries and parabolic traction bounds [129].

Semi-Hertzian approaches, such as STRIPES [123] and FaStrip [129], refined FASTSIM for tangential contact, improving spin creepage handling and flexibility coefficients. WEAR, an extension of Kalker's CONTACT algorithm, was developed for more accurate results in flange contact regions.

However, it faces challenges in terms of efficiency and has limitations in conformal contact situations [54].

Shen-Hedrick and Elkins' theory [130], a modification of a previous theory by Vermeulen and Johnson [131] incorporating Kalker's creepage coefficients, achieved efficiency improvements compared to FASTSIM and CONTACT but gave poor results in flange contact regions and was valid only under specific assumptions [125].

In FEA, sliding initiation is determined by the critical shear stress defined by the Coulomb friction model. Transition between sticking and sliding conditions is determined by the coefficient of friction. While FEA enables real-time transient analysis and consideration of elastic-plastic behaviour, it may suffer from imperfect dynamic relaxations and high vibrations, impacting tangential contact results [127]. For a comprehensive overview of the advantages, limitations, and applications of tangential contact models in S&Cs, refer to Table 5.

Table 6. Tangential contact modelling approaches

Advantages	Limitations	Reference examples
Shen-Hedrick-Elkins theory [125]		
Excellent efficiency [125]. Consideration of creepage [125].	Assumes small spin and unrestricted creepage [125]. Poor for rail flange/gauge corner contact [125].	Crossing: Substructure dynamics [105]

Advantages	Limitations	Reference examples
FASTSIM [125]		
<p>Good efficiency [128].</p> <p>Highly used for S&Cs [128].</p>	<p>Elliptical contact patch [128].</p> <p>Stresses/creepages assumed at ellipse centre [128].</p> <p>Parabolic traction bound gives inaccurate shear stress estimation [129].</p>	<p>Switch: Wear [22,47,52]; RCF [22,47,52]; Plastic deformation [52,101]</p> <p>Crossing: Wear [45]; Plastic deformation [45]</p> <p>Complete turnout: Wear [48,49,116]; RCF [49]</p>
Modified FASTSIM- STRIPES [132]		
<p>Improved consideration of spin creepage [47,54,123].</p>	<p>Parabolic traction bound, similar to FASTSIM [123].</p>	<p>Switch wear [46,47,50]</p> <p>Switch RCF [47]</p>
Modified FASTSIM- FaStrip [129]		
<p>Variety of contact ellipses considered [129].</p> <p>Improved consideration of high values of creepage. [129].</p> <p>Improved shear stress estimation with Elliptic traction bound [129].</p>	<p>Further validation required [129].</p>	<p>Switch wear [47]</p> <p>Switch RCF [47,53]</p>

Advantages	Limitations	Reference examples
Good efficiency [129].		
Kalker's CONTACT model [125]		
Unrestricted contact patch shape [18,128]. Considers elastic deformation [128].	Poor efficiency [18,47]. Elastic half-space assumption still a limitation [18].	Switch: Wear [47]; RCF [47]; Vehicle/turnout dynamics/ New contact model [54]
Modified CONTACT- WEAR [54]		Complete turnout: Wear [115]; RCF [115]
Accurate for conformal contact [54]. Considers spin creepage change within the contact patch [54]. Accurate consideration of yawing in contact point detection [54].	Very poor efficiency [54].	
Coulomb's friction law (FEA) [98]		
Also used in CONTACT, representative for rail applications [125]. Non-linear elastic-plastic material behaviour can be considered.	Poor efficiency. Imperfect dynamic relaxation and vibrations in FEA (for quasi-static simulations) [127].	Switch: Plastic deformation [95] Crossing: Wear [71,72,80,82,92–94]; RCF [24,72,74,78,92]; Plastic deformation [71,75,80–84,92–94]

2.1.3 Damage prediction models

Various approaches for predicting the failure mechanisms of wear, RCF, and plastic deformation have been outlined. Additionally, a summary of their capabilities, limitations, and the necessary input parameters derived from dynamic interaction and contact analyses for each damage prediction method has been provided.

2.1.3.1 Wear prediction models

Among the popular models used to study wear prediction, the $T\gamma$ model implements the concept of the energy expended within the contact patch to quantify rail wear and RCF intensity [133]. It is implemented in the whole life rail model, which is based on experimental correlation between rail crack occurrence and RCF damage simulation [134]. A study comprising experimental tests on rail grade R260 established the thresholds for $T\gamma$ for that particular material: values below 15 J/m indicated no rail damage, 15-65 J/m initiate RCF, 65-175 J/m signified increasing wear with reduced RCF risk, and values exceeding 175 J/m indicated severe wear without RCF, as excessive wear eliminates surface cracks [133]. It was noted that the $T\gamma$ threshold varied for different rail steels, with R350 HT rail steel having showed excessive wear only for $T\gamma$ values exceeding 400 J/m [135]. Further validation of this model for S&C rails was recommended [18]. The wear number $T\gamma$ can be obtained by the summation of the product of creep forces and creepages in longitudinal, transverse, and spin directions [136]. A more detailed insight to this model will be provided in Section 3.1.2.

Among the reviewed literature, the most popular S&C rail wear prediction model was the Archard's wear law, which is used to calculate the worn off material volume, by dividing the product of frictional work and the empirical wear constant with hardness of the two materials in contact [71,137]. The empirical wear constant, also called the non-dimensional wear coefficient, is a value based on the material hardness and contact pressure; with examples in literature available for different S&C materials. The presence of relative sliding distance/velocity between the surfaces would make the depth/volume of wear measured using this relationship non-zero, rendering this model suitable for predicting wear due to slip in the contact patch. It has been suggested that this approach is suited to

predict wear using the local method, where the contact patch is discretised into elements and if the global method, where wear is computed over the complete contact patch is to be used, then the model is limited since the effect of spin cannot be considered [138] .

Specific frictional power and work are the relationship between variables such as contact pressure, sliding velocity, and friction coefficient, which have been obtained from dynamic wheel/rail interaction in S&C FE models [71] . Although these results have been shown to be proportional to those obtained from Archard's wear model, more specific validation studies through comparison against micro-models and field experiments have been suggested [71] . A summary of modelling aspects of the most commonly used wear models for S&Cs along with references to examples in literature has been provided in Table 7.

Table 7. Summary of different wear models used with S&C numerical simulation

Capability	Input parameters	Limitation	Examples
T γ wear number [136]			
Qualitative risk of wear on the rail surface [136]. Categorisation of locations on railhead surface on the basis of the risk of wear/RCF occurrence [134].	Creep forces and creepages in longitudinal, transverse and spin directions [22].	Further validation is required for S&C [18].	Switch [51] Crossing [72] Complete turnout [48,49,115,116]
Archard's wear law [137]			
Magnitude of wear depth or volume [71].	Contact force/pressure, sliding distance/velocity,	Feasible only for small spin when computing wear	Switch [22,46,47,50,52]

Capability	Input parameters	Limitation	Examples
	duration of contact and material hardness [22,92].	globally across the contact patch [138].	Crossing [45,80,92,93]
Specific frictional work and power [71]			
Proportional to wear depth [71]. Input to Archard's Wear law to obtain wear depth [71].	Contact pressures, sliding velocity and friction coefficient [71].	Further validation required [71].	Crossing [71,82,94]

Studies in literature have shown that S&C wear has been incorporated into studies to analyse its influence on subsurface stress/strain behaviours during vehicle-track interactions [43]. Moreover, damage prediction models have the potential to forecast wear progression in field-measured rail profiles. Recently, statistical methods have emerged for predicting remaining useful life using simulation outputs that quantify the extent of damage. In one instance, for plain line rail, a meta-model leveraging response surface methodology (RSM) was employed to estimate the cycles required to reach critical wear depth based on outputs from a single run of the Archard's wear model [139]. This prediction was in good agreement with results obtained from cyclic numerical simulations.

2.1.3.2 RCF prediction models

Approaches to predict surface and subsurface RCF faults will be discussed in this section. One widely used method for predicting the initiation of surface RCF damage is the fatigue index (FI), which relies on dynamic vehicle/track interaction outputs that have been shown in Table 8 [14]. Any positive value of the index indicates the potential formation of surface-initiated RCF cracks. This model operates on the principle that surface cracks result from the accumulation of plastic damage or ratcheting and

incorporates the yield stress in shear for a work-hardened material [22]. To forecast the cyclic accumulation of fatigue damage under fluctuating loads, the Palmgren-Miner rule for linear damage can be applied to determine the proportion of utilised fatigue life within the localised region. It is important to note that the representativeness of the model is limited to specific contact conditions due to assumptions of full slip and Hertzian contact conditions.

The T γ model, discussed earlier in Section 2.1.3.1, serves a dual purpose since it not only distinguishes between surface wear and RCF-susceptible areas on rails but also helps determine the extent of RCF damage on S&C rails [133].

For crossing rail materials, a method has been explored to predict the initiation of surface RCF cracks during the initial loading cycles until elastic shakedown [81]. This approach relies on FE model outputs for the variables listed in Table 8 to calculate a damage indicator number, with micro-crack initiation occurring when this number reaches unity. However, this model is primarily suitable for predicting damage during the first few loading cycles and for tensile failure prediction [81].

Conversely, the fatigue life of a crossing material during the ratcheting phase, characterised by the accumulation of plastic deformation with each loading cycle, can be determined by calculating the equivalent ratchetting plastic strain per cycle using FE model outputs [78].

An empirical model introduced by Jiang and Sehitoglu [140] supports the prediction of railhead surface/subsurface cracks by utilising a fatigue damage parameter calculated from post-processing structural analysis outputs. This model identifies the critical crack initiation location along the turnout based on the highest Von Mises stress value. The plane of fatigue crack propagation is determined through tensor rotation of stresses/strains at this critical location. By establishing a relationship between material fatigue properties and model outputs, it estimates the remaining cycles to fatigue crack initiation. It is important to note that the fatigue crack initiation location differs between nominal and worn rail profiles, suggesting that estimations from the model should be implemented for cyclic studies rather than treated as a one-time accurate prediction. However, this surface/subsurface RCF

prediction approach is limited by the computational efficiency of the solver used to obtain the model inputs [140].

Another approach was implemented to calculate the propagation of existing subsurface RCF cracks [74]. This method determines the crack growth amplitude and direction by calculating the crack growth angle and strain energy at the crack tip using a 2D FE crossing model with the crack's geometry. However, this model is primarily suited for studying the propagation of existing cracks and does not predict crack initiation. It is worth mentioning that RCF damage, such as squats, can also be integrated into rail geometry to investigate their impact on dynamic response outputs [89]. A summary of the most commonly used RCF prediction models for S&Cs, along with references to examples in the literature, is provided in Table 8.

Table 8. Summary of different RCF models used with S&C numerical simulation

Capability	Input parameters	Limitation	Examples
Shakedown theory index [14]			
<p>Contact locations with risk of surface initiated RCF [14].</p> <p>Prediction of fatigue life with Palmgren-miner rule [141].</p>	<p>Normal and lateral contact forces</p> <p>Contact patch geometry</p> <p>Yield shear stress of work-hardened rail material</p>	<p>Full slip assumed [22].</p> <p>Assumes Hertzian contact patch [22].</p> <p>Does not estimate RCF damage type [22].</p>	<p>Switch [22,47,52,53]</p> <p>Crossing [92]</p> <p>Complete turnout [49,115]</p>

Capability	Input parameters	Limitation	Examples
Ty number [136]			
Wear/RCF locations using whole life rail model [134].	Creep forces and creepages in longitudinal, transverse and spin directions	Further validation for S&Cs suggested [18] Does not estimate RCF damage type [142].	Crossing [72] Complete turnout [115]
Jiang and Sehitoglu (J-S model) [140]			
Fatigue crack initiation location, plane and cycles to failure [140].	Maximum normal stress Normal strain range Shear stress and strain range Material fatigue properties	Inputs to the model require high computational times [140].	Crossing [24]
Surface crack FE model [74]			
Crack growth angle, crack driving forces and strain energy at the crack tip [74].	Total elastic-plastic strain energy Crack geometry (initial crack angle) Maximum contact pressure, contact patch size and slip.	Propagation of existing crack without studying crack initiation [74].	Crossing [74]

Capability	Input parameters	Limitation	Examples
Surface damage indicator model [81]			
Surface RCF damage development through merging of voids until elastic shakedown (initial cycles) [81].	Material constant Mean hydrostatic stress Equivalent Von Mises stress Incremental plastic strain vector Accumulated equivalent plastic strain	Only valid for initial loading until elastic shakedown [81]. Invalid if no tensile principal stress components present [81].	Crossing [81]
Equivalent ratchetting plastic strain [78]			
Fatigue crack initiation by ratchetting [78].	Axial and shear ratchetting strains at every cycle whilst implementing a non-linear elastic-plastic material model [78].	Only valid for low cycle fatigue [78]. Lack of validation with experimental data [78].	Crossing [78]

2.1.3.3 Plastic deformation prediction models

In literature, models predicting plastic deformation of S&C rails have focused on two main approaches: assessing the material response beyond the elastic limit under high impact loading over a single cycle and studying the cyclic accumulation of subsurface plastic damage. Section 2.1.3.2 discussed plastic damage leading to RCF cracks.

For plastic deformation due to high impact loads exceeding the yield limit, the Von Mises yield criterion is used [93]. This criterion considers the effect of both normal and shear traction on the rail. Locations experiencing plastic deformation are indicated by Von-Mises stress values higher than the

yield strength in all three dimensions. While some literature examples simplify the Von Mises criterion by excluding shear components, most consider both normal and shear components. An equivalent plastic strain, a scalar variable based on the Von-Mises yield criterion, is employed to represent locations undergoing plastic deformation [98].

In regions with high stress concentrations, the prediction of subsurface damage in crossing regions due to high cycle fatigue has been achieved by applying the Dang Van criterion [75,143]. This criterion, originally used for studying the initiation and propagation of surface RCF cracks, has also been employed to identify areas with potential plastic deformation beneath the crossing rails [75]. However, for accurate damage initiation estimation, the calculation of the Dang-Van damage number necessitates stabilised microscopic variable outputs obtained after elastic shakedown. Additionally, precise damage initiation prediction requires the use of a calibrated elastic-plastic material model since initiation relies on the equivalent stress exceeding the shear-torsion fatigue limit [75].

Load tests have been conducted on rail steel of various grades to capture material characteristics for use in cyclic material models. The accumulation of plastic strains in the subsurface rail, obtained from wheel/rail interaction models, has been extensively studied to predict plastic deformation while considering non-linear elastic-plastic hardening material behaviour. Ohno and Wang [144] developed a model to capture the accumulation of cyclic plasticity, incorporating a plastic multiplier parameter derived from loading conditions, deviatoric stress, and kinematic hardening. Many FE models in the literature incorporated material non-linearity using the cyclic Chaboche model, which combines isotropic and kinematic hardening [145]. The impact of non-linear elastic-plastic material behaviour and cyclic hardening on the accuracy of damage results has been discussed in Section 2.1.4.3. A summary of modelling aspects for the most commonly used approaches to predict plastic deformation for S&Cs, along with references to examples in the literature, is provided in Table 9.

Table 9. Summary of different models for plastic deformation used with S&C numerical simulation

Capability	Input parameters	Limitation	Reference examples
Von-Mises yield criterion [98]			
S&C locations with stresses beyond the yield limit.	Normal stresses and shear traction in all dimensions Representative material properties.	Limited by choice of material model and the efficiency of the solver.	Switch [95] Crossing [80,84,92–94]
Equivalent plastic strain [98]			
Rail locations with plastic deformation.	Plastic material properties.	Limited by material model choice. Poor efficiency of FE models limits it to single cycle.	Crossing [71,81–83]
Dang Van criterion [75,143]			
Subsurface rail plastic deformation due to high cycle fatigue.	Shear stress amplitude and hydrostatic stress at every time step [75]. Shear-torsion and tension-compression fatigue limits. [75].	Negative stress ratios propose a different failure limit [75]. Conservative for certain contact/slip conditions. [75]. Fatigue limit overestimated by Hydrostatic stress components [75]. FE requires simplifications for improving efficiency.	Crossing [75]

Capability	Input parameters	Limitation	Reference examples
Plastic strain cyclic accumulation [144]			
Plastic deformation accumulation in S&C rails.	Updated material model after each cycle. Material hardening test data.	FE requires simplification for cyclic prediction. [45,52]. Representative material model difficult.	Switch [52,101,146] Crossing [45,81]

2.1.4 Discussion of factors that would impact the choice of a modelling approach

In the preceding sections, various numerical simulation approaches for dynamic vehicle/track interaction, wheel/rail contact models, and rail damage prediction models for S&Cs were introduced. This section delves into the factors influencing the choice of an appropriate modelling approach.

2.1.4.1 Consideration of vehicle dynamics

In MBS models, the entire train, including the car body and bogies, is often included to account for vehicle dynamics. This comprehensive approach provides a more accurate representation of the wheelset trajectory for the entire train, yielding representative contact locations and forces which are crucial parameters for damage prediction. Conversely, FE models frequently omit vehicle dynamics but can incorporate detailed material degradation models that consider elastic-plastic behaviour and fatigue failure. These FE models can offer a detailed stress distribution for improved damage prediction.

Literature reveals the development of FE models that focus on wheel/S&C rail contact, often featuring a single wheel/rail, as depicted in Figure 16. While this approach enhances computational efficiency, it does so at the cost of accurately representing the lateral dynamic behaviour of the vehicle and turnout,

particularly in diverging routes. Utilising a single wheel can lead to inaccurate assumptions, such as negligible slip and low lateral and longitudinal tangential forces [81]. It has been observed that considering a complete wheelset, rather than a single wheel, helps maintain wheel stability [71]. However, it may require additional constraints for accurate simulation.

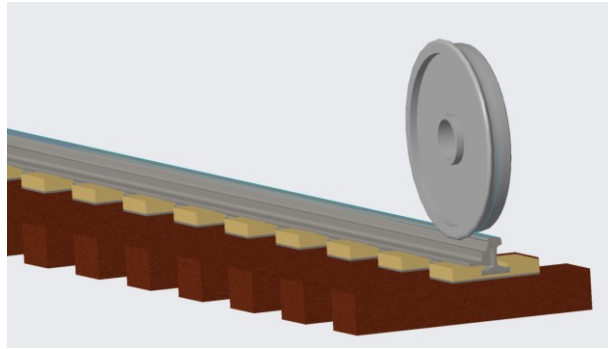


Figure 16. Solid element half-track switch model with a single wheel

Dynamic interactions between a complete wheelset and switch/crossing panels have been implemented in simulations, as illustrated in Figure 17. By considering a complete wheelset, it becomes possible to obtain a more representative motion and implement less displacement constraints than if a single wheel were modelled [91]. These models offer more detailed insights into lateral dynamic effects compared to those focusing on a single wheel. However, it is important to note that such models may overlook lateral dynamics resulting from bogie and car body connections.

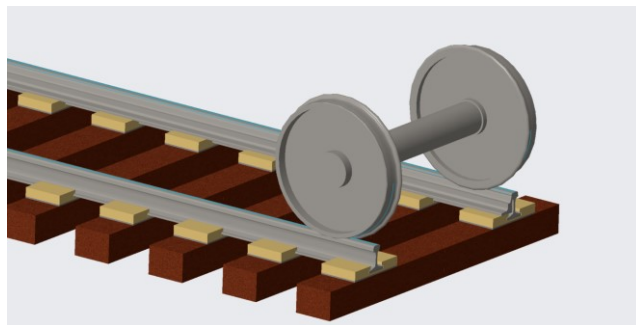


Figure 17. Solid element full track switch model with one wheelset

In simulations involving wheelset contact with switch panels, the influence of the sprung mass on this contact is relatively low in terms of frequency response but not entirely negligible [70]. Therefore,

many examples in the literature have considered vehicle dynamics up to the primary suspension and have simplified the secondary suspension along with the carriage and bogies as a lumped mass [70]. This simplification is particularly suitable for analysing the smoother load transition at the switch. However, for the discontinuous transition from the wing rail to the crossing, higher-frequency impacts cannot be avoided. Therefore, the consideration of lower-frequency vehicle dynamics becomes less critical, and the secondary suspension's effect on wheel-rail contact is minimal [127].

Additionally, numerical simulations can be conducted by directly applying contact loads onto S&C rails without the need for detailed wheelset geometry. These models primarily focus on analysing substructure behaviour and do not necessitate intricate wheel-rail contact modelling, helping achieve acceptable computational efficiency for FE models while considering a complete track model for longer turnout lengths [96,97].

2.1.4.2 Consideration of track dynamics

Considering the impact of substructure or track stiffness is a critical aspect since it directly affects the magnitude of impact forces exerted on the rail. The material characteristics of the railpad and ballast play a role in determining rail deflection, while the spacing between sleepers influences load distribution on the rail and the transmission of stress from the superstructure to the substructure [128].

In instances where a combined modelling approach involving MBS and FEA is employed [43], it is important to recognise that substituting impact load values and wheelset displacement data from a supported MBS track model into an FE model lacking bedding characteristics could potentially impact the accuracy of the results. In real-world scenarios, lower bedding stiffness allows for more significant vertical rail deflection, resulting in a more uniform distribution of axle loads over the sleepers, unlike a rigid track with higher stiffness [128]. Therefore, in combined MBS/FE models, it is crucial to calibrate the properties of the superstructure and bedding between the MBS and FE models.

For addressing higher-frequency track dynamics, multi-layer MBS track models with multiple degrees of freedom (DOF) are more precise compared to single-layer co-running track models [68]. These

multi-layer models enable the separation of bedding components and the adjustment of properties for individual rail and trackbed components. In the realm of FE modelling, the substructure can be simplified using rigid elements or represented using detailed solid elements. The process of calibrating FE track properties against MBS models and field measurements involves adjusting material properties to achieve similar rail receptance results [147].

2.1.4.3 Consideration of representative material properties

The choice of material properties has a notable impact on various aspects of rail analysis. It has been demonstrated that material property selection affects the size of the contact patch and the distribution of stress [111], as well as the distributions of wear and Rolling Contact Fatigue (RCF) surface damage [47]. Furthermore, it plays a role in determining the distribution of subsurface damage and Von Mises stress in regions with plastic deformation [80].

In studies exploring MBS interaction between vehicles and plain line rail, the Semi-Hertzian method [126] and the multi-hertzian method [132] have implemented the consideration of perfectly plastic material behaviour, albeit without material hardening. Interestingly, these studies yielded comparable results to elastic-plastic steady-state FEA, with the perfectly plastic material exhibiting larger contact patch sizes and reduced contact stress levels compared to materials with purely elastic behaviour [132].

For ductile materials, it is important to note that when material behaviour transitions into the elastic-plastic regime, the increase in strain for a given stress increment is greater compared to the linear-elastic region. Consequently, assuming linear-elastic material behaviour in regions with plastic deformation would lead to overestimated stress values, potentially impacting the accuracy of damage prediction [80].

Across the spectrum of reviewed literature, the majority of FE wheel/rail contact models used for damage prediction incorporate elastic-plastic material behaviour with hardening in S&C rails.

However, in many cases, linear elastic material behaviour has been attributed to the wheel, primarily

due to a lack of hardening data for wheel materials [75] or the assumption that the simulations involve new wheels undergoing cyclic passages [81]. Models that directly apply loads to complete S&C turnouts without detailed consideration of wheel geometry have also assumed linear elastic material properties for S&C rails [96,97]. These models often focus on substructure analysis [96] or vehicle dynamics [97].

2.1.4.4 Computational efficiency for numerical simulation of S&Cs

The efficiency of numerical simulation approaches is contingent on model complexity. Typically, MBS models are the fastest, followed by modal reduction flexible track models, combined MBS-FE models, and solid element FE models in terms of computational speed. When considering empirical wheel-rail contact models, the hierarchy from fastest to slowest consists of the Hertzian method, multi-hertzian methods, Semi-Hertzian methods, and Kalker's CONTACT boundary element model. Interestingly, the slower models tend to yield more representative results. It is also worth noting that elastic-plastic contact models are generally slower than their purely elastic counterparts, even when using the same contact method [126,132].

For models focusing on vehicle performance and wheel damage, it is possible to simplify track dynamics by representing the wheel-rail contact patch as linear springs and assigning each wheelset one vertical and lateral Degree of Freedom (DOF) [62,63]. To distinguish between stock and switch rails, one can modify the contact stiffness, halving it for the latter in the transition region, thereby simplifying modelling [62].

In order to obtain efficient damage predictions, empirical damage prediction models can be employed in a post-processing step. In-depth cyclic damage studies using the FEA approach may encounter limitations related to computational efficiency. Techniques such as selective meshing, geometry simplification, plane stress/strain assumptions, or sub-modelling can be used to improve computational efficiency in such cases.

2.1.4.5 Different frequency ranges for fault simulation

Material failure often arises from high lateral and normal contact forces during specific rail transitions, such as stock-switch and wing rail-crossing nose transitions. In these situations, it is crucial to capture dynamics at high frequencies for accurate damage prediction. FEA models are well-suited for this purpose, as they can provide the necessary high-frequency data. However, commonly used MBS models, particularly those with a single track layer, are generally limited to lower frequencies [52]. To address this limitation, MBS models with multiple track layers and higher DOF are employed to capture higher-frequency content effectively, as discussed in Section 2.1.4.2.

Variation in rail properties along the longitudinal direction and the need for field calibration are essential factors for ensuring that model results align with real-world conditions. Calibration of MBS track models to match field measurements is achievable and has been demonstrated in previous work [45]. For instance, rail receptance values in the model were calibrated up to 200 Hz to replicate field substructure properties, resulting in good agreement between the model and field data [45]. Field measurements of track stiffness in the frequency range up to 20 Hz have been conducted using specialized vehicles like the rolling stiffness measurement vehicle (RSMV) [68,148]. These measurements have led to the development of relationships for converting field data into substructure dynamic properties for both single and two-layered Switches and Crossings (S&C) track models [68]. To capture higher-frequency content effectively, various modelling approaches, including beam/solid element Finite Element (FE) models and models based on FE modal reduction, can be employed alongside multi-layered MBS track models to enhance the fidelity of results.

2.1.4.6 Methods of model validation

Many models discussed in the literature were subject to validation against field measurements, involving comparisons of dynamic outputs with well-established models. Validation methods commonly included qualitative comparisons of dynamic outputs, such as normal and lateral contact forces and Von Mises stress, against corresponding data from validated models in existing literature. Some validations went further, directly comparing simulation results with field measurements, which

included comparisons of contact forces, rail accelerations, transition regions, degradation (wear/plastic deformation) depth, and sleeper displacements [68,86,91,106,148]. Additionally, calibration-based validation was conducted by fine-tuning material properties through load tests and adjusting substructure dynamics using rail receptance values [56,68,147]. In MBS approaches, this often involved selecting appropriate stiffness and damping coefficients for track models with varying numbers of bedding layers.

For example, worn switch rail profiles, side wear, and worn areas measured in the field were compared with corresponding outputs from MBS simulations and Archard's wear model over the passage of 100 10 million gross tonnes (MGT) of rail traffic [46]. Results showed that the estimations from simulation results closely aligned with field measurements of side wear and worn areas. However, near the switch tip, simulations considerably underestimated wear due to contact occurring between the wheel and switch tip only after significant wear of the stock rail. In actual operations, dynamic relative displacement between the stock and switch rails increases the risk of wheel flange contact [46].

In another instance, a comparison was made between the predictions of wear and plastic deformation from FE simulations and degradation measured in the field after the passage of 15.10 MGT [93]. The regions displaying severe wear and plastic deformation in the field were consistent with the predictions obtained using Archard's wear model and the Von-Mises yield criterion in the simulation results. Furthermore, a RCF fault, known as spalling, was observed in the diverging direction based on field measurements [93]. Stresses obtained from the FE simulations in the vicinity of the fault occurrence were significantly higher in the diverging route than in the through route, demonstrating the potential of numerical simulations to predict specific RCF faults [93]. These findings indicate that damage prediction models have effectively predicted degradation locations for various S&C layouts.

2.2. Modelling methodology and assessment criteria

The evaluation of modelling methods that was published [12] and paraphrased in Section 2.1 has been implemented for determining a modelling framework for achieving the aims of this thesis. The approach to simulating the train-track switch interaction has been developed to meet two objectives. The first objective is to determine the most crucial locations for the development of surface defects and the second is to determine the locations for the installation of sensors for detecting the occurrence of defects. The overall simulation approach that will be implemented for achieving the two objectives has been graphically demonstrated in Figure 18.

To achieve the first objective with a high degree of efficiency and accuracy, the results that are obtained from MBS simulations of dynamic train-track switch interactions will be implemented to obtain the wear number, $T\gamma$. It will be shown in Chapter 3.1 that the MBS simulation outputs are obtained from a benchmark-based model that was already developed prior to this thesis, which will be a reference for developing the FEA model [41]. The results for the wear number, $T\gamma$, will help determine the crucial points along the length of the switch that will deteriorate as a result of surface-initiated rail damage.

Once the locations susceptible to wear and RCF are determined from the $T\gamma$ results, a model that will represent a shorter track with those crucial locations will be developed for FEA. The properties contributing to the dynamic behaviour of the track in the MBS model will be converted to the equivalent material properties for the FE model to ensure compatibility. This will be discussed in Chapter 3.2. The modelling details including the setup and the wheel-rail contact modelling in the MBS and FEA simulations will be set out in Chapters 3 and 4.

The accuracy of the material properties will be verified from the results for the rail receptance. The comparison of the rail receptance in the vertical and lateral directions at the frequency range of interest will not only help validate the calculated material properties but also determine the compatibility of

the track dynamics between the MBS and FE models. The concept of the rail receptance and the studies will be discussed in Chapter 3.3.

Finally, simulations of rolling contact between a wheel and the rails of the switch panel in the through route will be carried out whilst implementing the longitudinal, rotational and lateral vehicle wheelset movements that will be input to the FE model from the MBS model. This will be discussed in Chapter 4. In this way, a representative behaviour for the vehicle movement as well as the track dynamics will be implemented in the FE model.

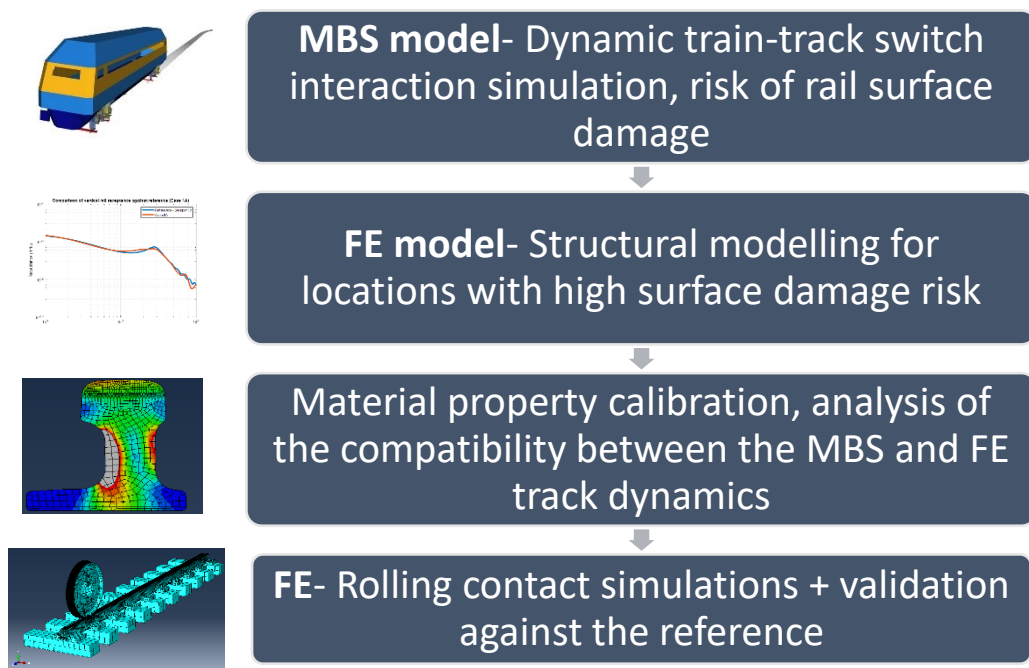


Figure 18: Simulation approach for the interaction between railway vehicles and track switches

Since the number of simulations for concluding the requirement for the accuracy of results are not enough, the modelling assessment will be based on whether the FEA model is able to roughly replicate or stay within the difference that was observed between the different reference models that are based on the MBS S&C benchmark [4]. This will also help with defining the compatibility between the simulation steps shown in Figure 18. Along with the MBS S&C Benchmark, the other reference models will be described in Chapter 3. The modelling assessment criteria for the FEA has been

proposed in Table 10 and links have been provided to the chapters and sections within this thesis where the terms in the table will be defined and the comparison of the results against the reference will be discussed. The reference models will be explained in Chapter 3.1.1.

The source of the threshold for the assessment parameters in Table 10 are as follows. The threshold for the rail receptance has been set based on the difference in the published results between the beam element FE model (reference model 2 [41]) and the two-layer, three-layer MBS models (reference models 2 and 3 [41]). The threshold for the wheel-rail interaction outputs, including the vertical contact force, vertical wheel displacement, contact point location and contact patch size have been set based on the difference in the published results between the three-layer MBS model (reference model 4) and the two-layer MBS model (reference model 3 [41]), the MBS benchmark model for S&C (reference model 1 [4]). A constraint has been imposed on the FE simulation run time to enable running multiple simulations for achieving the research objectives.

Table 10: Modelling assessment criteria

Parameter	Chapter and section where defined/discussed	Assessment criteria for the 3D FEA model
Vertical Rail receptance	Chapter 3: Sections 3.3, 3.4	< 15% different from the reference Model 2 (a beam element FE model explained in Chapter 3.1.1) for the amplitude of the resonant frequency, the receptance amplitude at 10 Hz, receptance amplitude at the resonant frequency
Lateral Rail receptance	Chapter 3: Sections 3.3, 3.4	< 15% different from Model 2 (3.1.1) just for the amplitude at 10 Hz.

Parameter	Chapter and section where defined/discussed	Assessment criteria for the 3D FEA model
Vertical wheel-rail contact force	Chapter 4: Section 4.3.1.	<p>< 10% different from the reference model at a distance of 9.13, 9.44 m from the switch toe. (Model 4, a three layer MBS track model, explained in Chapter 3.1.1)</p> <p>< 10% difference for the average value between 9 and 10.6 m from Model 4 (3.1.1).</p>
Vertical wheel displacement	Chapter 4, Section 4.3.1.	< 0.25 mm difference for the vertical displacement from 9 to 10.6 m with Model 4 (3.1.1).
Contact point location	Chapter 4: Section 4.3.1.	Difference of < 2 mm for the lateral contact position with Model 4 between 9 and 9.8 m (3.1.1).
Contact patch size	Chapter 4: Section 4.3.1.	< 10% difference for the area of the contact patch from Model 4 (3.1.1) at 9.4 m.
FE simulation run time	Chapter 4: Section 4.3.1.	< 1 day on a computer cluster with 20 cores (40 GB of RAM).

In Chapter 5, it will be shown that the two-step, MBS-FE simulation methodology will be implemented for numerical simulations in the presence of track defects and the strain measurement studies for detecting those specific defects will be discussed in Chapter 6.

With regard to sensor placement, the scope of this work will be limited to determining the possibility of measuring the rail strains for detecting the defects that will be introduced for representing the failure mechanisms of wear, RCF and voiding. Since the defects rail defects can take numerous shapes and forms, the scope of work will be constrained to demonstrating a modelling approach for the defects that have specific properties and/or geometry. The locations for introducing the defects will be based on the Ty results and supporting engineering judgement.

An assessment of the possibility of measuring the strains at common location/(s) for detecting the switch wear, RCF and voiding will be carried out. For this, the defects will be introduced separately in separate models but they will be close to one another, i.e. around the same longitudinal distance from the switch toe. Since the computational efficiency of FEA will be a restriction, a finite number of runs/parametric studies will be carried out. The minimum number of samples needed for obtaining the Pearson correlation coefficient is 25 [149,150]. Therefore, the number of parametric runs from which results will be assessed will exceed 25.

Therefore, the aim of this work will be to show how numerical simulation, in particular 3D FEA of a switch can be implemented for studying the possibility of measuring strains for monitoring the switch condition. Since this is an original, first-time investigation, the improvement of numerical simulation efficiency, sensor placement approach and the implementation of defects that have been measured in the field can be a matter of future work beyond this thesis.

2.3. Digital Twin and selection of the reference model in the context of this thesis.

As explained in the beginning of Chapter 2, an important phrase in the definition of a Digital twin is ‘virtual replica’. Ideally, a Digital twin model of a railway switch should be able to replicate the properties of a reference asset. However, due to the lack of access to data from field experimentation, the 3D FEA model of the switch will be based on the turnout layout that was published in the Multibody simulation benchmark for dynamic vehicle–track interaction in switches and crossings in 2021 [151]. A beam element FE model and multi-layer MBS model that are based on the S&C

benchmark will be taken as the reference models for the modelling work and explained in detail in Chapter 3.1.1. The track modelling layout will be the 60E1-760-1:15 turnout in the through route.

It is noteworthy that a model for the 60E1-760-1:15 turnout was validated during a study in 2015 against field measurements that were carried out in 2009 by the same author that has led the Multibody simulation benchmark study [68]. The field tests were performed at two demonstrator turnouts at Eslöv, Sweden for the 60E1-760-1:15 turnout layout. The tests were carried out for three sets of railpads, soft, medium/standard and stiff. The reference models used for the comparison of results this thesis will implement the same value for the static track stiffness that were implemented in the 2009 tests for the medium/standard railpad.

Track stiffness as well as contact force measurements were executed during the 2009 tests. The vertical track stiffness was measured with a rolling stiffness measurement vehicle (RSMV) by Trafikverket. During the tests, the wheel–rail contact forces were measured using an Interfleet instrumented wheel set equipped with strain gauge bridges on each side of the wheel disc, calibrated for vertical and lateral static wheel–rail contact forces. Data loggers on board the train recorded these forces, along with GPS signals, train speed, and reference location pulses for analysis. The facing move involved mounting the instrumented wheel set as the front wheel set on a freight car with Y25 bogies and a 20-tonne axle load, with measurement signals sampled at 1200 Hz and low-pass filtered at 250 Hz. The MBS models that were validated, i.e. Models I to IV in Table 11, included the measured rail and instrumented wheel profiles. The track models was also fine-tuned and the data was sampled at the same rate as the measurements.

Table 11: Track characteristics of the models that were validated and the field measurements.

Key from Figure 19	Measurement/Model type	Space-variant track stiffness and damping	Track irregularities
IWT	Instrumented wheelset measurement	Yes	Yes

Key from Figure 19	Measurement/Model type	Space-variant track stiffness and damping	Track irregularities
I	Single layer track model	No, but fine-tuned to the average value of the dynamic stiffness measurement.	No
II	Single layer track model	Same as I	Yes
III	Single layer track model	Yes	Yes
IV	Multi-layer track model	No, but fine-tuned to a different test site.	Yes

The vertical wheel-rail contact forces along the length of the turnout have been plotted in Figure 19 for simulations and measurements in the through route with soft railpads. The low frequency oscillations can be seen in the results for models II, III and IV since they have implemented the track irregularity, unlike model 4. In the publication, it has been discussed that the dynamic excitation in Figure 19 is larger for the measured signal (IWT) than the modelling outputs since the lateral track irregularity data was not modelled into the switch panel. Therefore, it was suggested in the publication that the track irregularity excitation is slightly smaller in the model compared to the measurements [68].

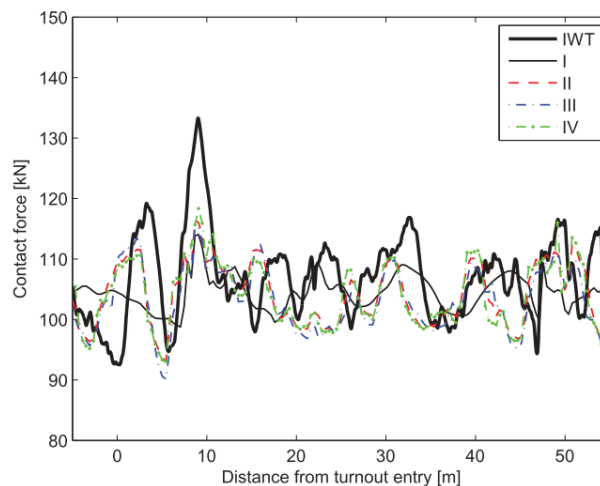


Figure 19: Measured and simulated vertical contact forces in the through route with soft railpads, reproduced from [68].

It is worth noting that the train and track properties that will be replicated during the modelling work in this thesis are from reference models that exist as benchmarks only for modelling/academic purposes. In Chapter 3.1.1, it will be shown that they contain assumptions which are not valid in field conditions (e.g. no track irregularities). Ultimately, they have been taken up as the comparison/fine-tuning reference in this thesis since the results are readily available and replicable. Also, as discussed and shown through Figure 19 and Palsson et al. [68], approaches to MBS that are similar to the benchmark modelling have been subject to validation against field measurements, albeit with more field-relevant modelling properties.

As the title of this thesis suggests, it will present a move “towards (building) simulation-based digital twins”. There are other aspects of Digital Twins that have not been addressed within this thesis, i.e. connected, in-service and mirroring the life and experience of the asset. These will be possible once the primary step of developing the model has been achieved through this thesis.

2.4. Conclusions

As defined in the title of this thesis, the research contributions will only be a step towards the creation of a Digital Twin and the thesis will explore a methodology of developing a FEA model that is based on a reference track model. The evaluation of the numerical simulation approaches, wheel-rail contact and damage prediction modelling have set out the modelling methodology for achieving the objectives that were set out in Chapter 1. The modelling methodology will implement a two-step, MBS-FEA simulation approach for train-switch dynamic interactions. The modelling will be carried out for the 60E1-760-1:15 switch layout and the reference models are based on a modelling benchmark study. Field experimentation for this S&C layout has been discussed in literature but they had not implemented the same parameters that were implemented in the benchmark model, and thus the modelling contributions within this thesis. The scope of the sensor placement studies within the thesis will be restricted to understanding the possibility of measuring rail strains to detect wear, RCF and voiding. The assessment criteria that have been set out in Table 10 will be implemented for assessing the performance of the FEA model, whose development will be shown in Chapter 3.

CHAPTER 3. DEVELOPING SOLID MODELS AND SIMULATING THE APPROPRIATE TRACK DYNAMICS FOR THE RAILWAY SWITCH IN TWO-STEP MBS-FE SIMULATIONS

A background to the failure modes of railway switches and the case for the potential improvement of maintenance practices through the implementation of continuous condition monitoring for the rails of switches was first highlighted in Chapter 1. It was then recognised in Chapter 2 that numerical simulations can be powerful tools for anticipating the locations that will potentially experience the most rail damage or the critical failure points, as well as for determining the placement and selection of sensors for the condition monitoring of rails. The different approaches for simulating the vehicle-track dynamic interaction, wheel-rail contact and the prediction of damage locations were reviewed in Chapter 2.

Building off previous work identified by the literature reviewed in Chapter 2, an approach will be discussed for making decisions with regard to the predictive maintenance of railway switches in this chapter. Firstly, the results from holistic simulations for train-switch dynamic interactions will be implemented in a damage prediction model to determine the locations that are highly susceptible to rail damage. Following this, the approach to developing an FEA model that can capture the wheel-rail contact interaction as well as the stresses and the strains that will be experienced by the rails for the specified section of the track with a high risk of damage will be discussed.

Two approaches will be implemented for meeting the two aforementioned objectives. The first will be a holistic and computationally efficient approach to capture the train-track switch interactions for determining the sections of the track where the highest risk of rail damage can be anticipated. This approach and the results for predicting the sections that will undergo the highest damage will be highlighted in Section 3.1. The second modelling approach will be implemented to capture the detailed

mechanical behaviour for a specific section of the track where a high risk of damage will be anticipated. A description of the procedure for modelling the 3D solid track components will be provided in Section 3.2. As the results from the holistic model will be used to determine the locations for more detailed modelling, the detailed model will need to capture the track dynamics that are the same as the MBS model. Therefore, the approach to modelling the track with the appropriate boundary conditions in the detailed model to capture the same behaviour as the holistic model will be discussed in Section 3.3.

In Section 3.4, the approach to determining the track properties for the FE model will be explained and the results for the rail receptance from the FE model will be compared against the reference for ensuring that the model can be implemented further in rolling contact analysis. Section 3.5 would conclude this chapter on modelling the switch track and will be followed by Chapter 4 where the track switch model will be implemented for wheel-rail rolling contact analyses.

3.1 Determining the sections of the switch track to monitor for the development of surface-initiated rail damage.

The risk of damage to the surface of the switch panel rails due to their interaction with the train wheels will be determined from the results obtained from the dynamic vehicle-track interaction simulations [41]. Firstly, the models that will be used for the validation of the numerical simulations described in this thesis will be elucidated [41,151,152]. Secondly, the empirically developed damage prediction model, T_y will be described along with its advantages and limitations. Finally, the length of the track section will be chosen to model in detail in FE.

3.1.1 Different track models for vehicle-track interaction dynamics using MBS.

The holistic models for simulating the train-turnout dynamic interaction were developed at the Birmingham Centre for Railway Research and Education (BCRRE) for the S&C MBS benchmark project [4,41,151,152]. The results obtained from these models will inform the development of the FE models in this study and will be implemented to support model verification.

Four different track models will play a role in informing the development of the detailed FE model and its validation.

1. Model 1- The S&C Multibody benchmark project model [4].
2. Model 2 - The simplified beam element 3D FE model [152].
3. Model 3 - The MBS model with varying track properties and 2 track layers [41].
4. Model 4 - The MBS model with varying track properties and 3 track layers [41].

Model 1 is the simplest model out of the four and includes two different track parameters for the switch and crossing regions of the turnout. The second model is a 3D beam element FE model but can consider more complexity through the variation of the track properties along the length of the S&C track [152]. Track models 3 and 4 consist of two and three-layered track models respectively whose track dynamic properties varied along the length of the turnout. These varying track dynamic

properties were derived from Model 2. Model 4 was developed with an additional track layer over track model 3 for capturing the high-frequency dynamic content more effectively.

Out of the four track models, models 1, 3 and 4 were implemented for carrying out the vehicle-track dynamic interaction analysis in the reference example [152]. The results from model 2 were primarily used for the derivation of varying properties for the track dynamics for models 3 and 4. The results for the rail receptance from model 2 have also been implemented for verifying the track dynamics of the detailed 3D solid element FE model that has been presented in this thesis.

The track models were implemented for a turnout layout of 60E1-760-1:15. Model 1 is a simplified model and can effectively capture the track dynamics at lower frequencies. Model 2 is the most complex and also the one that most closely replicates a real turnout and can capture the track dynamics at higher frequencies. With position-dependent track properties, model 3 was a more accurate representation of model 1 and is based on the inputs from model 2; this allows it to capture accurate results up to 200 Hz [152]. Model 4 included an additional track layer in addition to model 3 for capturing the track dynamics up to 1 kHz.

The simulations for the dynamic vehicle-turnout interaction were carried out for models 1, 3 and 4, where the Manchester Benchmark passenger vehicle model represented the MBS vehicle model with a single carriage and two bogies [153].

The material properties for the 3D solid element FE model that will be shown to be developed during this PhD work will be derived from those implemented in the beam element FE model. The results for the rail receptance from the 3D solid FE model will be compared against the beam element model, i.e. Model 2.

However, the comparison of the results from the wheel-rail contact simulations for the 3D solid element FE model will be carried out against the results that were obtained from model 4. The first reason is that model 2 is a beam element FE model that was not implemented for train-track interaction analysis. The second reason is that both the 3D solid element FE model and the MBS

model 4 are able to capture high-frequency content but models 1 and 3 are unable to. The published literature also shows a good agreement for the results of the rail receptance between Track models 2, 3 and 4.

To restate, Models 2 to 4 are based on the S&C benchmark model (Model 1). The FEA model whose development is a contribution of this PhD thesis is calibrated against and based on Model 2, which is a beam element model and the results for the wheel-rail interaction have been compared against Model 4, the three layer MBS track model.

Model 2 is a two-layer beam element track model that can capture the flexibility of the track at higher frequencies [41,152]. The rails and the sleepers in the model were modelled with Timoshenko beam elements. The railpads and ballast in the model were modelled with discrete Kelvin bushing elements with stiffness and viscous damping. Two-noded linear beam elements were implemented for modelling the rails. The rail nodes were free to displace in the vertical and lateral directions and the sleeper nodes were only free to displace in the vertical plane through each sleeper. The rail nodes in the beam element model were not allowed to displace longitudinally or to rotate along the longitudinal axis.

The track properties for the switch panel of Model 2, the beam element model, has been shown in Table 12 and a top view schematic is shown in Figure 20. The complete turnout has been plotted in Figure 20, as reproduced from Shih et al. [41]. However, since the scope of this thesis concerns the switch panel, only the relevant results from the switch panel will be discussed.

Table 12: Track properties- Beam element FE model (Model 2)

Parameter	Stock	Switch	Units
Rail mass density	7850	7850	kg/m ³
Rail Young's modulus	207×10^9	207×10^9	N/m ²
Rail shear constant	0.4	0.4	

Parameter	Stock	Switch	Units
Rail area	0.0076668	0.0056262 to 0.009353	m ²
Rail second moment inertia in the vertical direction	3.03×10 ⁻⁵	5.23×10 ⁻⁶ to 3.03×10 ⁻⁵	m ⁴
Rail second moment inertia in the transversal direction	5.13×10 ⁻⁶	5.13×10 ⁻⁶ to 7.45×10 ⁻⁶	m ⁴
Sleeper			
Sleeper mass density	2400	2400	kg/m ³
Sleeper Young's modulus	37.5×10 ⁹	37.5×10 ⁹	N/m ²
Sleeper area	0.054824	0.054824	m ²
Sleeper second moment inertia in the vertical direction	224×10 ⁻⁶	224×10 ⁻⁶	m ⁴
Sleeper length	2.5	2.5	m
Stiffness and damping			
Vertical rail pad stiffness	120×10 ⁶		N/m ²
Vertical rail pad damping	25×10 ³		Ns/m ²
Lateral rail pad stiffness	25×10 ⁶		N/m ²
Lateral rail pad damping	10×10 ³		Ns/m ²
Sleeper spacing	0.6		m
Ballast			
Ballast vertical stiffness per unit length	20×10 ⁶		N/m ²
Ballast vertical damping per unit length	200×10 ³		Ns/m ²

Parameter	Stock	Switch	Units
Ballast lateral stiffness per unit length	10×10^6		N/m^2
Ballast lateral damping per unit length	100×10^3		Ns/m^2

The static track stiffness at each sleeper location in the vertical and lateral directions have been plotted in Figure 20 B,C respectively. These were calculated from the rail receptance at 1 Hz from the beam element Model 3 at each sleeper [41]. It can be seen in Figure 20B that the vertical stiffness of the stock rail remained roughly the same throughout the length of the switch panel. The vertical stiffness of the switch rail is lower than the stock rail but increases gradually along the length of the switch panel. In case of the lateral stiffness, Figure 20C shows that the lateral stiffness for the switch and the stock rails is roughly equal and both increase along the length of the switch panel.

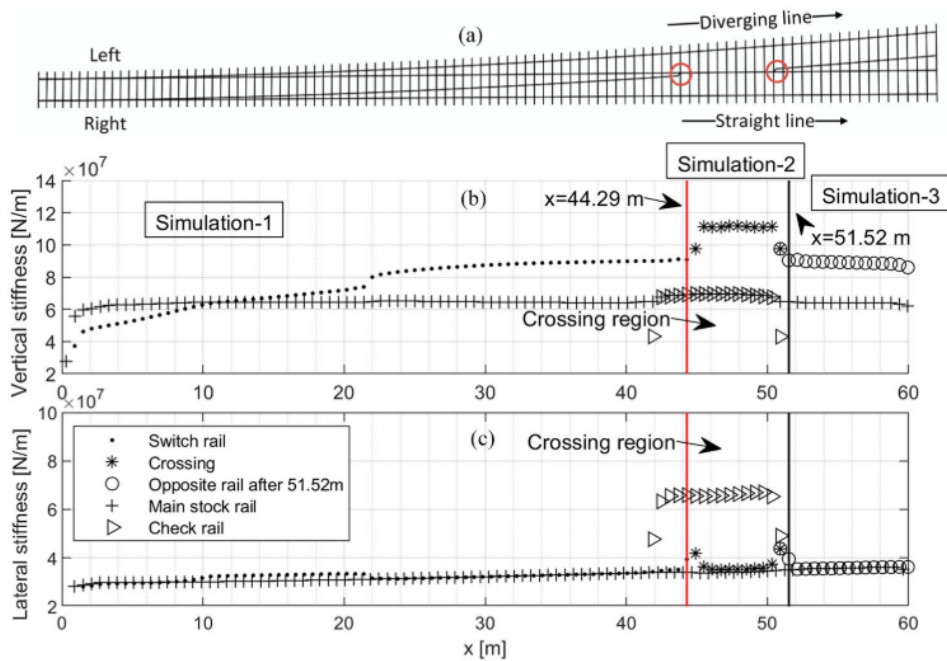


Figure 20: (a) Schematic of the turnout; (b) static track stiffness of the turnout in vertical; (c) lateral directions; reproduced from [41].

This variation in the track stiffness from Model 2 has been modelled in Model 4. Model 4 is a co-running track model and the MBS simulations were carried out in Simpack software. Due to the limitations of the co-running set-up, the mass properties were constant across the length of the switch panel in MBS, whereas the stiffness and damping values were continuously variable. Space-dependent mass variation and different mass distributions in two directions could not be modelled since Simpack restricts mass to be constant in both vertical and lateral directions during a simulation [41]. However, the stiffness and damping properties of the different force elements were continuously varied as a function of the rail position in the running direction [41].

The detailed derivation of the equations for implementing the variable track stiffness and damping in Model 4 is available in the original contribution by Shih et al. [41] and is not an original contribution of this thesis. However, the principles will be discussed and the track model properties have been included in Table 13 since the outputs from Model 4 were fed into and implemented for verifying the wheel-rail interaction results of the solid FE model which will be presented as a contribution of this thesis.

The position-dependent stiffness and damping properties in Model 4 have been captured by implementing a parameter called the effective length, which is the wavelength of the system when a unit point load is applied [41]. The effective length for each rail of the turnout was calculated as a ratio of the static track stiffness and the stiffness of an equivalent continuous support layer. The calculation of the static track stiffness has included the parameters that are dependent on the position of the rail, such as the bending stiffness of the rail. The calculation of the stiffness of an equivalent continuous support layer included parameters such as the railpad and ballast vertical stiffness and the sleeper spacing that was implemented in the beam element FE model (Model 2). Thus, the position-dependent stiffness and damping properties were calculated for Model 4 based on the parameters assigned for Model 2 in Table 12 by Shih et al. [41].

Unlike the stock rail, the switch rail could not be considered as an infinite beam, as its cross-section changes continuously along the length of the turnout. Therefore, the vertical support stiffness of the

switch rail was estimated based on the parameters derived for the stock rail and multiplied with a factor ' Δz '. This factor is the ratio of vertical support stiffness between the switch rail and stock rail in the beam element FE model (Model 2).

Similarly, for the calculation of lateral stiffness of the switch rail, a factor Δy was implemented, which is the ratio of lateral support stiffness between the switch and the stock rail based on the parameters from the beam element FE model (Model 2).

The calculation of the effective length would also vary depending on the rail support position, i.e. whether it is supported in middle (e.g. switch rail in the closure panel) and edge of the sleeper (e.g. stock rails on plain track) or when the support stiffness of the rail varies continuously (e.g. switch rail with varying cross-section) [41].

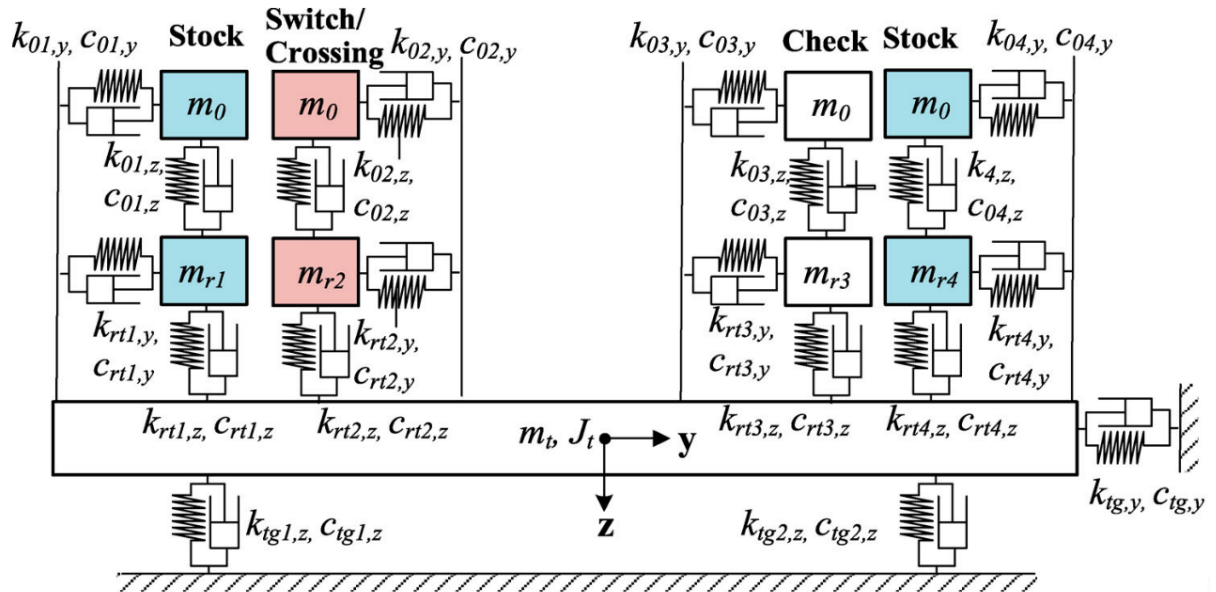


Figure 21: Track schematic for the three-layer MBS model, reproduced from Shih et al. [41].

The schematic of the three-layer MBS track model has been shown in Figure 21 and includes the parameters for the complete turnout. The stock and switch rails, as well as the opposite stock rail shown in Figure 21 form a part of the switch panel, which is of interest to this thesis. In Figure 21, the first or the bottom-most layer represents the equivalent properties of the sleeper and ballast. The

second or the middle layer represents the rail and the railpads. The third layer does not represent any physical components, but rather is a virtual spring-mass-damper system to better approximate the higher frequency responses. Table 13 highlights the track properties, where the symbols following conventional naming convention with k representing stiffness, c denoting damping, m denoting mass and J the moment of inertia. As shown in Figure 21, the lateral and vertical directions have been represented with y and z respectively. The terms Δy and Δz were explained before Figure 21 as factors that help obtain the varying track properties for the switch rail. Further details on the formulae for varying these properties along the length of the turnout is provided in Shih et al. [41].

Table 13: Track properties- Three layer MBS model (Model 4), adapted from Shih et al. [41].

Vertical properties		Lateral properties	
$k_{01,z}$ (N/m)	369×10^6	$k_{01,y}$ (N/m)	280×10^6 Figure 21
$c_{01,z}$ (Ns/m)	315×10^3	$c_{01,y}$ (Ns/m)	315×10^3
$k_{02,z}$ (N/m)	$369 \times 10^6 \Delta z$	$k_{02,y}$ (N/m)	$280 \times 10^6 \Delta y$
$c_{02,z}$ (Ns/m)	315×10^3	$c_{02,y}$ (Ns/m)	315×10^3
$k_{03,z}$ (N/m)	369×10^6	$k_{03,y}$ (N/m)	$280 \times 10^6 \Delta y$
$c_{03,z}$ (Ns/m)	315×10^3	$c_{03,y}$ (Ns/m)	315×10^3
$k_{04,z}$ (N/m)	369×10^6	$k_{04,y}$ (N/m)	$280 \times 10^6 \Delta y$
$c_{04,z}$ (Ns/m)	315×10^3	$c_{04,y}$ (Ns/m)	315×10^3
$k_{rt1,z}$ (N/m)	369×10^6	$k_{rt1,y}$ (N/m)	$56 \times 10^6 \Delta y$
$c_{rt1,z}$ (Ns/m)	77×10^3	$c_{rt1,y}$ (Ns/m)	$22 \times 10^3 \Delta y$
$k_{rt2,z}$ (N/m)	$369 \times 10^6 \Delta z$	$k_{rt2,y}$ (N/m)	$56 \times 10^6 \Delta y$
$c_{rt2,z}$ (Ns/m)	$77 \times 10^3 \Delta z$	$c_{rt2,y}$ (Ns/m)	$22 \times 10^3 \Delta y$
$k_{rt3,z}$ (N/m)	369×10^6	$k_{rt3,y}$ (N/m)	215×10^6
$c_{rt3,z}$ (Ns/m)	77×10^3	$c_{rt3,y}$ (Ns/m)	45×10^3
$k_{rt4,z}$ (N/m)	369×10^6	$k_{rt4,y}$ (N/m)	$56 \times 10^6 \Delta y$

Vertical properties		Lateral properties	
$c_{rt4,z}$ (Ns/m)	77×10^3	$c_{rt4,y}$ (Ns/m)	$22 \times 10^3 \Delta y$
$k_{tg1,z}$ (N/m)	$77 \times 10^6 \Delta z$	$k_{tg,y}$ (N/m)	$56 \times 10^6 \Delta y$
$c_{tg1,z}$ (Ns/m)	$77 \times 10^4 \Delta z$	$c_{tg,y}$ (Ns/m)	56×10^4
$k_{tg2,z}$ (N/m)	77×10^6		
$c_{tg2,z}$ (Ns/m)	77×10^4		
Masses			
m_0 (kg)	2.5		
m_t (kg)	500		
m_{r1} (kg)	111		
m_{r2} (kg)	111		
m_{r3} (kg)	111		
m_{r4} (kg)	111		
J_t (kgm ²)	265		

A 3D schematic for the switch and the stock rails of the 60E1-760-1:15 switch layout has been presented in Figure 22. It shows the geometries of the switch and the stock rail as well as their cross-sections at specific longitudinal positions and has been included here to support the discussion of the MBS results in the subsequent sections. This schematic only shows the right hand switch and stock rails of the panel rather than the complete switch panel since they will be the focus in this thesis.

It will be shown in Section 3.2 that this 3D model has been implemented in FEA and it is based on the rail profiles that were implemented in the S&C benchmark project. As highlighted in Figure 22, the switch toe begins at a distance of 0.805 m from the start of the turnout radius in the nominal configuration [22,65,66]. Figure 20B also shows the result for the vertical stiffness of the switch first plotted around this longitudinal position and after the after the first plot for the stock rail. Therefore, wherever the results along the length of the switch panel are discussed in this thesis, they will be

highlighted in terms of the distance from the switch tip/toe rather than the position of the wheel at the beginning of the MBS simulation. Along with indicating the position of the front wheel at the beginning of the simulation, Figure 22 also highlights the switch and stock rail cross-sections every 2 m from the beginning of the switch toe until a distance of 15 m from the switch toe. Further details on the rail cross-sections and any differences in the rail profiles between the MBS and the FEA models will be discussed in Section 3.2, where the development of the FEA model will be explained.

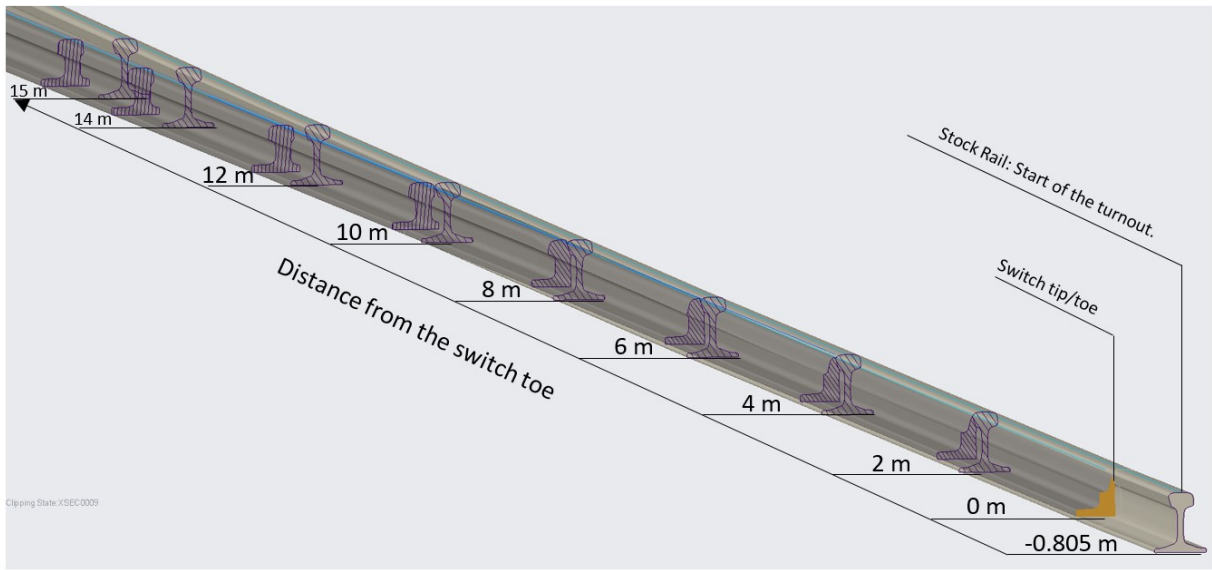


Figure 22: 3D schematic of the rails of the 60E1-760-1:15 switch layout with the key longitudinal positions.

The simulations of the dynamic train-track interactions were carried out between the three-layer MBS track model (Model 4) and the Manchester Benchmark passenger vehicle model with two bogies. The complete details of the simulations have been provided in the following references [41,154]. The analysis parameters are based on the Multibody simulation benchmark for dynamic vehicle–track interaction in switches and crossings [4,151], which specifies the use of the Manchester Benchmark passenger vehicle model [151]. The schematic for the components of this vehicle model is shown in Figure 23. The important parameters relevant to this thesis have been mentioned herein and the detailed further details of the vehicle model can be found in following references [151,153].

The Manchester Benchmark passenger vehicle is based on the ERRI B176 benchmark vehicle, without yaw dampers, and with the following major simplifications:

- Simple primary suspension
- Symmetric vehicle
- Non-inclined dampers with simple damping rates

The bogie schematic across the length and the width of the vehicle has been provided in Figure 23. It shows the longitudinal and lateral connections between the wheelset and the bogie and highlights the primary and secondary suspension components.

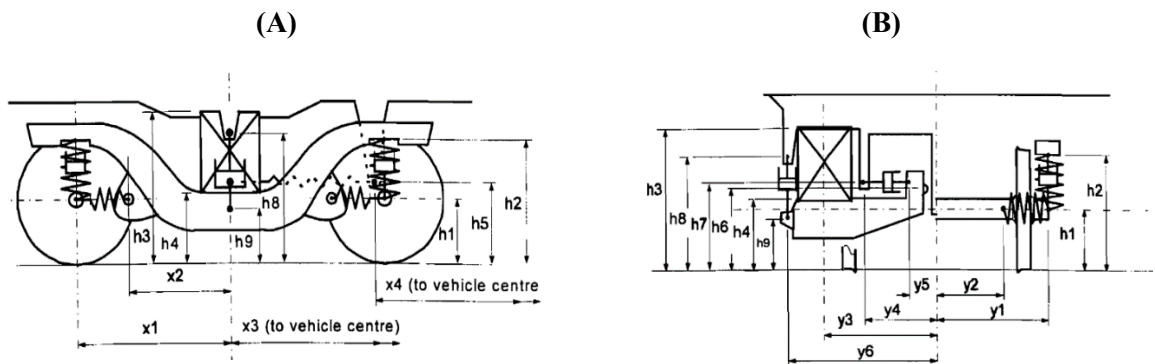


Figure 23: Schematic of the bogie for the Manchester Benchmark passenger vehicle, reproduced from [153].

Each vehicle has one body (carriage), two bogies and four wheelsets. The key mass properties affecting the dynamic train-track interaction have been listed along with their values in Table 14.

Table 14: Masses and inertia for the Manchester Benchmark passenger vehicle

Component	Mass (kg)	Roll Inertia (kgm^2)	Pitch Inertia (kgm^2)	Yaw Inertia (kgm^2)
Wheelsets	1813	1120	112	1120
Bogies	2615	1722	1476	3067

Component	Mass (kg)	Roll Inertia (kgm^2)	Pitch Inertia (kgm^2)	Yaw Inertia (kgm^2)
Body	32,000	56800	1,970,000	1,970,000

The longitudinal dimensions of the vehicles and distances from the key components have been listed in Table 15 since they are relevant to the 3D solid FE model, which will be shown to be a key contribution of this research thesis.

Table 15: Vehicle dimensions and distances, adapted from [153].

Description	Suspension component	Value (mm)
Wheelset end semi-spacing (x1)	Primary springs	1280
Bogie frame end semi-spacing (x2)	Primary springs	830
Longitudinal semi-spacing bogie end (x3)	Secondary springs	9500
Longitudinal semi-spacing body end (x4)	Secondary longitudinal traction rod	8300
Vertical element Height of wheelset end (h1)	Primary springs, Primary vertical damper	460
Height of bogie frame end (h2)	Primary springs, Primary vertical damper	880
Height above the rail level of the top (h3)	Secondary springs	1130
Height above the rail level of the bottom (h4)	Secondary springs	525
Height above the rail level (h5)	Secondary longitudinal traction rod	600
Height above the rail level (h6)	Secondary lateral bumpstop	650
Height above the rail level (h7)	Secondary lateral dampers	700
Height above the rail level of the top (h8)	Secondary vertical dampers	925
Height above the rail level of the bottom (h9)	Secondary vertical dampers	400

The key suspension properties affecting the dynamic train-track interaction have been listed along with their values in Table 16. Further details of the vehicle can be found in the listed references [151,153].

Table 16: Vehicle suspension properties, adapted from [153].

Parameter	Value
<u>Primary suspension</u>	<u>(4 per bogie)</u>
<i>Longitudinal stiffness</i>	<i>31391 kN/m</i>
Nominal damping in parallel	15 kNs/m
Damping series stiffness	60000 kN/m
<i>Lateral stiffness</i>	<i>3884 kN/m</i>
Nominal damping in parallel	2 kNs/m
Damping series stiffness	7500 kN/m
<i>Vertical stiffness</i>	<i>1220 kN/m</i>
<u>Secondary springs</u>	<u>(2 per bogie)</u>
Longitudinal shear stiffness	160 kN/m
Lateral shear stiffness	160 kN/m
Vertical stiffness	430 kN/m
Bending stiffness	10.5 kNm/rad
<u>Secondary roll bar</u>	<u>(1 per bogie)</u>
Stiffness	940 kNm/rad
<u>Secondary longitudinal traction rod</u>	<u>(1 per bogie)</u>
Stiffness	5000 kN/m
Nominal damping in parallel	25 kNs/m
Damping series stiffness	10000 kN/m
<u>Secondary lateral bumpstop</u>	<u>(1 per bogie)</u>

Parameter	Value
<u>Primary vertical dampers</u>	<u>(4 per bogie)</u>
Damping	4 kNs/m
Series stiffness	1000 kN/m
<u>Secondary lateral dampers</u>	<u>(2 per bogie)</u>
Damping rate	32 kNs/m
Series stiffness	6000 kN/m
<u>Secondary vertical dampers</u>	<u>(2 per bogie)</u>
Damping rate	20 kNs/m
Series stiffness	6000 kN/m

The nominal dynamic train-track simulations were carried out with the three layer track model (Model 4 [41]) according to the procedure described in the Multibody simulation benchmark for dynamic vehicle–track interaction in switches and crossings [4,151]. Only the simulations that were carried out in the through route of the 60E1-760:1:15 will be summarised, with a specific emphasis of the switch panel since the simulations in the diverging route do not form a part of the contributions from this thesis.

The wheel profile that was implemented in all the simulations was the S1002 profile. As prescribed [4,151], the simulations were carried out in the facing through route at a constant speed of 160 kilometres per hour (km/hr). In the model setup, the simulation begins 25 m before the start of S&C [4,151]. The through route simulation cases were set up on an infinite tangent track and the rail profiles for the switch and the stock rail vary along the length of the switch [151]. Track cant was taken as zero along the complete length and no track irregularities were applied. In each simulation, the vehicle was run for 25 m on a perfectly tangent track before reaching the front of the S&C. During this run before reaching 25 m, quasi-static condition is found and the vehicle is perfectly centred on the track in this quasi-static condition to avoid the effect of initial disturbances on the results

downstream. It was also assumed that the S&Cs have constant radii and there were no transition zones. For the diverging route, a short transition route is modelled but is outside the scope of the work discussed in this thesis [4].

The normal contact was modelled as discrete elastic contact employing a semi-hertzian approach by Ayasse and Chollet [123] and the tangential contact was modelled with Fastsim [155]. The wheel-rail coupling contact search algorithm in Simpack accounts for the change in wheel profile geometry and the longitudinal shift of contact patch location(s) due to wheelset yaw. Since the development of Model 4 is an input rather than a key contribution of this thesis, only the key results will be discussed. The detailed simulation procedure and method statements for the S&C benchmark can be found in the literature [151] and the simulation approach as well as the results from Model 4 [41,154].

First, the results for the contact point positions and the transition of the contact patch from the stock to the switch rail will be discussed. Figure 24 shows the two-dimensional rear view of a three-dimensional model for the switch and stock rails of a 60E1-760-1:15 through route switch panel. The central vertical plane for the right rails in the through (straight or non-diverging) turnout has been labelled and the lateral distances from this plane have been highlighted for the effective visualisation of Figure 25.

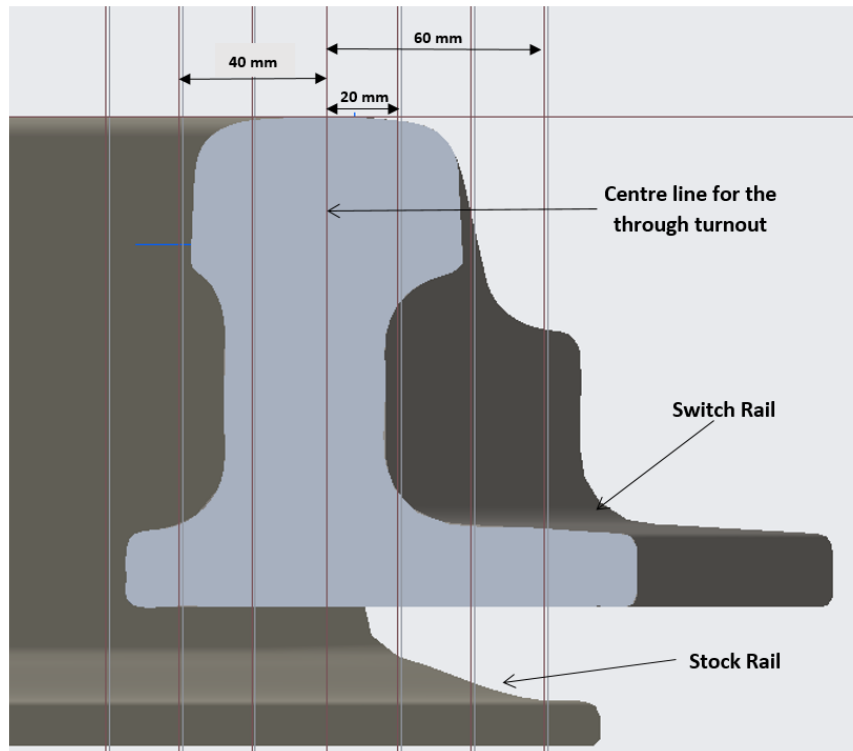


Figure 24: Lateral distances along the switch and stock rails.

The simulation results for the contact point positions from Model 4 have been plotted in Figure 25. It can be observed that there is just a single set of contact points between the wheel and the stock rail (CP1) and two sets of contact points between the wheel and the switch rail (CP1 and CP2). For the switch rail, CP1 predominantly falls closer to the running surface and CP2 closer to the gauge corner. The results presented in Figure 25 can be further understood through the schematics provided in Figure 22 and Figure 24. The first point of contact with the switch rail occurs at a distance of 6.92 m from the switch toe (as defined in Figure 22) and the last point of contact with the stock rail occurs at a distance of 7.24 m from the switch toe. Thus, the wheel-rail contact patch would transition from the stock to the switch rail between 6.92 and 7.24 m. The contact points beyond a lateral position of -25 mm would result in gauge corner contact with the switch rail, particularly CP2. The resulting multi-point contact from the transition, particularly around the gauge corner of the switch rail will result in a high amplitude of wheel-rail dynamic forces. The results for the wheel-rail contact point positions from Model 4 have shown a good agreement with the results from the publication of the S&C

benchmark simulations [4]. To restate, model 4 is a validated model based on the MBS S&C benchmark project whose results have been published [41,154].

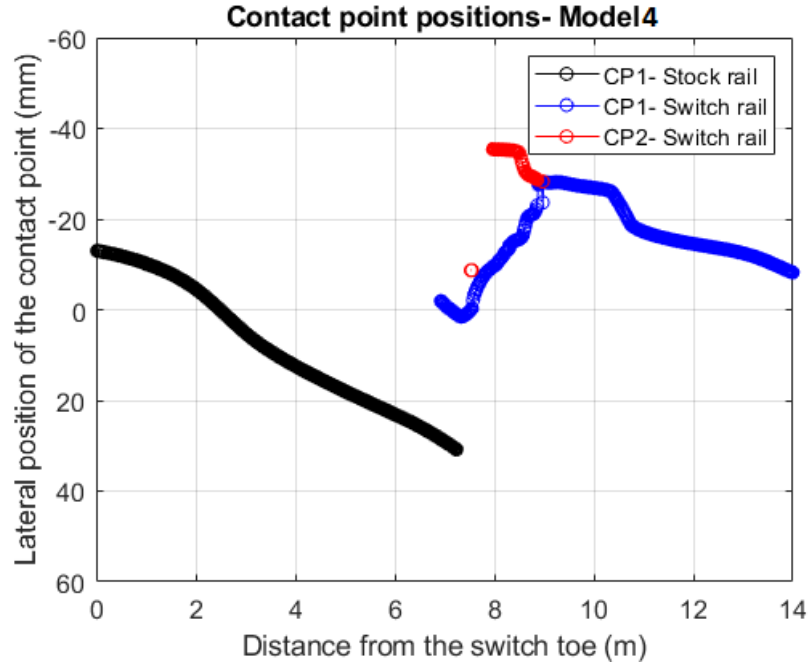


Figure 25: Simulation results from Model 4: lateral and longitudinal positions for the contact points.

The published results for the vertical contact force between the lead right-hand wheel and the switch rail has been plotted in Figure 26. The results from the beam element FE co-simulation (Model 2), Equivalent MBS 2 layer (Model 3) and Equivalent MBS 3 layer (Model 4) have been compared [41].

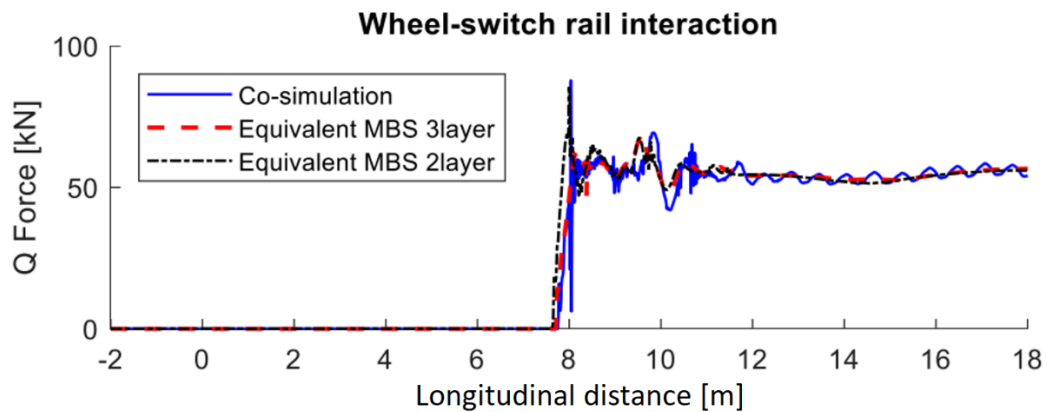


Figure 26: Vertical wheel-rail contact forces for the switch rail in the through route, adapted from [41].

As shown in Figure 26, a good agreement can be observed between the three models for the wheel-switch contact force along the length of the model. Unlike Figure 26, Figure 27 demonstrates the results for the wheel-rail contact force from Model 4 whilst accounting for the distance between the start of the turnout and the switch tip (0.805 m), previously explained and highlighted in Figure 22. The results plotted in Figure 26 and Figure 27 are the total amplitude of the vertical wheel-switch contact force, which is obtained from both the contact points. It can be seen from Figure 22 that the multi-point, gauge corner contact at a distance of 8 to 9 metres from the switch toe has resulted in a high amplitude of the wheel-rail dynamic force in Figure 27. The maximum total amplitude for the vertical contact force of 67.15 kN has been obtained at a distance of 8.75 m from the switch toe.

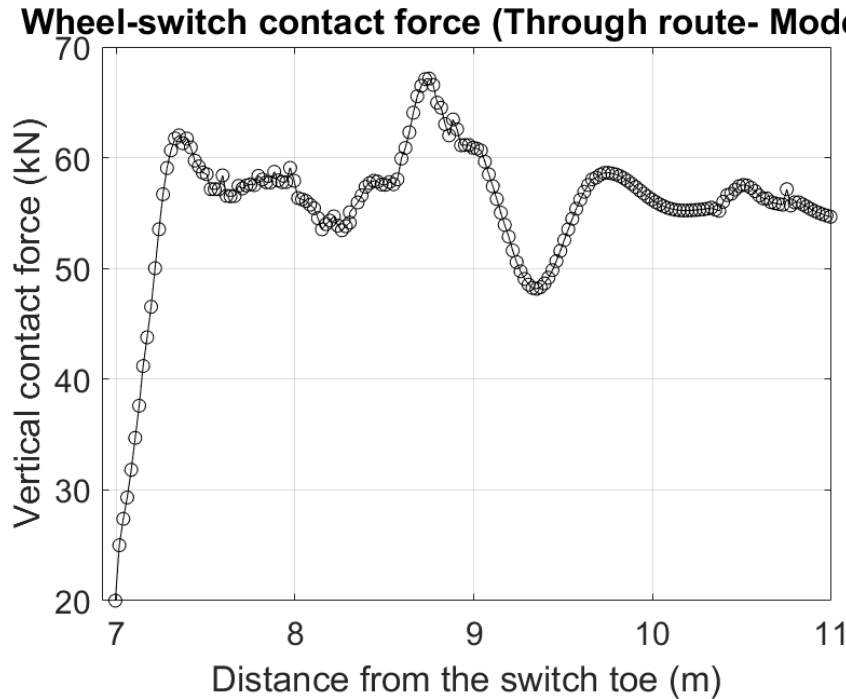


Figure 27: Total vertical wheel-rail contact force- Model 4.

This concludes the key discussions that are relevant to this thesis around the setup and simulations of the MBS model, which will be conducive for developing and verifying the results of the 3D solid FE model- the key original work presented through this thesis. A significant amount of detail about the MBS model has been provided in the following references, where the procedure for and various results from modelling the complete turnout have been discussed [4,41,151,154].

As discussed in Chapter 2.2, one of the modelling objectives is to model a short length of the 3D switch panel in FE for enabling computational efficiency and parametric studies. Thus, a location that has a high chance of occurrence of both wear and RCF would need be modelled. To this end, the Wear number ($T\gamma$) will be implemented.

3.1.2 Description of the damage prediction model, the Wear number - ($T\gamma$).

One approach to determining the locations for monitoring the development of rail damage is through understanding the initiation of faults at the wheel-rail interface. The Wear number, $T\gamma$, which was used to empirically relate the occurrence of surface wear and RCF damage in different rail steels, has been employed to determine the critical locations that will need to be monitored for the development of surface faults. The calculation of $T\gamma$ would involve the calculations for the longitudinal, lateral and spin creepages and creep forces. These parameters can be effectively determined from MBS models whilst considering the detailed dynamics of the railway vehicle.

The Wear number can be determined by summing up the products of the creep forces and creepages in the longitudinal, lateral and spin directions as demonstrated in Equation 1.

$$T\gamma = (T_x \times \gamma_x) + (T_y \times \gamma_y) + (M_z \times \varphi) \quad \text{Equation 1}$$

In Equation 1, T_x and T_y represent the creep forces in the longitudinal and lateral directions respectively. γ_x and γ_y represent the creepages in the longitudinal and lateral directions respectively. M_z represents the spin moment and φ the spin creepage.

The $T\gamma$ value that is obtained from Equation 1 can help determine the occurrence of rail wear and surface-initiated RCF by linking the amplitude of the wear number to the bilinear RCF damage function, and was demonstrated by Burstow [134]. This relationship is dependent on the grade of the rail material and the model is known as the Whole Life Rail Model (WLRM). As shown in Figure 28, a comparison of the $T\gamma$ values for the rails of grade R260 against field observations determined that values for the $T\gamma$ number that is less than 15 J/m would result in no damage. The values between 15 to 65 J/m would indicate rail sections that are prone to RCF. Values between 65 and 175 J/m would

indicate a reduction in RCF and an increase in wear and values greater than 175 J/m would indicate the track sections where excessive wear can be anticipated, resulting in the removal of any RCF cracks on the rail surface [135].

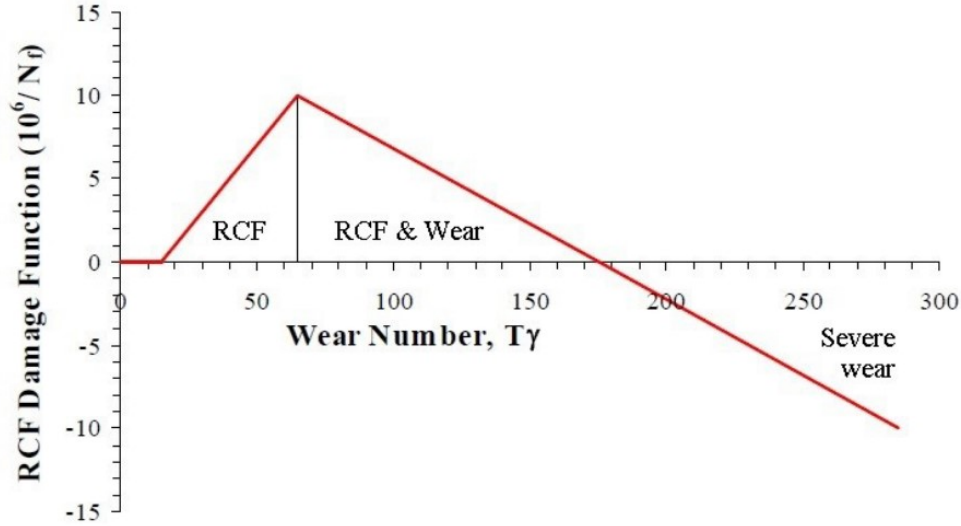


Figure 28: Bilinear RCF damage function [134].

In contrast, the model for R350HT rail steel states that excessive wear would occur only when $T\gamma > 400$ J/m [135]. Since the rails with material properties for rail grade R260 are being modelled, the relationship in Figure 28 has been used to determine the locations susceptible to high surface damage.

The initial WLRM damage model was established using empirical methodologies. It involved a comparison between anticipated $T\gamma$ levels and actual RCF site observations, utilising version 4.32 of the Vampire software for vehicle dynamics [156]. In that particular version of Vampire, lateral creep forces ($T_y\gamma_y$) accounted for the impact of spin creepage, while the pure spin moment ($M\phi$) was neglected [156].

The most recent version of Vampire Pro has improved handling of spin, now encompassing the pure spin moment term. Therefore, further research was conducted on the implementation of this term and its impact on predicted $T\gamma$ by Molyneux-berry and Bevan [156]. The research focused on quantifying how the spin component would contribute to $T\gamma$ and its effect on predicting RCF damage.

Additionally, the research aimed to ascertain if adjustments to the original WLRM damage function were necessary to account for changes in the calculation of $T\gamma$.

The findings of the investigations were as follows:

- Incorporating the spin component generally leads to an increase in $T\gamma$ with a rise in the contact angle [156].
- The impact of the spin component on $T\gamma$ and consequent damage is contingent upon site conditions such as curve radius, cant deficiency, and contact circumstances [156].
- Variations in these conditions, such as track irregularities and wheel/rail profiles, and other assumptions related to RCF modelling, diminish the influence of the spin component on damage predictions [156].
- Site simulations, previously utilised for validating the damage function, exhibited minimal disparity in predicted damage when considering the spin component. These results remained within the acceptable range of accuracy for unknown parameters common in this type of modelling, such as friction conditions [156].

It was also suggested that in future RCF calculations, $T\gamma$ should encompass the spin component. Furthermore, it was indicated that there is minimal advantage in readjusting the initial damage function to accommodate this modification [156].

The tangential contact model that was implemented for Model 4 in SIMPACK, i.e. FastSim does not compute the tangential torque (M_z) [100] and therefore the $T\gamma$ calculations that will be discussed through this thesis are based on Equation 1, but without the spin moment/creepage term, i.e. ($M_z \times \varphi$).

However, certain limitations in using the $T\gamma$ number for the prediction of Wear and RCF damage have been recognised. The most significant limitation is the restriction that can be attributed to the site conditions where the model was developed and validated. This has been observed in the form of a poor agreement demonstrated between the predicted and observed levels of rail RCF on routes such as

the TransPennine Express (TPE) in the UK that have low tonnage [156]. Over-prediction of RCF damage on flange contact, especially at lower coefficients of friction has also been reported [156]. For curved rail sections, an over-prediction of the wear number at the entry transition of curves relative to the main body of the curve has been reported. Moreover, the results do not agree well when the model is applied to the lower rail in tight curves where the effects and the forces that lead to damage to rails need to be studied more. These limitations can be observed because the site conditions in the aforementioned instances differed from the ones that were existent whilst developing the empirical model.

It is also worth noting that the development of the model was carried out whilst assuming a coefficient of friction of 0.45. However, the impact of the change in the coefficient of friction was later investigated where it was found that the “predictions for classic high rail RCF” on “typical moderate radius RCF sites” do not vary much for $0.25 < \mu < 0.45$ [134].

The WLRM predicts Wear and RCF jointly from the amplitude of the T_y number that is obtained from the values of the creep forces and creepages. Moreover, the wear damage parameter in the WLRM represents the removal of the surface RCF defects. It does not play a role in determining the loss of material or change in rail shape.

Since the direction of the creep force is regarded whilst obtaining the amplitude for the T_y number, the value for the Wear is underestimated. This is because wear occurs at higher amplitudes of the T_y number as shown in Figure 28. If the values of the creep forces are taken as absolute, i.e. if the negative values are taken as positive, the amplitude of the creep forces and thus the T_y number will be higher. As a result, the locations that will experience Wear will no longer be underestimated. Since Wear and RCF are interrelated in the WLRM, avoiding the underestimation of Wear will also help avoid the overestimation of RCF. Moreover, the conventional models that are widely implemented for predicting just the wear of the rails and wheels neglect the direction of the creep forces and implement their absolute values.

However, research has indicated that it is important to consider the direction of the action of the creep force whilst estimating the risk of RCF damage. Follow-up research that was carried out for the Rail Safety Standards Board (RSSB) determined that the damage that is purely associated with wear must be calculated by using the raw value for the $T\gamma$ number, i.e. the values where the absolute value for the creep forces are considered. On the other hand, damage resulting from RCF should be predicted from the values for the $T\gamma$ number that are scaled by the direction of the creep forces.

The WLRM and the $T\gamma$ number have been implemented in this research for determining the sections of the track that are highly susceptible to surface rail damage. Therefore, it is not a quantitative estimation of material removal but a mere recognition of the sections of the track that need to be monitored which is the objective of this exercise. The material properties that will be implemented in the FEA model would represent the R260 grade of rail steel. Therefore, under usual elliptical contact patch conditions the results can be deemed representative even though a switch will be modelled.

Firstly, the objective of the damage prediction will be to select the rail positions that demonstrate an adequately high value for the $T\gamma$ number to introduce both wear and RCF, i.e. where the removal of cracks due to excessive wear will be prevented. It will be shown that these conditions are achieved under the usual single elliptical patch conditions at the location of the defect introduction (Table 35) and thus the implementation of the $T\gamma$ number will be justified. It will also be shown that a reasonably long length of the track that will be modelled in FEA and thus encompass the crucial locations after the transition region.

The results for the $T\gamma$ number for the switch and the stock rails on the passage of a Manchester Benchmark passenger vehicle at a speed of 160 km/hr with a friction coefficient of 0.3 in the through route of a 60E1-760-1:15 railway turnout switch will be discussed in Section 3.1.3. It was shown in Figure 25 that a maximum of two contact points were obtained between the wheel and switch rail and a single contact point was obtained for the contact between the wheel and the stock rail from the results of the dynamic train-track switch interaction from Model 4. The $T\gamma$ number for these contact points will be discussed in Section 3.1.3.

3.1.3 Discussion of the results obtained for the Wear number ($T\gamma$) on the stock rail for simulations in the through route.

Figure 29 shows the results for the $T\gamma$ number for the contact between the right-hand stock rail and the leading, trailing wheels of the first bogie from the beginning of the switch toe up to the transition of the wheel-rail contact to the switch rail. The $T\gamma$ number of 15 J/m is marked in Figure 29, highlighting the limit after which there is a risk of surface-initiated RCF damage. The overall value of the $T\gamma$ number is under 15 J/m for the contact between the leading wheel and the stock rail, demonstrating that the risk of rail surface damage due to the passage of this wheel is negligible according to the WLRM for R260 rails.

A higher amplitude of the $T\gamma$ number than the leading wheel is obtained for the contact between the trailing wheel and the stock rail. When the contact of the leading wheel with the rail transitions from the stock to the switch rail, the switch rail is pushed downwards since the vertical track flexibility of the switch rail is independent of the stock rail in the MBS model. Since the leading wheel pushes the switch downwards, the trailing wheel exerts a larger proportion of the total load on the stock rail in the transition region. Therefore, the contact force between the switch rail with the leading wheel is more than that with the trailing wheel. Similarly, the contact force for the stock rail with the trailing wheel is higher than that with the leading wheel.

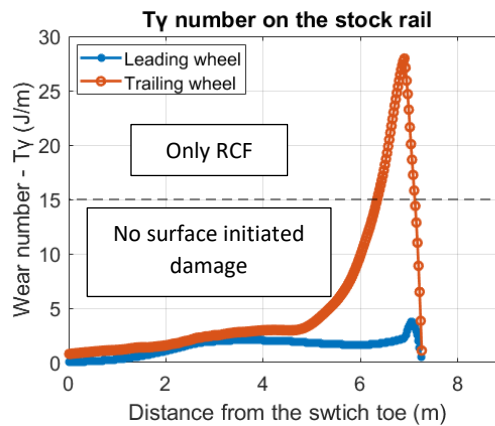
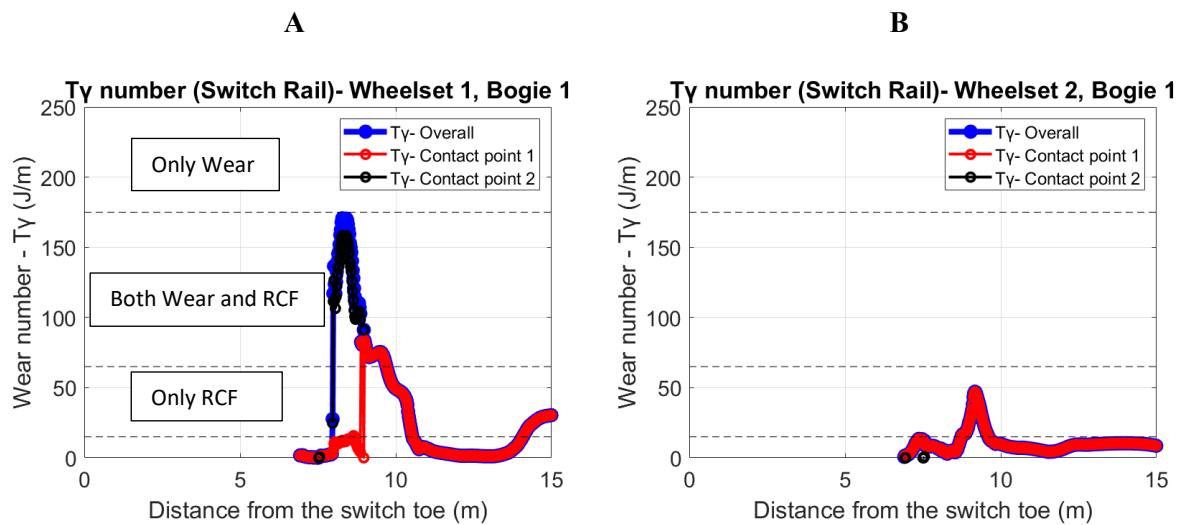


Figure 29: Wear number ($T\gamma$) on contact between the right-hand stock rail and the leading, trailing wheels of the first bogie.

3.1.4 Discussion of the results obtained for the Wear number ($T\gamma$) on the switch rail for simulations in the through route.

Figure 30 demonstrates the wear number resulting from the contact between the wheel and the switch rail. The overall $T\gamma$ number is the summation of the results obtained from the two contact points, Contact point 1 and Contact point 2. Contact point 1 is the contact between the wheel tread and the railhead surface. Contact point 2 is predominantly the point of contact between the wheel flange and the gauge corner of the rail. The damage arising from the contact between the wheel flange and the gauge corner was higher than that resulting from the contact between the wheel tread and the railhead. The $T\gamma$ values of 15, 65 and 175 J/m have been highlighted in all the plots subsequently to demonstrate the regions that are susceptible to just RCF, both wear and RCF and excessive wear.

The results obtained for the Wear number from the contact of the switch with the leading wheels (wheelset 1) of both the leading (bogie 1) and trailing (bogie 2) bogies (Figure 30 (A and C)) result in the highest amplitude for the $T\gamma$ number. The trailing wheels (wheelset 2) of the leading and trailing bogies (Figure 30 (B and D)) show a lower value. Relatively higher amplitudes for the $T\gamma$ number are observed between 8 and 10 metres from the switch toe, which is the section of the track where the wheel-rail contact patch shifts from the stock to the switch rail. The damage resulting from the contact of the switch rail surface with the leading wheelset is higher than the trailing wheelset.



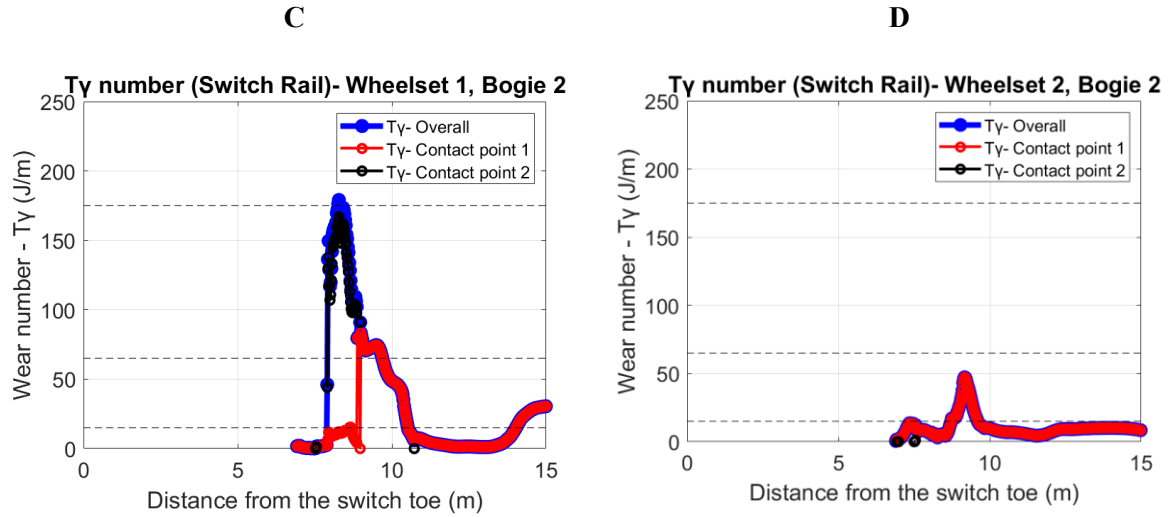


Figure 30: Wear number (T_γ) on contact between the switch rail and the wheel for A. Wheelset 1 of Bogie 1; B. Wheelset 2 of Bogie 1; C. Wheelset 1 of Bogie 2; D. Wheelset 2 of Bogie 2

To restate the discussion in Section 3.1.2, the tangential contact model that was implemented for Model 4 in SIMPACK, i.e. FastSim does not calculate the spin moment or the creep torque [100]. Therefore, only the lateral and the longitudinal components have been considered in the calculation of the T_γ number, similar to what was carried out during the initial development of the WLRM [156]. The creep forces and creepages that contribute to the value for the T_γ number are important to discuss and have thus been plotted in Figure 31 to Figure 33.

The longitudinal creep force is the tangential force in the longitudinal direction of the rail contact reference marker at the contact reference point, i.e. it is positive in the direction of travel. The lateral creep force is the tangential force in the lateral direction of the rail contact reference marker at the contact reference point, i.e. it is positive when the motion of the wheel is towards the outer side of the curve.

The longitudinal creepage is the longitudinal contact relative velocity divided by the absolute value of the creep reference velocity and has the same sign as the longitudinal creep force. The lateral creepage is the lateral contact relative velocity divided by the absolute value of the creep reference velocity and has the same sign as the lateral creep force.

The results have been plotted separately for the two points of contact between the wheel and the switch. The two sets of contact points on the switch can be seen in Figure 25. Figure 31 shows the longitudinal and lateral creep forces for the first set of contact points (Contact point 1 or CP1). The maximum negative amplitude for the longitudinal creep force of 17.36 kN is found at a distance of approximately 9 m from the switch toe. At this point, the wheel-rail contact point is on the gauge corner of the rail. After hitting this point, as shown in Figure 25, the wheel-rail contact point starts moving towards the away from the gauge corner or towards the outer side of the track curve, thus reducing the amplitude of the creep force.

At a distance between 8 and 8.86 m from the switch toe, Figure 31 shows that the lateral creep forces are higher than the longitudinal creep forces. It can be seen in Figure 25 that the wheel-rail contact point moves towards the gauge corner or the inner side of the curve, thus resulting in a high negative amplitude for the lateral creep force at this section.

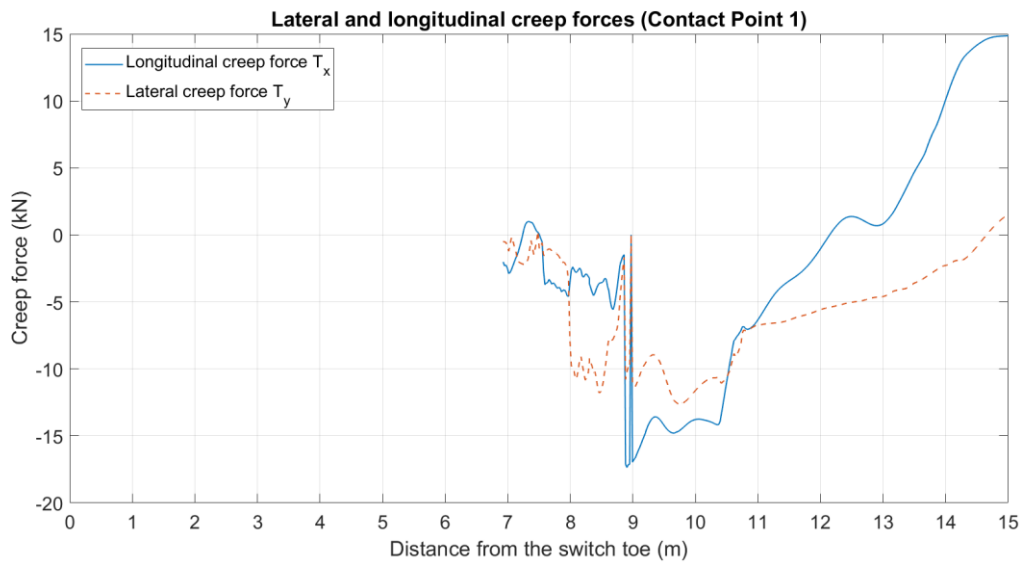


Figure 31: Lateral and longitudinal creep forces for Contact Point 1, Wheelset 1 of Bogie 1.

The creepages that would result in the creep forces shown in Figure 31 have been plotted in Figure 32. Since the wheel-rail contact for CP1 is mostly between the wheel tread and normally running surface of the rail (Figure 25), the amount of the creepage is lower for CP1 (Figure 32) than it will be shown

for CP2 (Figure 33B) where this is gauge corner contact. The maximum amplitude for the longitudinal creepage is -0.005 for CP1 whereas it is -0.025 for CP2.

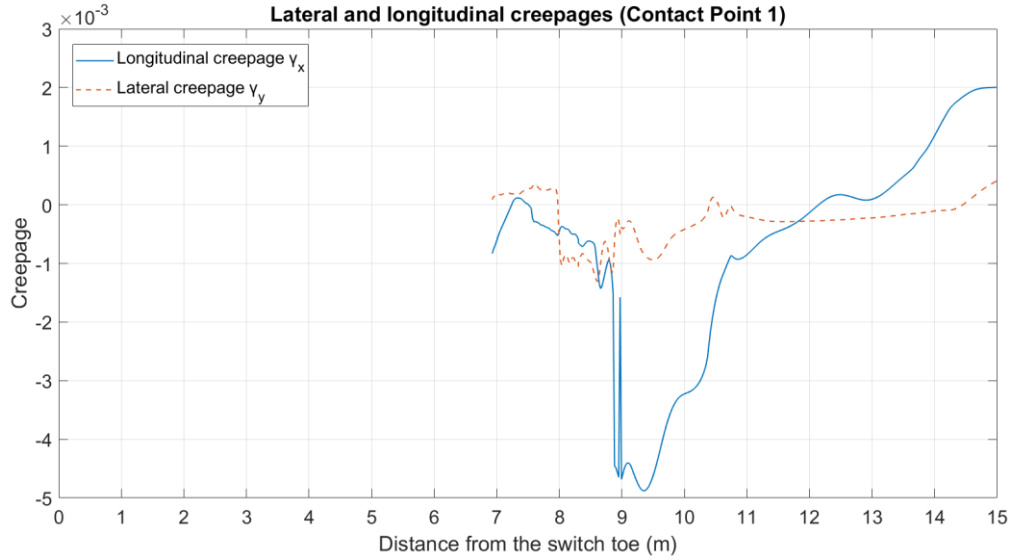


Figure 32: Lateral and longitudinal creepages for Contact point 2, Wheelset 1 of Bogie 1.

Figure 25 shows contact between the wheel flange and the gauge corner of the rail just around a longitudinal distance of 8 m from the switch toe for CP2. This is reflected in Figure 33B, where a high amount of wheel-rail longitudinal creepage can be observed at a distance of 8 m from the switch toe. The amplitude of the maximum creepage that has been plotted is much higher for CP1 than CP2 between a distance of 8 and 9 m from the switch toe. This, coupled with a high amplitude for the creep forces for CP2 (Figure 33A) has resulted in a much higher overall amplitude for the $T\gamma$ number for CP2 than CP1 at a distance of 8 to 9 m from the switch toe. This can be observed in Figure 30A and Figure 34, where the rail section between 8 to 9 m from the switch toe shows high chance of wear and RCF occurrence based on the value for the $T\gamma$ number.

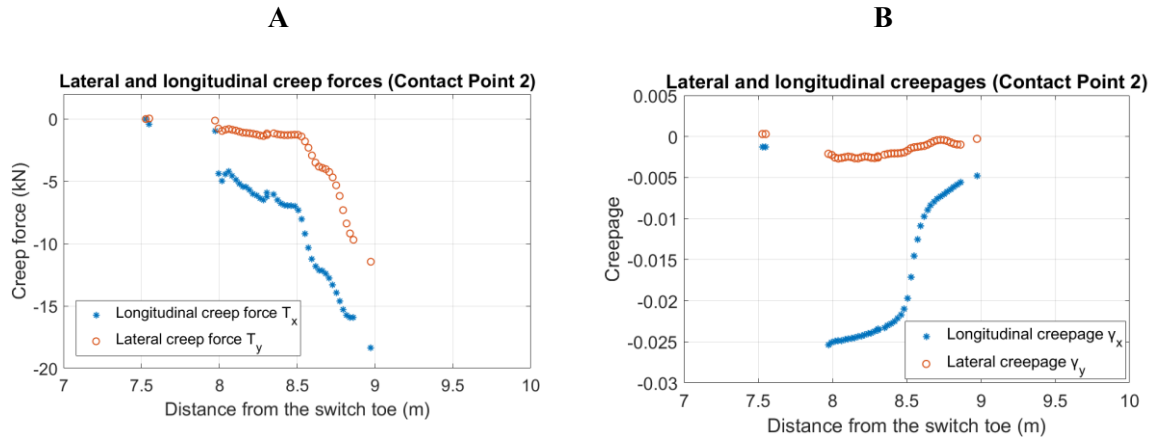


Figure 33: Creep parameters for Contact point 2, Wheelset 1 of Bogie 1; (A). Lateral and longitudinal creep forces; (B). Lateral and longitudinal creepages.

Therefore, the high tangential forces and creepages that are shown to occur at the switch at CP2 between 8 and 9 m would result in a high risk of wear at that section. Where the risk of wear occurrence is high, the risk of RCF occurrence would be lower in comparison since RCF cracks would be worn off by wheel-rail friction. In contrast, locations with a high value for the creep forces and creepages and thus the $T\gamma$ number at CP1 show the possibility of the occurrence of both Wear and RCF in Figure 30A. The results focusing on CP1 will thus be implemented for selecting the location for developing a 3D solid element FEA model in Section 3.1.5.

3.1.5 Discussion of the results obtained for the Wear number ($T\gamma$) on the stock and switch rails for simulations in the through route

Figure 34 demonstrates the wear number resulting from the interaction between the leading wheelset of the leading bogie with the switch and the stock rails. It can be seen from Figure 34 that the transition of the wheel-rail contact patch from the stock to the switch rail begins just before 8 m, where lower values for the wear number are obtained. The results for the switch and the stock rails have been plotted together to demonstrate the much higher risk of damage on the switch rail than on the stock rail. On considering Figure 30A and Figure 34 together, it can be noticed the longitudinal position between 9 and 9.5 m from the switch toe demonstrates the possibility of the occurrence of both RCF and wear. The contact point at this location is CP1, demonstrating that the results will be

obtained for an elliptical contact patch between the wheel tread and normally running surface of the R260 switch rail (subsequently proven in Table 35). As the contact conditions and the switch rail grade have inspired reasonable confidence in the results for the wear number, the focus of 3D FEA modelling will be between the longitudinal positions between 9 and 9.5 m from the switch toe. Depending on the requirements for the track dynamics, a longer length of the track will be modelled and the results between 9 and 10.5 m from the switch toe will be the focus of the discussion of results.

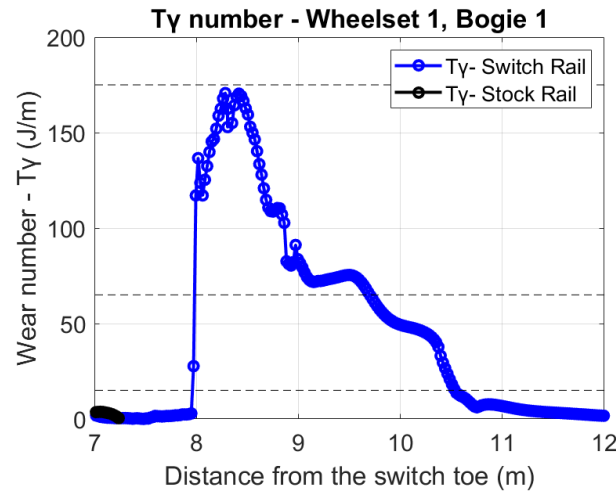


Figure 34: Ty number for the contact between the leading wheel of the leading bogie and the stock and switch rails for Track model 4.

3.2 Developing a 3D, solid Finite Element Model of a railway track switch

The development of the 3D model for the railway track switch will be introduced in this section. This model is a half-track model modelled in three dimensions for representing the layout shown in Figure 35. The geometry has been modelled in 3D so that it can be implemented in FE analysis for assessing the mechanical behaviour of the rails and taking decisions for the structural health monitoring of the switch.

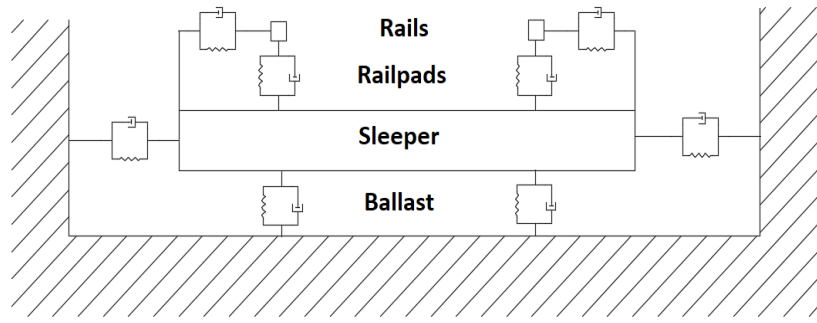


Figure 35: Schematic for the MBS track model [12].

As shown in Figure 36 A and B, the track model with the topology shown in Figure 35 has been modelled with the 3D solid components. A few crucial components have been added to the 3D model for making it more detailed and representative of the field.

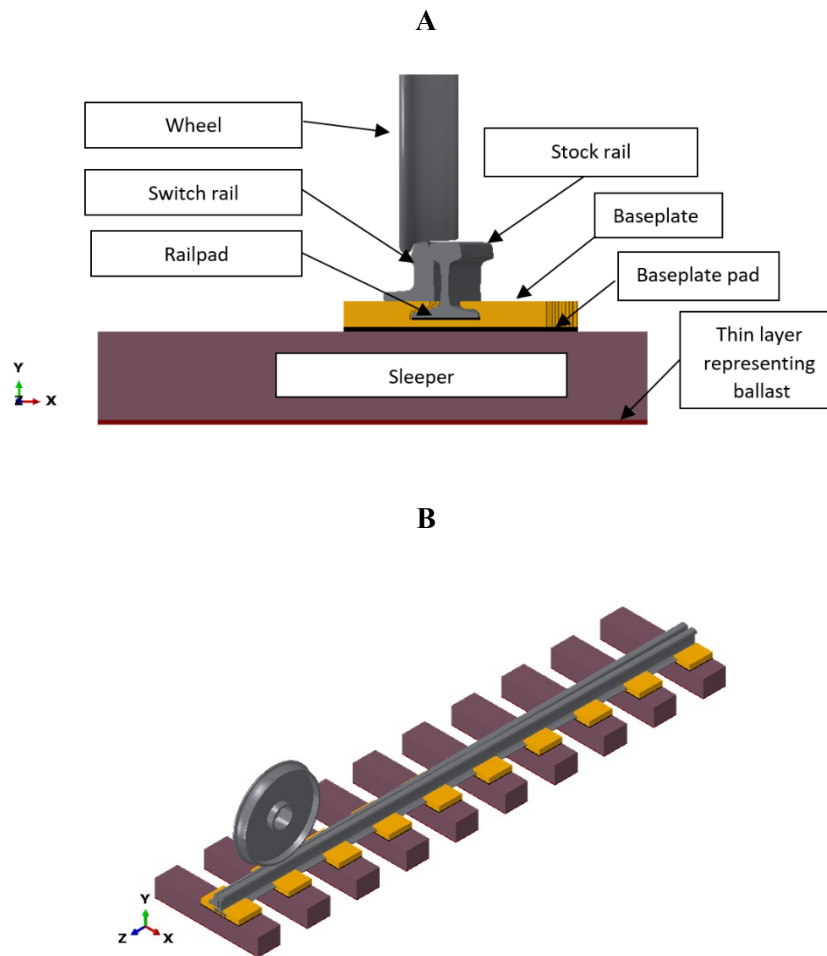


Figure 36: Assembly of the track model along with the wheel; (A) Front View; (B) Isometric view.

As shown in Figure 36A, the stock rail has been connected to the sleeper through a railpad, baseplate and baseplate pad. The baseplate has been included for appropriately supporting the model for the shallow depth switch rail. Therefore, appropriate material properties have had to be derived for representing the stiffness of the railpad layer in the MBS model through the equivalent stiffness of the railpad, baseplate and baseplate pad in the FE model. The derivation of the equivalent material properties for the components modelled with solid elements will be described later.

The stock and switch rails have been modelled in the through route for the S&C layout of 60E1-760-1:15 [65]. The stock rail has been modelled with the 60E1 rail cross-section profile and the switch rail follows the 60E1A1 profile [157].

The same procedure that was adopted for modelling the switch and the stock rail profiles for the S&C benchmark project has been implemented for developing the 3D solid models for the stock and the switch rails [65].

For modelling the switch rail, a solid model for the whole cross-section of a 60E1A1 switch rail profile that follows the longitudinal trajectory for the specified turnout length and radius was modelled (Figure 37A). The next step was the material removal through a milling tool profile corresponding to the chamfer on the side of the stock rail, as shown in Figure 37B. Finally, the material was removed from the solid rail as prescribed by the vertical and lateral motions of the milling tool profile as shown in Figure 37C [65].

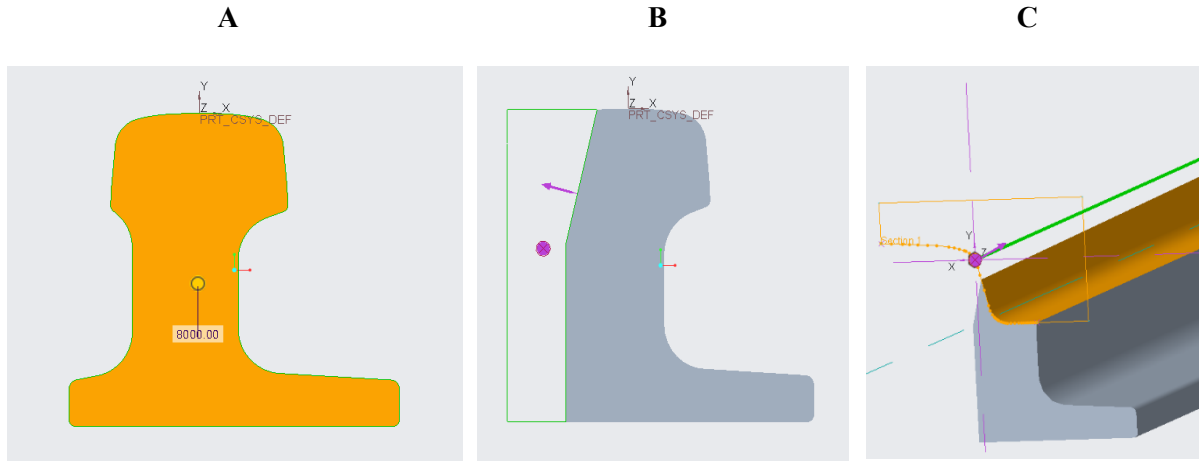


Figure 37: (A) Nominal 60E1A1 switch rail profile; (B) Swept material removal on the field side; (C) Swept material removal on the track-side whilst implementing the milling tool profile

The MBS rail profiles have been reproduced from the original reference in Figure 38 [65]. These profiles have been mirrored for the S&C benchmark project and thus this thesis. A comparison of these profiles against the mirrored 3D schematic that was shown in Figure 22 shows a good agreement between the MBS rail profiles and the 3D solid model for FEA. The rail cross-sectional view has been highlighted every 2 m from the beginning of the switch toe in the 3D solid model of the switch in Figure 22 and it shows a good agreement for the gradual build of the switch rail with Figure 38. It can be observed in Figure 22 that the full cross-section of the switch is not reached until after a distance of 10 m from the switch toe, which is similar to what is shown for the MBS rail profiles in Figure 38.

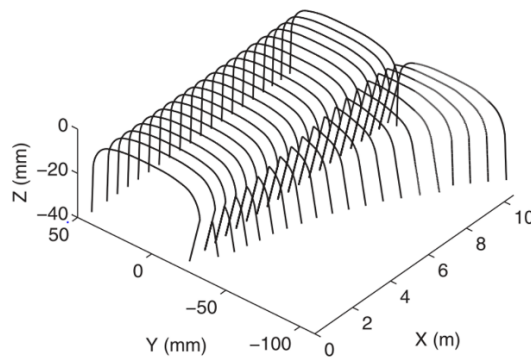


Figure 38: MBS rail profiles- switch assembly after milling, reproduced from [65].

The compatibility between switch rail geometry implemented in the MBS and FE analysis was ensured by comparing the cross-sectional rail profiles from the two models. An example of one such comparison is shown in Figure 39 and Figure 40.

The cross-section of the rail at a longitudinal distance of 9.13 m from the switch toe has been plotted in Figure 39. The rail profile at the same longitudinal position from the MBS model has been plotted in Figure 40A.

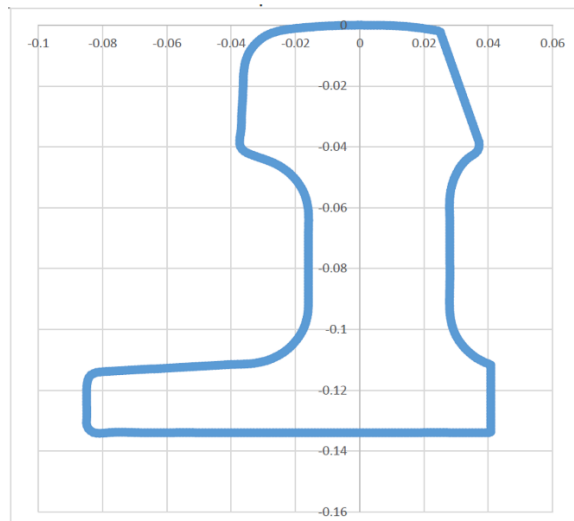


Figure 39: Rail cross-section from the solid model at a longitudinal distance of 9.13 m from the switch toe.

As shown in Figure 38 and Figure 40A, the rail profiles have been modelled for MBS only up to a depth of 35 mm from the railhead since they are mainly implemented for studying the wheel-rail contact characteristics. Figure 40B shows the same profile as Figure 39 but up to a depth of 35 mm from the railhead for demonstrating the good agreement between the MBS and FE rail profiles. Both the vertical and lateral profile co-ordinates show a good agreement when observed.

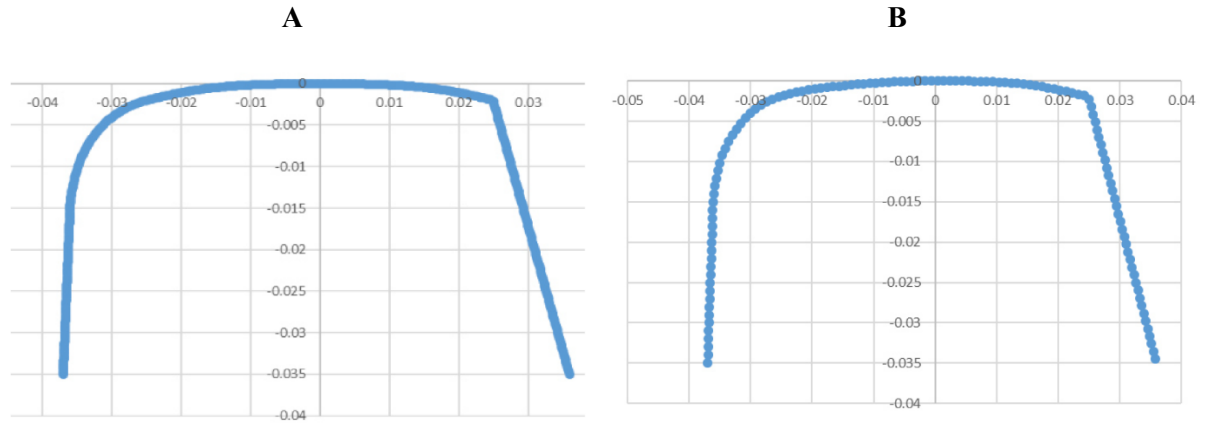


Figure 40: Rail profiles at a longitudinal distance of 9.13 m from the switch toe; A. MBS rail profile; B. Profile from FE model (up to a depth of 35 mm).

The geometry of the switch rail that has been implemented for the FE simulations has been shown in Figure 41A and B.

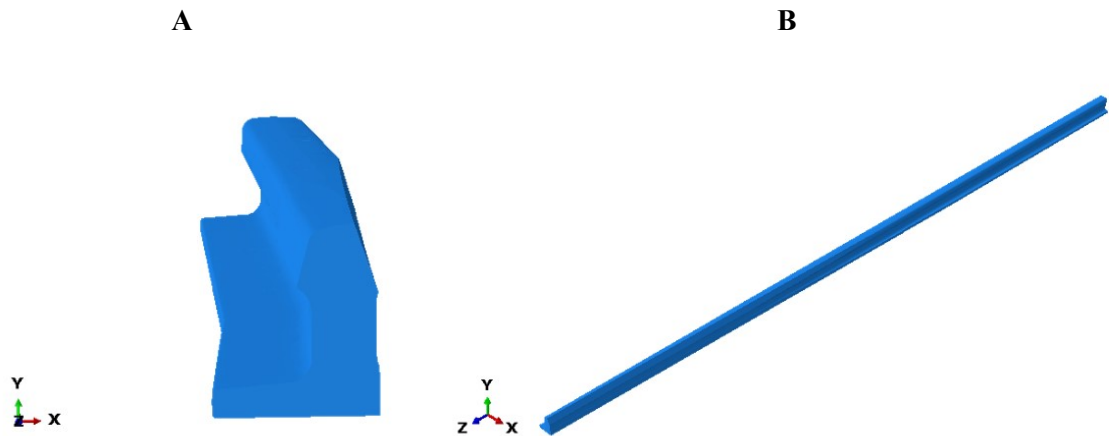


Figure 41: Switch rail solid geometry used for analysis; (A) Perspective front view; (B) 3D plan view

Similarly, the stock rail was modelled in 3D for its complete cross-section for the specified turnout radius. The material was then removed on the track side of the stock rail to ensure appropriate contact with the switch rail along its length according to the procedure followed in the reference [65].

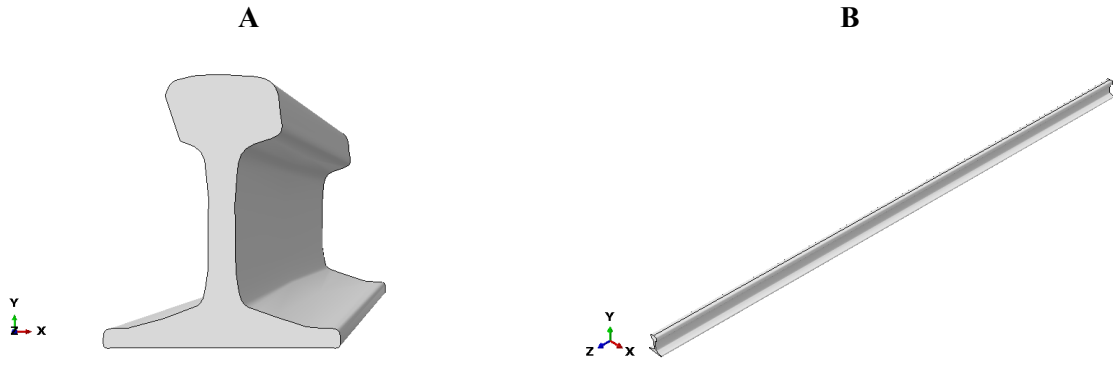


Figure 42: Solid geometry of the stock rail; (A) Perspective front view; (B) 3D plan view

An approximate and simplified geometry for the solid baseplate that has been shown in Figure 43 has been modelled according to the manufacturer's specifications [158]. The 3D model illustrates two different parts that have been joined together to form a cuboidal structure. Material has been removed from the centre to accommodate the stock rail and its movement relative to the railpad and the baseplate. This layer with approximate geometry has been modelled for balancing the height difference between the full depth stock rail and shallow depth switch rail and adding an extra level of representative detail. It was not modelled in the reference Models 2 and 4.

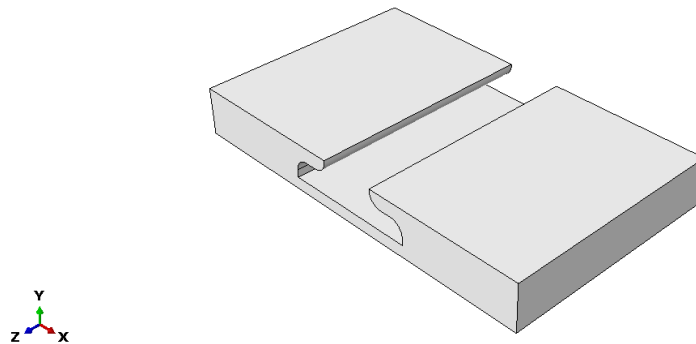


Figure 43: Geometry of the baseplate that holds the stock and the switch rails

Pads are generally used in railway track systems to dampen heavy vibrations and increase the reliability of track components. According to Network Rail's Track design handbook (NR/L3/TRK/2049) [159], the 60E1-760-1:15 layout of the railway switch includes a railpad between the stock rail and the baseplate. The material for the railpad is Ethylene-Vinyl Acetate (EVA). A

second pad, known as the baseplate pad connects the baseplate to the sleeper and is manufactured out of rubber. The pads were modelled as a cuboid structure and have been highlighted in the assembly shown in Figure 36A.

Since the model is a half-track model, the sleepers have been modelled with a cuboid shape for a length of 1.25 m which is 50% of the value of the total length of the sleeper as shown in Figure 36. A full-length sleeper model was also implemented but only for studying the effect of the sleeper length on the track dynamics.

The spring and dashpot elements have been implemented for modelling the vertical and lateral dynamics of the ballast layer. The summary of geometry and material for the components can be seen in Table 19 and the equivalent material properties for ensuring the compatibility of the track dynamics will be discussed in Section 3.4. After fine tuning, the material properties for the different components of the track model that will be implemented in wheel-rail interaction studies will be shown in Table 30.

A 3D solid geometry for the wheel shown in Figure 36 has been modelled with the S1002 profile for the wheel tread and flange [151,160], whilst the rest of the geometry has been modelled based on a simplified cross-section for a railway wheel from another reference [161].

Eight node linear brick solid elements with reduced integration (C3D8R) have been implemented for modelling the wheel, rails, baseplates, railpads, baseplate pads, sleepers and the ballast layers in ABAQUS [98]. For the wheel-rail interaction, the inner flange and the tread of the wheel surface have been meshed using a maximum element size of 2 mm. The other non-contact parts of the wheel have been meshed coarsely for improving the efficiency of the simulations. The maximum aspect ratio in the regions for results extraction is less than 10.

The railpad was meshed with a larger element size than the stock rail. Likewise, the baseplate mesh was coarser than the railpad, the baseplate pad coarser than the baseplate, the sleeper coarser than the baseplate pad and the ballast layer under each sleeper was modelled using a single element. The mesh

sensitivity studies that were carried out for ensuring the convergence of results have been explained in Chapter 4.

The interaction between the connecting surfaces of the aforementioned components in the track model was modelled with tie constraints. The implementation of a tie constraint involves a master-slave relationship between the surfaces in contact. On implementation, the DOF of the slave surface is controlled by the master surface [98]. Generally, the surface with the coarser mesh is set as the master region and that with a finer mesh is set as the slave region to avoid the error of element penetration during the interaction between surfaces [98]. A tie constraint was applied between the bottom surface of the stock rail and the top surface of the railpad. Tie constraints were also implemented for the surface interactions between the railpad and the baseplate; the baseplate and the baseplate pad; the baseplate pad and the sleeper and the sleeper and the ballast.

The effect of modelling a longer length of the rail was achieved by introducing the symmetry constraint on the front and rear faces of the stock rail. The symmetry constraints disabled the translational DOF in the longitudinal direction as well as the rotational DOF along the lateral and vertical axes for the surface nodes.

The springs and dashpots that were implemented for simulating the vertical and lateral stiffness and damping were allowed to translate only in the vertical and lateral directions respectively. As shown in Figure 44, the bottom face of the sleeper was allowed to translate in the vertical direction for the simulation cases where the simplified bedding was implemented.

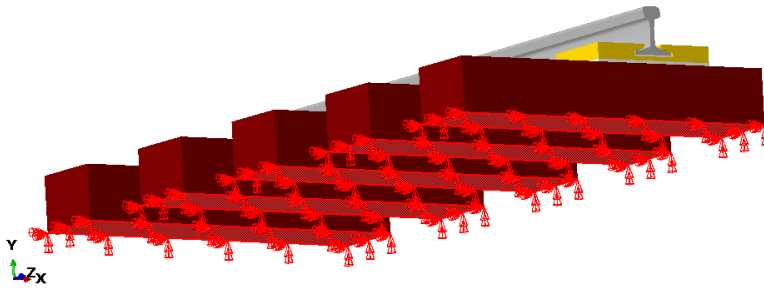


Figure 44: Boundary condition for the bottom surface of the sleeper when implementing simplified bedding

The assumption for implementing the tie constraint, especially between the bottom of the switch rail and the baseplate is based on a combination engineering judgement, literature review and modelling assessment criteria. Generally, a single point contact with the track clips is implemented in the field for preventing the upward motion of the track. The presence of the track clip on either side of the switch also constrains the lateral motion of the stock and the switch rails to some extent, which are in contact with each other (Figure 36A) in the simulation region of interest. The continuous contact between the rail foot and the baseplate would constrain the downward motion of the rail in the field. In addition to aiming to fulfil the requirements of the quantifiable modelling criteria, i.e. achieving a reasonable agreement for the rail receptance between the reference model 2 and the 3D FEA, the tie constraint has been implemented to constrain the upward and lateral motion of the rail. The fulfilment of the modelling criteria will be discussed in Section 3.4.

The effect of modelling a discrete support and continuous layer on the vertical mobility of the rail was investigated by Thompson [162]. The discrete support condition that has been plotted in Figure 45 was modelled as a point contact constraint over the sleeper. The continuous support condition represents the scenario of sustaining the substructure track properties across the track length. Figure 45 shows that the results for the vertical mobility are relatively similar for the continuous support and excitation over a sleeper at lower frequencies. It is around 1 kHz, where the pinned-pinned resonance occurs

when the wavelength of the bending waves of the rail is twice the sleeper spacing that the track dynamics become dependent on the method of constraint.

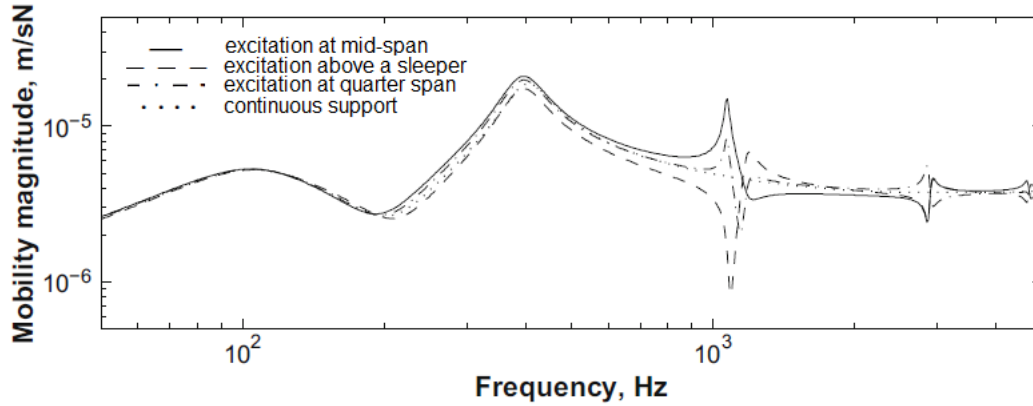


Figure 45: Vertical point mobility of track with discrete and continuous support, adapted from Thompson [162].

The assumptions made during the modelling will undoubtedly make the simulations different from the field occurrence. This cannot be quantified at this stage as the quantifiable comparisons can only be made against the reference model due to the lack of availability of data from field experimentations. The model will be developed to meet objectives and the modelling assessment criteria laid out in sections 2.2 and 2.3 of Chapter 2.

3.3 Introducing rail receptance and determining the length of sleeper, longitudinal length of the track for the 3D FE model.

The switch has been modelled to focus on the locations that were predicted to have a high susceptibility to surface-initiated damage in Section 3.2. In this section, the total sleeper and track length as well as the accuracy of the boundary conditions in the model will be determined by ensuring the compatibility of the track dynamics that will be captured by the FE with the reference model (Model 2). To achieve this, the receptance from the FE track model in the vertical and lateral directions will be obtained and compared against the published results from Model 2 [41].

The receptance is the ratio of the track deflection and the force exerted on the track, thus giving deflection in metres per Newton of the load. The results for the vertical and lateral rail receptance for the reference models 2, 3 and 4 that have been plotted in Figure 46 have been published in the literature [41].

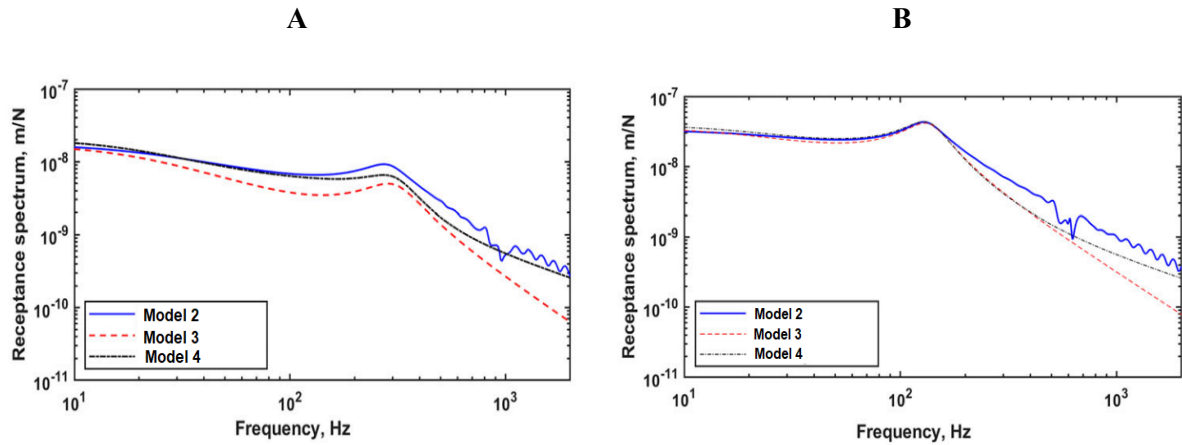


Figure 46: Comparison of the rail receptance between Models 2, 3 and 4; A. Vertical receptance; B. Lateral receptance, adapted from [41].

To recapitulate the discussion in Section 3.1.1, the reference MBS (Model 4) is based on the beam element FE model (Model 2). For the model whose development will be shown in this thesis, i.e. the 3D solid FE model, the track dynamics will be calibrated and the receptance compared against Model 2 and the wheel-rail interaction results will be compared against Model 4.

Outputs for the rail receptance will be obtained after applying a unit excitation load at the centre of gravity of the stock rail cross-section. The analysis of the rail receptance will only be carried out for the stock rail for the reasons highlighted below.

1. Unlike the switch rail, the cross-sectional area of the stock rail does not vary. Therefore, easy and reliable comparisons for the rail receptance can be carried out for the stock rail across all models. Only the results for the rail receptance for the stock rail have been published and available for Models 2, 3 and 4 that were described in Chapter 3.2 [41].

2. The rail support is the same for both the stock and the switch rails. Therefore, the values derived for the dynamic material properties of the railpads, baseplate pads and the ballast will still have validity for the switch rail even if the simulations were just carried out for the stock rail.

Numerical simulations have been carried out to ascertain the validity of the FE track model for further implementation in the time domain analysis of wheel-rail contact. It was established in Section 2.2 that the results obtained for the vehicle movement from the MBS model would be used as the boundary conditions for the wheel assembly that has been modelled in FE. The approach defined in Section 2.2 can be implemented more effectively if the FE track model can achieve similar vertical and lateral track dynamic behaviour as the reference track model that was constructed for the MBS studies. The vertical and lateral rail receptance for the MBS and FE models have been compared in the frequency range of 10-1000 Hz, which is the potential frequency range for capturing P1 and P2 forces [39,163,164].

The influence of frequency on the measurement of vertical contact forces at the crossing rail was investigated [12,39,44,148,163,164] where it was observed that the ability to capture the effect of track dynamics at higher frequencies was an important factor in the measurement of the vertical contact forces at the crossing. For instance, it can be observed in Figure 47A that a large difference can be obtained between the vertical contact forces captured at 10 and 100 Hz and a smaller yet considerable difference was obtained for the same results at 100 and 1000 Hz [44].

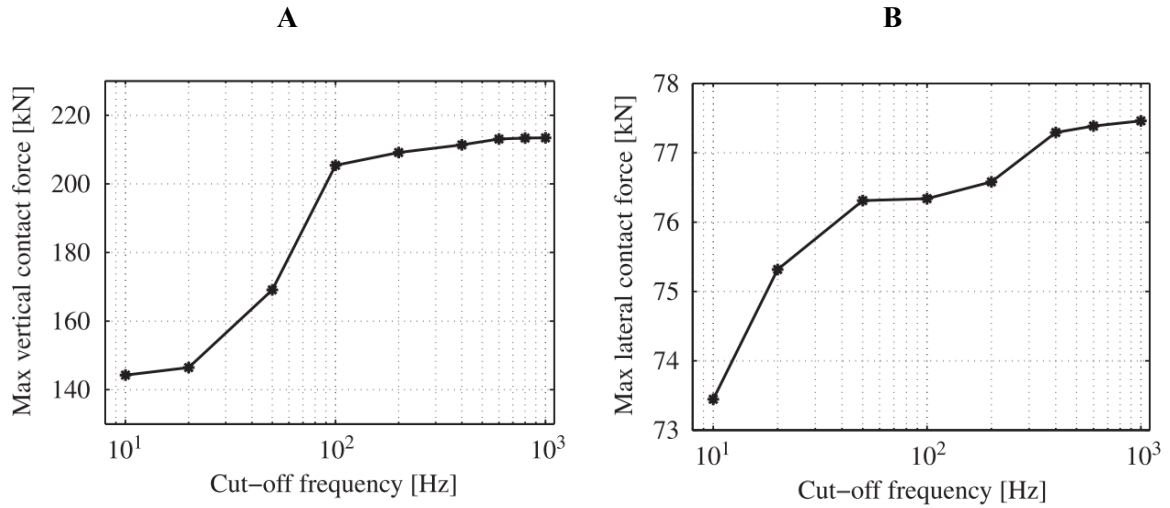


Figure 47: A. Measured maximum vertical contact forces in the crossing panel; B. Measured Maximum lateral wheel-rail contact forces in the switch panel.

The same investigation was carried out for capturing the lateral contact forces for the switch rail and a negligible effect of higher frequencies on the measurement of the lateral contact forces were observed [44]. As shown in Figure 47B, a maximum difference of 5 kN can be observed for the results of the lateral contact force captured at 10 and 1000 Hz at the switch whereas a difference of almost 80 kN can be observed in Figure 47B for the vertical contact force at the crossing for the same frequency range [44]. Considering the higher frequency content is more necessary for the crossing region because of the discontinuity during the wheel transfer from the wing rail to the crossing nose. Contrarily, a smoother transition occurs at the switch region and hence the wheel/rail impact forces are usually within lower frequency range. The lateral dynamics is important to model with adequate accuracy since research methodology has incorporated the Wear number ($T\gamma$) for determining the locations susceptible to damage, where the lateral components for the creep forces and creepages, along with the longitudinal components have played an important role in determining the modelling locations.

Based on the aforementioned evidence, it has been determined that a good agreement for the lateral rail receptance between the MBS and FE models at lower frequencies will be sufficient. However, a good agreement for vertical rail receptance is desired even at higher frequencies. This is especially

important where the simulations will be carried out for the passage of the vehicle over the switch in the straight or through route, where the vertical forces are still dominant. The turnout radius is more for high-speed switches which means that the vertical contact forces, especially in the through route will be more dominant. The dominance of vertical over lateral contact forces would lower the rate of removal of the RCF cracks due to less wear and capturing the RCF cracks from the vertical contact forces will demand capturing the high-frequency content.

3.3.1 Determining the length of the sleeper

The results for the rail receptance obtained from a half-sleeper, half-track model and a full-sleeper, half-track model will be compared for determining whether the appropriate track dynamics can be captured with a half-sleeper length. The comparisons for the rail receptance that will be shown in this section have not been carried out for the final, sensitivity-tested material properties and are just preliminary comparisons for picking a length of sleeper and switch length for modelling.

The derivation of the track properties for fine-tuning the pads and ballast against Model 2 will be shown in Section 3.4 and the final material properties for implementation in time domain simulations will be shown in Table 30. Apart from the value of the damping coefficient for the pads, the comparisons of the rail receptance in Sections 3.3.1 and 3.3.2 have implemented the same values for the track properties that will be presented in Table 30. The final value of the stiffness proportional damping after fine tuning the rail pads with the reference is 0.001 (Table 30), whereas simulations for the analysis of track, sleeper length in Sections 3.3.1 and 3.3.2 were carried out after implementing a value of 0.002. This has been elaborated to highlight that the receptance results are for relative comparisons for the track and sleeper lengths rather than model validation.

As shown in Figure 48A, the length of the sleeper for the half-sleeper, half-track model is half the length of an original sleeper along with one set of rails in the switch panel. The motivation behind checking the suitability of implementing this approach was reducing the total number of modelling elements. As shown in Figure 48B, the full-sleeper, half-track model includes the full length of the sleeper of 2.5 m but only one set of rails in the switch panel.

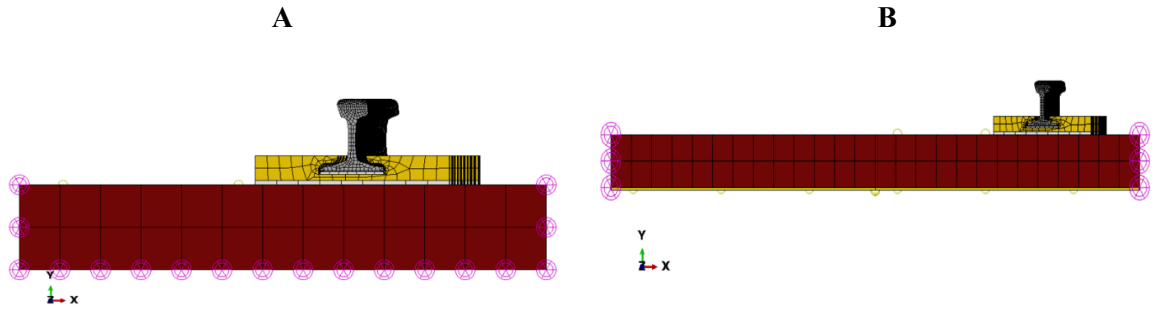


Figure 48: (A) The Half-sleeper, Half-track model; (B) The Full-Sleeper, Half-track model

For a given cross-section of the stock rail, the rail receptance has been obtained after applying a unit excitation load at the centre of gravity for the stock rail section above the centre of the sleeper along the longitudinal axis of the rail.

The results for the vertical and lateral rail receptance that have been obtained from the models with the short and the long sleepers have been plotted in Figure 49 A, B. One track resonance would occur because of the bouncing of the railpads between 200 and 600 Hz [128]. In the plot for the vertical rail receptance in Figure 49A, this can be observed at 250 and 280 Hz for the 3D FEA and reference models (Model 2) respectively. A difference of 5.5% has been obtained for the value of the resonant frequency between the reference model and the half, full sleeper models. With regard to the relative comparison between the models with the half and the full sleeper lengths, a good overlap between the plots for both the vertical and lateral rail receptance can be noticed in Figure 49 A, B.

However, the results for the lateral receptance from the FEA do not show a good overlap with the results from the reference (Model 2) in Figure 49B. These are predominantly due to the track length and property differences. It will be shown in Figure 52 that an increase in the track length can improve damping reduce the signal noise that can be observed at higher frequencies. Similarly, Figure 55 will show that increasing the value for the damping coefficient has the potential for achieving the same but also reduce the amplitude of the receptance at the resonant frequency.

It will also be shown in Section 3.4 that there is an inherent difference between the reference and the 3D FE models, since components such as the shallow depth switch, baseplate, railpad and the baseplate pad were modelled for 3D FEA with solid elements, unlike the reference model.

For the model with the short sleeper, the movement of the bottom surface of the sleeper was restricted to one DOF, i.e. translation in the vertical direction. The sleeper was allowed to translate only in the vertical direction whilst it was connected to the ground with spring-dashpot elements (ballast layer).

For the model with the long sleeper, the bottom of the sleeper was allowed to displace in both the vertical and lateral directions. Since the sleeper was modelled with its complete length of 2.5 m, high lateral track stiffness for the sleeper was avoided by allowing the lateral DOF for the bottom whilst implementing lateral spring-dashpot connections.

Therefore, the models with the short as well as the longer sleeper demonstrate a good relative agreement with each other, thereby implying that the boundary conditions that have implemented in both models are appropriate. It can thus be concluded that a model with a half-length sleeper can be implemented in time domain analysis of the FE analysis and will thus reduce the total number of elements in the model.

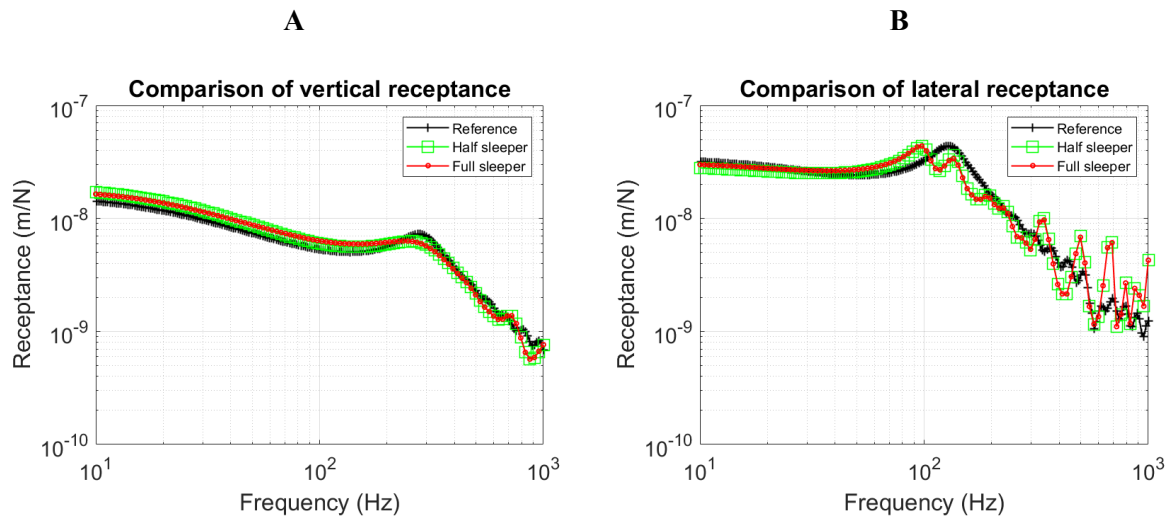


Figure 49: Comparison of the rail receptance against the reference MBS model for determining the length of the sleeper model; (A) Vertical Rail Receptance; (B) Lateral Rail receptance

3.3.2 Investigating the effect of the length of a track model on the results for the rail receptance.

The results for the Wear number in Section 3.2 helped conclude that the locations for the wheel-rail rolling contact analysis would lie between 7.8 and 10.6 m from the beginning of the switch toe. The locations with the highest risk for the development of surface-initiated RCF damage on the switch rail lie near the longitudinal position of 9.3 m away from the switch toe.

The results for the rail receptance over the sleepers that are closest to the distance of 7.8, 9.5 and 10.6 m from the switch toe will be discussed to comment on the relationship between track length and dynamics. The length of the track has been increased by adding additional sleepers before the location where the rolling contact analysis would begin and after the location where the wheel-rail rolling contact analysis will end.

As shown in Table 17, four different track lengths have been tested. The model for the track section between distances of 7.8 to 10.5 m from the switch toe, shown in Figure 50, only includes the regions where the rolling contact analysis will be carried out. Simulation cases L1, L2 and L3 have been run for this model.

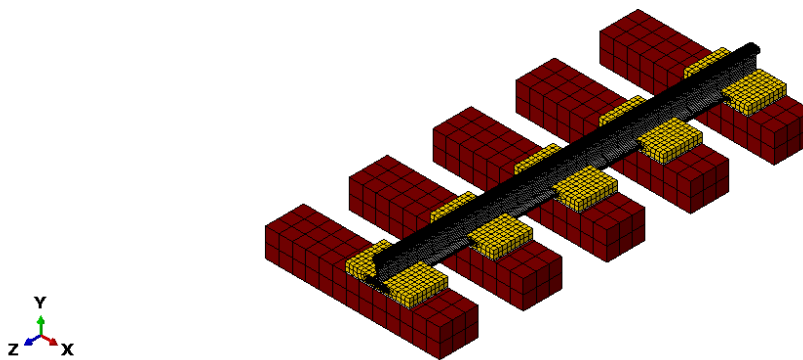


Figure 50: Region of interest- 7.8 to 10.5 m from the toe

The track section at a distance of 7.2 to 11 m from the beginning of the switch toe has been modelled as the extension of the previous model by two sleepers, one before the beginning of the previous track

section (i.e. 7.8 m) and another after the end of the track section (i.e. 10.5 m). Simulation cases L4, L5 and L6 have been run for this model.

The model for the track section between 6.6 to 11.7 m, has included modelling two extra sleepers before the location where the rolling contact will begin (i.e. 7.8 m) and two extra sleepers after the location where the rolling contact will end (i.e. 10.5 m). Simulation cases L7, L8 and L9 have been run for this model. The final model for the track section at a distance of 6.6 to 12.3 m from the switch toe, shown in Figure 51, has included modelling an extra sleeper length at the end of the track section for the model for cases L7, L8 and L9. Simulation cases L10, L11 and L12 have been run for this model.

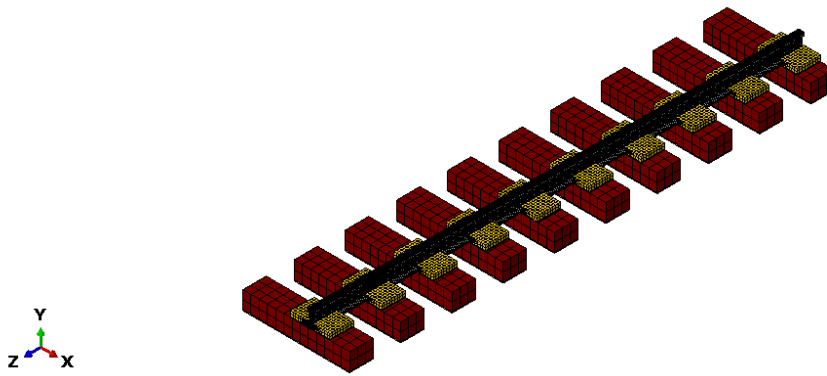


Figure 51: Region of interest with four additional sleepers- 6.6 to 12.274 m from the toe

The vertical and lateral rail receptance have been obtained after applying a unit excitation load to the Centre of Gravity (CG) of the sleeper-supported stock rail cross-sections where the rolling contact will begin and end; as well as the CG for the cross-section of the sleeper-supported rail where the highest degradation is anticipated. The cases for the simulations have been demonstrated in Table 17. This includes the details for the track section or the overall track length as well as the longitudinal positions for the rail cross-sections where a unit excitation load will be applied to obtain the rail receptance.

Table 17: Case studies to determine the appropriate length for modelling

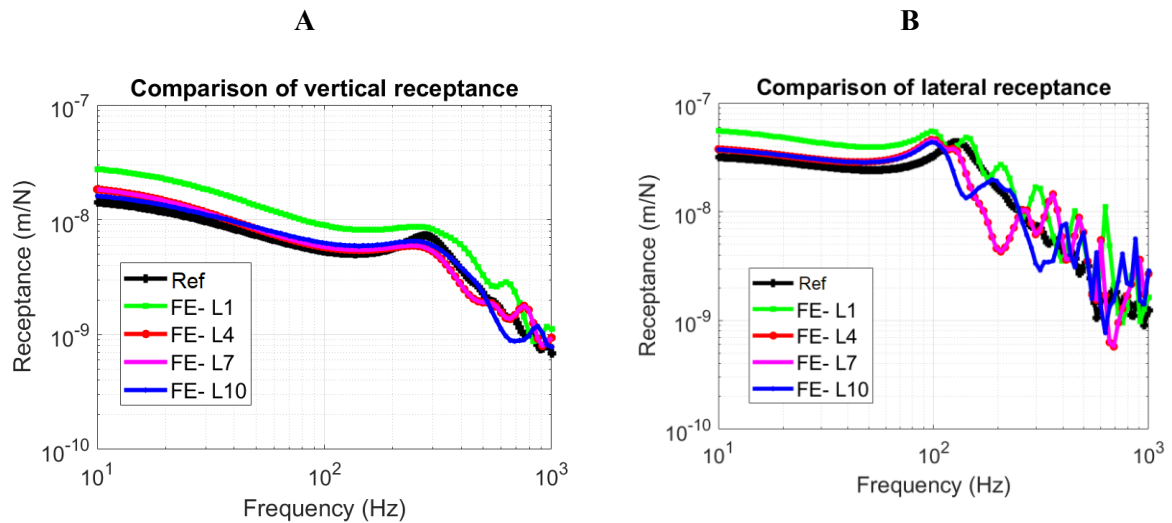
Case number	Track section (m)	Longitudinal position for calculating the receptance (m)
L1	7.8 to 10.5 m	7.9
L2	7.8 to 10.5 m	9.1
L3	7.8 to 10.5 m	10.3
L4	7.2 to 11. m	7.9
L5	7.2 to 11 m	9.1
L6	7.2 to 11 m	10.3
L7	6.6 to 11.7 m	7.9
L8	6.6 to 11.7 m	9.1
L9	6.6 to 11.7 m	10.3
L10	6.6 to 12.3 m	7.9
L11	6.6 to 12.3 m	9.1
L12	6.6 to 12.3 m	10.3

The results for the vertical and the lateral rail receptance have been compared for the models with the different track lengths in Figure 52. Figure 52 A, B demonstrate the results for the vertical and lateral receptance for the models that were modelled for different track lengths at 7.9 m from the switch toe, where the rolling contact simulation would begin. It can be observed that the agreement with the reference is the best for the model that has been modelled at 6.6 to 12.274 m from the switch toe, which is also the longest length of the track out of all the models. The results for the vertical rail receptance for the track modelled for this length show a good agreement against the reference MBS model. The model with the shortest length of track, i.e. L1, cannot capture a close agreement with the reference model as shown in Figure 52 A, B. The difference in the value for the vertical resonance frequency, lateral track stiffness at 10 Hz between the reference and the shortest (L1), longest (L10)

tracks in Table 18 and overall comparisons for the overlap between the plots in Figure 52 A, B has shown that the model with the longer length has better compatibility with the reference.

Although less than shorter models, poor damping is observed for the results of the lateral receptance in the mid-frequency range, i.e. between 100 and 500 Hz even in the longer models. This is because the longitudinal position of the rail section that has been analysed is 7.9 m and close to the beginning of the track model. However, as justified in Section 3.3 and set out in the modelling criteria, the comparison for the lateral receptance at 10 Hz is more important.

In Figure 52 C, D, the results for the vertical and the lateral rail receptance at a distance of 9.1 m from the switch toe have been demonstrated. The agreement with the reference results is important to consider at this location since it is near the vicinity of this location where the highest risk of fault occurrence exists. The agreement in the results for the vertical rail receptance improves for the model as the length increases, with the best agreement obtained for the modelled between 6.6 to 12.3 m. Similarly, a good agreement with the reference for the lateral receptance results is obtained for the model with the longer length of the track. A better agreement for the lateral receptance between 100 and 500 Hz can be observed for the model with the longer track length in Figure 52 (D) than in Figure 52 (B). This is because the track position of 9.1 m is close to the centre of the model. The quantitative comparisons for the important parameters with the reference will be shown in Table 18.



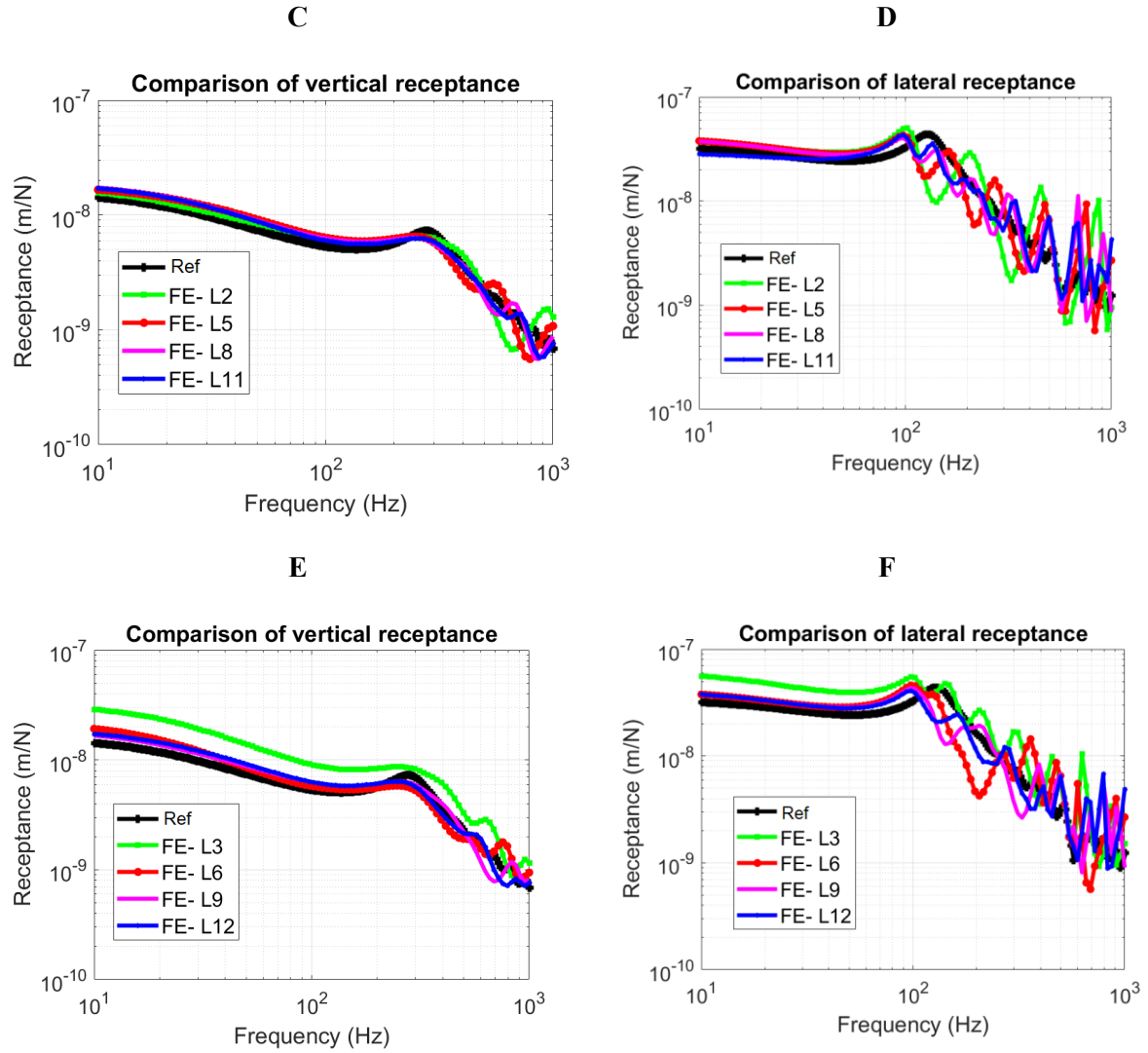


Figure 52: Comparison of the vertical and lateral rail receptance against the reference for different track lengths; (A) Vertical receptance at 7.9 m; (B) Lateral receptance at 7.9 m; (C) Vertical receptance at 9.1 m; (D) Lateral receptance at 9.1 m; (E) Vertical receptance at 10.3 m; (F) Lateral receptance at 10.3 m.

Figure 52 E, F demonstrate the results for the vertical and lateral receptance for the rail section at the distance of 10.3 m from the switch toe. This location is still near the vicinity of the location with the highest risk of fault occurrence and thus a good agreement for the vertical and the lateral rail receptance against the reference is essential. It can be observed in Figure 52 E that the results from the model with the shortest length (simulation L3) do not show a good agreement with the reference for the vertical receptance. The models with the longer track lengths show a good agreement with the

reference for the results of the vertical receptance. Similarly, the agreement for the results of the lateral rail receptance against the reference improves for the track model as its length increases.

It can be noticed that the simulation case L12 where the track has been modelled between 6.6 to 12.3 m from the switch toe demonstrates a good agreement with the reference as well as better damping behaviour for the lateral receptance up to 500 Hz than the shorter modelling lengths. Table 18 shows that the amplitude for the lateral receptance at 10 Hz would increase by 88% along the track ends for the shortest model when compared to the reference model. In contrast, the same value for the longest model would only increase by up to 10%.

Since results obtained from the simulations modelled for the longest length show a good agreement with the reference at the crucial locations for the development of faults, this modelling length will be implemented for rolling contact simulations in the time domain. Although the results can be improved by increasing the track length, modelling the track between 6.6 and 12.3 m offers a good trade-off between efficiency and accuracy by capturing the important track dynamic behaviour at the important locations. Section 3.4 will discuss the fine tuning of the material properties for the track model and the final results for the comparison of the rail receptance. This section has only demonstrated the selection of a track length through relative comparisons of the receptance data.

Table 18: Quantitative differences for the receptance results between the models with the shortest and longest lengths.

Parameter	Resonant frequency (from the vertical receptance plot)	Amplitude of lateral receptance at 10 Hz.
Amplitude for the Reference model	278 Hz	3.18×10^{-8} m/N

Difference between Reference and 3D FEA (L1/shortest)	−3.3%	88%
Difference between Reference and 3D FEA (L10/longest)	−5.1%	10%
Difference between Reference and 3D FEA (L2/shortest)	−3.3%	13.21%
Difference between Reference and 3D FEA (L11/longest)	−5.1%	−10%
Difference between Reference and 3D FEA (L3/shortest)	−3.3%	88%
Difference between Reference and 3D FEA (L12/longest)	−5.1%	10%

3.4 Derivation of the track properties and comparing the rail receptance against the reference

The details for the geometry, material type and the reference or standard for the different track components included in the model assembly have been included in Table 19. Homogenous materials will be considered for each component and the origin of their property values has been described.

The mass density for EVA material has been considered for modelling the railpad as specified by Network Rail for this particular turnout layout [159]. However, the equivalent Young's modulus for the EVA material was obtained from the value for the stiffness for a railpad with EVA material that was implemented in a turnout in [159]. The mass density of rubber material has been considered for the baseplate pad, as specified by Network Rail for this particular turnout layout [159]. The equivalent Young's modulus for the baseplate pad has been obtained from the reference where the baseplate pad

was implemented in a turnout [119]. According to Schwihaag [158], a manufacturer of switch baseplates [159], the baseplate material is ductile cast iron. Therefore, Young's modulus and the mass density for ductile cast iron have been implemented for the baseplate.

Table 19: Geometry and material details for the modelled components

Component	Dimensions/Configuration			Material	Reference/Standard
	L (mm)	B (mm)	H (mm)		
Stock Rail	60E1			R260 rail steel	[41,65,157,165]
Switch Rail	60E1A1			R260 rail steel	[41,65,157,165]
Sleeper	1250	274.12	200	Concrete	[41]
Baseplate	Schwihaag			Ductile cast iron	[158,159]
Railpad	460	150	5	EVA	[4,41,119,159]
Baseplate pad	460	274.12	10	Rubber	[119,159]
Wheel	S1002 profile			Steel	[4,160]

3.4.1 The stiffness for the pads and the baseplate

In the MBS model, the layer connecting the stock rails to the sleeper has been described as the railpad layer (Figure 35). However, in the FE model, the layer connecting the stock rail to the individual sleepers consists of the railpad, baseplate and baseplate pad (Figure 36A). The layer connecting the switch rail to the sleeper comprises the baseplate and the baseplate pad (Figure 36A).

The equivalent vertical stiffness in series for the railpad, baseplate and baseplate pad layers has been obtained to describe the overall vertical stiffness of the layer that connects the stock rail to the sleepers in the FE model. For ensuring compatibility between the track models, this value has been compared against the vertical stiffness for the railpad layer of the reference MBS model [41]. Ensuring this compatibility is essential because the research method involves substituting the results for the wheel

movement into FE. The motion of the wheel during the dynamic vehicle-track interaction simulations is influenced by the dynamic properties of the track.

The deflection/displacement ' x ' of a spring can be calculated from Hooke's law as shown in *Equation 2*; where the applied force ' f ' and stiffness ' k ' for a spring are known.

$$f = k \times x \quad \text{Equation 2}$$

The stiffness of the material is represented through the property of Young's modulus in the FE model. It can be calculated from the relationship that can be implemented to obtain the uniaxial deflection for a beam with a cuboid cross-section shown in *Equation 3*.

$$\delta = \frac{P \times L}{A \times E} \quad \text{Equation 3}$$

Where δ is the deflection/displacement, P is the applied force, L is the thickness of the component, A is the surface area of the component at the face where the load is applied and E is Young's modulus of the material.

The displacement (x) in *Equation 2* and deflection (δ) in *Equation 3* are the same quantities and so are the applied loads (P) and (f).

Therefore, after applying a unit load, the known vertical stiffness of a component can be used to obtain the deflection x and δ using *Equation 2*. Subsequently, *Equation 3* can be used to calculate the unknown equivalent Young's modulus of the material, using the known values of the applied load, deflection and the geometry of the component.

The equivalent stiffness in series k_e for the components of the track layer have been calculated using *Equation 4* and the description and values of the variables in the equation have been described in Table 20.

$$\frac{1}{k_e} = \frac{1}{k_{RP}} + \frac{1}{k_B} + \frac{1}{k_{BP}} \quad \text{Equation 4}$$

Table 20: Variables in Equation 4 and their meaning

Notation	Term	Stiffness (kN/mm)	Reference/Comments
k_e	Equivalent stiffness of the track layer in series	Unknown variable	Calculated/unknown variable
k_{RP}	Vertical stiffness of the railpad in the FE model	120	Obtained from [4,41,119].
k_B	Vertical stiffness of the baseplate in the FE model	4.913×10^{11}	Obtained from <i>Equation 2</i> and <i>Equation 3</i> using $E = 170 \times 10^9$ for ductile cast iron material.
k_{BP}	Vertical stiffness of the baseplate pad in the FE model	6000	Obtained from [119].

From *Equation 4*, a result value of 117.647 kN/mm was obtained for the vertical stiffness of the layer connecting the stock rail to the sleeper in the FE model (k_e). This value is close to the value of the vertical railpad stiffness of 120 kN/mm of the reference MBS model [151]. This demonstrates that it is correct to implement *Equation 2* and *Equation 3* for obtaining the equivalent Young's modulus for the appropriate simulation of the vertical track stiffness for the railpad and the baseplate pad components.

Table 21: Stiffness and Equivalent Young's modulus for the railpad, baseplate and baseplate pad layers.

Component	$k(N/m)$	$x, \delta (m)$	$F, P(N)$	$L (m)$	$A (m^2)$	$E (Pa)$
Railpad	1.20×10^8 (known)	8.33×10^{-9}	1	5.50×10^{-3}	0.041	160×10^5 (calculated)
Baseplate	4.97×10^{11} (calculated)	2.01×10^{-12}	1	1.50×10^{-2}	0.044	1.7×10^{11} (known)
Baseplate pad	6.00×10^9 (known)	1.67×10^{-10}	1	0.01	0.126	4757×10^5 (calculated)

The values for the equivalent Young's modulus for the railpad and Young's modulus for the baseplate are representative of the actual material. However, the value for the stiffness of the baseplate pad that has been obtained from another reference model [119] and its equivalent Young's modulus is quite high, which is ideally manufactured with rubber for this turnout layout and is less stiff. Despite this, the baseplate pad contributes to the accurate modelling of the track dynamics as the value for its vertical stiffness results in the compatibility between the layers implemented for connecting the stock rail to the railpads in the MBS and FE models. However, the results for the mechanical stresses and strains that are obtained from the baseplate pad should not be used for making quantitative conclusions since its modulus is not the same as that of its natural material.

3.4.2 Modelling the effect of damping of the pads

Among the components comprising the layer connecting the stock rail and the sleeper, it is important to consider the material damping of the pads since they are critical components for reducing the impact of high vibrations.

The material damping can be introduced into the time-domain FE simulations by calculating the Rayleigh damping coefficients for the material.

The Rayleigh damping coefficients can either be mass proportional, stiffness proportional or a combination of both. *Equation 5* shows the relationship describing the damping ratio in terms of the resonant frequency and the Rayleigh damping coefficients.

$$\zeta_i = \frac{\alpha}{2 \times \omega_i} + \frac{\beta \times \omega_i}{2} \quad \text{Equation 5}$$

Where ζ denotes the damping ratio, α denotes the mass proportional damping, β denotes the stiffness proportional damping and ω denotes the resonant frequency.

The Rayleigh damping coefficient can be included in the FE model by either using the mass proportional damping coefficient or the stiffness proportional damping coefficient. If the mass proportional damping (α) is assumed to be 0 in Equation 5, the value of stiffness proportional damping (β) can be obtained. Similarly, if the stiffness proportional damping (β) in Equation 5 is assumed to be 0, then the value for the mass proportional damping (α) can be obtained. The resonant frequency resulting from the rail bouncing on the railpads that is implemented in Equation 5 can be obtained from the results of the receptance from the Model 2 and is expected to lie between 200 and 600 Hz [128]. The damping ratio (ζ) is assumed to be half the value of the loss factor (η).

The mass and stiffness proportional Rayleigh damping coefficients have been obtained for the same value of the loss factor (0.3) and the same resonant frequency. The influence of these coefficients on the results for the rail receptance can be observed in Figure 53 and the key quantitative comparisons are included in Table 22. A good agreement can be observed between the reference model and the model that incorporates the stiffness proportional damping. For the simulations that have been run with the mass proportional damping coefficient, the results at the higher frequencies experience more oscillations due to the absence of the stiffness proportional damping coefficient, which is more dominant at these frequencies. Therefore stiffness proportional Rayleigh damping would need to be implemented for the pads in the model for capturing the appropriate dynamics of the railpad.

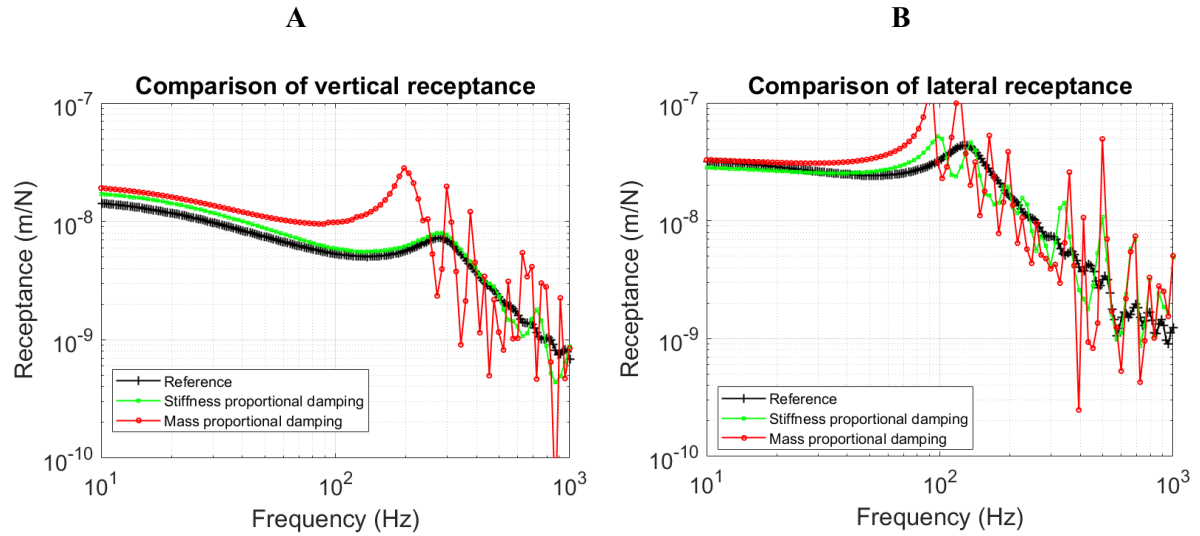


Figure 53: Comparison of the approaches to including pad damping in FE; (A) Comparison of Vertical receptance against the reference; (B) Comparison of the lateral receptance against the reference

Table 22 shows that whilst the agreement with the reference for the amplitude of lateral receptance at 10 Hz is slightly better when the mass proportional damping is implemented, the results from this approach show a reduction of the resonant frequency by 30%. Moreover, as shown in Figure 53, the overall overlap for the vertical rail receptance between the reference and 3D FEA is better when stiffness proportional damping is implemented.

Table 22: Quantitative comparisons for the rail receptance- mass and stiffness proportional damping.

Parameter	Resonant frequency (from the vertical receptance plot)	Amplitude of lateral receptance at 10 Hz.
Amplitude in case of the Reference model	278 Hz	3.18×10^{-8} m/N
Difference between Reference and 3D FEA (Stiffness proportional damping)	1.4%	-10%

Parameter	Resonant frequency (from the vertical receptance plot)	Amplitude of lateral receptance at 10 Hz.
Difference between Reference and 3D FEA (Mass proportional damping)	-30%	3.15%

There are two approaches for incorporating the stiffness-proportional Rayleigh damping for the pads in the FE model. The first approach was explained earlier, where the value of the stiffness proportional damping coefficient (Only β) can be obtained whilst assuming that the value of α Equation 5 is 0. The frequency at which resonance could be observed between 200 and 600 Hz in the plot for the vertical rail receptance of the reference MBS model, i.e. 277.86 Hz, was implemented as (ω_i) in Equation 5.

In the second approach, both the mass and stiffness proportional Rayleigh damping coefficients are calculated. It is commonly assumed that the sum of the α and β terms are nearly constant over a range of frequencies. Therefore, given ξ and a frequency range ω_1 and ω_2 , two simultaneous equations can be solved for obtaining both α and β . The mass proportional damping is obtained from Equation 6 and the stiffness proportional damping is obtained from Equation 7.

$$\alpha = 2 \times \zeta \times \frac{\omega_1 \times \omega_2}{(\omega_1 + \omega_2)} \quad \text{Equation 6}$$

$$\beta = \frac{2 \times \zeta}{(\omega_1 + \omega_2)} \quad \text{Equation 7}$$

For obtaining α and β from the second approach, two different sets of the frequency range were analysed. For the first frequency range, the first value for the resonant frequency was obtained from the results for the receptance from the MBS model and the second value for the resonant frequency was taken as 10% higher than the first value. Thus, the value of ω_1 was taken as 277.86 Hz and ω_2 was assumed to be roughly 10% more than ω_1 , so a value of 300 Hz was used.

For the second frequency range, the range at which the resonance can be found due to the rail bouncing over the railpad as suggested by Iwnicki was implemented [128]. Thus, a value of 200 Hz was implemented for ω_1 and a value of 600 Hz was implemented for ω_2 .

The results for the vertical and lateral receptance that were obtained whilst implementing the different approaches for calculating the damping coefficient for the pads have been demonstrated in Figure 54 A,B. The results obtained from both approaches demonstrate a good agreement with the reference. Sensitivity analysis was carried out by implementing the different values for the loss factor and the loss factor for which the best agreement was obtained is shown in Figure 54 A,B. The quantitative differences between the reference and the different approaches to implementing the stiffness proportional damping has been shown in Table 23.

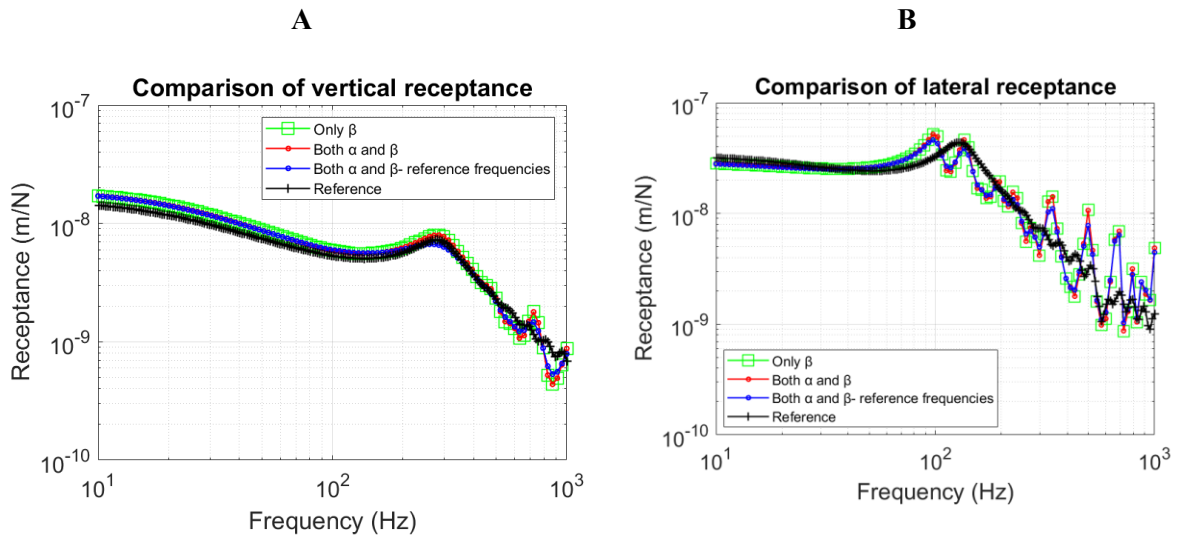


Figure 54: Comparison of the different approaches for including the stiffness-proportional Rayleigh damping coefficient; (A) Comparison of the Vertical receptance against the reference; (B) Comparison of the lateral receptance against the reference

Table 23 allows for the relative comparison of the different approaches for including the stiffness proportional damping in the simulations. A closer result for the resonant frequency as well as the amplitude of the lateral receptance at 10 Hz has been achieved for the approaches that were fine-tuned against the reference model than where a wider frequency range was implemented. However, in terms

of the absolute amplitude, the difference between the results that have been obtained after implementing the three approaches is less than 2%.

Since the objective of this study is to devise an approach for capturing the same track dynamics in FE as the MBS model, the first approach to calculating stiffness-proportional Rayleigh damping coefficient by using Equation 5 would be adequate. Using this approach, the value for the resonant frequency (ω_i) can be directly extracted from the receptance results for the MBS model, thus increasing the chances of achieving better compatibility with the MBS model.

Table 23: Quantitative comparisons for the rail receptance- different approaches to obtaining the stiffness-proportional damping.

Parameter	Resonant frequency (from the vertical receptance plot)	Amplitude of lateral receptance at 10 Hz.
Amplitude in case of the Reference model	278 Hz	3.18×10^{-8} m/N
Difference between Reference and 3D FEA (Only β)	1.4%	-10%
Difference between Reference and 3D FEA (Both α and β)	1.4%	-10%
Difference between Reference and 3D FEA (Both α and β - Reference frequencies)	-3.21%	-11.5%

Thus, the value for the resonant frequency can be obtained analysing the results of the receptance for the reference model for calculating the stiffness-proportional Rayleigh damping coefficient. However, the appropriate damping ratio would need to be implemented in Equation 5 for fine-tuning the 3D

FEA with the reference. To this end, sensitivity studies after implementing different values of the loss factor have been carried out. Figure 55 A,B shows the influence of implementing the values between 0.2 and 0.5 for the loss factor on the vertical and lateral rail receptance. The key quantitative results have been presented in Table 24.

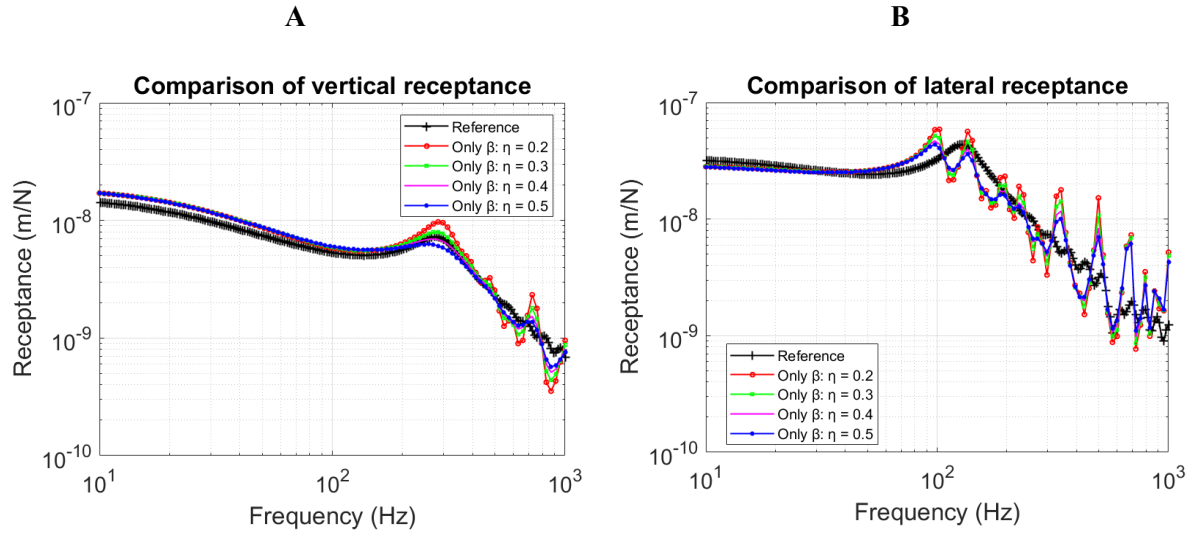


Figure 55: Sensitivity studies for the loss factor to obtain the appropriate stiffness-proportional Rayleigh damping coefficients; (A) Comparison of the Vertical receptance against the reference; (B) Comparison of the lateral receptance against the reference.

A good agreement for the results of the vertical and the lateral rail receptance against the reference at 10 Hz demonstrates the accuracy of the approach for calculating the value of the Equivalent Young's modulus of the pads which contributes to the overall track stiffness. The plots in Figure 55 and the results for the amplitude of lateral receptance in Table 24 affirms the consistency of the results at 10 Hz. For fine-tuning the model, the first step is to establish that the resonant frequency for the rails bouncing on the railpads is <5% when compared to the reference. The results that are obtained on implementing the loss factor of 0.2 and 0.3 have shown the best agreement for the value of the resonant frequency with the reference in Table 24. Secondly, it is important to ensure that the amplitude of the vertical receptance that is obtained at this resonant frequency is <10% when compared to the reference. As shown in Table 24, this has been achieved on implementing a loss factor of 0.3. Finally, Table 24 shows that the results for the amplitude of the lateral receptance at 10

Hz is also <15% when a loss factor of 0.3 is implemented. Therefore, the value for the stiffness-proportional Rayleigh damping coefficient that will be obtained value of a loss factor of 0.3, i.e. a damping ratio of 0.15 will be implemented for the pads during wheel-rail interaction studies.

Table 24: Results from the sensitivity studies for the loss factor for implementing stiffness-proportional damping.

Parameter	Resonant frequency (from the vertical receptance plot)	Amplitude of vertical receptance at resonant frequency.	Amplitude of lateral receptance at 10 Hz.
Amplitude in case of the Reference model	278 Hz	8.28×10^{-9} m/N	3.18×10^{-8} m/N
Difference between Reference and 3D FEA (Loss factor of 0.2)	1.49%	33.4%	-10%
Difference between Reference and 3D FEA (Loss factor of 0.3)	1.49%	9%	-10%
Difference between Reference and 3D FEA (Loss factor of 0.4)	-3.1%	-5.2%	-10%
Difference between Reference and 3D FEA (Loss factor of 0.5)	-5.1%	-13.8%	-10%

Based on the results from the sensitivity studies shown in Figure 55 and Table 24, the value for the stiffness proportional damping coefficient that will be implemented in the time-domain simulations has been calculated from *Equation 5* after implementing a value of 0.3 for the loss factor. The value of the calculation parameters and the result for the stiffness proportional damping have been shown in Table 25.

Table 25: Final damping values for the railpad and baseplate pad

Property	Value
Structural damping Loss factor (η)	0.3
Damping ratio (ζ)	0.15
ω_i (Hz)	278
β - Stiffness proportional damping (Calculated)	0.001

3.4.3 The track properties for the ballast layer

Unlike the pads, representing the equivalent ballast layer with solid elements is be computationally expensive and will not add to the modelling accuracy as the representation would still be for an equivalent layer rather than actual ballast dimensions. Therefore, this layer has been modelled with spring-dashpot elements for replicating the properties of Model 2. The FEA software allows the solution of steady-state or implicit dynamic problems by using the spring and dashpot elements that directly connect the ground to the nodes on the sleeper, which is the method that has been implemented for modelling the ballast layer.

Implementing spring elements for representing the vertical stiffness of the ballast layer

The vertical stiffness of the ballast layer has been described in terms of the unit length of the track ($s_{b,z}$) in the reference MBS model [41]. This can be described in the FE model by deriving the vertical stiffness assigned per node per sleeper (K). The value for the vertical stiffness for a unit length of the

track ($s_{b,z}$) is first multiplied with the length of the sleeper (L_t) to obtain the vertical bedding stiffness under each sleeper. The value for the vertical stiffness connecting each node of the sleeper to the ground is then obtained by dividing this value by the total number of nodes (n_{nodes}) supporting the sleeper as shown in Equation 8. The results from these calculations have been shown in Table 26.

$$K = \frac{s_{b,z} \times L_t}{n_{nodes}} \quad \text{Equation 8}$$

Table 26: Calculations for capturing the vertical stiffness of the ballast layer in FE

Component	$s_{b,z}$ (N/m ²)	L_t (m)	n_{nodes}	K (N/m)
Vertical ballast stiffness	20x10 ⁶	1.25	56	446430

Implementing dashpot elements for representing the Vertical Damping of the ballast layer

The damping properties of the track bedding is captured in the FE model by connecting the nodes at the bottom surface of the sleeper to the ground by using dashpot elements. The viscous damping coefficient per sleeper is obtained by first multiplying the dashpot coefficient (d) used in the MBS model by the sleeper length (L_t). Finally, the dashpot coefficient for connecting each node at the bottom of the sleeper (C) to the ground is obtained by dividing this value by the total number of nodes (n_{nodes}) at the bottom of the sleeper as shown in Equation 9. The values for the variables in Equation 9 and results from the calculation have been shown in Table 27.

$$C = \frac{d_{b,z} \times L_t}{n_{nodes}} \quad \text{Equation 9}$$

Table 27: Calculations for capturing the vertical damping properties of the ballast layer in FE

Component	$d_{b,z}$ (Ns/m ²)	L_t (m)	n_{nodes}	C (Ns/m)
Vertical dashpot coefficient	200x10 ³	1.25	56	4464.3

Implementing spring elements for representing the lateral stiffness of the ballast layer

The approach that has been used for calculating the vertical stiffness of the ballast layer has also been used for calculating its lateral stiffness. The value for the lateral ballast stiffness used in the MBS model was multiplied by the length of the sleeper (L_t) and divided by the total number of nodes on both the left and right side faces of the sleeper (n_{nodes}). As shown in Equation 10, the final stiffness value was multiplied by 2 for considering both ends of the sleeper, which is a valid assumption subject to there being the same number of nodes at each end face. The values for the variables in Equation 10 and results from the calculation have been shown in Table 28.

$$K = \frac{2 \times s_{b,y} \times L_t}{n_{nodes}} \quad \text{Equation 10}$$

Table 28: Calculations for capturing the lateral stiffness of the ballast layer in FE

Component	$s_{b,y}$ (N/m ²)	L_t (m)	n_{nodes}	K (N/m)
Lateral ballast stiffness	10x10 ⁶	1.25	24	1041.7x10 ³

Implementing dashpot elements for representing the lateral damping of the ballast layer

The approach that was used for calculating the vertical damping of the ballast layer has also been used for calculating its lateral damping. However, the figure for the total number of nodes included the

nodes on the left as well as right faces of the sleeper. In addition, the damping value was multiplied by 2 for considering the contribution of damping at both ends of the sleeper, which is a valid assumption subject to there being the same number of nodes at each end face. The relationship for calculating the lateral ballast damping for each sleeper node in FE from the value for the viscous damping used in the reference model has been shown in Equation 11. The values for the variables in Equation 11 and results from the calculation have been shown in Table 29.

$$C = \frac{2 \times d_{b,y} \times L_t}{n_{nodes}} \quad \text{Equation 11}$$

Table 29: Calculations for capturing the lateral stiffness of the ballast layer in FE

Component	$d_{b,y}$ (Ns/m ²)	L_t (m)	n_{nodes}	C (Ns/m)
Lateral dashpot coefficient	100x10 ³	1.25	24	1041.7

For the simulation results shown in Figure 55 A,B, the ballast in the FE simulations was modelled with viscous spring-dashpot elements. The achievement of the modelling assessment criteria after fine tuning the track properties in Figure 55 A,B therefore demonstrates that the properties that have been calculated for the ballast are representative. The final track properties that can be implemented in the model for the time domain wheel-rail contact analysis in FE whilst ensuring compatibility with the MBS model have been shown in Table 30. For clarity, the mass density for all the materials was obtained from the different references that have been highlighted in Table 19. The Young's modulus for the material was implemented for the rails, sleeper and baseplate whereas the equivalent Young's modulus was calculated from the reference stiffness values for the pads and the solid ballast layer. The Rayleigh damping coefficients for the pads and the ballast were obtained from the sensitivity analysis

for the loss factor. The stiffness and the viscous damping for the simplified ballast layer from the reference MBS model were distributed among the appropriate nodes in FE.

Table 30: Final track properties for implementation in FE

Component	Mass density (kg/m ³)	Young's modulus (Pa)	Rayleigh Damping		Spring stiffness (N/m)	Dashpot coefficient t (Ns/m)
			α	β		
Switch Rail	7850	207×10^9	N/A	N/A	N/A	N/A
Stock Rail	7850	207×10^9	N/A	N/A	N/A	N/A
Sleeper	2400	37.5×10^9	N/A	N/A	N/A	N/A
Baseplate	7200	170×10^9	N/A	N/A	N/A	N/A
Railpad	940	16×10^6	N/A	0.001	N/A	N/A
Baseplate pad	950	4.76×10^8	N/A	0.001	N/A	N/A
Vertical ballast layer	N/A	N/A	N/A	N/A	446430	4464.3
Lateral ballast layer	N/A	N/A	N/A	N/A	1041.7×10^3	1041.7

3.5 Conclusions from the chapter

The process for implementing a two-step MBS-FEA approach for modelling the switch was explained through this chapter. The MBS model was implemented for determining the locations along the length of the switch for modelling with FEA. Essentially, after considering the holistic vehicle and track dynamics, it is able to determine the location where the wheel-rail contact patch would transition from the stock to the switch rail in the facing route. A damage prediction model based on the wear number was implemented for determining the crucial sections along the length of the switch where there is a

high risk of surface rail damage initiation. Moreover, the MBS results for the motion of the wheel and the forces that would act on it can be implemented in the FEA.

The approach for modelling the 3D, solid FE model of the switch track was described. After introducing the crucial components for modelling the track, the boundary conditions that were applied to the track model were described. It was shown that modelling the half sleeper length would be sufficient for capturing the track dynamics that would be captured if the full sleeper length were to be modelled. This was ascertained after comparing the modelling results for the vertical and lateral rail receptance with the reference beam element model whose track properties have been closely represented through the 3D, solid FE model.

The longitudinal length for modelling the switch for capturing the appropriate vertical and lateral rail receptance at the locations that will be subject to wheel-rail contact interaction was also determined. The derivation of the values for the material and element properties for closely replicating the track dynamics of the reference model were also explained. The results for the vertical and the lateral rail receptance from the reference and the constructed models have shown a good agreement. In Chapter 4, the implementation of this calibrated track model for wheel-rail interaction studies will be described.

CHAPTER 4. FINITE ELEMENT ANALYSIS FOR THE ROLLING CONTACT INTERACTION BETWEEN THE TRAIN AND THE SWITCH.

The track model that was explained in Chapter 3 will be subject to wheel-rail contact FEA for determining the subsurface rail stresses and strains. The simulation approach for the wheel-rail contact analysis will be described in Section 4.1. The appropriate mesh density for modelling the wheel-rail contact will be determined by discussing the results from the mesh sensitivity analysis in Section 4.2.

Firstly, the results for the vertical wheel-rail contact forces, vertical wheel displacement and contact patch locations that will be obtained from the MBS and the FEA will be compared in Section 4.3.1. In Section 4.3.2, the results from the FEA of the detailed model will be compared against the results that will be obtained from a model where the substructure will not be modelled in detail, i.e. the rails will be directly fixed to the ground. Finally, the influence of modelling the track dynamics on the results for the rail strains will be assessed in Section 4.3.3.

Section 4.4 will summarise the outputs from Chapter 4 and will introduce how the wheel-rail interaction model will be implemented for supporting decisions on structural health monitoring in the subsequent chapters.

4.1 Description of the FE model for the wheel-rail interactions

The FE model for the switch track assembly was previously described in Chapter 3.1. Figure 56 shows the final detailed FE model including the wheel, stock and switch rails, railpad, baseplate, baseplate pad and the sleeper. Overall, eight-node linear brick solid elements with reduced integration (C3D8R) have been implemented for all the components shown in Figure 56 and spring-dashpot elements have been implemented for the ballast layer. The meshing of the switch rail will be discussed in more detail in Section 4.2.

The wheel has been modelled with a radius of 460 mm and with S1002 profile. The rolling contact interaction between a train wheel and the S&C rails has been developed to investigate the strain/stress distribution of the surface and the subsurface rail.

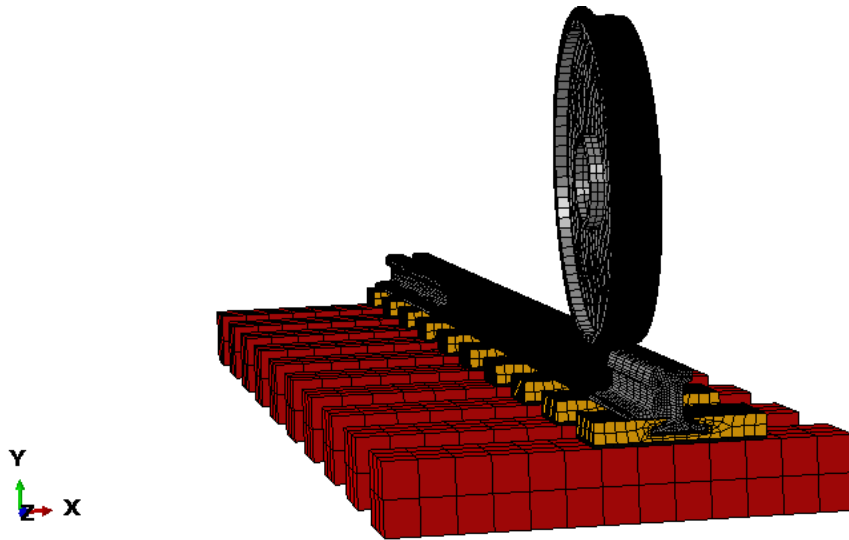


Figure 56: 3D FE model for the analysis of wheel-rail rolling contact

4.1.1 Steps in the simulation

The simulation for the rolling contact interaction between the wheel and the rails of the switch panel has been carried out in ABAQUS in two steps. The first step is a dynamic implicit step that involves stabilising the contact between the wheel and the rail by applying the load on the centre of the wheel for a unit second. The stable positioning of the wheel on the rail has been ascertained by ensuring that no oscillations are present for the results of the vertical wheel displacement, contact pressure and subsurface stresses for the final time increments at the end of this step. Additional forces obtained from the MBS simulation are applied at the centre of the wheel according to the longitudinal position of the wheel. The total time duration for the step that comprised loading the wheel over the rail is 1s, with an analysis carried out with a step time increment of 0.01 s.

The second step involves carrying out implicit dynamic analysis for simulating the rolling contact between the wheel and the rails for a vehicle speed of 160 km/hr. The time duration of the analysis

carried out in the second step is the same as the duration of the passage of the wheel over the same section of the track in the MBS model. The results have been output at 2 kHz in the second step, which is the same frequency as the results output from the MBS model. It will be shown in Section 4.3 that the contact patch locations for the MBS and the FE models are in close proximity at each time step for ensuring a reliable comparison of the results between the two models.

4.1.2 Wheel-rail Contact model

The normal and tangential contact interaction between the wheel and the rail has been carried out in the FE simulations by implementing the hard contact and Coulomb friction penalty contact, respectively. The wheel-rail normal contact interaction, 'hard contact', is enforced in the absence of the clearance between two surfaces and removed when a contact pressure of zero magnitude is reached, leading to the separation of surfaces [12,98].

The tangential contact model is based on the coulomb friction model and assumes that the surfaces in contact can carry a maximum amount of shear stress in a phenomenon known as sticking, beyond which they undergo relative sliding. The critical shear stress for initiating sliding is defined by the Coulomb friction model, after which sliding considers the magnitude of the contact pressure. The calculation of the ratio of stick and slip, also known as the coefficient of friction, is carried out to determine the transition between the two conditions [12,98]. The tangential contact model for the simulations described in this chapter has implemented a friction coefficient of 0.3. Along with the wheel-rail contact interaction, the contact between the switch and the stock rail has been modelled by the same normal and tangential contact models.

For controlling the motion and the displacement of the complete wheel, a reference point has been implemented at the centre of the wheel shown in Figure 56. This reference point has been set to control the motion of the wheel as well as the loads that would act on it by implementing a rigid body constraint between the reference point and the complete geometry of the wheel.

4.1.3 Loading and the boundary conditions for the wheel

The force representing the loading of the vehicle has been exerted on the reference point at the centre of the wheel. Numerical simulations have been carried out after implementing two different loading conditions for the wheel for ascertaining the importance of modelling the vehicle dynamics. The first loading condition involves applying a steady static load that is equivalent to the distributed mass of the vehicle components that would act on the leading right wheel of the leading bogie. The value for this load has been obtained from the MBS results and set constant throughout the step. The second loading condition involves implementing the dynamic loads acting on the wheel that have been obtained from the results of the MBS simulations. Furthermore, along with the external forces, gravity loading has been implemented in the simulations.

As the Manchester Benchmark passenger vehicle was modelled for a single carriage that consisted of two bogies and four wheelsets i.e. eight wheels, the static load for the passenger vehicle that would act on the centre of the wheel was calculated from *Equation 12*. The static wheel load has been modelled by assigning the appropriate value for the mass density to the solid FE wheel geometry. Therefore, this value for the wheel load was subtracted from the total load for determining the vertical load to be assigned to the centre of the wheel as shown in *Equation 12*.

$$L_{wc,static} = \left[\frac{M_{carriage}}{8} + \frac{M_{bogie}}{4} + \left(\frac{M_{wheelset}}{2} - M_{wheel} \right) \right] \times 9.81 \quad \text{Equation 12}$$

The meaning of the variables in *Equation 12* along with their values has been explained in Table 31.

Table 31: Mass and static loading properties for the vehicle

Notation	Full-form	Unit	Value
$L_{wc,static}$	Static load on the centre of the wheel in the FE model	N	51800
M_{body}	Mass of the vehicle body/ carriage	kg	32000

Notation	Full-form	Unit	Value
M_{bogie}	Mass of the bogie	kg	2615
$M_{wheelset}$	Mass of the wheelset	kg	1813
M_{wheel}	Mass of the wheel	kg	906.5

The second loading condition involves implementing the results from the MBS for the vertical and lateral dynamic loads that would act on the right wheel of the leading bogie. Essentially, the suspension forces that would act on the wheel have been obtained from the results of the MBS simulations and then implemented in FEA. Moreover, the MBS results for the lateral and longitudinal displacement have been implemented as inputs for the FEA. It was shown in Figure 23 that the primary suspension comprises vertical, longitudinal and lateral springs connecting the wheel to the rest of the vehicle as well as a dashpot in the vertical direction.

The vertical spring and the dashpot forces that would act on the wheel at each time step have been extracted from the MBS simulations and then implemented for FEA. For reference, the vertical force acting on the centre of the wheel when the leading wheel is in contact with the switch rail has been plotted in Figure 57. The plot for the contact points in Figure 25 showed that the contact between the wheel and the switch rail starts just before a distance of 7 m from the switch toe. As shown in Figure 57, there is little variation in the force acting on the wheel along the length of the switch (< 4%). This value for the vertical suspension force acting on the centre of the wheel has been implemented in the FEA model.

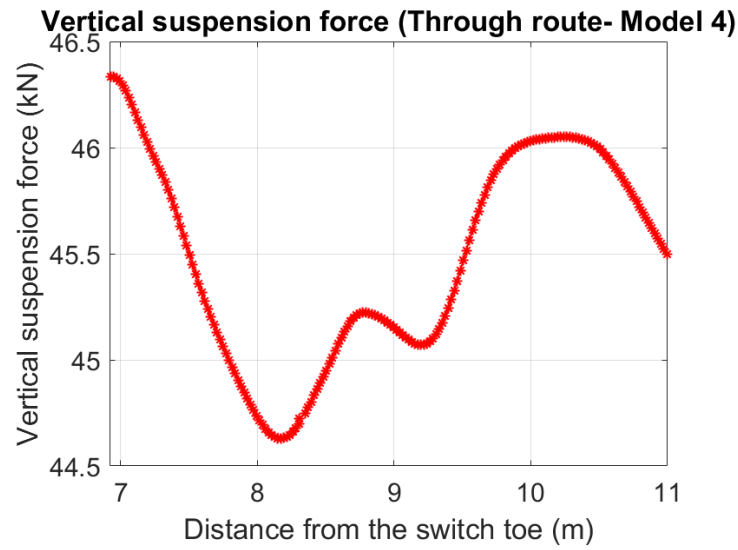


Figure 57: Vertical wheel suspension force

Moreover, it can be seen in Figure 58 that the variation in the force acting on the wheel along the length of the switch is very less when compared to the variation in the wheel-rail contact force.

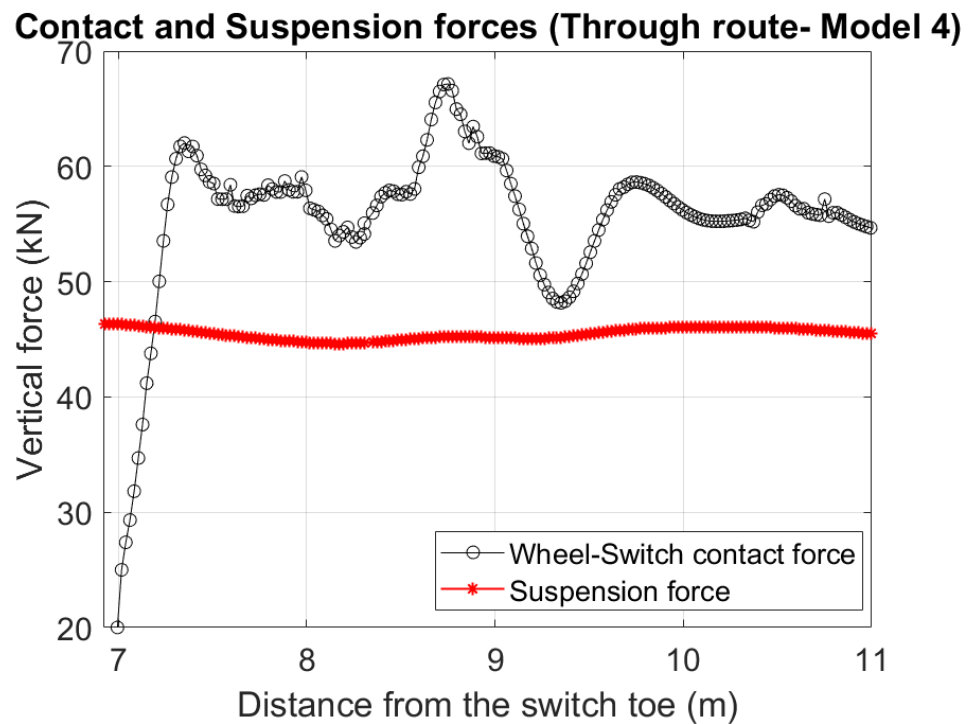


Figure 58: Vertical suspension forces on the wheel and wheel-switch contact force.

In terms of the placement and motion of the wheel for FEA, the position of the wheel at the beginning of the analysis has been determined from the position of the leading right wheel of the leading bogie of the MBS vehicle model. In the first step of the analysis where the wheel is loaded on the rail, the reference point controlling the motion of the wheel has been allowed to displace only in the vertical direction. In the second step, the wheel is free to move vertically and the amplitude of the longitudinal and lateral displacement of the wheel as it would traverse along the length of the switch have been obtained from the output results for the vehicle dynamics from the MBS model. The rotatory displacement of the wheel has been linearly interpolated against the longitudinal displacement for the given linear velocity and radius of the wheel. The only rotational DOF that is free for the wheel is along its lateral axis.

The vertical wheel displacement as well as the contact force in the MBS and the FEA models will be compared in Section 4.3.1 to demonstrate the compatibility between the two models and the suitability of the modelling approach.

4.2 Meshing approach and mesh sensitivity analysis

Mesh sensitivity analysis will be carried out for determining the appropriate mesh strategy for capturing the appropriate mechanical behaviour of the rails. The approach to carrying out the mesh sensitivity analysis would comprise three steps.

In the first step, the mesh strategy that has been implemented in similar examples of modelling work will be reviewed to determine the optimum mesh density at the wheel-rail contact patch. The element size will be based on the trade-off between accuracy and computational efficiency.

In the second step, the geometry of the complete switch rail will be meshed uniformly by implementing a single element size. This will help analyse the effect of mesh density on capturing the stresses for a complete cross-section of the rail. Subsequently, the mesh density on the rail head of the switch will be retained whilst making the element size for the web and foot coarser to check the ability of the model to capture the appropriate mechanical behaviour with fewer elements.

The third and final step would involve analysing the results from the rolling contact analysis between the wheel and the switch rail in the time domain at a longitudinal position where a high risk of damage was determined in Chapter 3.2. The results for the vertical strains at the rail head and web will be discussed in the time domain for investigating the differences in the amplitude.

4.2.1 Determining the ideal element size at the contacting surfaces

A review of the implementation of solid element models for the FEA of S&C has shown that the overwhelming majority of wheel-rail contact surfaces have been meshed with an element size between 1 and 3 mm at the rail surface. Table 32 shows that around 48% of the literature that were reviewed in Chapter 2 and contained information about the mesh strategy implemented a mesh size over 1 mm but below 3 mm for the rail surface. 43% implemented a surface element size of 1 mm and less than 10% of the reviewed literature implemented a surface element size of less than 1 mm. The trade-off between computational efficiency and accuracy were stated as the main reasons for selecting the appropriate element size.

Table 32: Rail surface element sizes implemented in the FEA of S&Cs.

Surface element size	Proportion of reviewed literature (%)	Examples of research interest and references.
1.3 to 3 mm	48	Rail wear: [71], [91]. Rail RCF and plastic deformation: [24,74,78,81]. Wheel-crossing impact behaviour: [83,85–87].
1 mm	43	Rail wear: [45,52,72,82,92,93]. Rail RCF and plastic deformation: [43,70,75,81].
< 1 mm	8	Wheel-crossing impact: [85]. Crossing wear: [94]. Rail corrugation: [25].

For instance, Figure 59 shows the results from a mesh sensitivity study for wheel-rail interaction was undertaken by El-sayed et al. [77]. In the study, the results from a global FEA model of wheel-rail interaction comprising the wheel, rail and the substructure were fed into a local FEA sub-model that was restricted to a certain portion of the wheel-rail interaction. A mesh sensitivity analysis was undertaken by varying the overall element size and plotting the value for the peak wheel-rail contact pressure, number of elements and the resulting simulation time. As shown in Figure 59, it was found that convergence was obtained at 1530 MPa and for a mesh size of 0.8 mm in this particular study. When compared to an element size of 2 mm, the value of the contact pressure increased by <15% but the processing time increased by 172% when the element size was reduced to 0.8 mm.

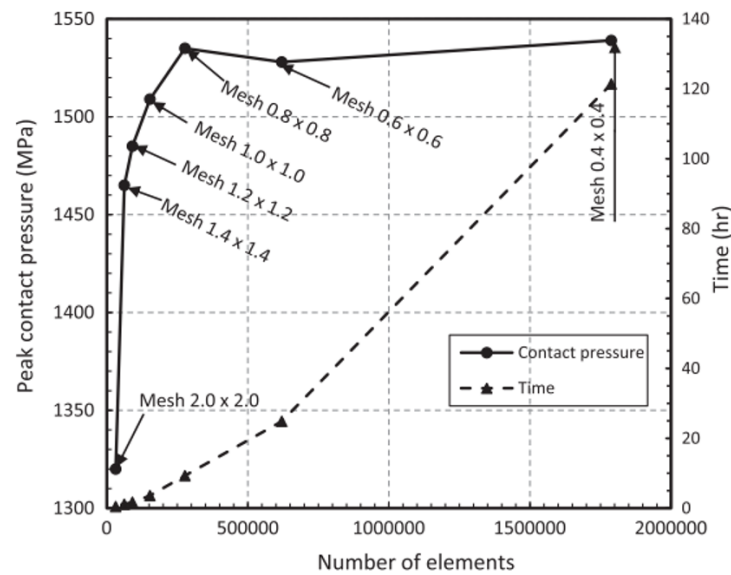


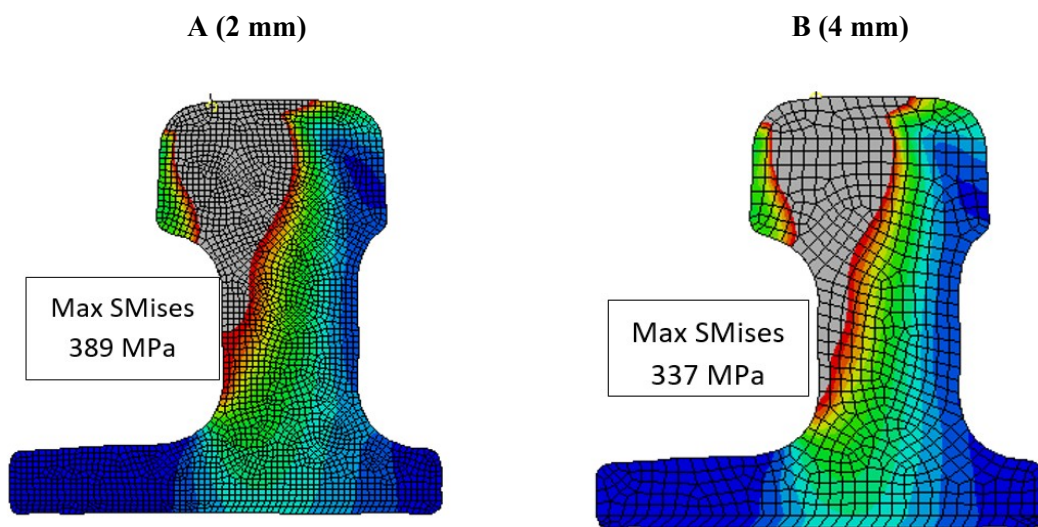
Figure 59: Relationship between the peak contact pressure, number of elements and computational time, reproduced from [77].

Therefore, considering together the predominant surface element size for S&C in FEA in literature of 1.3 to 3 mm (Table 32), mesh sensitivity analysis (Figure 59), the FEA efficiency requirements (Table 10) and the fact that the results from the rail locations that are away from the railhead will be analysed for sensor placement studies, a surface element size of 2 mm will be adopted in the 3D FEA modelling.

4.2.2 Assessment of the stress distributions at a specific cross-section of the rail for different mesh sizes

Subsequently, the complete section of the switch rail has been meshed uniformly with C3D8R elements for evaluating the effect of mesh density on cross-sectional stress distributions. Wheel-rail contact analysis has been carried out for the loading of the leading wheel of the Manchester Benchmark passenger vehicle over the rail. A vertical downward force of approximately 50 kN is applied to the centre of the wheel with S1002 profile and the results are allowed to settle and converge. For different mesh sizes, the results for the Von-Mises stress (SMises) for the cross-section of the rail where a high risk of damage initiation is anticipated has been plotted in Figure 60. The scale

of the colour plot has been kept constant for discussing the results for the Von-Mises stress that have been obtained from the different mesh densities and the key for the plots is provided in Figure 60F. A filter of 20 MPa to the scale of the colour plot has been applied to focus on the areas near the rail web and the foot. It will be shown in Table 33 that the value for the Von-Mises stress is close to 20 MPa on the rail web and much less on the rail foot. For all the mesh sizes, the maximum value for the Von-Mises stress has occurred on the rail head but the values are significantly different due to the different element sizes at the wheel-rail contact interface. Figure 60A, where a mesh size of 2 mm is used as an reference case that can capture the most intricate changes in the stresses within the rail cross-section. When compared to the results shown in Figure 60A, Figure 60B, C & D demonstrate similar cross-sectional stress distributions. However, the results at the lower gauge corner of the rail head are not captured appropriately for the cross-section with the coarser 10 mm mesh size as shown in Figure 60E. Therefore, for capturing the appropriate wheel-rail contact conditions, the adoption of a fine mesh size near the contact interface will be investigated whilst implementing a coarser mesh size in the other regions. For ensuring the compatibility of the different mesh sizes along the length of the switch rail, an intermediate layer that will be meshed with tetrahedral elements for the effective transitioning between the fine and the coarse mesh will be shown in Figure 61. Moreover, the quantitative results from the plot in Figure 61 will be discussed for determining the mesh strategy.



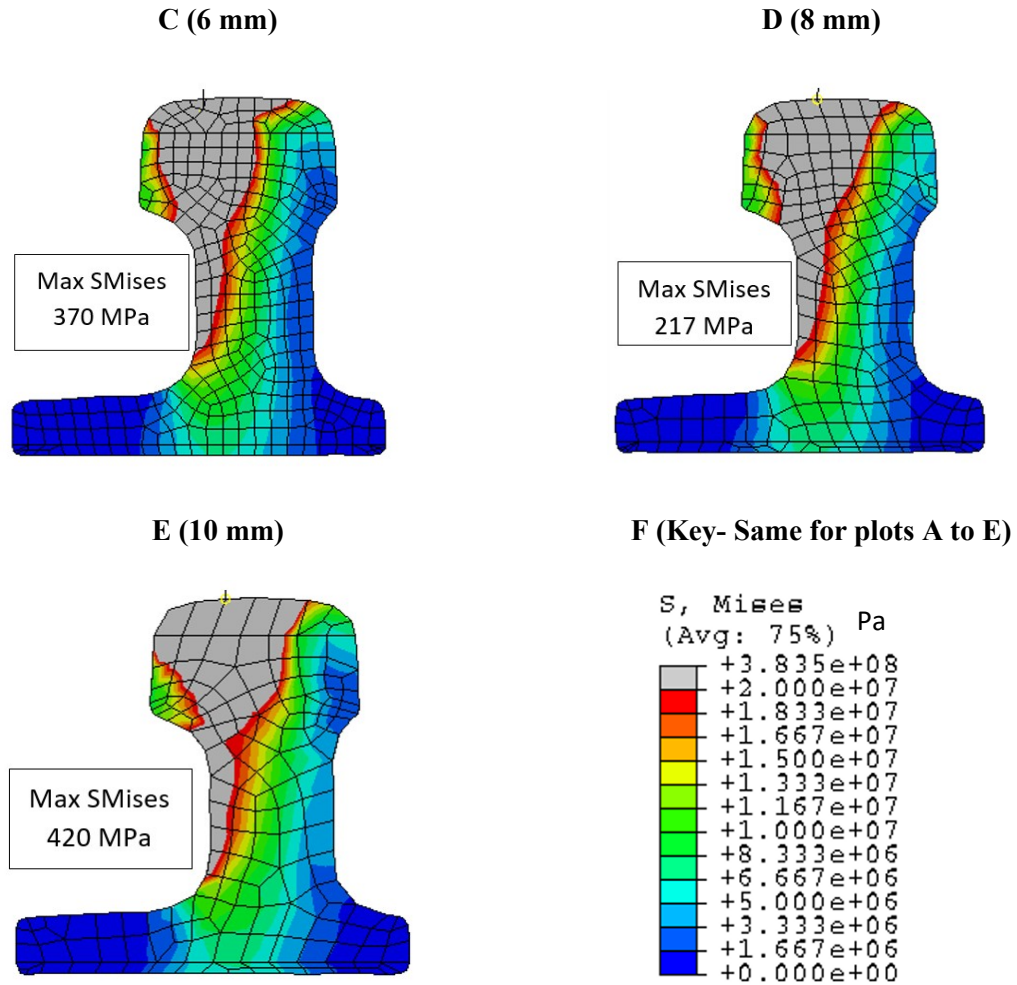


Figure 60: Mesh sensitivity analysis for capturing accurate cross-sectional distributions for the different mesh strategies; A to E. von Mises stress distributions; F. Key for the plots with von Mises stress values in Pascals.

In Figure 61, the top of the rail has been meshed with fine hexahedral elements with a maximum element size of 2 mm at the surface. The bottom portion of the rail has been meshed with an element size of 6 and 8 mm as shown in Figure 61A and B respectively. The different element size at the bottom, i.e. along the non-contacting regions, has been implemented along the vertical, longitudinal and lateral directions. The intermediate layer that would connect the two regions has been meshed with quadratic tetrahedral elements (C3D10) for ensuring a smooth transfer of stresses between the regions meshed. A good qualitative agreement has been obtained for the results plotted in Figure 60A, where a 2 mm element size was adopted throughout the rail and both plots in Figure 61. For the

meshing strategy followed in Figure 61B, a good agreement with the finer mesh size of 2 mm (Figure 60A) for the overall cross-sectional stress distribution can be observed, along with less number of elements (when compared to Figure 61A) whilst maintaining a non-abrupt change in the mesh size along the vertical direction. The quantitative results at the rail head, web and the foot will be discussed in Table 33.

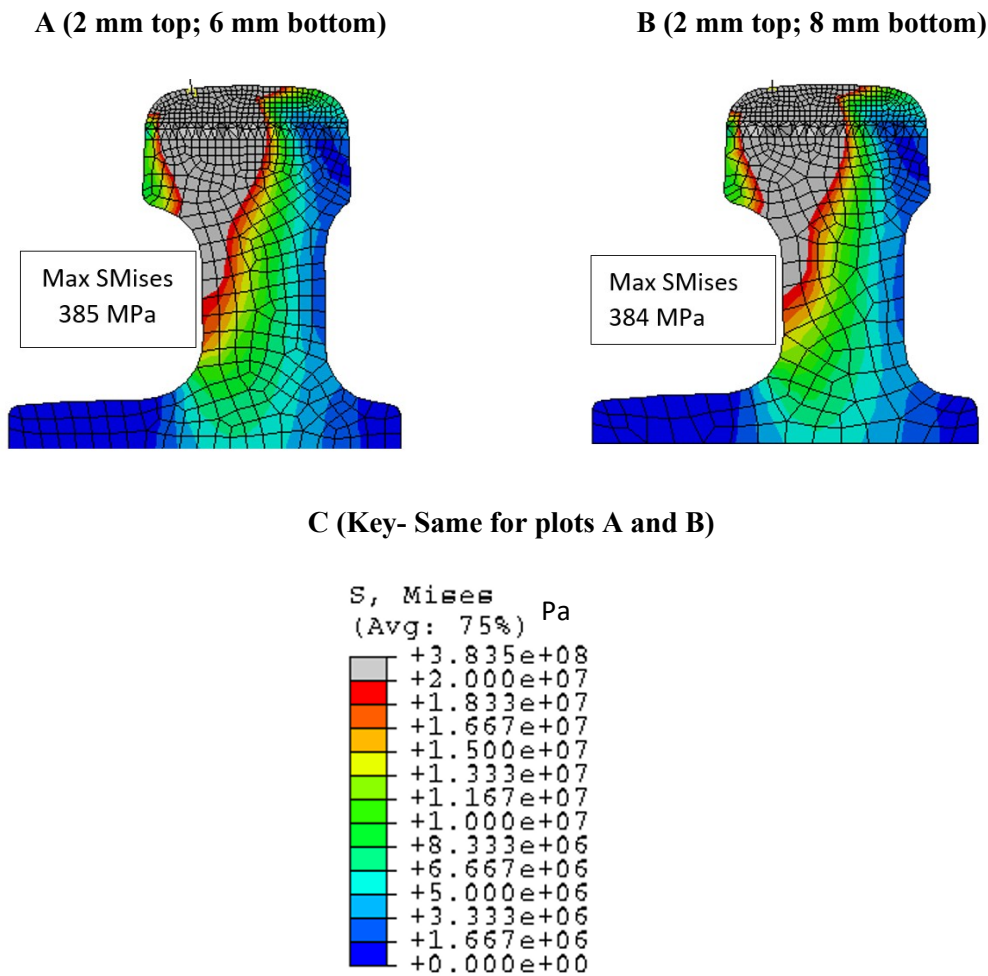


Figure 61: Mixed tetrahedral and hexahedral meshing for capturing the appropriate cross-sectional stress distributions; A, B. von Mises stress distributions for the different mesh strategies; F. Key for the plots with von Mises stress values in Pascals.

Table 33 shows the results for the amplitude of the maximum Von Mises stresses that have been obtained from the rail head, web and foot for the mesh strategies that were adopted in Figure 60A, Figure 61A and Figure 61B, with the 2 x 2 mm mesh strategy in Figure 60A acting as the reference for

accuracy. It has been shown that the overall difference with the reference for the maximum Von-Mises stress across all locations for the mesh strategies shown in Figure 61 is less than 3.5%. The least difference between the reference and the adopted strategies can be found on the railhead, with a difference of less than 1.65% despite the occurrence of the highest amplitude of the stresses on the rail head. This is because the maximum element size at the contacting surface is 2 mm in all the mesh strategies that have been compared. Although the amplitude of the von Mises stress on the rail web is much lower than the rail head, there is a slight increase in the percentage difference for its amplitude between the different mesh strategies. However, the overall value for the difference in the stress on the rail web is less than 0.7 MPa between the three strategies. Similarly, the difference between the amplitude of the von Mises stress at the rail foot between the different mesh strategies is less than 0.21 MPa. This shows that either of the meshing strategies that have been shown in Figure 61A and B can be adopted for the FEA studies to obtain a good agreement with Figure 60A. However, the total number of elements in the switch rail would increase by up to 8% if the bottom portion were to be meshed with 6 instead of 8 mm. For simulations over longer lengths of tracks this difference can be considerable. Therefore, the mesh strategy demonstrated in Figure 61B will be adopted for subsequent analysis.

Table 33: Quantitative comparison of the results for the Von-Mises stress from the different meshing strategies.

Parameter	Mesh Strategy		
	2 x 2 mm: Figure 60A	2 x 6 mm: Figure 61A [% difference from 2x2 mm)]	2 x 8 mm: Figure 61B [% difference from 2x2 mm]
Von Mises stress on the Rail head (MPa)	390	385 [1.37%]	384 [1.62%]
Von Mises stress on the Rail web (MPa)	22.6	23 [1.56%]	23.3 [3.13%]

Parameter	Mesh Strategy		
	2 x 2 mm: Figure 60A	2 x 6 mm: Figure 61A [% difference from 2x2 mm)]	2 x 8 mm: Figure 61B [% difference from 2x2 mm]
Von Mises stress on the Rail foot (MPa)	5.97	6.12 [2.45%]	6.18 [3.37%]

Another interesting observation is that a more converged result for the maximum Von Mises stress can be observed in Figure 61 than in Figure 60. This is because the minimum element size at the wheel and the rail faces that are in contact with each other is 2 mm in all the figures that have been plotted in Figure 61, whereas the minimum element size on the contacting faces would differ in Figure 60. To reiterate, a maximum element size on the contacting surfaces is chosen based on the results shown in Table 32 and Figure 59 where it was concluded that the assumption of a maximum element size of 2 mm will balance the trade-off between the accuracy of the results with the efficiency with which it is obtained. As discussed, the mesh strategy shown in Figure 61B will be adopted since it will help obtain the representative values for the stresses on the rail head, web and foot and cross-sectional distributions for the stresses whilst reducing the total number of elements in the model.

4.2.3 Effect of the mesh size on the strain time series on the rail head

The ability to capture the time series results for the vertical strains at the rail head and web positions by implementing the chosen mesh strategy has been ascertained. The mesh strategy that was discussed and selected in Section 4.2.2, i.e. 2x2 mm mesh size at the contacting and 8x8 mm mesh size in the non-contacting regions of the rail (Figure 61B) has been implemented for the time domain simulations. The complete approach to this wheel-switch rolling contact modelling in the time-domain can be found in Section 4.3. This section will only discuss the results for the vertical rail strains for ascertaining the suitability of the mesh strategy to differentiate between the impact of the wheel-rail contact on the rail head and the web. The different positions along the depth and width of the rail where the results for the vertical rail strains will be plotted in Figure 63 has been shown in Figure 62.

As shown in Figure 62, five positions along the edge of the rail head and web have been selecting for plotting the results of the vertical rail strains. Positions 1 to 3 are on the rail head and positions 4 and 5 are on the rail web. Apart from position 1, the results have been plotted for positions where a sensor could realistically be installed for measuring the vertical rail strains, with positions closer to the rail head being less realistic due to a higher likelihood of sensor damage.

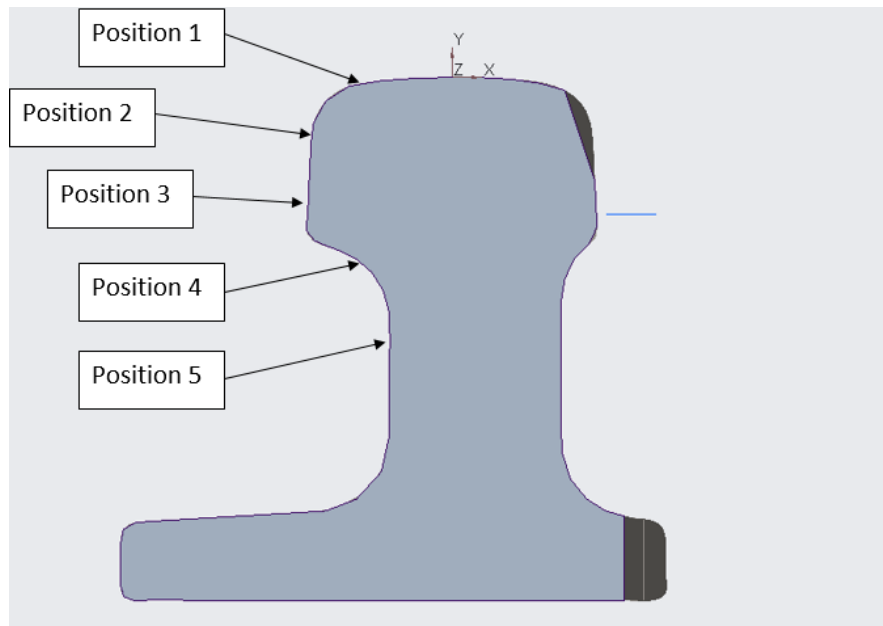


Figure 62: Different positions on the rail head and web for plotting the vertical strains.

The time domain results for the vertical rail strains from the FEA wheel-rail contact analysis for the elements at the different positions in Figure 62 have been plotted in Figure 63. The results have been plotted between 1.045 and 1.05 s from the beginning of the simulation, when the wheel will pass over the longitudinal position of 9.83 m from the switch toe that is being studied. The amplitude of the strain reaches its peak for all positions at around 1.0475 s, when the wheel-rail contact takes place exactly at position 1.

Figure 63 shows that the amplitude of the compressive vertical strain starts increasing much earlier on the rail web (positions 4 and 5) than the rail head due to the effect of rail bending. This is especially true for position 4, where the amplitude of vertical rail strains are more compressive (negative sign) than at position 5 due to its location in the transition between the rail head and the web. In contrast to

the rail web, after the passage of the wheel over the rail head, the rail element at Position 1 would experience momentary tension which is reflected in the positive amplitude of the vertical strain at 1.048 s. The maximum amplitude for the vertical rail strain at positions 1, 2, 3, 4 and 5 are 5000, 365, 250, 145 and 90 $\mu\epsilon$ respectively.

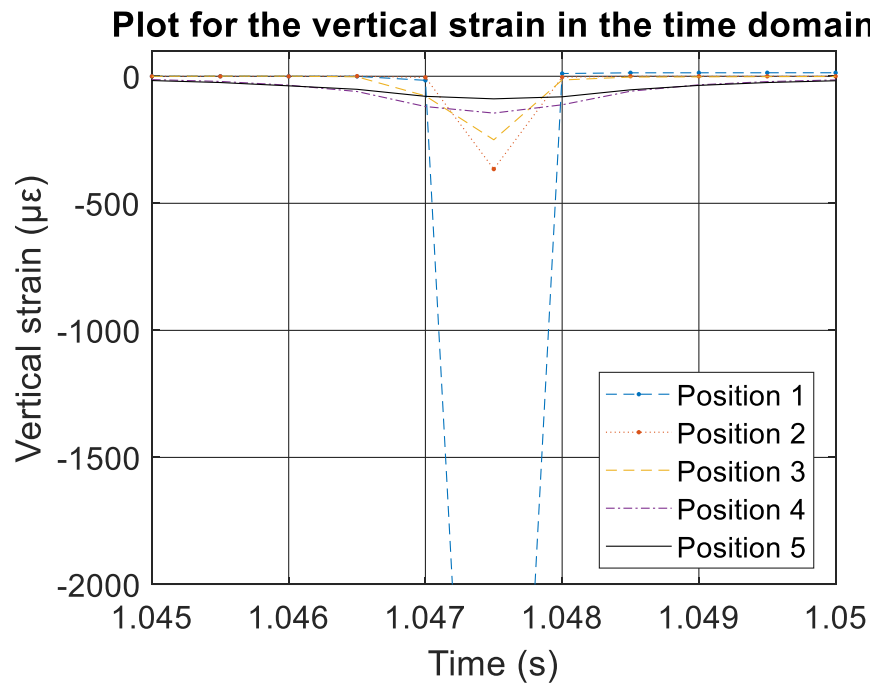


Figure 63: Plot for the vertical strains at different locations along the rail head in the web in the time domain.

The results that have been discussed demonstrate that the mesh strategy is able to capture the difference in the trend as well as the peak amplitude for the rail strains at the different positions. Thus, the discussion of the qualitative as well as quantitative results for the different mesh strategies have demonstrated that the meshing strategy that has been adopted for the switch in Figure 61B can help capture a good overall amplitude for the stresses, strains and can thus to fulfil the objectives that have been set out in this thesis.

4.3 Simulations for the wheel-switch contact interactions and comparing the outputs against the reference

The development of the detailed 3D solid FE track model and the compatibility of its track dynamic properties with the MBS model was discussed in Chapter 3. The results had shown a good agreement for the rail receptance and thus ensured that the track properties and boundary conditions that will be implemented in the detailed FE track model are compatible for implementing the inputs for the vehicle dynamics from the MBS model (Model 4) into the FE model.

The results from the time domain numerical simulations for the interaction between the leading wheel of the Manchester Benchmark passenger vehicle model [153] and the half set of switches for the 60E1-760-1:15 right-hand turnout will be discussed in this section. The methodology described in Section 4.1.1 has been followed for the FEA whilst substituting the outputs that have been obtained from the MBS (Model 4) for the passage of a passenger vehicle at 160 km/hr with a wheel-rail friction coefficient of 0.3.

In Section 4.3.1, the results that will be obtained after implementing varying levels of detail for the vehicle and the track dynamics in the FE model for the simulation of wheel-switch rolling contact interaction will be compared against the results from the MBS (Model 4). The comparison of the results from the FE rolling contact simulations and the reference MBS track model will be shown to validate the ability of the 3D solid FE model to capture the appropriate wheel-rail rolling contact behaviour in the region of interest.

The results for the vertical wheel force, absolute vertical motion of the wheel and the contact patch locations from the FEA will be compared against the results from the three-layered reference MBS track model (Model 4) [41].

The region of interest for the discussion of results will be the longitudinal position between 9 and 10.6 m from the switch toe, where the defects will be introduced in Chapter 5, as informed from the results

for the T_y number in Chapter 3. To restate, the longitudinal positions were chosen based on the T_y results that highlight the locations where both the wear and RCF defects can co-occur.

The first simulation output that will be compared between the MBS and the FEA would be the vertical wheel-rail contact force. This output for the vertical contact force from the MBS simulations is the summation of the normal and the tangential components of the contact force that is exerted by the wheel of the railway vehicle on the rail through the contact points. The equivalent result that can be output from FE is the total contact force in the vertical direction (CFT2), which is the sum of the normal and tangential components of the contact force in the vertical direction for all nodes that are involved in surface-to-surface contact [98].

The second simulation output that will be compared between the FEA and the MBS is the vertical displacement of the wheel. The absolute vertical motion of the wheel that will be obtained from both the MBS and the FEA models is the vertical displacement of the centre of the wheel from its position at the beginning of the simulation. The vertical wheel displacement from will be compared between the longitudinal positions of 9 and 10.6 m from the switch toe.

The third output variable is the location of the contact patch relative to the rail profile reference marker. The rail profile reference marker is essentially the plane of symmetry for the rail head profiles for the switch and the stock rails. The results for the contact point locations will be obtained from the FEA results after implementing a post-processing script to extract the coordinates for the elements on the rail head that will experience the highest amplitude for the Von-Mises stress as a result of the wheel-rail contact at each time step.

A good agreement for the results for the rail receptance with the reference model, confirmation of mesh convergence and comparison of the results output from the FE wheel-rail interaction will together ensure the suitability of implementing the modelling approach for further sensor studies.

In Section 4.3.1, the aforementioned dynamic wheel-rail interaction outputs from the FEA will be compared against the outputs MBS model 4. In Section 4.3.2, the importance of modelling the

appropriate track dynamics will be discussed by comparing the wheel-rail interaction results that were obtained from the models with different levels of track detail. The importance of implementing the substructure dynamics for achieving representative results for the subsurface rail strains will be discussed in Section 4.3.3.

4.3.1 Comparison of the wheel-rail interaction outputs between the MBS reference and the FE simulations

The results for the vertical contact force, vertical motion of the wheel and the contact patch locations that have been obtained from the MBS and the FE simulations have been compared.

For all the FEA simulations that have been discussed in this section, the longitudinal and lateral motion of the wheel has been implemented from the MBS results. In most examples that were reviewed from the literature evaluating the different S&C numerical simulation approaches, this aspect has been neglected and holds especially for simulations in the through route [12]. The lateral displacement of the wheel along the length of the turnout would influence the locations for the wheel-rail contact patch and hence the overall stresses in the rail.

The lateral motion of the wheel that was obtained from the MBS simulation has been shown in Figure 64. Figure 36 shows the assembly of the wheel and the switch for FEA. A positive increase in the amplitude of the lateral wheel displacement would indicate the movement of the wheel to the right, thereby increasing the change of the contact between the wheel flange and the gauge corner. A reduction or a negative change in the amplitude would indicate its motion to the left and the motion of the wheel flange away from the gauge corner of the rail. Under normal circumstances, the positive increase would result in an upward vertical displacement for the wheel and a negative trend would result in a downward vertical displacement. However, the vertical motion of the wheel is also dependent on the build-up of the cross-section of the switch rail along its length which can be seen in the 3D schematic in Figure 22. Therefore, the leftward motion of the wheel would not necessarily

correspond to the downward vertical motion of the wheel under a scenario where the switch rail profile is still building up along the length of the turnout.

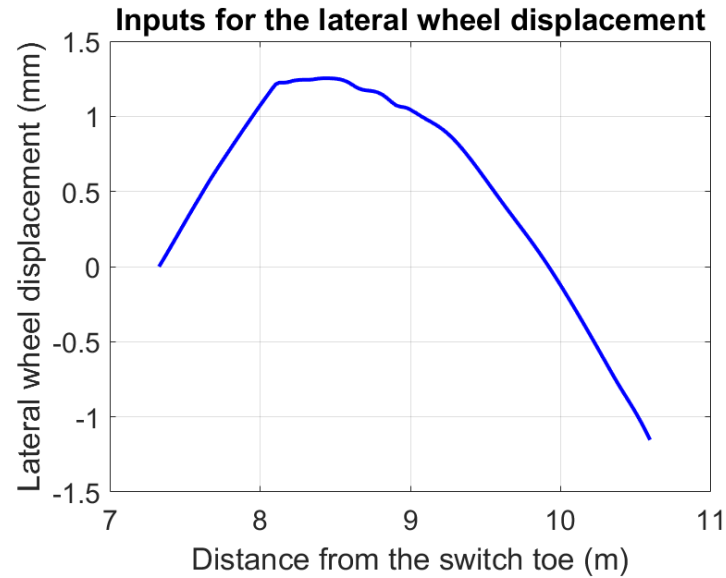


Figure 64: Amplitude for the lateral wheel displacement from the MBS simulation

The results for the vertical wheel-rail contact force along the length of the rail have been compared between the MBS and the FEA models in Figure 65. It was discussed in Section 4.1.1 that the results for the suspension forces that were output from the MBS (Figure 57, Figure 58) were input to the FEA to act at the centre of the wheel. Unlike the MBS model, the FEA model does not implement the detailed suspension elements but applies the amplitude of the load to the centre of the wheel directly as a point force. Therefore, although the rise and fall of the result for the contact forces from the FEA is directly proportional to the MBS, Figure 65 shows that a good overlap between the plots is obtained only at specific longitudinal positions.

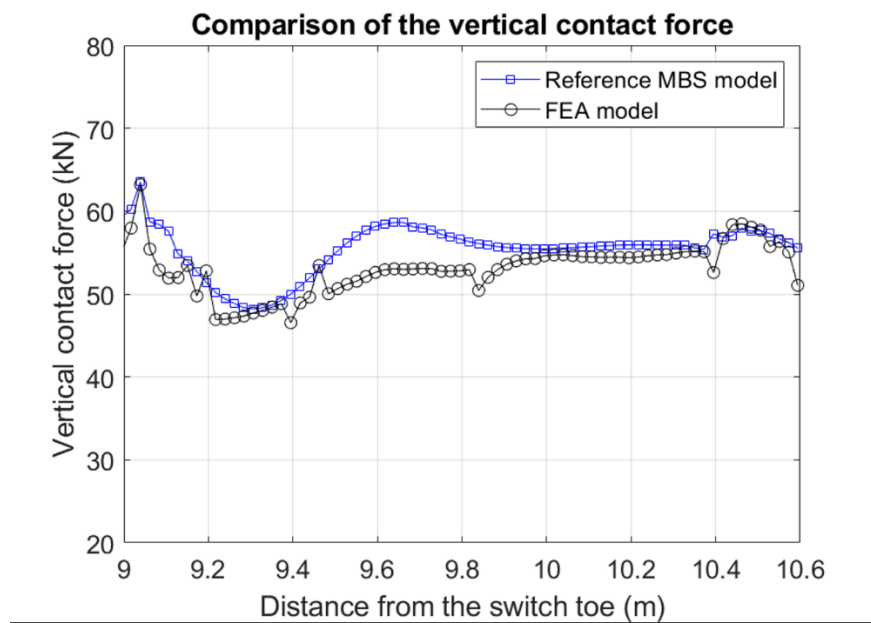


Figure 65: Comparison of the vertical contact force against the reference MBS model for dynamic and static loading in FE.

According to the modelling criteria that was set out in Table 10, the difference between the MBS and FEA for the results of the amplitude of the vertical contact force would need to be <10% at the longitudinal positions of 9.13 and 9.3 m, where the surface rail defects will be introduced. Moreover, the average value for the contact force along the length of the analysed region should be less than 10%. The results highlighted in Table 34 show that these criteria have been met and the quantitative difference in the amplitude is <5.5% and <3 kN for all criteria. However, it is also worth noting that the maximum difference in the vertical contact force occurs at a longitudinal position of 9.64 m, where the difference between the contact forces between the MBS and the FEA models is close to 5.58 kN but still less than 10%.

Table 34: Comparison of the vertical wheel-rail contact force

Parameter	Contact force (kN): MBS	Contact force (kN): FEA	Difference (%)
Vertical contact force at 9.13 m	54.83	52	5.33

Parameter	Contact force (kN): MBS	Contact force (kN): FEA	Difference (%)
Vertical contact force at 9.44 m	51.93	49.62	4.55
Average value for the vertical force	56.7	54	4.87

The results for the vertical wheel displacement obtained from the MBS and the FEA have been compared in Figure 66. As shown in Figure 66, a good qualitative agreement for the rise and fall of the wheel has been achieved between the results for the FEA and the MBS. It can be observed in Figure 64 that there is a sharp negative amplitude or leftward movement of the wheel after a longitudinal position of 9.25 m from the switch toe. The leftward movement means that the wheel flange would move away from the gauge corner of the rail rather than towards it, resulting in a downward motion for the centre of the wheel. The position of the wheel on the switch rail can be visualised in Figure 36 for better understanding the leftward motion. According to the modelling assessment criteria that was set out in Table 10, the maximum difference between the MBS and FEA results for the vertical displacement of the wheel from 9 and 10.6 m should be less than 0.25 mm.

The results plotted in Figure 66 show that the maximum difference between the MBS and FEA results is obtained at 10.6 m with a value of 0.15 mm. More significantly, the behaviour for the vertical wheel displacement between 9 and 9.5 m is consistent between the MBS and the FEA model. It is along this longitudinal distance that the rail defects will be introduced and the ability to capture a similar vertical wheel motion as the MBS demonstrates the suitability of the FEA modelling approach that has been adopted.

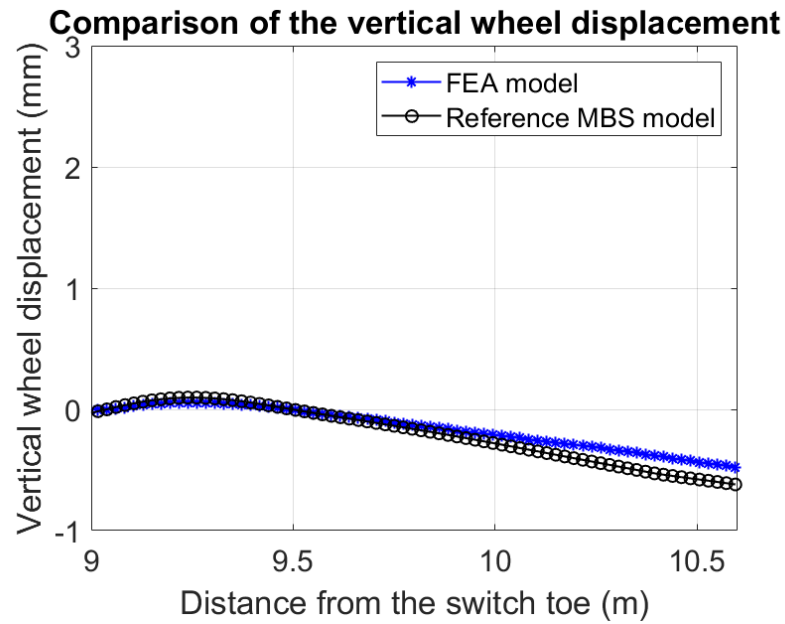


Figure 66: Comparison of the vertical displacement of the wheel; a. Comparison of the amplitude of the wheel raise from the point where the FE simulation would begin; b. Influence of the static and dynamic wheel loading on the overall amplitude of the vertical wheel displacement.

Finally, the locations for the wheel-rail contact points have been compared between the FE and the reference MBS models. The results for the locations of the contact points for the MBS and the FE models when viewed from the top of the rail head have been plotted in Figure 67. Since the extraction of the contact pressure and patch areas from the FEA could not be automated because of software limitations, the elements on the railhead where the maximum value for the Von Mises stress would occur at each time step have been extracted and plotted in Figure 67. The contact point locations have been plotted and compared at the longitudinal positions that are of interest for the introduction of surface defects. Since the results for the locations of the elements have been plotted for the FEA results instead of the contact points, the contact point trajectory in the FEA appears to be straight. Between 9 and 9.4 m, the elements along the lateral rail position of 28 mm contain the highest amplitude of the rail strains. However, the elements with the maximum strain move to the right to a lateral position of 27 mm after 9.4 m. The same contact positions and lateral movement for the contact points as the FEA can be observed for the results from the MBS. In agreement with modelling

assessment criteria in Table 10, Figure 67 shows that the difference in the lateral position for the contact points between the MBS and FEA results is <2 mm.

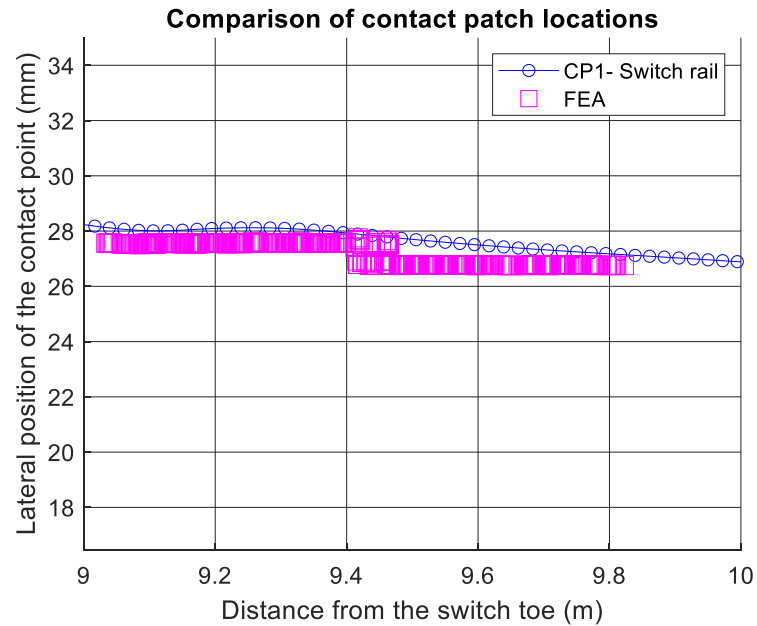


Figure 67: Comparison of the contact point locations between MBS (CP1- Switch rail) and FEA

Figure 68 overlays the FEA contact points at the locations of interest over the different contact points from the MBS model for the stock and the switch rails. The schematic of the lateral position along the switch rail that was plotted in Figure 24 shows that the contact point position of 28 mm would lie on the top surface of the gauge corner of the rail. It can be observed in Figure 68 that the contact point locations that have been plotted from the FEA simulations fit suitably in the context of the expected wheel-rail contact positions.

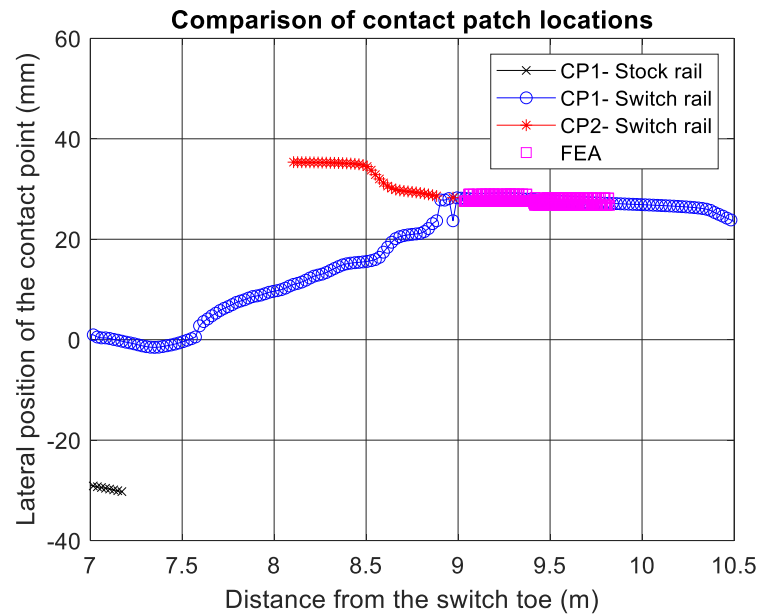


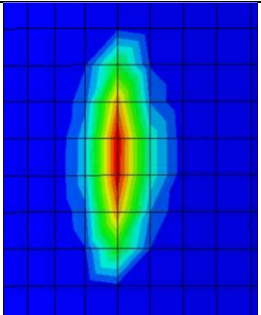
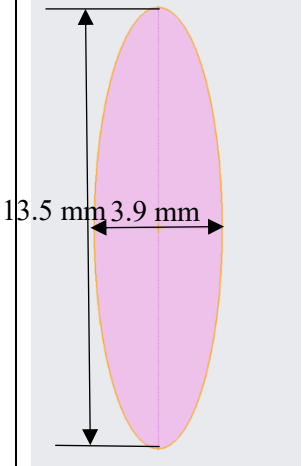
Figure 68: Overlap between the MBS and the FEA contact points at the key locations.

The dimension of the contact patch at the longitudinal distance of 9.3 m from the switch toe has been compared between the Reference MBS and the FEA models in Table 35. At this longitudinal position, it was shown in Figure 65 that a good agreement for the vertical contact force was achieved from the wheel-rail contact simulations. Table 35 shows that the area for the elliptical contact patch that has been obtained from the FEA and Reference MBS model is 41.3 and 41.5 mm² respectively. The difference between the values is 0.5%, which meets the modelling assessment criterion of achieving a difference of <10% for this parameter.

Although the contact patch areas are similar, the comparison for the length and width of the contact patch shows that the contact patch in the MBS model is less broad and slightly longer than the FEA model. It can also be seen in Table 35 that the FEA model is able to achieve a good representation for the contact patch when an element size of 2 mm is implemented at the wheel-rail contact surface.

The wheel-rail contact force at 9.3 m is lower for the FEA than the reference MBS model, which justifies the smaller area of the contact patch for the FEA model at this position. Overall, a good agreement for the size of the contact patch has been achieved, demonstrating that the impact load is effectively transferred from the wheel to the rail in the FEA.

Table 35: Comparison of the contact patch dimension between the MBS and the FEA models at 9.3 m.

Model	Length of contact patch- 2a (mm)	Width of contact patch- 2b (mm)	Contact patch area (mm ²)	Representation
3D FEA	12	4.4	41.3	
Model 4	13.5	3.9	41.5	

The simulation whose results have been discussed in this section was carried out with a sampling frequency of 2 kHz. The ABAQUS log file showed that the difference between the start and end times from the simulation is 17 hours, which is 30% lower than the value of 1 day that was set out in the modelling assessment criteria. The simulation has been carried out on a computer cluster with 20 cores and 40 GB of RAM. In contrast, a turnout FE model that was developed for analysing the impact of switch run through at the University of Birmingham took 160 hours to run with the same computational power [95]. It is worth noting that the run-through model excluded the modelling of the substructure track dynamics but included the geometry and elastic-plastic material properties for the rails and switch components that included but were not limited to the both sides of switch/stock rails,

stretcher bars, lock and drive rods and two wheelsets that were connected to each other to form a simplified bogie. Although the research interests of the two models are different, the two-step MBS-FE simulation approach that has been presented through this thesis is more suitable for multiple and repetitive simulations which will be needed from a Digital Twin. The accuracy and compatibility requirements with the MBS model have also been met. The fulfilment of the modelling criteria by the FEA approach for the contact patch locations, contact forces and vertical wheelset displacement has therefore validated the ability of the FE simulations for capturing similar wheel-rail contact behaviour as the reference MBS model at the longitudinal position of interest.

4.3.2 Influence of modelling the substructure dynamics on the results for the vertical contact forces

The results for the contact forces and vertical wheel displacement have been compared between the simulation where the substructure track dynamics were implemented and the one where the bottom of the switch and the stock rails was directly fixed to the ground, i.e. all the DOF were constrained. In both cases, rolling contact simulations were carried out in the time domain whilst implementing the static load for the vehicle at the centre of the wheel and modelling the lateral motion of the wheelset. The comparison of the vertical wheel-rail contact forces has been shown in Figure 69, where more prominent and higher amplitude peaks can be observed for the model where the rail is fixed. The average value for the vertical wheel-rail contact forces is approximately 55 kN for both the modelling approaches. The results have shown that the consideration of the substructure dynamics would not significantly impact the overall amplitude of the contact forces. Section 4.3.3 will analyse the impact of the difference in substructure conditions on the results for the rail strains and show that it is considerable.

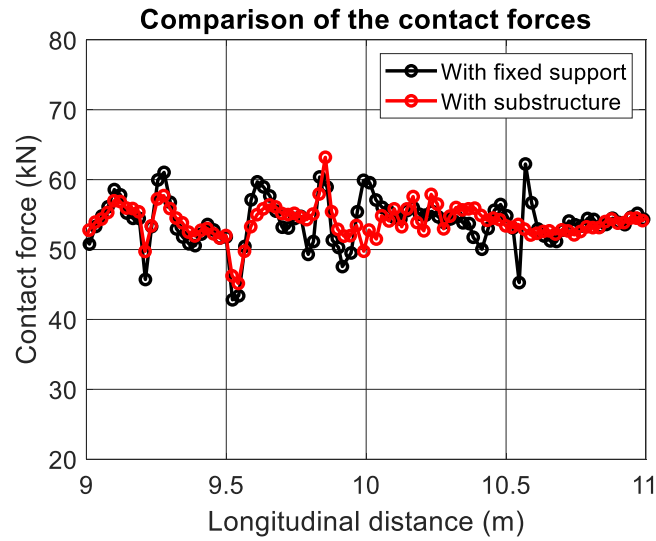


Figure 69: Comparison of vertical wheel-rail contact forces for the models with and without the support stiffness.

4.3.3 Influence of the substructure dynamics on subsurface rail strains

The results for the rail strains in the global spatial directions, i.e. vertical (E22), longitudinal (E33) and lateral (E11) will be discussed since these are crucial for discussions on structural health monitoring.

The influence of modelling the substructure dynamics on the results for the strains of the rail in the longitudinal, lateral and vertical directions has been demonstrated in Figure 70, Figure 71 and Figure 72. As opposed to the model with the fixed rail, the model with the detailed substructure included the geometry of the railpads, baseplates, baseplate pads, sleepers and the ballast layer. The compatibility of the track properties between the reference model and the FE model with the detailed substructure was ascertained by comparing the results for the vertical and lateral rail receptance between the two in Chapter 3. In contrast, the simulations with the fixed rail were carried out whilst constraining the motion of the track at the rail foot.

In Figure 70A,B, the strains in the longitudinal direction have been plotted for the cross-section of the rail for the impact of the wheel on the rail in the sleeper spacing. A significant difference in the overall stress distributions can be observed. As quantified in Table 36, the model with the fixed rail in Figure

70A does not experience a high amount of tension or positive strain values near the rail foot, unlike the more flexible rail with the substructure shown in Figure 70B.

Table 36: Comparison of the longitudinal strains on the rail web and foot during wheel-rail contact in the sleeper spacing.

Rail section	Average value for the longitudinal strain E33 ($\mu\epsilon$)	Nature of the strain
Rail web (with substructure)	–50	Compressive
Rail web (without substructure)	–25	Compressive
Rail foot (with substructure)	70	Tensile
Rail head (without substructure)	–25	Compressive

Table 39 also shows that a higher negative amplitude for the compressive strains near the rail web is captured for the model with the detailed substructure. The same can be observed close to the rail head in Figure 70. This is a result of better flexibility of the rail when the substructure is modelled. When the results are illustrated in 3D in Figure 70C,D, it can be observed that the overall locations and amplitude for the tensile and compressive strains are different. This shows the importance simulating the track dynamics to include key details and with the appropriate track properties.

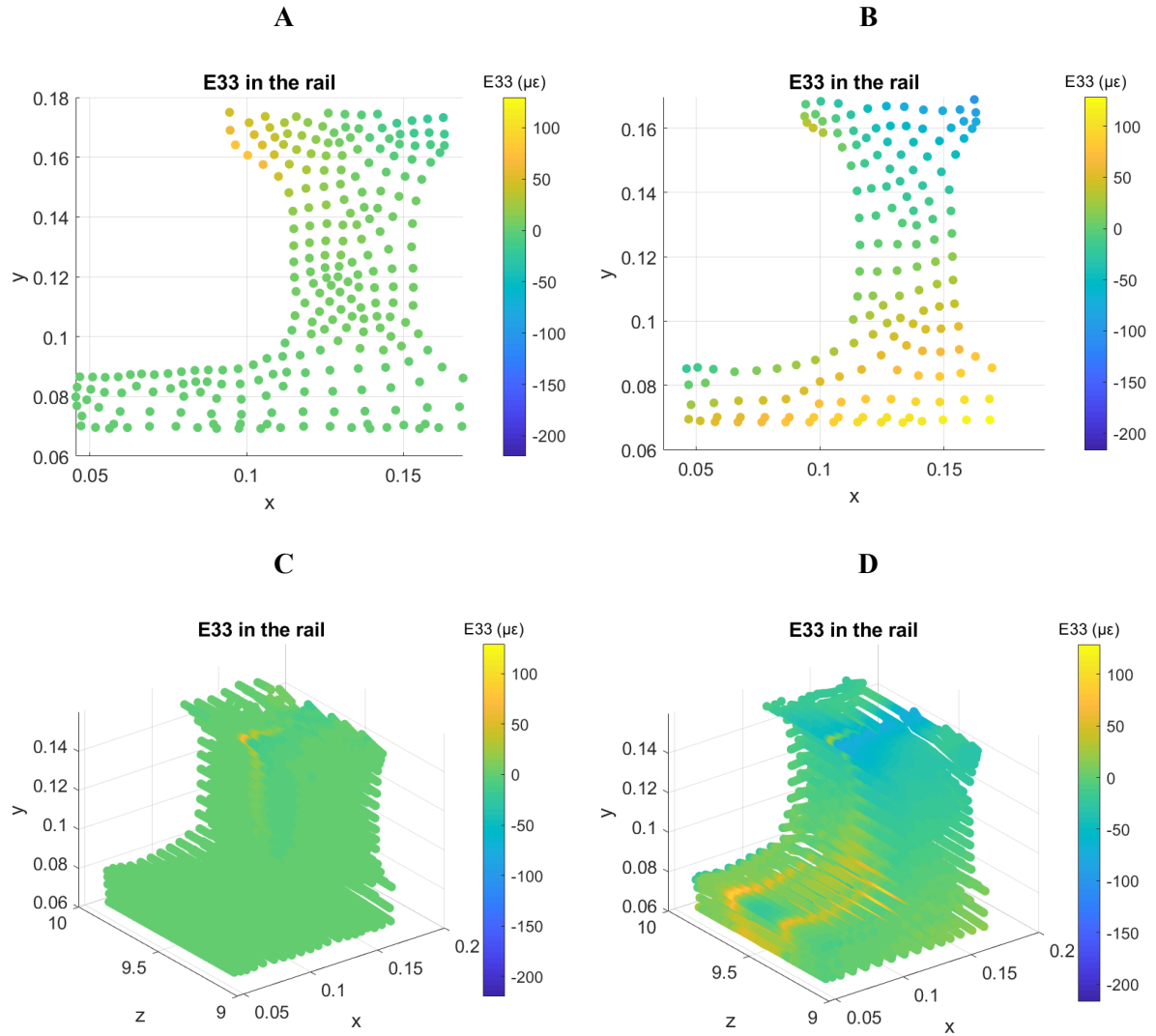


Figure 70: Influence of modelling the substructure dynamics on the longitudinal strains for the switch rail. Cross-sectional strains: (A) Model with fixed rail; (B) Model with detailed substructure.

Visualised for a longer length of the rail in 3D: (C) Model with fixed rail; (D) Model with detailed substructure.

The influence of modelling substructure dynamics on the vertical strains has been demonstrated in Figure 71. It has been illustrated in Figure 71B,D that the vertical strains for the model where the detailed substructure has been implemented are compressive on the whole, with an average value of $-70 \mu\epsilon$. As shown in Figure 71D, the presence of the sleepers would also affect the distributions for the vertical strain, with compressive strains up to $-200 \mu\epsilon$. This is in stark contrast with the results from the fixed rail that have been illustrated in Figure 71A,C, where compressive stresses are predominantly

observed on the track side (left) of the rail head and the web. It has also been demonstrated in Figure 71 C,D that the locations that experience the positive/tensile vertical strains are more prominent for the model with the fixed rail than the one with the softer substructure support. This is because the track flexibility would result in the downward deflection for a longer length of the rail, resulting in more elements that undergo compressive strains for the model with the ballasted substructure support. On the contrary, as demonstrated in Figure 71C, the locations that undergo compressive vertical strains in the model with the fixed support are limited to the locations that are close to the wheel-rail contact region. This demonstrates that the amplitude and direction of the strains are highly dependent on the type of substructure support. This makes it important to model the track dynamics appropriately for the determining the sensor placement for specific turnout layouts.

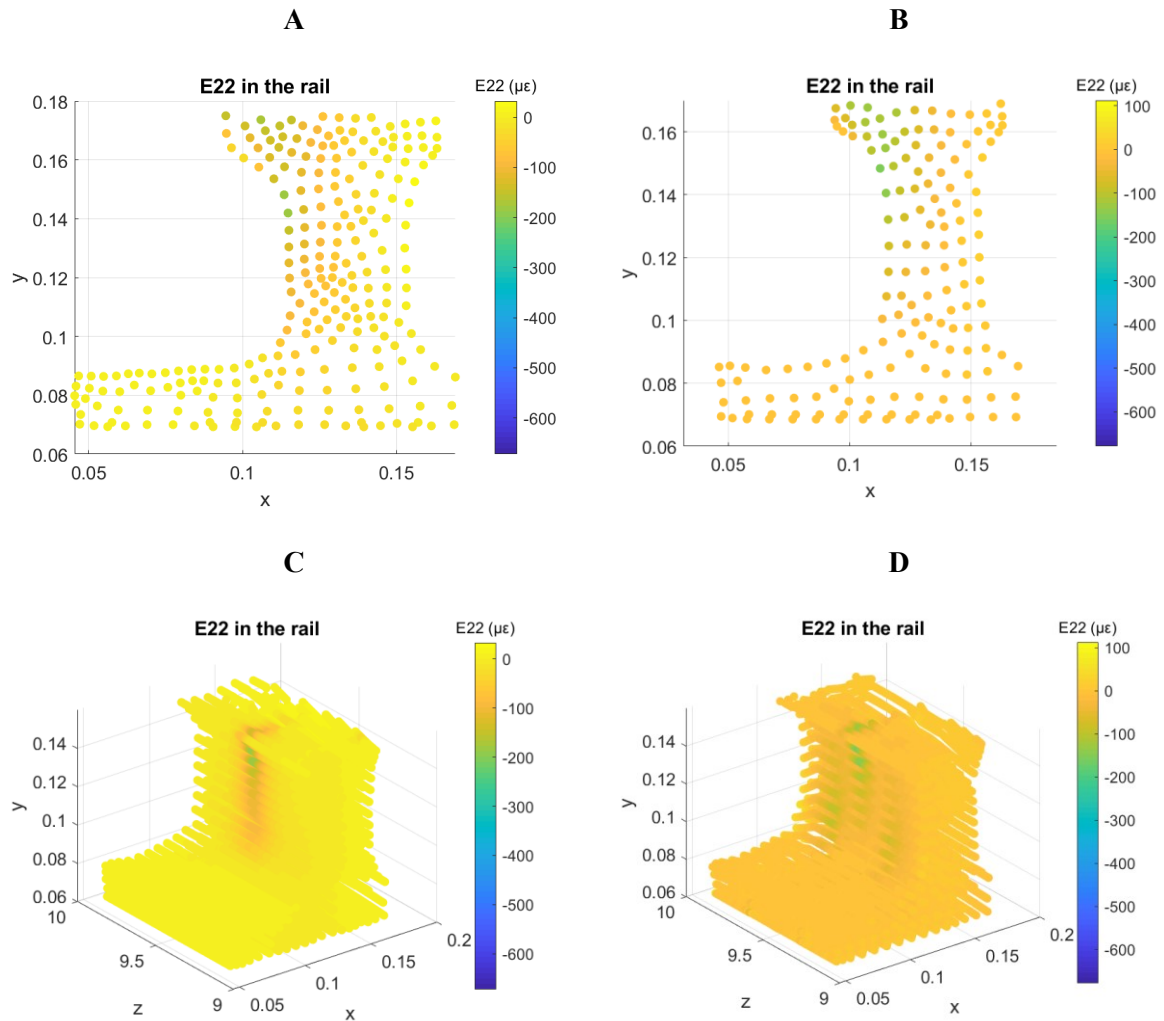
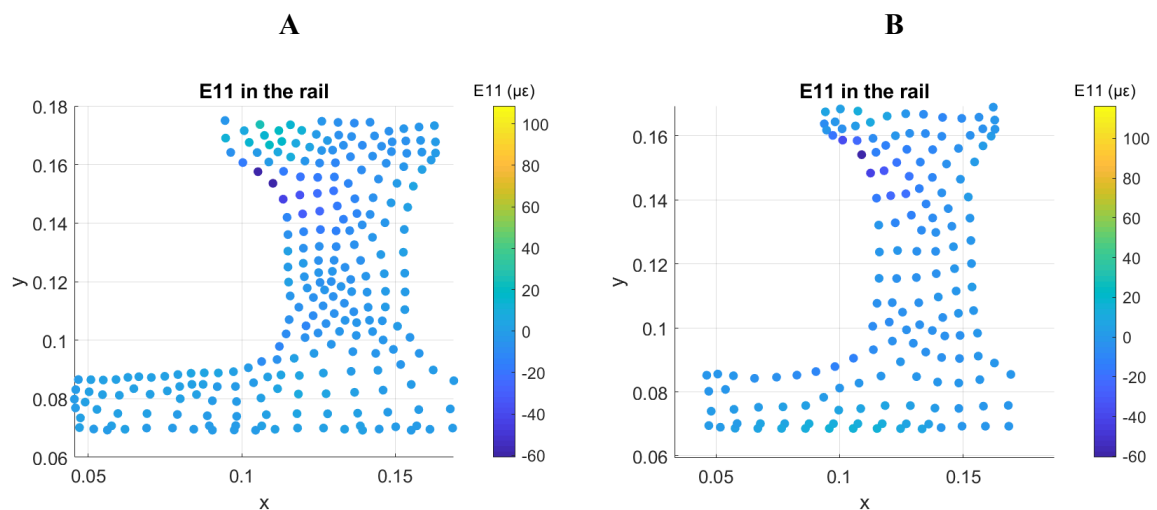


Figure 71: Influence of modelling the substructure dynamics; Vertical strains for the cross-section of wheel-rail contact: (A) Model with fixed rail; (B) Model with detailed substructure; Vertical strains for the switch rail in 3DI: (C) Model with fixed rail; (D) Model with detailed substructure.

The influence of modelling the substructure on the lateral strains has been plotted in Figure 72. Figure 72 A,B show the lateral strains captured at a specific time step for the cross-section of the switch rail where the wheel and the rail are in contact in the sleeper spacing. A negative amplitude for the lateral strains upto $-60 \mu\epsilon$ denotes compressive behaviour at the lower gauge corner of the rail head for the simulations carried out whilst implementing the fixed as well as detailed substructure. The amplitude of the lateral strains are more compressive for the model with the fixed rail constraint. The implementation of the substructure would also result in a difference in strain amplitudes for a longer length of the track, as shown in Figure 72C,D. The amplitude for the lateral strains in the web-foot connection on the track side is higher for the ballasted track model than for the model with the fixed rail, with an average of $-25 \mu\epsilon$ as opposed to $-20 \mu\epsilon$ as shown in Figure 72C,D. The difference in the overall strain distributions is also a result of the difference in track flexibility. The longitudinal position of the wheel over the rail in the model with the detailed substructure in Figure 72D is in the spacing between two sleepers. The different support conditions have therefore resulted in different contours for the lateral strain.



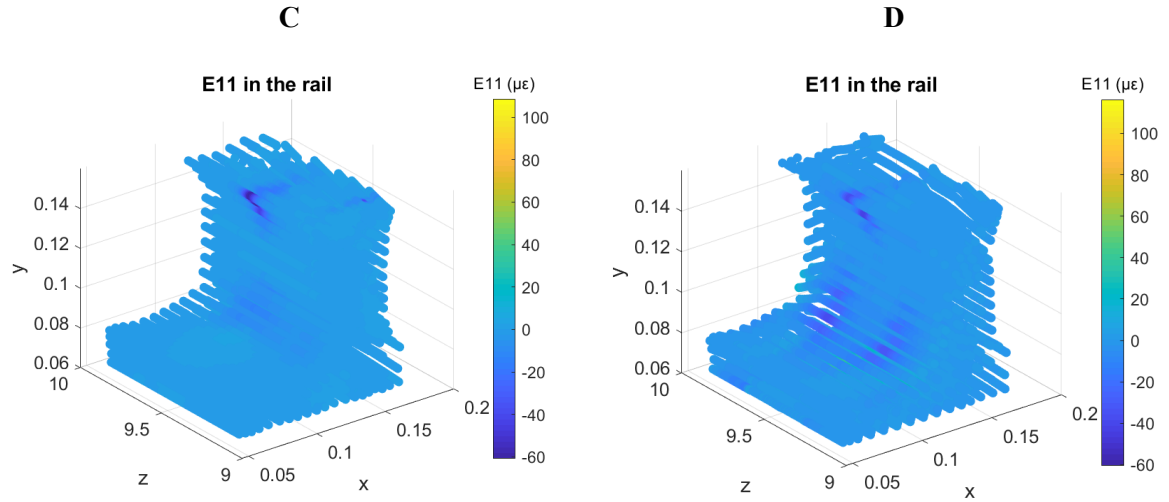


Figure 72: Effect of considering the detailed substructure; Lateral strains for the cross-section of wheel-rail contact: (A) Model with fixed rail; (B) Model with detailed substructure; Lateral strains for the 3D switch rail: (C) Model with fixed rail; (D) Model with detailed substructure.

To conclude, it is important to note that despite the similarity in the results for the contact force, vertical wheel displacement and the contact patch locations for the different types of track model, the results for the strains are heavily influenced by the track setup. This demonstrates that in addition to the measurement of the wheel-rail contact force by installing sensors on the rolling stock, the sensors that are able to capture the track dynamic behaviour will need to be implemented for condition monitoring.

4.4 Conclusions

This chapter implemented the 3D FEA model of the switch with fine-tuned substructure dynamics in wheel-rail rolling contact simulations. With the objective of balancing the trade-off between accuracy and computational efficiency an optimum maximum element edge length of 2 mm was chosen for meshing the surfaces that will experience wheel-rail interaction. The locations away from the contact regions were meshed with a maximum element size of 10 mm along the length and 8 mm in the vertical direction of the switch. The meshing strategy was backed up by providing evidence from references and analysis of subsurface strain distributions and amplitude.

A two-step implicit dynamic analysis approach involving the application of a preload and subsequent rolling contact between the wheel and rail was implemented in ABAQUS. The results for the vertical wheel-rail contact force, wheel displacement and contact patch locations were compared against the reference MBS model for assessing the performance of the model according to the modelling criteria that were set out in Chapter 2. It has been successfully demonstrated that the results obtained after implementing the two-step modelling approach meet the comparison criteria against the reference simulations.

The outputs from the simulations that were carried out with the detailed two-step approach have been compared against the results that were obtained after implementing the modelling assumptions that were discussed in Chapter 2. These assumptions include the simplification of the substructure dynamics by fixing the bottom of the rail to the ground i.e. constraining all DOF at the bottom of the rail, ignoring/simplifying the lateral movement of the wheel as it passes over the rail and implementing a single static load on the wheel [12]. The effect of these simplifications on the results for the wheel-rail contact force and subsurface rail strains was evaluated.

The investigation highlighted that the distributions, as well as the amplitude of the strains in the lateral, longitudinal and vertical directions were different for the models with the fixed rail and substructure support. The sleeper spacing, as well as the track stiffness, will affect the results for the

strains. Although a reasonably close agreement was obtained for the vertical contact forces between the simulation that was carried out with fixed rail and the one with substructure support, a notable difference for subsurface strain behaviour was observed between the two models. The analysis of the results have led to the inference that the sole measurement of contact forces by implementing onboard measurement sensors on trains could potentially lack the level of detail that is needed for predicting change in the support conditions.

The values for the strains that are obtained from the switch rail can be used as the results that are directly proportional to the expected results that will be obtained from the strain sensors. Therefore, the result for the strains can help with the determination of the locations for placing the sensors for the condition monitoring of switches.

In Chapters 5 and 6, the introduction of specific defect geometries for surface-initiated RCF, rail wear and voiding will be explored. The locations that will be able to capture the change in the strain results ($\Delta\epsilon$) as well as the direction for measuring the strain values (lateral/longitudinal/vertical) will be investigated. Furthermore, the placement of the sensor for capturing all three faults under different conditions will be evaluated by carrying out parametric studies for different axle loads and friction conditions for the set line speed. The proposed simulation approach presents the ability to implement the important details for the track substructure for making a reasonably informed decision for the placement of sensors for the condition monitoring of railway switches. The results shown in the chapter conclude that the approach that has been shown for fine-tuning the 3D FEA model against the reference can be investigating for field calibration in future research.

CHAPTER 5. WHEEL-RAIL ROLLING CONTACT ANALYSIS

AFTER THE INTRODUCTION OF TRACK DEFECTS

In this chapter, the effect of introducing surface-initiated rail damage and track voiding on the dynamic behaviour of the track will be explored. The track defects were introduced into the FE model that had shown a good agreement with the reference MBS model in Chapter 4. The description of the defects as well as the approach to introducing them into the track model will be explained in Section 5.1.

The effect of the introduction of the defects on the results for strains in the vertical and the longitudinal direction will be discussed in Section 5.2. The influence on the results for the strains in the lateral direction will not be discussed because it was shown in Chapter 4 that the amplitude of the strains is much lower in that direction as opposed to the vertical and longitudinal directions.

The simulations were also carried out with different masses for the vehicle for representing the tare and the laden loading conditions. Therefore, the influence of the vehicle loads on the vertical contact force and the strains in the vertical and the longitudinal direction for the simulations that were carried out with and without the defects will be discussed in Section 5.3.

The results from the parametric studies constituting different track defects, vehicle loads and friction coefficients form a part of the dataset that will be analysed for determining the placement of sensors for detecting the faults of rail wear, RCF and voiding in Chapter 6. The conclusions from this chapter have been discussed in Section 5.4.

5.1 Introduction of the defects in the track model

Three types of defects have been introduced into the track model. Out of these, two are surface damage defects on the switch rail and the third is voiding under a rail sleeper. The surface damage defects of wear and RCF were introduced at the locations where a high risk of both wear and RCF was predicted by implementing a damage prediction model. The model that was implemented for the

prediction was the Whole life rail model (WLRM) that the $T\gamma$ number, as shown in Chapter 3.2. This location is just after the transition of the wheel-rail contact from the stock to the switch rail in the facing route. Voiding has been simulated by changing the stiffness for the ballast under the sleepers where that would experience the highest amplitude for the vertical wheel-rail contact force. This is at the longitudinal position where the transition of the wheel-rail contact patch from the stock to the switch rail would take place in the facing route. The flange contact would result in a high amplitude for the lateral and vertical forces over the sleeper and thus result in a variation in the track stiffness along the length of the track over time, which will result in voiding. The voiding, which essentially manifests in the form of a gap between the sleeper and the ballast has been simulated in the form of the loss of stiffness support under the sleepers, i.e. a reduction in the vertical stiffness of the ballast layer. Thus, the wear, RCF and voiding have been introduced close to each other and the measurement of strains to detect these faults occurring in the transition region will be investigated. The surface-initiated faults have been introduced on the unsupported rail section that would lie between the sleepers. In Chapter 6, sensitivity studies will also be carried out for determining the influence of defect introduction on the section of the rail supported by the sleeper.

The geometry of the crack that can be attributed to the RCF failure mechanism has been introduced on the switch rail and is based on a squat defect that was modelled to study the mechanical characteristics of a rolling contact squat-type crack by Bogdanski et al. [166]. Squats are one of the many forms that surface initiated RCF can take. They result from the longitudinal displacement of railhead cracks, followed by propagation into the subsurface rail and subsequent lateral spread [17,167]. The defect has been introduced at the approximate longitudinal position of 9.43 m from the switch toe and laterally towards the gauge corner of the rail for ensuring that the wheel-rail contact occurs over the fault. The drawing for the geometry of the squat [166], the defect that was modelled in FE and the evidence of the occurrence of squats on the switch rail have been shown in Figure 73 A, B and C respectively.

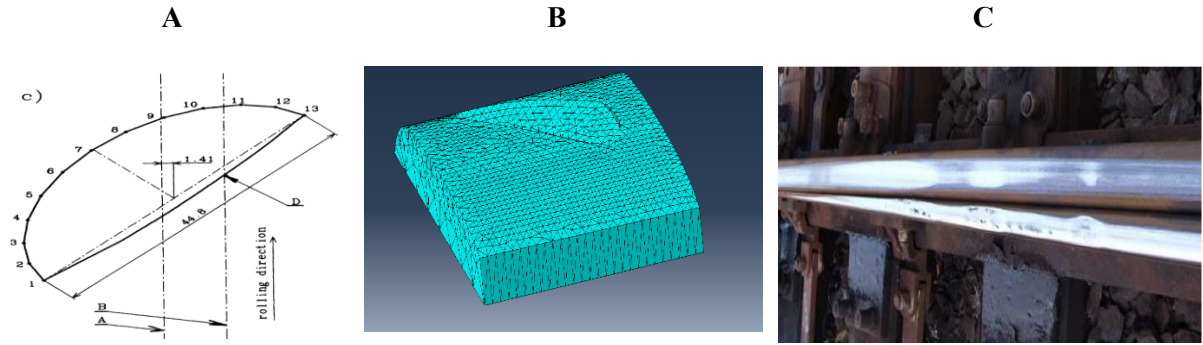


Figure 73: Introduction of the RCF fault into the model; (A) Reference drawing [166]; (B) The fault introduced to the FE model; (C) occurrence of squats on a switch.

Due to the lack of access to field measurements for this particular layout, the implementation of worn rail profiles in similar research was investigated. The worn rail profiles along the switch and the stock rails for CN60-350-1:12 turnout measured with MiniProf instrument by Xu et al. [43] and the wear depth was plotted, which has been reproduced in Figure 75. Figure 75 shows that the vertical wear of the switch rail exceeded 5 mm at certain sections along the switch length. Since the curve radius of this reference turnout is 350 m [43] and the curve radius in the 3D FEA switch model is more than twice at 760 m, a wear depth that does not exceed 2.15 mm will be incorporated into the 3D FEA model.

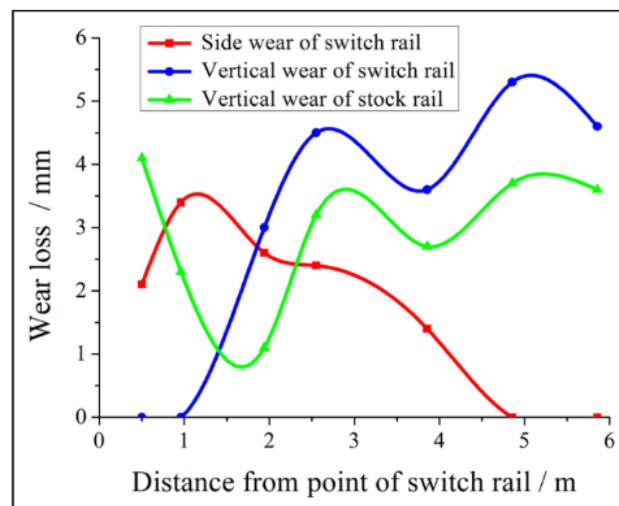


Figure 74: Measured wear along the length of the CN60-350-1:12 turnout, reproduced from [43].

As shown in Figure 75A, rail wear has been incorporated along the length of switch rail between a distance of 9.05 to 9.8 m from the switch toe. The maximum depth of wear that has been incorporated into the rail is 2.12 mm and the average wear depth is 1.47 mm. Figure 75B shows the change to the vertical trajectory of the switch rail milling tool profile for reducing the material on the rail surface. The milling tool profile can be seen in Figure 37C. The depth of wear was varied between 9.05 and 9.8 m to be directly proportional to the $T\gamma$ number that was obtained from Model 4. This means that longitudinal positions with a larger value for the $T\gamma$ number were modelled with a higher wear depth than those with lower values.

This approach cannot be considered reflective of how wear would occur in the field since it has been introduced abruptly for a finite length of the switch and is based on the aforementioned assumptions. However, convergence and meshing issues have been avoided in the simulations due to the finite depth and length of worn rail that has been modelled. The model has therefore been implemented academic interest of changing rail profiles along a finite length of the track and should not be considered as an accurate representation of how wear should occur along the turnout.

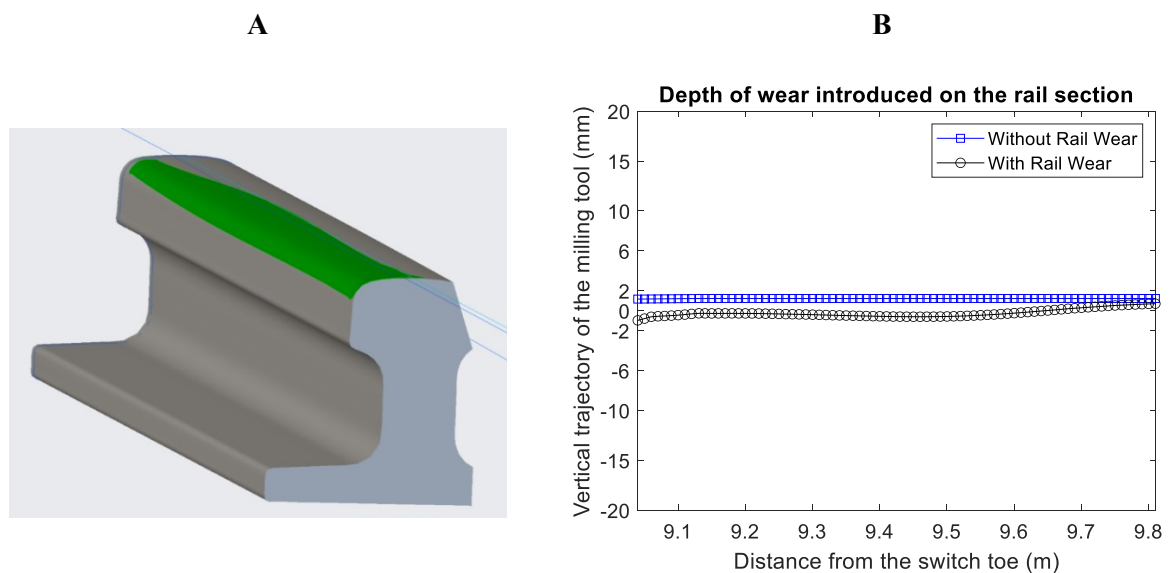


Figure 75: Modelling the rail wear: (A) Modified rail profile with the rail wear (only a finite length has been shown); (B) Depth of wear that was introduced on the rail section

An approach that would result in a sudden change in the track stiffness has been implemented for representing the voiding defect. This has been carried out by reducing the ballast stiffness under three sleepers. The vertical ballast stiffness of 25 MN/m that was implemented in the reference MBS model has been reduced to 10 MN/m and introduced under the sleepers that lay at a distance between 8.4 and 9.87 m from the switch toe in the FE model. The locations along the switch track where the wear, RCF and voiding have been introduced are shown in Figure 76. As demonstrated in Figure 76, analysis will be carried out to detect the three faults of wear, RCF and voiding at specific locations.

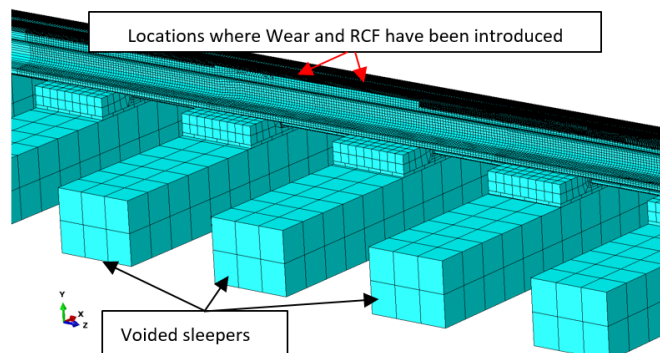


Figure 76: Locations for introducing wear, RCF and voiding in the model

5.2 Effect of modelling track defects on the rail strains

The two-step MBS-FE simulation approach that was adopted in Chapter 4 has also been adopted for carrying out the numerical simulation of train-switch interaction in the presence of the defects. At first, the simulations were carried out in MBS, following which the MBS results for the wheelset lateral displacement and loads acting on the wheel have been implemented in the FE simulations.

The simulations were carried out for the passage of a Manchester Benchmark passenger vehicle in the through route of a 60E1-760-1:15 switch at a speed of 160 km/hr with a wheel-rail friction coefficient of 0.3. The results for the vertical wheel-rail contact force that were obtained from the simulations carried out in the presence of the rail defects for two different wheel loads, representing the tare and the laden conditions will be discussed in Section 5.3 and a significant effect of the defects on the amplitude of the strain will be shown.

There will also be a significant influence of the track defects on the results for the subsurface rail strains, which will be discussed in this section. The change in the vertical strains as a result of introducing the track defects of wear, squat and voiding has been plotted in Figure 77. The plotted values for the change in the strain are the difference in the amplitude of the strain values from the simulations that were carried out with and without the track defect.

The presence of the track defect is expected to result in an increase in the amplitude of the impact force and the subsurface rail strains. In Figure 77A, the difference in the strain amplitude has been plotted for the time step where the wheel is in contact with the RCF defect. From the scale of the results, a change in the strain values of up to 200 $\mu\epsilon$ can be observed. The change in the strain amplitude is closer to the railhead since the strain amplitudes are also higher in those locations.

Similarly, the change in strains because of introducing the wear and the voiding track defects have been plotted in Figure 77 B,C respectively. The change in strain values of up to 800 and 160 $\mu\epsilon$ can be observed for the models with wear and voiding respectively. The results for the strains are dependent on the contact patch location. For example, if the contact between the wheel and the rail is closer to the gauge corner of the rail, compressive (negative) strain values on the track side of the rail will be captured. If the contact point is further to the right, then the measurement of the strains at the same location will be more positive or tensile. Among the three track defects, the highest difference in the amplitude of the vertical strain is obtained due to wear (up to 800 $\mu\epsilon$) since there is a significant variation in the vertical wheel-rail contact force along the length of the rail (Figure 81).

The relationship between the strains and the contact force will be investigated in Chapter 6. The results for the change in strains due to introducing defects will also be implemented for determining the distance from the defect location for measuring the rail strains for detecting the three track defects.

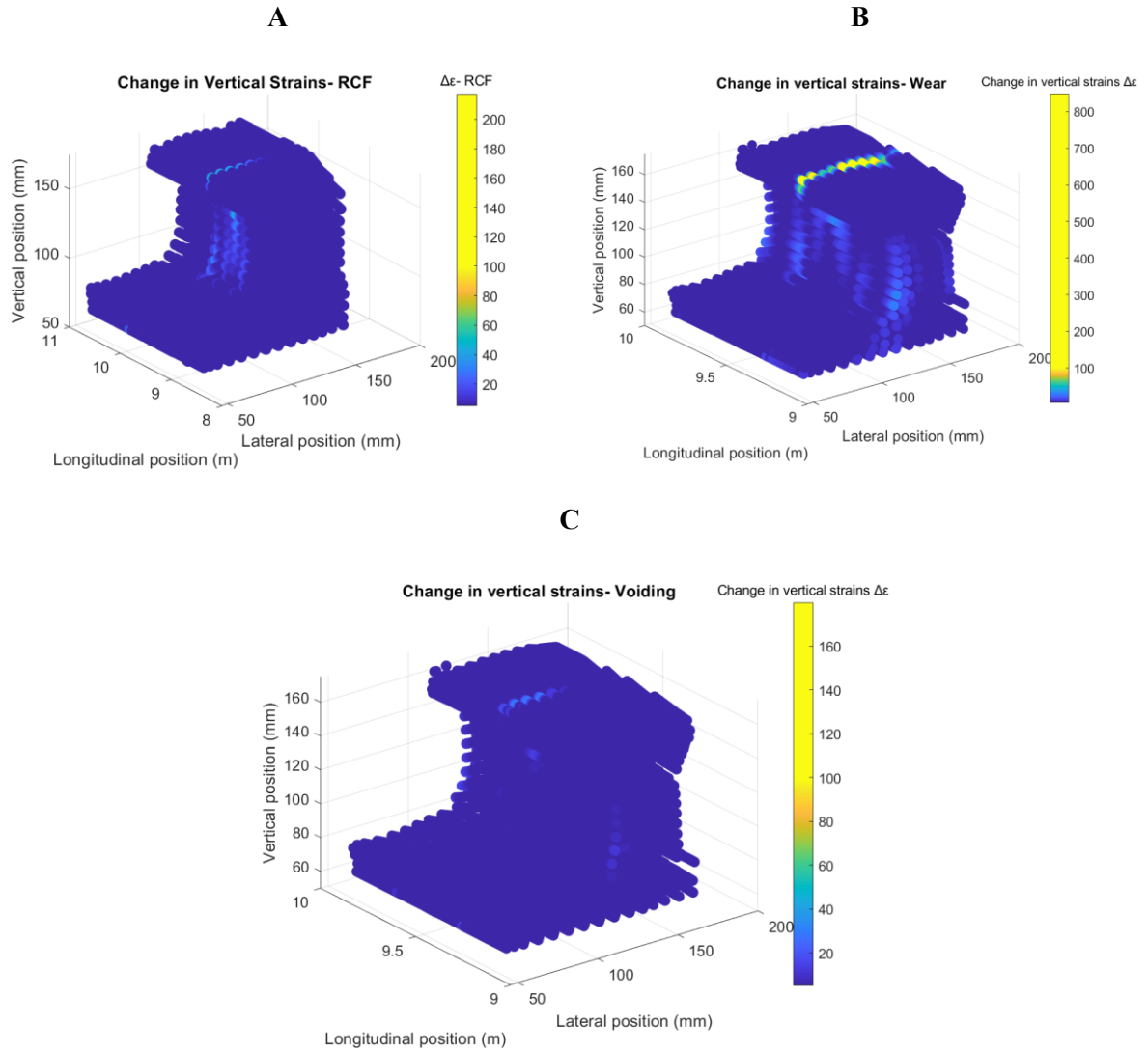


Figure 77: Change in the vertical strains due to fault introduction; (a) RCF damage; (b) Wear damage; (c) Voiding

The results for the change in the longitudinal strains due to the presence of the track defects have been plotted in Figure 78. Although the amplitude of the change in the longitudinal strains is not as high as the vertical strains that are shown in Figure 77, this amplitude is well beyond the resolution of the sensor and should be able to detect the presence of the defect. The highest difference in the longitudinal strains can be observed for the model with the Wear (Figure 78B) defect followed by those with the voiding (Figure 78C) and the RCF defects (Figure 78A). For the RCF results, a maximum difference of $70 \mu\epsilon$ has been obtained and the longitudinal distances between 9.25 and 9.75 m from the switch toe show some potential for measuring the strains for fault detection. For wear, a

maximum change of $180 \mu\epsilon$ has been obtained and the same longitudinal positions as the RCF (9.25 to 9.75 m from the toe) show the potential for measuring strains to capture the defect. The results for change in the longitudinal strains due to the presence of voiding show the impact of change in the track stiffness on its longitudinal flexibility and a maximum change of $120 \mu\epsilon$ has been captured. A systematic approach will be implemented for the screening and ranking of locations for the measurement of rail strains in Chapter 6.

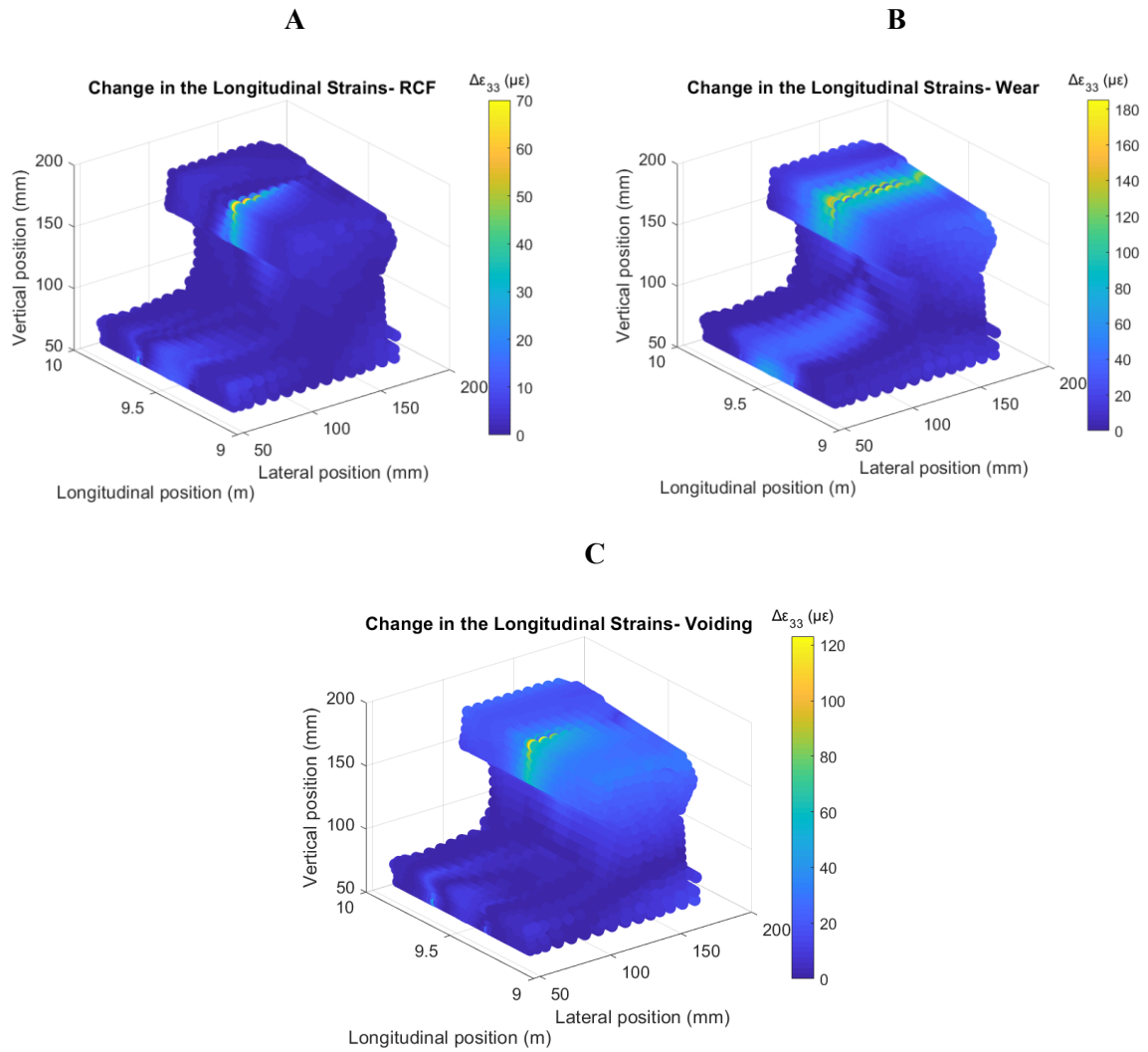


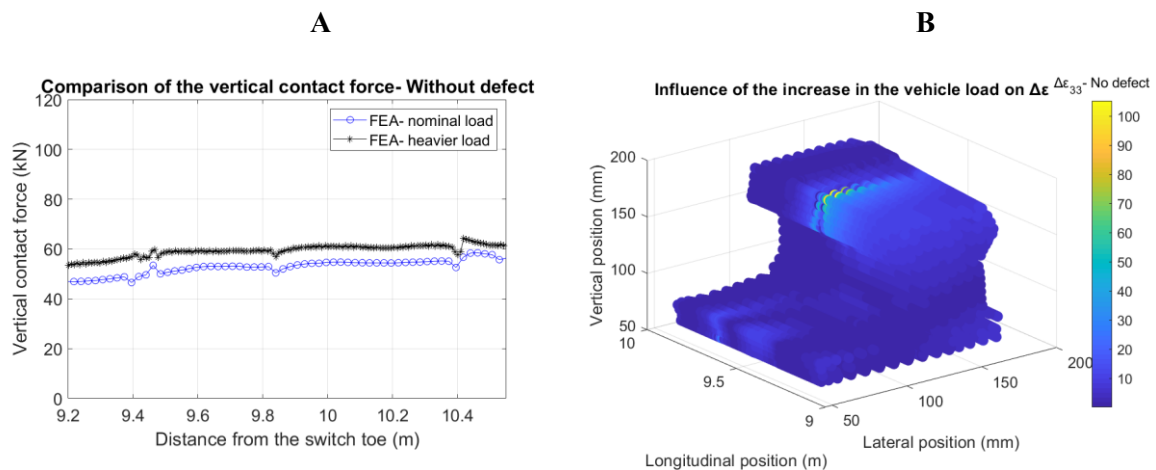
Figure 78: Change in the longitudinal strains due to fault introduction; (a) RCF damage; (b) Wear damage; (c) Voiding

5.3 Effect of modelling the different vehicle loads on the results for the wheel-rail interaction and subsurface rail strains

The axle load that is exerted by the Manchester Benchmark passenger vehicle has been increased by 20% to reflect the laden condition. In the examples that have been referred to in the literature, the axle load for a laden passenger vehicle has been presented as 17 to 40% heavier than its tare load [61]. For implementing an increase of 20% for the axle loads for the Manchester Benchmark passenger vehicle comprising one carriage, two bogies and four axles, only the mass of the carriage has been increased from 32000 to 40896 kg.

The influence of the axle load on the vertical wheel-rail contact forces, wheel displacement and subsurface rail strains will be described subsequently. The results will be compared against the ones that were obtained whilst implementing the lower amplitude of the axle load.

For the model without any track defects, the comparison of the vertical contact force in Figure 79A shows a higher amplitude of up to 10 kN when the vehicle load is increased. In Figure 79B,C, the influence of increasing the axle loads on the rail strains have been plotted. A difference of up to 400 $\mu\epsilon$ can be observed for the vertical strains (Figure 79C) than that of 100 $\mu\epsilon$ for the longitudinal strains (Figure 79B).



C

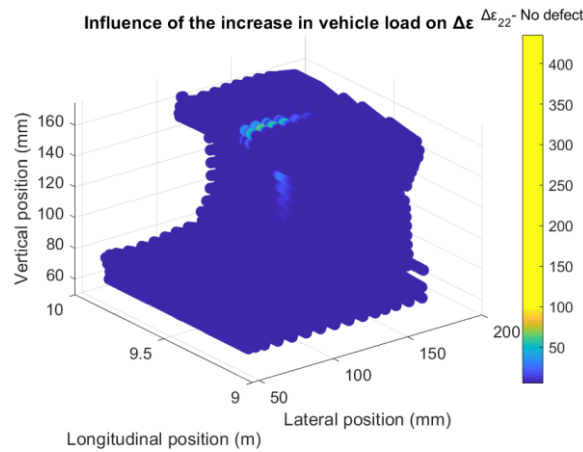


Figure 79: Influence of the increase in the vehicle load on the results for (A) Vertical wheel-rail contact force; (B) Longitudinal strains; (C) Vertical strains.

In Figure 80, a disturbance in the amplitude of the contact force can be observed at the location where the RCF defect was introduced, i.e. after a longitudinal distance of 9.45 m from the switch toe when both the nominal and heavier vehicle loads are modelled. The value for the contact force for both the nominal and heavier loads momentarily increase by 25% at the location of the wheel-rail squat impact. An average increase of 10 kN over nominal loading can be observed for the amplitude of contact force when laden conditions are implemented in the simulations. The change in the wheel load has also resulted in an increase of the vertical and longitudinal rail strains by up to 200 and 55 $\mu\epsilon$ respectively. It was shown in Figure 77 and Figure 78 that the change in nominal strain values was greater in the vertical than the longitudinal direction for the introduction of the squat.

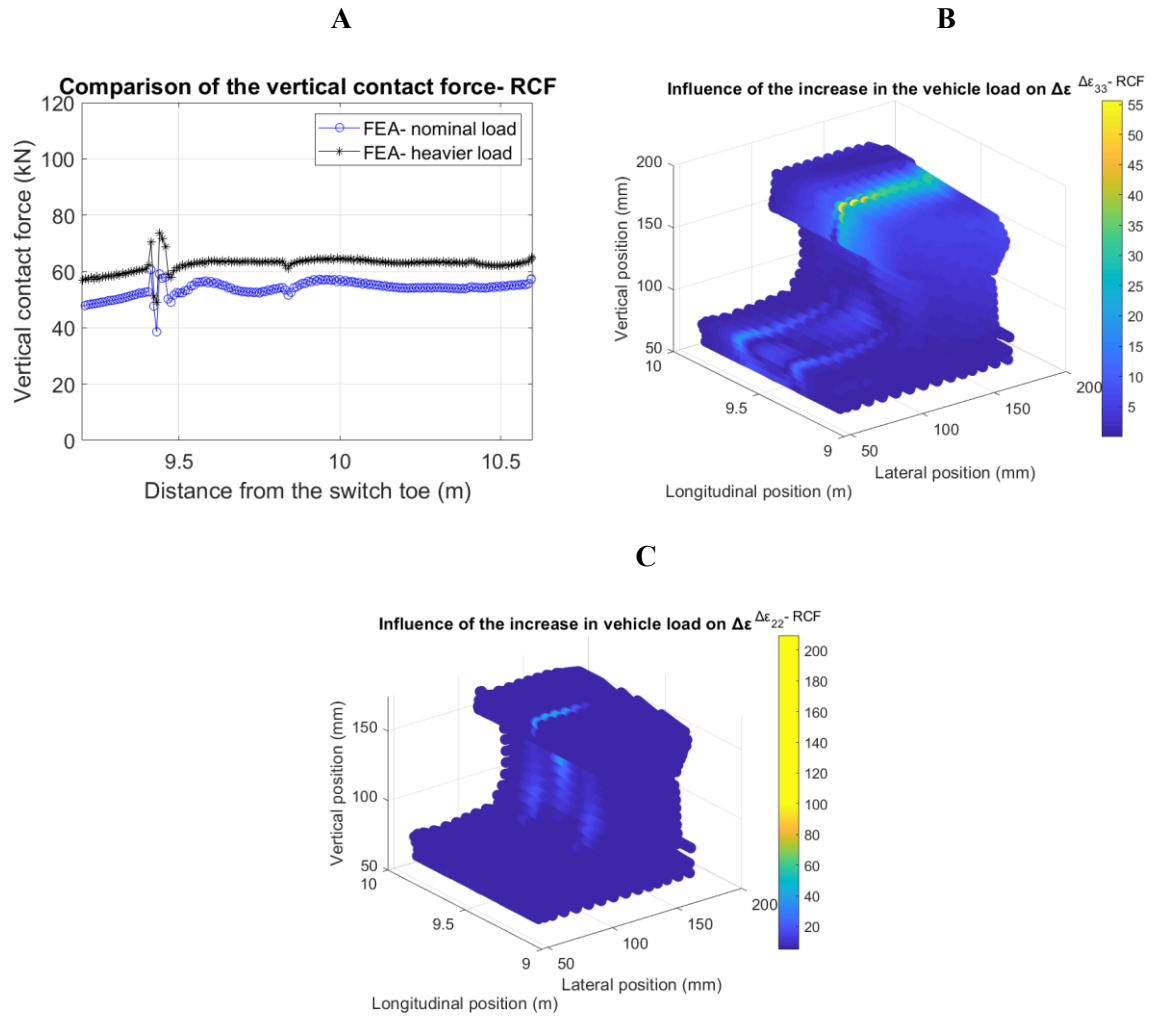
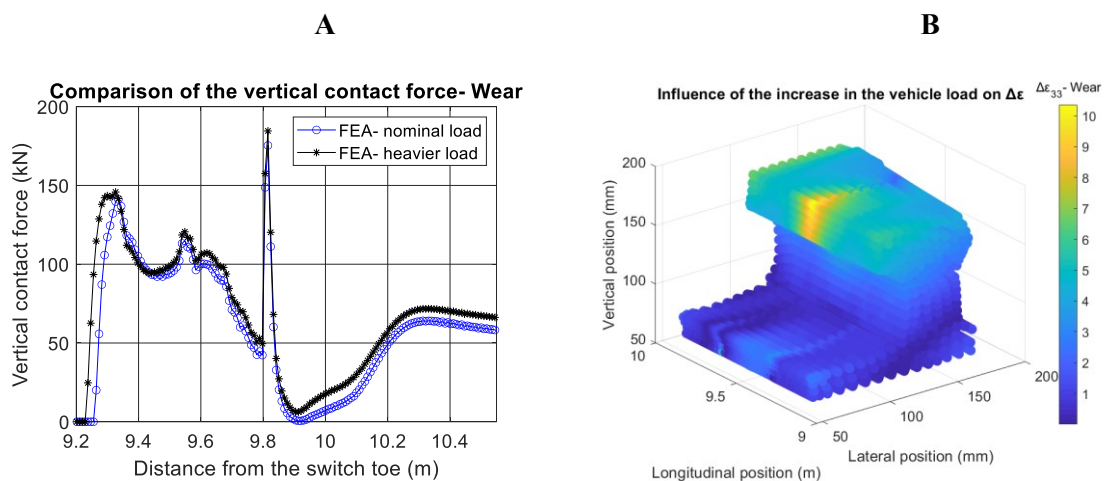


Figure 80: Influence of the increase in the vehicle load on the results for (A) Vertical wheel-rail contact force; (B) Longitudinal strains; (C) Vertical strains.

For the contact between the wheel and the switch rail in the presence of wear, Figure 81A shows the amplitude of the contact force to be zero up to a longitudinal position of 9.25 m. This is because the wheel loses contact with the worn rail at this position and is supported by the stock rail instead. This can be observed from the plot for the contact points on the stock and the switch rails in Figure 81D, where the lateral position of the surface element with the highest amplitude of the Von Mises stress at the relevant time steps have been plotted for the stock and switch rails. It can also be observed that when the wheel and the switch rail regain contact at a longitudinal position of 9.27 m, it is close to a

lateral position of 0 mm which is close to the centre of the switch rail. When the wheel and the switch rail regain contact, there is a sudden increase in the amplitude of the contact force in Figure 81A which exceeds 100 kN and is much higher than what is observed in the simulations that were carried out with no defect (Figure 79A). The contact point gradually moves away from the centre of the switch rail and towards the gauge corner. At the longitudinal position between 9.6 and 9.7 m, two contact points can be observed on the switch rail as well as the fluctuations in the contact force can be observed.

The change in strains for an increase in the wheel load when the wheel is in contact with the rail at a distance of 9.45 m from the switch toe has been plotted in Figure 81B,C. Since the difference in the vertical contact force and wheel displacement between the two models is negligible, the amplitude of the change in the longitudinal and vertical strains is also minimal. The change in the vertical and lateral strain is less than $10 \mu\epsilon$ and corresponds well with the plot showing minimal difference for the contact force between the nominal and heavier loads in Figure 79A. To restate the discussion in section 5.1, the results from this section are should not be considered as an accurate representation of how wear should occur along the turnout.



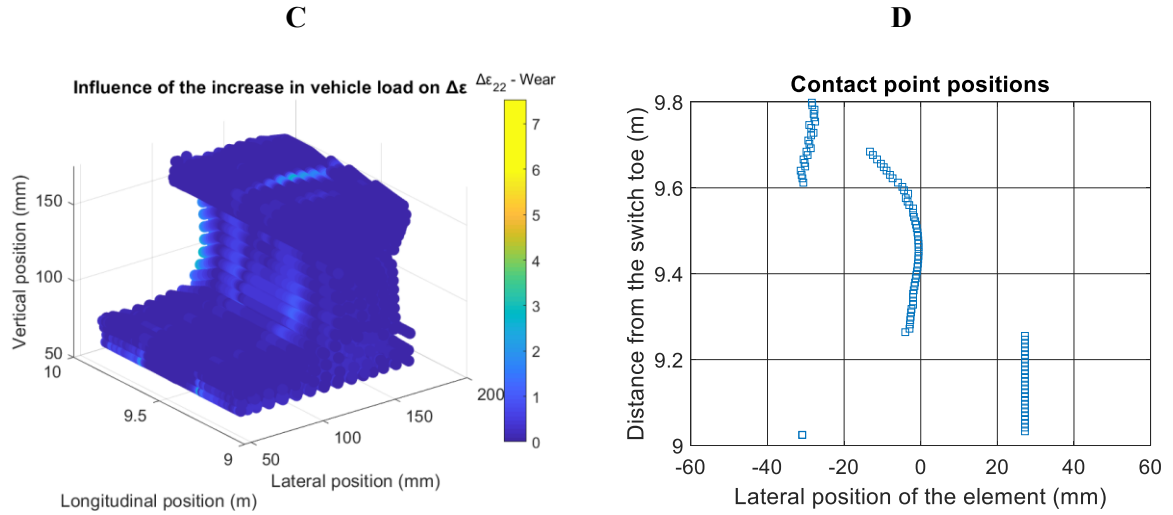


Figure 81: Influence of the increase in the vehicle load on the results for (A) Vertical wheel-rail contact force on the switch rail; (B) Change in longitudinal strains; (C) Change in vertical strains; (D) Contact point positions- nominal load

The result for the vertical wheel-rail contact force that has been obtained from the model with voiding (Figure 82A) shows that the amplitude of the wheel-rail contact force is higher at around 9.4 m, where track voiding was introduced than in the model with no defect (Figure 79A). Similar to the simulations with no defect and RCF, the passage of a vehicle with increased vehicle loads in the presence of voided sleepers will increase the amplitude of the vertical contact force by up to 10 kN as shown in Figure 82A. The plot for the change in the longitudinal and vertical strains have been plotted in Figure 82B and Figure 82C respectively. The change in the vertical strain due to increased vehicle loading is up to 100 $\mu\epsilon$, whereas for the longitudinal strain it is up to 130 $\mu\epsilon$. It is noteworthy that the amplitude for the change in the result for the longitudinal strain is higher than that for the vertical strains, whereas the converse is true for the simulations in the presence of wear and squat. This is potentially because increased vertical loading in the presence of voiding (reduced track stiffness) would result in increased longitudinal flexibility/bending of the rail.

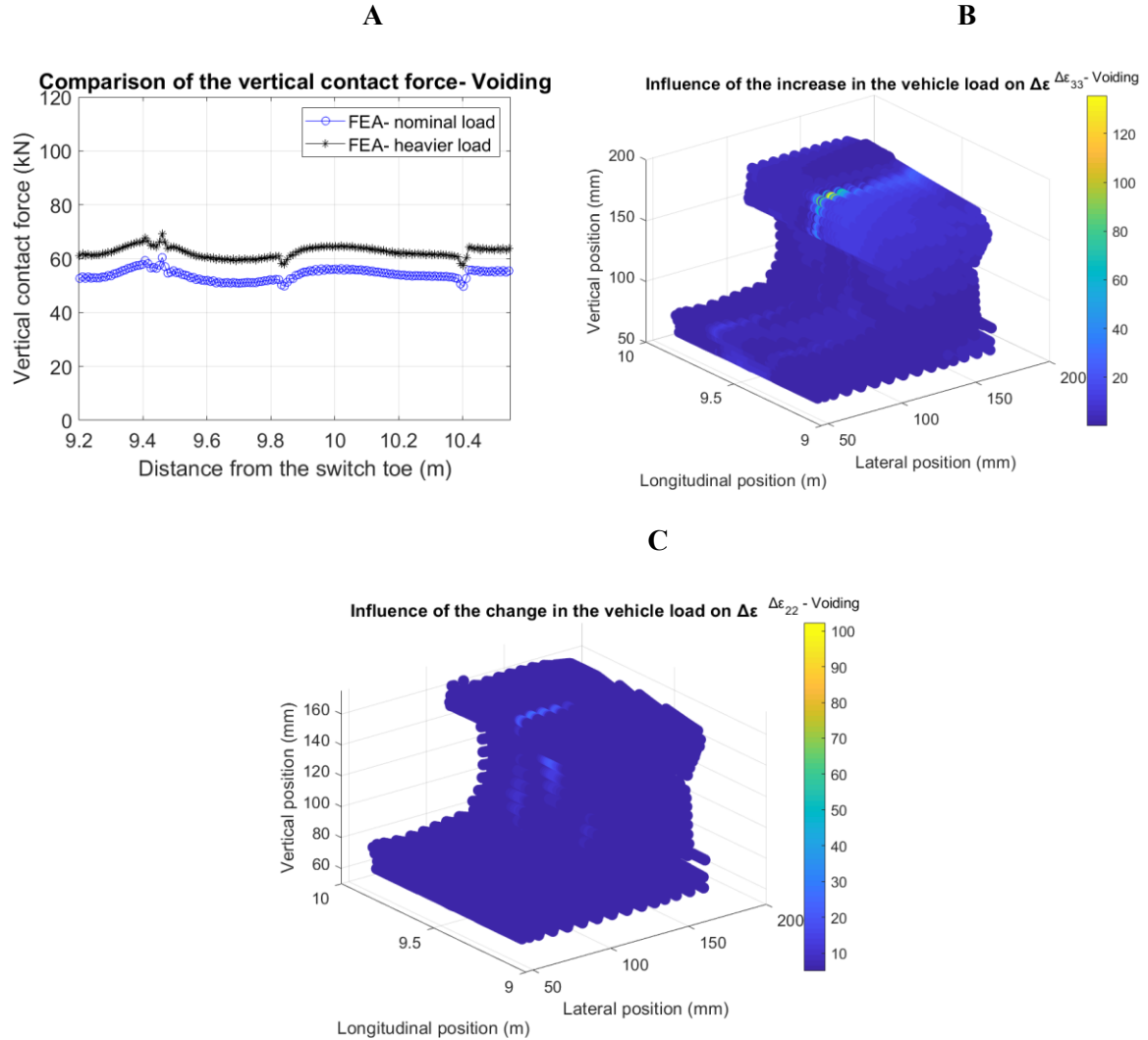


Figure 82: Influence of the increase in the vehicle load on the results for (A) Vertical wheel-rail contact force; (B) Vertical wheel displacement; (C) Change in the subsurface rail strains for the model with the voiding defect.

5.4 Conclusions from Chapter 5

In this Chapter, the mechanical behaviour of the track when it is subject to wheel-rail interaction simulations in the presence of defects was discussed. Three types of track defects were introduced, including wear, RCF and voiding. The locations on the switch rail where the Wear and RCF defects were introduced were estimated from the results for the Wear number that were discussed in Chapter 3.2. The RCF defect that was modelled is essentially a squat defect whose geometry is based on an

existing model that was presented in literature. Wear was modelled by linearly interpolating the permissible wear depth between zero and the maximum amplitude of the wear number. The maximum amplitude of the wear number was assumed to correspond to the maximum permissible wear depth that was obtained from literature review. Track voiding was introduced by reducing the vertical stiffness under three sleepers.

It is also worth remembering that the simulations have been carried out for specific instances of defect geometry and track voiding. The variation in the geometry, track properties will significantly vary the outputs from the simulations. However, it is also worth restating that the objective of the parametric case studies is to demonstrate the implementation of the modelling framework for preliminary studies on assessing the suitability of measuring strains for the condition monitoring of switches.

The outputs for the motion of the wheel and the forces that would act on it were obtained from the MBS simulations and then implemented in FEA. A change in the amplitude of the contact force at the location where the defects were introduced could be observed for all the models. On increasing the vehicle load from the tare load, an increase in the amplitude of the vertical contact force as well as higher values for the strains have been captured from the simulations with the defects. The results showed that disturbances are observed in the contact force where the defect was introduced and the amplitude of the rail strains also increased, demonstrating the potential of being implemented for condition monitoring.

In Chapter 6, the results for the vertical and longitudinal strains will be implemented for determining the locations for measuring the rail strains for detecting the defects that were introduced in this chapter.

CHAPTER 6.DETERMINING THE SENSOR PLACEMENT AND TESTING THE ABILITY OF FAULT DETECTION

The results from the simulations that were previously described in Chapters 4 and 5 will be implemented for determining the location for measuring rail strains for detecting the defects that were introduced into the model. The results for the strains that are induced in the switch rail on wheel-rail contact will be subject to correlation analysis with the impact force for determining whether there is a good relation between the two outputs to investigate the potential for condition monitoring by installing strain measurement sensors. The overall approach to determining sensor placement will be described in Section 6.1. The results that will be obtained without and in the presence of the defects will be compared for assessing the potential position for sensor placement in Sections 6.2 to 6.5.

The correlation between the wheel-rail impact force and the strain measurements at the proposed locations will be explored in Section 6.6 and the potential for fault detection will be discussed. Finally, the results presented in this chapter will be summarised in Section 6.7.

6.1 Approach to determining sensor placement

In Chapter 5, the parametric numerical simulations for the wheel-rail contact that were carried out with different track conditions and vehicle model setups were described. The track conditions were changed by introducing wear, RCF and voiding defects into the model. The vehicle model was modified to reflect a change in the carriage mass as well as the wheel-rail coefficient of friction.

As shown in Table 37, a total of 30 simulations have been carried out with different track and vehicle model setups. The simulations for the models with no defect, track voiding, wear and RCF have been carried out with three values for the coefficients of friction and two values for the axle loads.

The two main situations for which the placement of sensors have been determined include the detection of the defect in between the sleeper spacing and on the sleeper supported rail. As shown in Table 37, since the wear is introduced over a long length of the track, the execution of a simulation

would consider the presence of the wear defect on the switch rail in the sleeper-supported as well as sleeper spacing sections. However, two separate models have been implemented for modelling the RCF on and in between the sleepers. Therefore, 6 simulations from a single model will be enough for obtaining the results for all the case studies involving wear. Further, a total of 12 simulations from two different models have to be carried out for obtaining the inputs for all the case studies involving RCF. Since the voiding is only introduced under the sleeper, 6 simulations have been carried out. The total number of simulations are 30 but the total number of scenarios are 36 as shown in Table 37.

Table 37: List of the parametric studies that have been implemented for determining sensor placement

Vehicle load	Tare loads			Laden loads		
<i>Friction coefficient</i>	<i>0.2</i>	<i>0.3</i>	<i>0.4</i>	<i>0.2</i>	<i>0.3</i>	<i>0.4</i>
No defect	X	X	X	X	X	X
Wear (between sleepers)	X	X	X	X	X	X
Wear (on sleeper)						
RCF (between sleepers)	X	X	X	X	X	X
RCF (on sleeper)	X	X	X	X	X	X
Voiding (under 3 sleepers)	X	X	X	X	X	X

For obtaining the value of the Pearson correlation coefficient, it is suggested that the number of samples should exceed 25 [149,150]. Therefore, a sample size of 36 simulations would meet the criteria for performing the statistical analysis for sensor placement.

A reference sensor from the studies of condition monitoring of S&C on the West Coast mainline in the UK will be implemented as the benchmark for the assessment of strain results [39]. This sensor has a measurement range of $\pm 5\%$, frequency response of 8 kHz and the field experimentations had implemented a sampling rate of 16 kHz [39]. The results from field and laboratory experiments have shown that the sensor is able to reliably measure values over $5 \mu\epsilon$ [39]. The frequency response of the

sensor is four times higher than the sampling rate that has been implemented in the FEA. It was shown in Chapter 4.2.3 that the time series results of the vertical strains that are sampled at 2 kHz in the FEA are able to differentiate between the amplitude of the rail strains at the different vertical positions along the rail cross-section. Due to its higher frequency response, it is expected and assumed that the results from the sensor will be able to achieve the same, but will need to be further investigation and validation in the future.

A screening and ranking approach has been adopted for determining the best locations for placing the sensors. Screening essentially refers to filtering out the locations, i.e. the elements that are unable to meet a constraint. A constraint is essentially a non-negotiable restriction on a property.

The screening step would set a constraint on the minimum amplitude of the change in the strain that would need to be captured for fault detection. Thereby, the locations on the rail where the change in strain on the introduction of the defects is at least equal to the resolution of the sensor ($5\mu\epsilon$) will be retained as the candidate locations [39]. The change in strain can be obtained by subtracting the amplitude of the strain for the model with no defect from the model with the defect. The condition for the screening step for obtaining the locations that can detect the RCF, Wear and Voiding defects has been represented in *Equation 13*, *Equation 14* and *Equation 15* respectively and the abbreviated components of the equation have been explained in Table 38.

$$\Delta\epsilon_{2jk} = \epsilon_{2jk} - \epsilon_{1jk} \geq 5\mu\epsilon \quad \text{Equation 13}$$

$$\Delta\epsilon_{3jk} = \epsilon_{3jk} - \epsilon_{1jk} \geq 5\mu\epsilon \quad \text{Equation 14}$$

$$\Delta\epsilon_{4jk} = \epsilon_{4jk} - \epsilon_{1jk} \geq 5\mu\epsilon \quad \text{Equation 15}$$

This difference will be obtained from the simulations that have been carried out under similar conditions, i.e. for the same vehicle type (axle load) and friction coefficient. The candidate locations for installing the sensor will therefore be determined for the results from every single scenario.

The type of defect, vehicle and the wheel-rail friction coefficient that have been implemented in the simulations have been presented in Table 38. As highlighted in Chapter 5, voiding was introduced under three sleepers that lie just before the sleeper spacing where wear and RCF were introduced. However, additional results were later generated from the simulations where wear and RCF were introduced on the section of the railhead which is supported by the sleeper. Those results have been implemented for testing the ability of the strains to derive the impact force to detect the defect at the proposed sensor locations.

Table 38: Different variables in the simulations

Notation	Value	Meaning
Fault type (i)	1	No fault/nominal rail profile
	2	RCF (on or between sleepers)
	3	Wear (on or between sleepers)
	4	Voiding
Vehicle type (j)	1	Passenger vehicle with tare load
	2	Laden passenger vehicle
Wheel-rail friction coefficient (k)	1	0.2
	2	0.3
	3	0.4

The results will be organised in a way that the impact of the independent variables that have been listed in Table 38 can be assessed.

Firstly, the placement of sensors for detecting one type of defect for the different values of the coefficient of friction for the same axle load will be determined. Thereby, the locations for installing sensor that will be able to detect particular defects on the passage of the lighter and the heavier vehicles will be obtained.

Secondly, an intersection of the locations that can detect the defect on the passage of the rolling stock with lighter as well as heavier axle loads will be obtained. Thereby, all the candidate locations will be able to detect the individual defect for the passage of all types of simulated rolling stock under all the simulated wheel-rail contact conditions.

Subsequently, the locations that are able to detect the presence of surface defects, i.e. wear and RCF on the passage of all kinds of simulated rolling stock and wheel-rail contact conditions will be obtained. Finally, the sensor locations that are able to detect the surface defects as well as voiding under the sleeper will be obtained.

Once the locations have been screened, they will be ranked with the objective of maximising the change in strains. The locations that will obtain a high amplitude for a change in strain will also be more likely to detect a defect than a location where the sensor placement will demonstrate a low amplitude for the change in strains. Therefore, for each of the candidate locations, the mean value for the change in strains will be calculated. The value for the change in strain will be determined by obtaining the difference between the strain that is captured at the candidate location with and without the defect. For the results from all the scenarios, it will be obtained when the wheel is in contact with the rail at the same longitudinal position, which would simplify the study pertaining to the detection of multiple defects at the same location. The mean value for the change in the strains is the average that has been calculated from the individual values for the change in strains that will be obtained from each scenario.

Under this approach to determining sensor placement, the best location for placing the sensor for detecting different surface defects will be based on obtaining the location that has the highest mean amplitude for the change in strains. However, if this location is expected to be near the railhead, then it will be impractical to install the sensors as they will be susceptible to damage. Since a detailed optimisation exercise is beyond the scope of the current work, the high-ranking locations that are closer to the rail web or the foot will be prioritised for sensor placement.

The best locations for placing the sensors for detecting each defect will be first determined from *Equation 16* by calculating the mean change in strains from all the simulations/scenarios that are associated with that defect for the elements that successfully passed the screening steps.

$$\text{Best elements} = \text{maximum}(\overline{\Delta\varepsilon_{2jk}}, \overline{\Delta\varepsilon_{3jk}}, \overline{\Delta\varepsilon_{4jk}}) \quad \text{Equation 16}$$

Subsequently, the best locations for placing the sensors for detecting all the defects will be determined from the overall mean of the change in strains on the passage of railway vehicles over the faults under different circumstances as highlighted in *Equation 17*. Future work could include a more sophisticated analysis of the trade-off between the fatigue, plastic deformation and the change in strains that will be considered for ranking the candidate sensor placement locations.

$$\text{Best elements} = \text{maximum}(\overline{\Delta\varepsilon_{2jk}}, \overline{\Delta\varepsilon_{3jk}}, \overline{\Delta\varepsilon_{4jk}}) \quad \text{Equation 17}$$

Following the ranking procedure, the results for the strains that are obtained from the best candidate locations will be analysed for correlation with the wheel-rail impact force. This will help determine whether the results for the impact force can be accurately determined from the sensors that are installed at the proposed location for implementation in damage detection models. As the range of the reference strain sensor range is $\pm 5\%$, the assessment of the location for installing the sensor will be based on achieving a minimum difference of $\pm 10\%$ between the results for the value of the rail strains from the simulations with no defect and simulations with wear/RCF/voiding.

The screening and the ranking steps for determining the sensor placement for detecting the presence of the surface rail defects over an unsupported section of the rail in the sleeper spacing will be discussed in sections 6.2 and 6.3. The determination of sensor placement for detecting the surface defects occurring on a sleeper-supported rail section will be discussed in section 6.4. On recognising the longitudinal positions for installing the sensors, the results for the strains for the rail cross-section at the proposed longitudinal position will be discussed in section 6.5. Finally, the potential ability of the

sensor measurement at the proposed placement locations to detect the defect will be discussed in section 6.6.

6.2 Results from the Screening step when the wheel-rail contact results are captured where the surface rail defects are introduced in the sleeper spacing

The location of the defect would significantly influence the results for the amplitude of the strain and thus the sensor placement. The influence of the coefficient of friction on the sensor placement is less significant than the change in the axle load. Therefore, the results for the change in strain on introducing the defects have been discussed for the simulations that were carried out whilst implementing a friction coefficient of 0.3. The results that are obtained on implementing both the tare and laden axle loads have been discussed. It is important to note that the results have been obtained in this case at the time step when the wheel is in contact with the defective track at the centre of the sleeper spacing at 9.45 m from the switch toe. The surface wear and RCF defects are present at the location where the wheel is in contact with the rail. Voiding in the form of reduced ballast stiffness has been introduced under 3 sleepers preceding this location. Since the determination of sensor placement for detecting the presence of the defects on sleeper-supported rail is equally important, it will be discussed separately in section 6.4.

Presently for the results extracted from the sleeper spacing, the results that have been obtained from the simulations for the RCF model with a wheel-rail friction coefficient of 0.3 have been plotted in Figure 83. The number of candidate locations that meet the screening requirements are the lowest for the measurement of the change in the lateral strains ($\Delta\epsilon_{11}$), as shown in Figure 83 A,B.

For both the tare and the laden loads, the measurement of vertical strain at the rail web will have a high probability of capturing the defect. It can be observed in Figure 83 C,D that more locations can capture at least the required amount of the change in the vertical strain on the passage of the heavier load and values of up to 700 $\mu\epsilon$ and 200 $\mu\epsilon$ have been achieved on the rail head and web respectively. The locations that are able to detect the change in vertical strain ($\Delta\epsilon_{22}$) are spread over a longer length

of the track when the results on implementing the laden load are compared against the results that are obtained from the tare load. The same can be observed for the change in the longitudinal strain ($\Delta\epsilon_{33}$), where a change in the strain value of up to 70 $\mu\epsilon$ and 140 $\mu\epsilon$ are observed for the tare and laden conditions respectively.

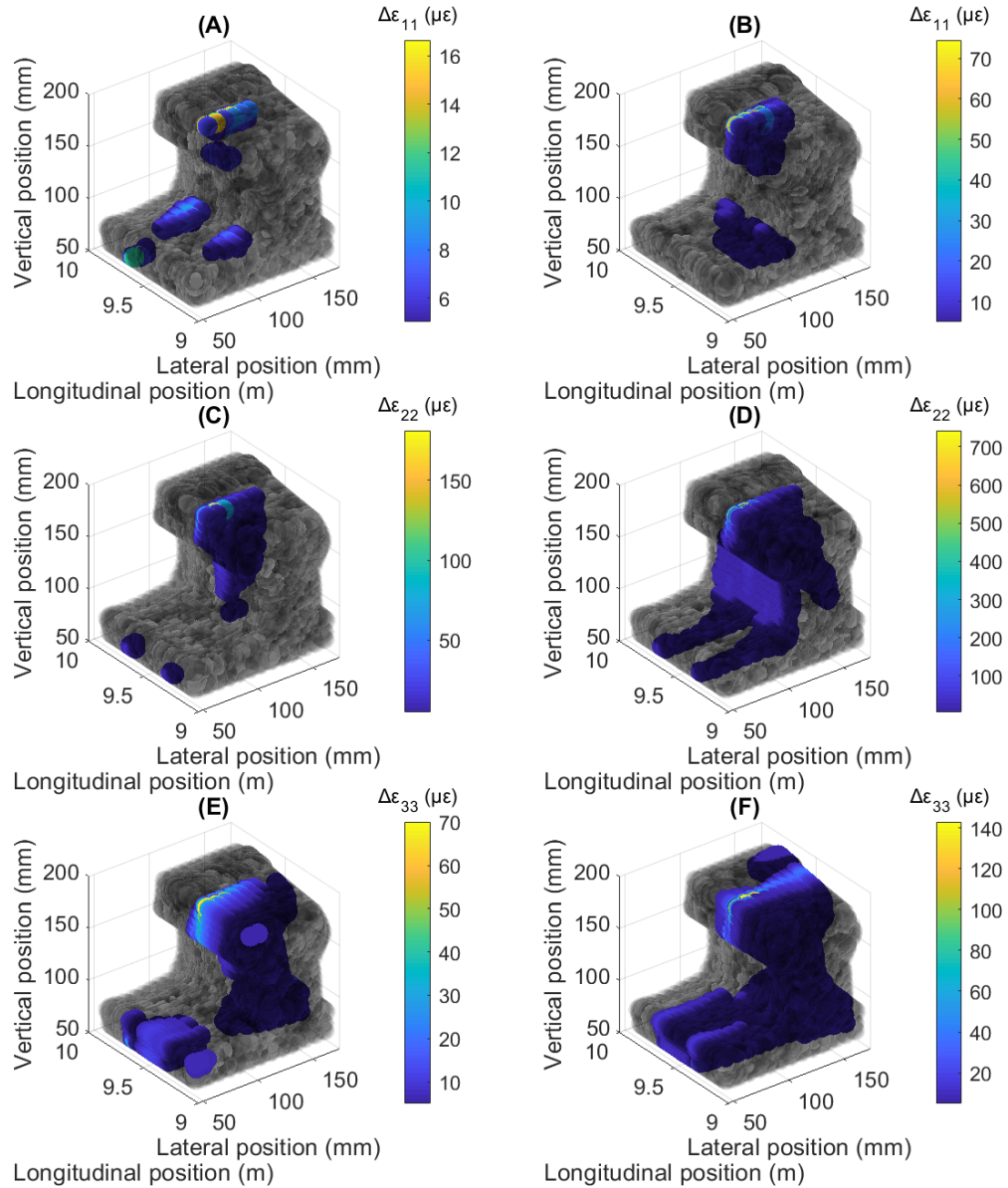


Figure 83: Locations that meet the screening constraints for detecting the presence of the modelled RCF defect; (A) Lateral strains and tare load; (B) Lateral strains and heavier load; (C) Vertical strains

and tare load; (D) Vertical strains and laden load; (E) Longitudinal strains and tare load; (F)

Longitudinal strains and laden load.

Similarly, the change in the strain for the model where the wear was introduced has been presented in Figure 84. The change in the lateral strain has been plotted in Figure 84 A, B and it can be observed that more locations have been able to pass the screening step for the model with the wear than in the RCF model. However, the number of elements/locations that can meet the screening constraints are roughly the same for the results obtained from the passage of the wheel loaded with either the tare or the heavier loads for the wear model. As shown in Figure 84 E,F, a large number of locations are able to capture a change in the longitudinal strains for detecting the wear defect when compared to the results from the model with the RCF defect. A change of up to $120\ \mu\epsilon$ can be observed for the strain in the lateral direction when compared to the simulations that were carried out with no defect. In the vertical and longitudinal directions, this change is up to $800\ \mu\epsilon$ and $150\ \mu\epsilon$ respectively.

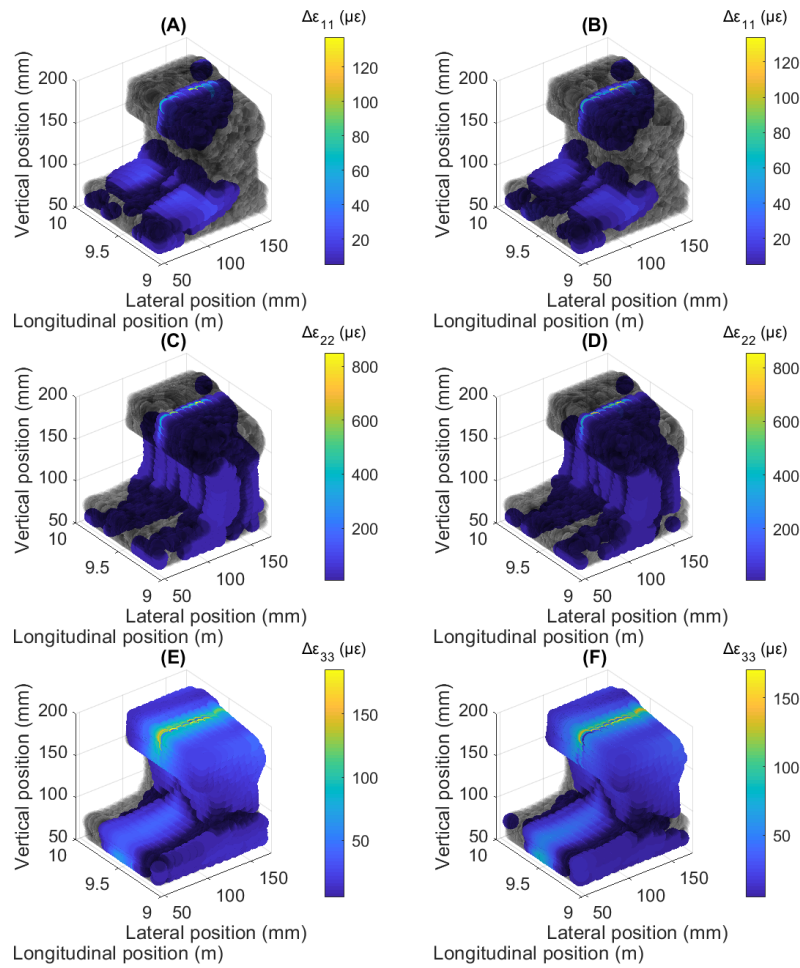


Figure 84: Locations that meet the screening constraints for detecting the presence of the modelled wear defect; (A) Lateral strains and tare load; (B) Lateral strains and heavier load; (C) Vertical strains and tare load; (D) Vertical strains and laden load; (E) Longitudinal strains and tare load; (F)

Longitudinal strains and laden load.

The results from the screening step for the model with the voiding defect have been plotted in Figure 85. Although the presence of voiding is under the sleeper, the results in this case have been obtained on the passage of the wheel at the location between the sleepers. The objective of this exercise is to examine whether the passage of the wheel over the same longitudinal rail position will be able to detect all the introduced defects. It can be observed in Figure 85 A,B that the measurement of the lateral strains shows a rather low potential for the detection of voiding. The maximum value for the

change in strain does not exceed $35 \mu\epsilon$ for the tare condition and this value is also achieved closer to the railhead. In Figure 85 C,D, it can be observed that the detection of the vertical strains will still present considerable potential for detecting the presence of voiding, with the value for the change in strain reaching up to $150 \mu\epsilon$ for the tare condition. The highest number of candidate locations is obtained for the measurement of the strains in the longitudinal direction as shown in Figure 85 E,F, which is over a length of 1 m and achieving a change in strain of up to $120 \mu\epsilon$ for the tare condition.

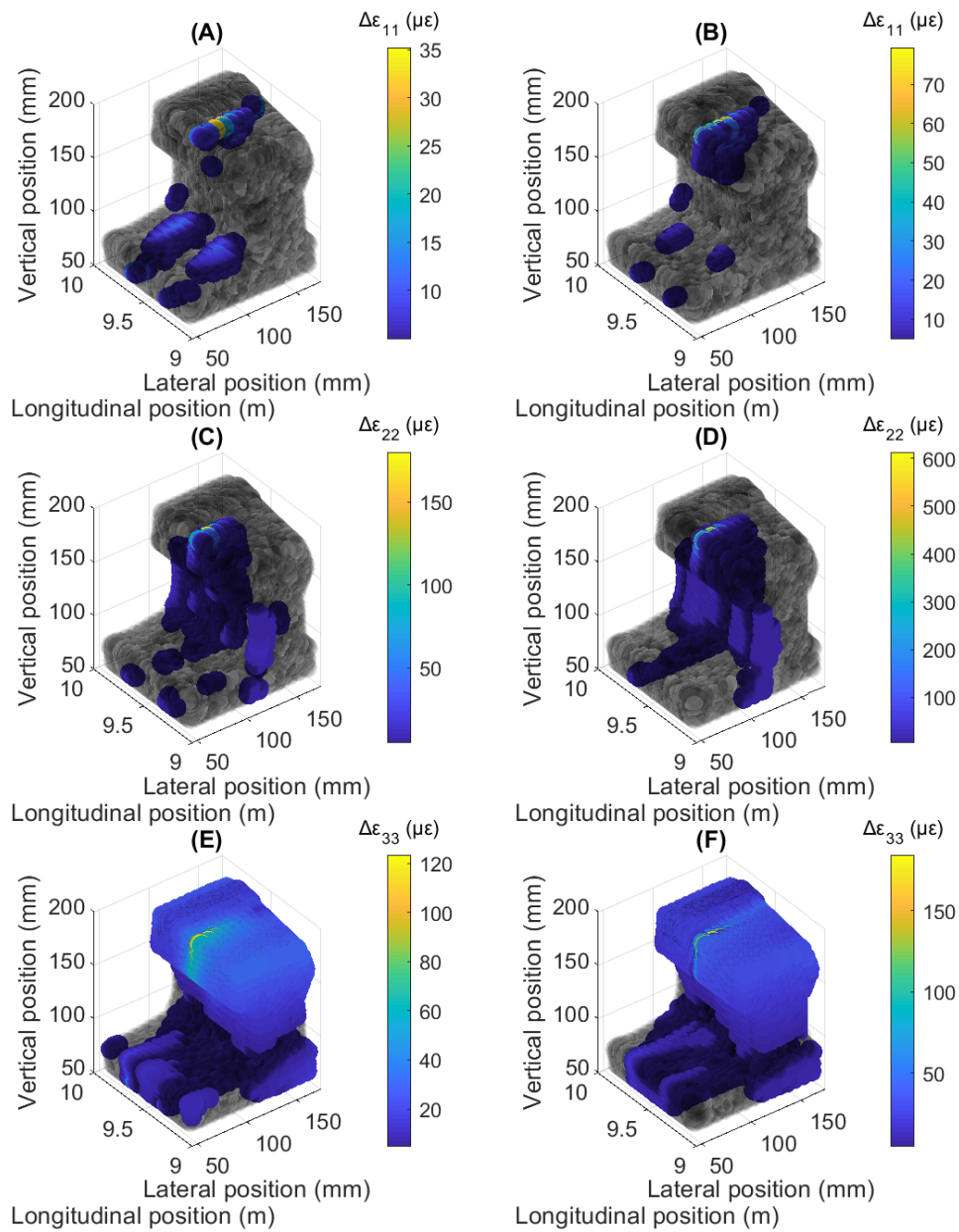


Figure 85: Locations that meet the screening constraints for detecting the presence of the modelled voiding defect; (A) Lateral strains and tare load; (B) Lateral strains and heavier load; (C) Vertical strains and tare load; (D) Vertical strains and laden load; (E) Longitudinal strains and tare load; (F) Longitudinal strains and laden load.

6.3 Ranking the locations for determining the placement of sensors for the detection of the defect when the wheel-rail contact results are captured in the sleeper spacing

The locations that passed screening in section 6.2 and show a high potential for detecting the defects that have been introduced into the model have been ranked. In Figure 86, the locations that are ideal for sensor installation for detecting the RCF defect that would occur on the rail along the centre of the sleeper spacing have been ranked. The locations that will be able to capture the difference in strains for detecting the RCF defect have been filled with the colours that are represented on the colour bar. The colour bar indicates the mean change in the strain at the proposed sensor placement location. As described earlier, the mean change in strain is the average of the change in strains that have been obtained from each case scenario. The locations that show the highest amplitude for the change in strains also have the highest potential for fault detection. However, other practical considerations such as the required distance from the railhead would need to be considered for the practical implementation of the sensor measurements.

Figure 86 A shows the locations where the sensor can be installed for detecting the lateral strains for detecting the RCF defect that was introduced between the sleepers. The number of proposed locations as well as the amplitude for the change in strain is rather less, not exceeding $45 \mu\epsilon$ on the railhead, which would reduce the probability of fault detection and make the measurement of the lateral strains less desirable.

Figure 86 B ranks the locations where the sensor can be installed for measuring the vertical strains to detect the RCF defect. The proposed locations are concentrated on the track side of the rail. The

locations that are away from the wheel-rail contact interface but are still able to effectively capture the change in strains are on the web of the rail, with certain positions on the rail web capturing a change of more than $40 \mu\epsilon$. A location that can capture an effective change in the strain due to RCF introduction will be suited for installing the strain sensor.

Figure 86 C shows the locations where the sensor can be installed for detecting the longitudinal strains for detecting the RCF defect. The intersection of the results from all the simulations has presented a list of robust candidate locations with a high potential for detecting the introduced defect. The suggestions for sensor placement involve locations that are spread around the vicinity of the location where the defect was introduced. It can also be observed that the longitudinal strains can either be detected at the rail head or foot, with values for the change in strain of up to $100 \mu\epsilon$ on the railhead. As the locations near the rail foot are away from the wheel-rail contact interface, they would be ideal for installing the strain sensor in the longitudinal orientation. However, the average value for the change in strain is lower at $20 \mu\epsilon$.

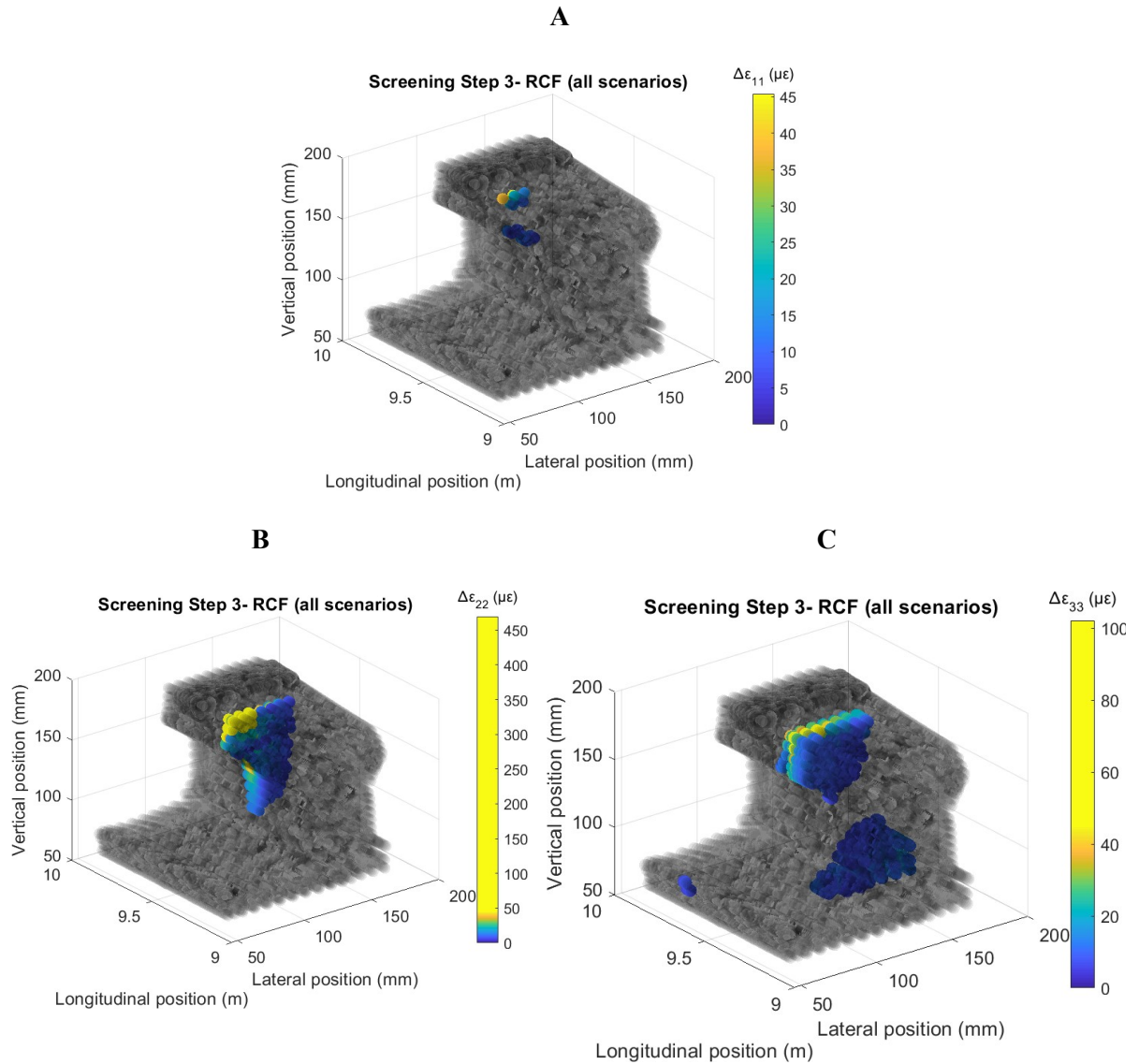


Figure 86: Intersection of the locations from all simulations for detecting the RCF defect; (A) Lateral strains; (B) Vertical strains; (C) Longitudinal strains.

Similarly, the proposed sensor placement locations for detecting the presence of wear between the sleepers have been plotted in Figure 87.

As shown in Figure 87A, the potential for the detection of wear by measuring the lateral strains is low. In Figure 87B, the locations where the sensor can be placed for detecting the vertical strains have been plotted. Again, with a strain change of up to 70 $\mu\epsilon$, the locations on the rail web on the track side present good potential for the detection of wear and they are also reasonably away from the wheel-rail contact interface.

The locations that will potentially be able to capture the longitudinal strains for fault detection have been plotted in Figure 87C. It can be observed that the number of elements/locations where the longitudinal strains can be measured for detecting the wear defect is more than the RCF defect. In addition, it is advisable to place the sensor away from the rail head for detecting the defect, which would make the rail foot an ideal choice. The value for the change in strain is up to $100 \mu\epsilon$ at this position.

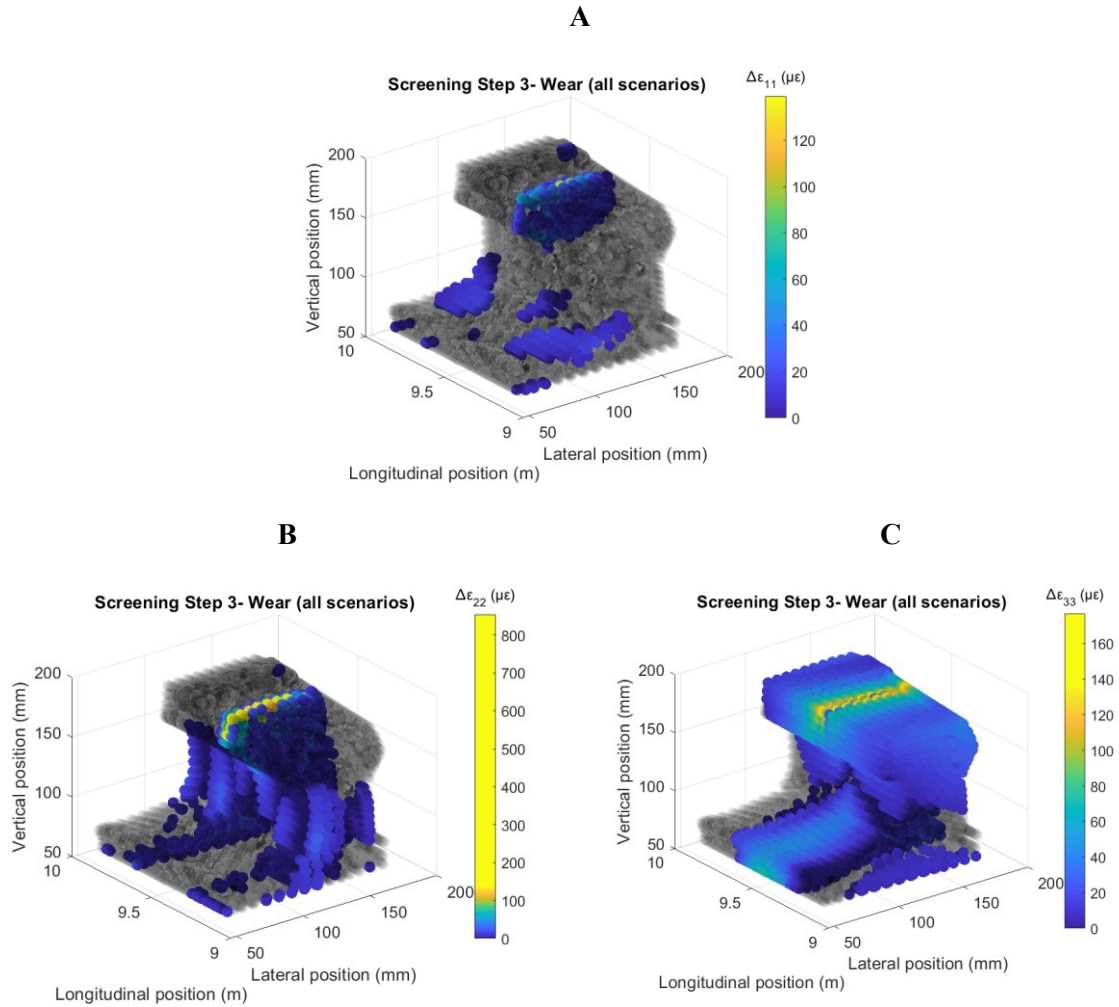


Figure 87: Intersection of the locations from all simulations for detecting the wear defect; (A) Longitudinal strains; (B) Vertical strains; (C) Lateral strains.

The proposed locations for placing the sensor for detecting the voiding defect when the wheel passes over the wear/RCF defect positioned between the sleepers has been plotted in Figure 88. The voiding

defect has been introduced under the sleeper and the position of the wheel for the visualisation of results in Figure 88 is in between the sleeper spacing.

It can be observed from Figure 88A that the choice for sensor placement for detecting the lateral strains is quite low.

In contrast, Figure 88B shows that the number of locations for detecting the fault through the measurement of vertical strains is a bit higher, with a strain change of up to $50 \mu\epsilon$ being achieved on the rail web. Figure 88C shows a large candidate pool for placing the sensors for detecting the longitudinal strains. However, the amplitude for the mean change in strains is much higher for the vertical strains on the web than the longitudinal strains on the foot, which does not exceed $25 \mu\epsilon$.

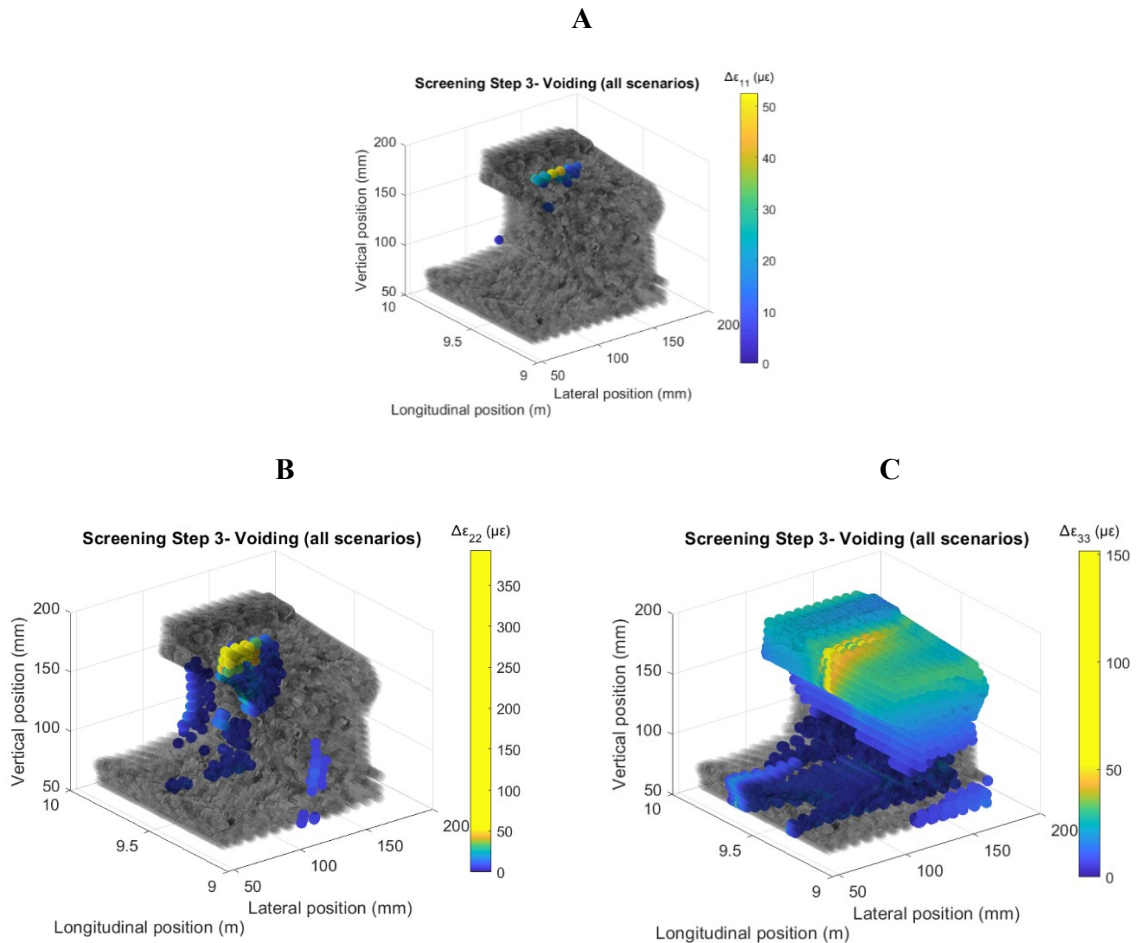


Figure 88: Intersection of the locations from all simulations for detecting the voiding defect; (A) Longitudinal strains; (B) Vertical strains; (C) Lateral strains.

Figure 89 shows the locations where the sensors can be installed for the detection of the surface defects that were introduced on the section of the rail in the sleeper spacing for all scenarios. As shown in Figure 89A, there are very few locations where the sensors can be installed in the lateral orientation, making the measurement of the lateral strains an impractical solution.

In the vertical orientation, the locations where the sensors can be installed has been shown in Figure 89B. The vertical sensors can be installed on the rail web on the track side for detecting the presence of the surface defects, achieving an average strain change value of 50 $\mu\epsilon$. Figure 89C shows the locations where the sensors can be installed in the longitudinal orientation. They can either be installed on the rail head or the rail foot, with the rail foot being more practical for implementation as it will ensure the physical integrity of the sensor. At this position, an average strain change value of up to 30 $\mu\epsilon$ has been achieved.

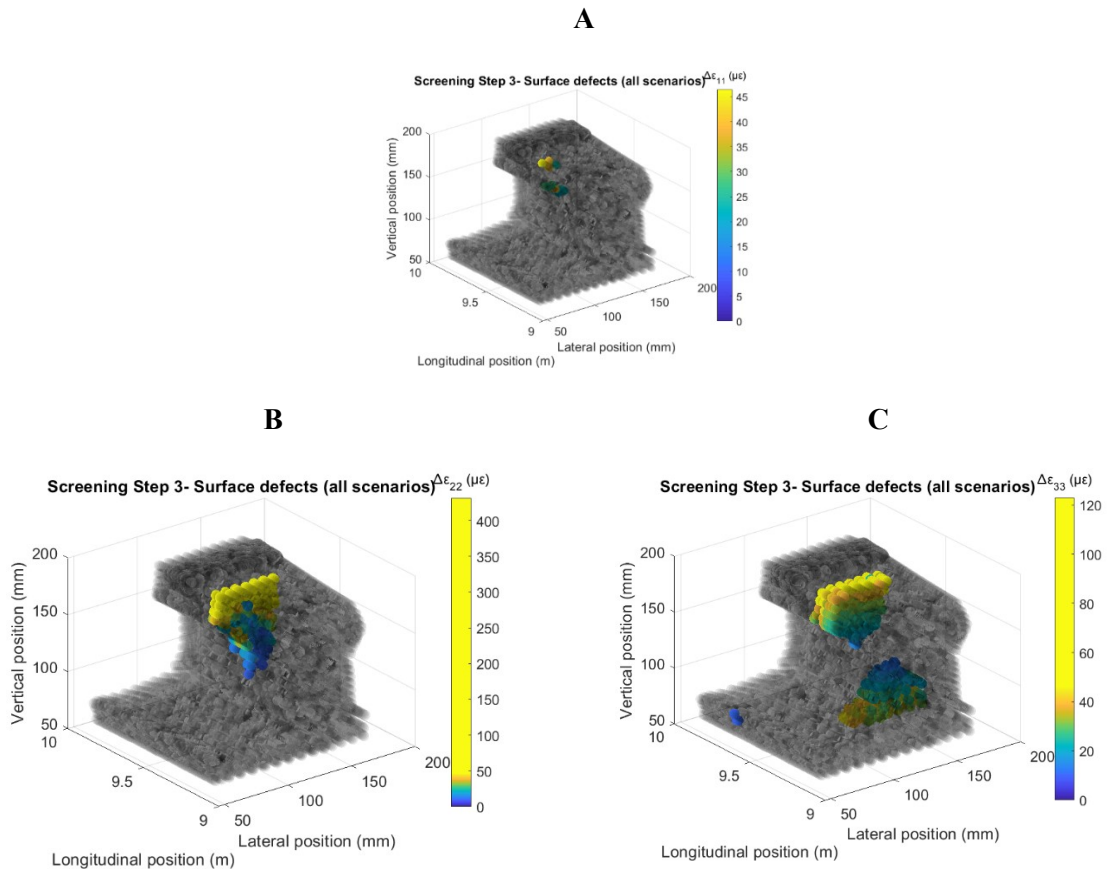


Figure 89: Intersection of the locations from all simulations for detecting the surface defects; (A)

Longitudinal strains; (B) Vertical strains; (C) Lateral strains.

Figure 90 shows the locations where the sensor can be installed for detecting the surface defects that were introduced on the rail in the sleeper spacing as well as voiding. Figure 90A confirms that the installation of a single sensor for detecting the lateral strains is not a feasible option for the detection of all the defects. Figure 90B shows the locations where the sensors can be installed for measuring the vertical strains to detect all the defects. A lower number of candidate locations are obtained for the results for all defects than those for surface defects. Figure 90C shows the locations where the longitudinal sensor can be installed for detecting all the defects. The sensors can either be installed at the rail head or the foot in the longitudinal orientation. The average vertical strain change on the web is $30 \mu\epsilon$ and the similar value has been achieved for the average longitudinal strain change on the foot.

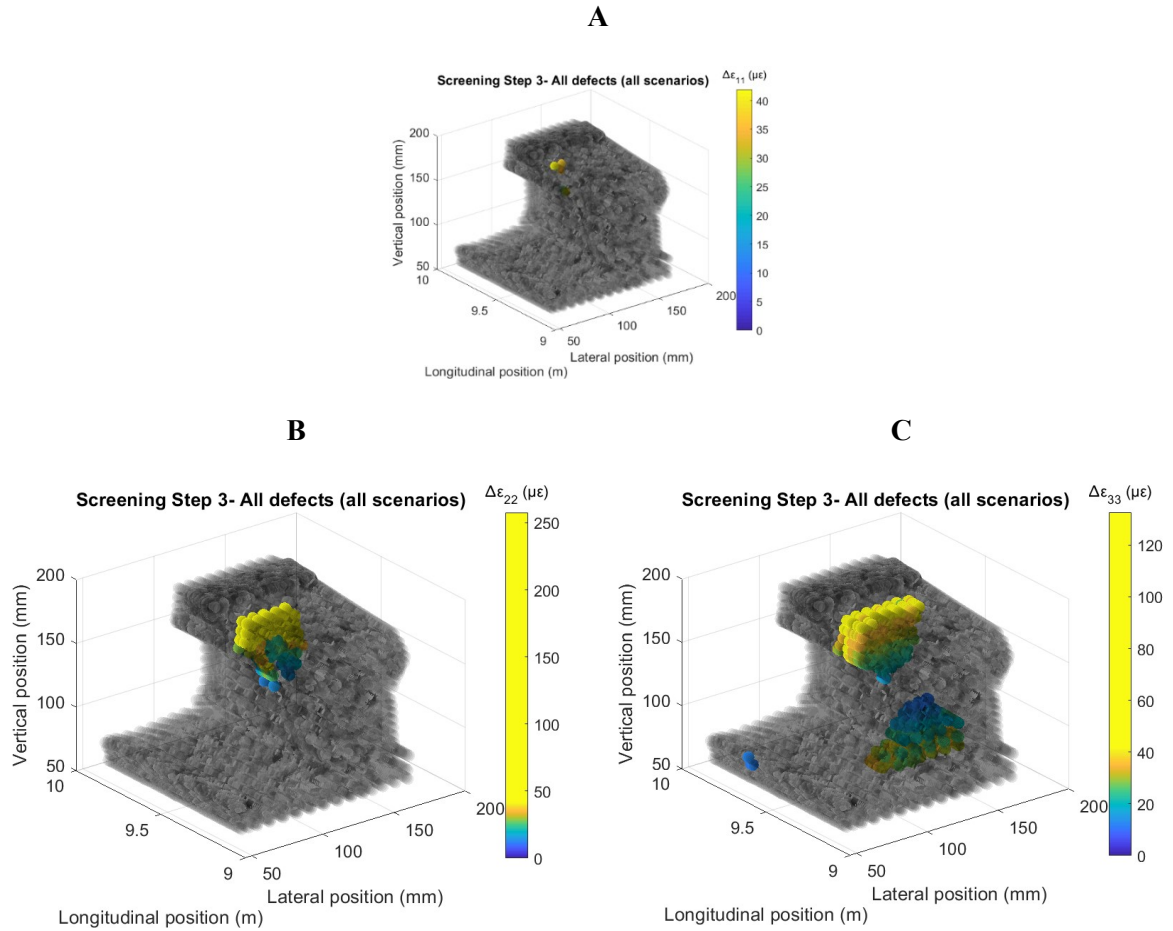


Figure 90: Intersection of the locations from all simulations for detecting all the simulated defects; (A) Longitudinal strains; (B) Vertical strains; (C) Lateral strains.

6.4 Determining sensor placement for monitoring the development of the defect at the sleeper-supported rail section

The approach that was explained in Section 6.1 was also implemented for determining the sensor placement for detecting the presence of the defect on the sleeper. Only the results for the vertical and the longitudinal strains have been shown because the installation of sensors for measuring the lateral strains shows a very low potential for condition monitoring. Figure 91A,B show the locations for measuring the vertical and the longitudinal strains respectively for detecting the presence of the wear on the sleeper. A good number of potential candidate locations have been obtained. The average vertical strain change on the web is $130 \mu\epsilon$ and the same for the longitudinal strain on the foot is $50 \mu\epsilon$.

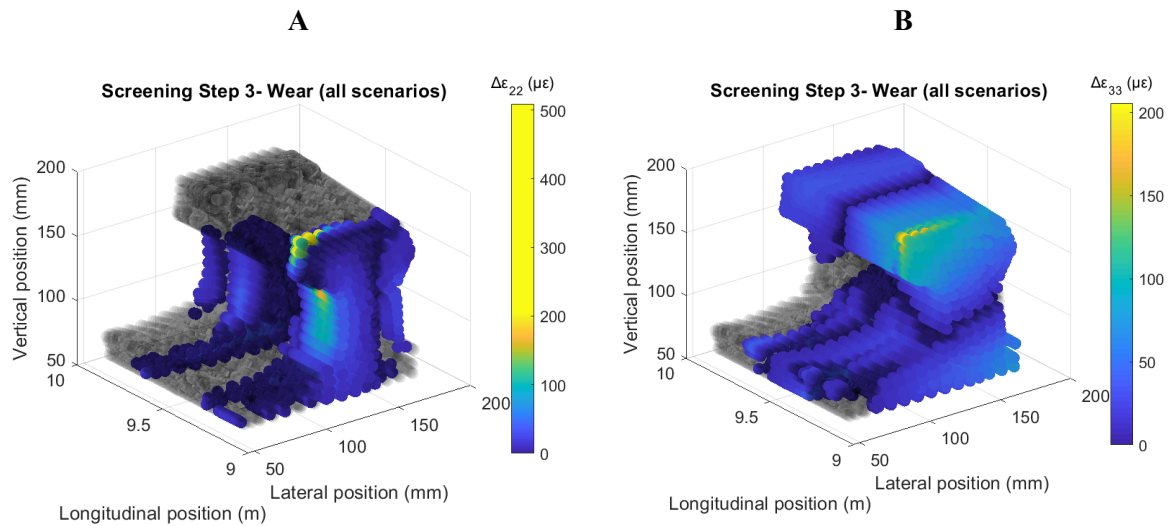


Figure 91: Intersection of the locations from all simulations for detecting the Wear defect on the sleeper; (A) Vertical strains; (B) Longitudinal strains

Figure 92 shows the potential locations where the sensors can be installed for detecting the RCF defect on the sleeper. The number of candidate locations are slightly less than the ones for detecting the Wear defect that were shown in Figure 91. The average vertical strain change on the web is $100 \mu\epsilon$ and the same for the longitudinal strain on the foot is $50 \mu\epsilon$.

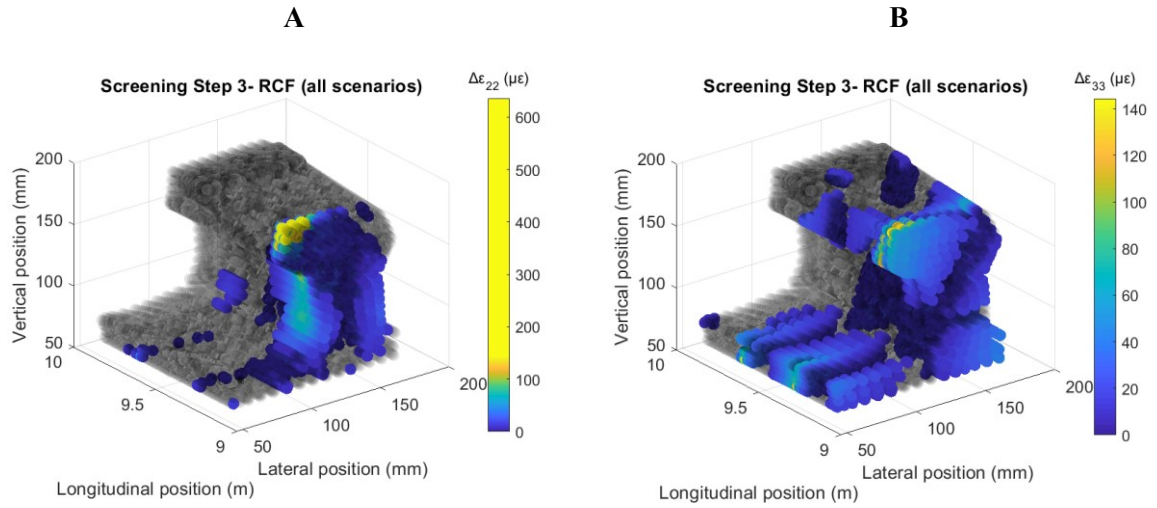


Figure 92: Intersection of the locations from all simulations for detecting the RCF defect on the sleeper; (A) Vertical strains; (B) Longitudinal strains

Interestingly, the number of candidate locations that have been obtained for detecting the voiding defect is lesser than that for detecting the wear and RCF defects as shown in Figure 93. The potential reason for this will be explained in more detail in Section 6.7, where the results for the strain distribution from the cross-section of the rail will be discussed.

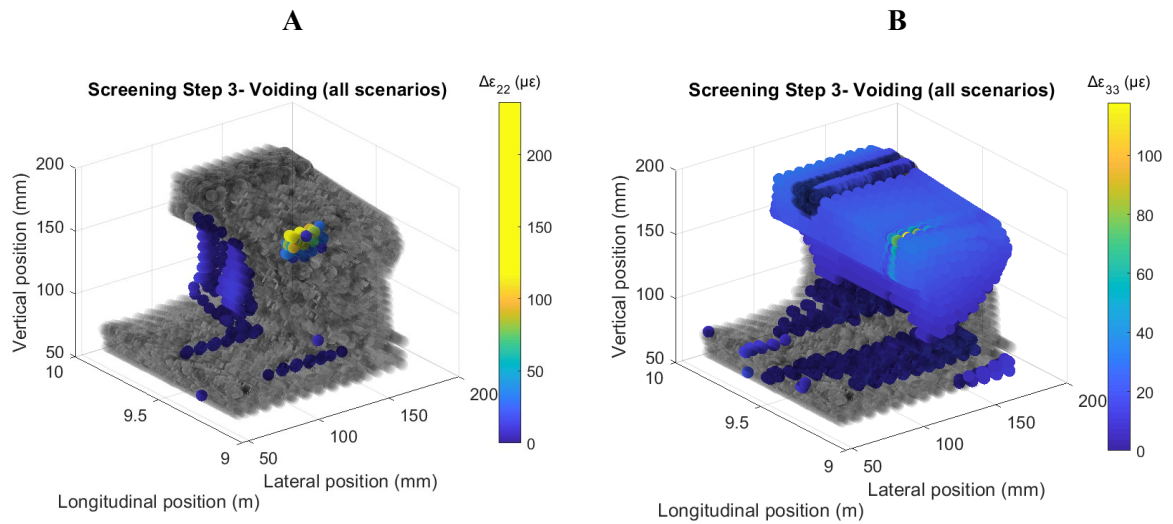


Figure 93: Intersection of the locations from all simulations for detecting the voiding defect on the sleeper; (A) Vertical strains; (B) Longitudinal strains

Figure 94 shows the intersection of the locations for detecting the Wear and RCF surface defects. This indicates that the installation of the sensor at one of the proposed locations will be able to detect either of the defects. The average vertical strain change on the rail web is $70 \mu\epsilon$ and the same for the longitudinal strain on the foot is $50 \mu\epsilon$.

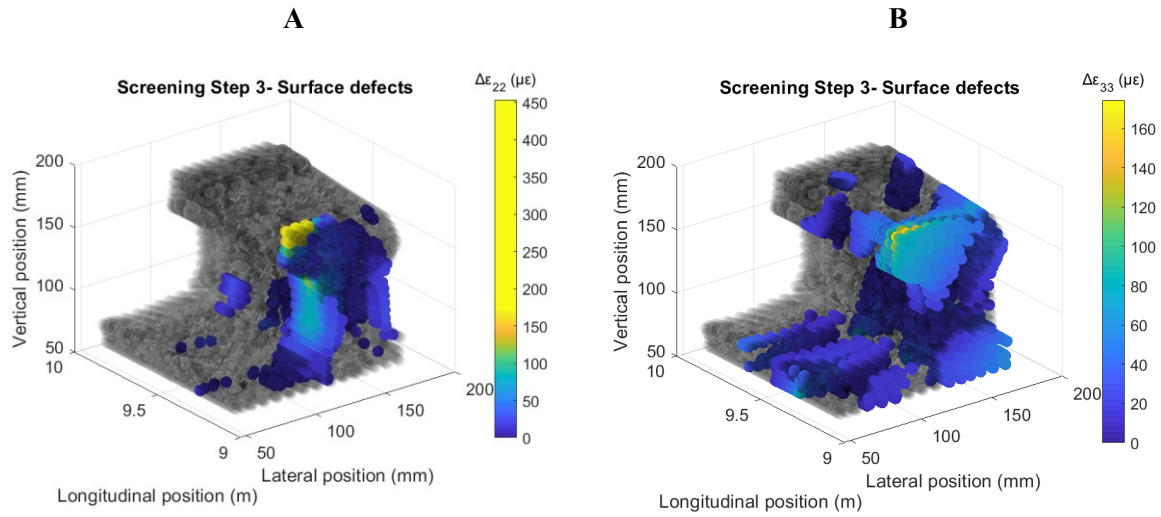


Figure 94: Intersection of the locations from all simulations for detecting the surface defects on the sleeper; (A) Vertical strains; (B) Longitudinal strains

Figure 95 shows the potential locations for detecting the presence of all the defects that would occur on sleeper-supported rail. These results are the intersection of the locations shown in Figure 91, Figure 92 and Figure 93. As the potential for detecting the voiding defect is low as shown in Figure 93, the candidate locations installing the sensor for detecting all three defects is also less in Figure 95. The results that have been obtained from the rail cross-section will be discussed in greater detail in Section 6.7.

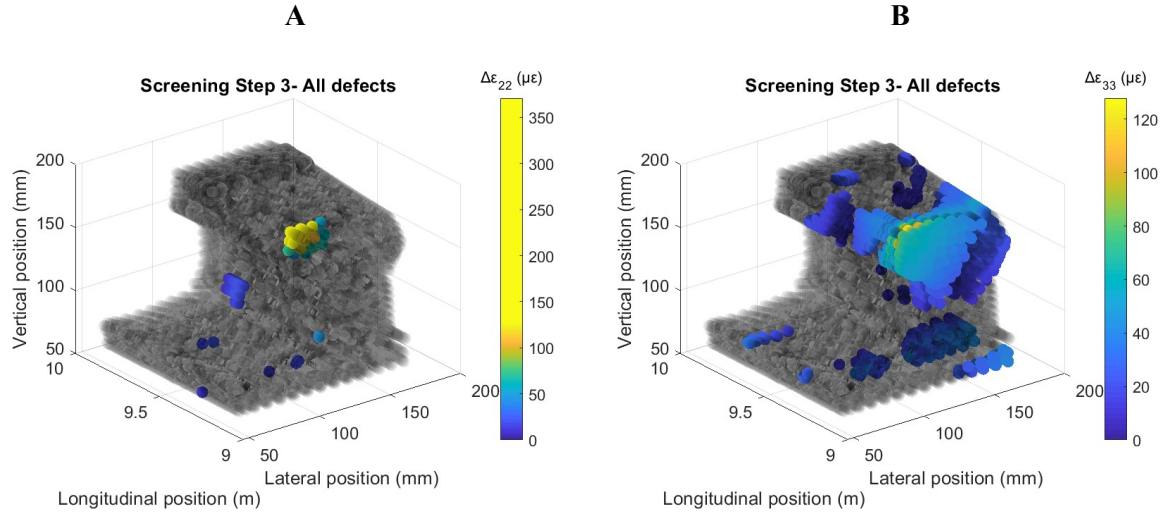


Figure 95: Intersection of the locations from all simulations for detecting all defects on the sleeper; (A) Vertical strains; (B) Longitudinal strains

6.5 Results from the cross-section of the rail that shows the highest potential for fault detection

The results for the sensor placement at the rail cross-section where the wheel and the rail are in contact in the simulations that were carried out with wear on the sleeper has been shown in Figure 96. The locations where the sensors can be placed for detecting the vertical strains has been shown in Figure 96A. A large number of candidate locations can be observed but the locations on the rail web on the track side that have been encircled in red show a high potential for detecting the defects due to a higher amplitude for the mean change in the strains, which is over 150 $\mu\epsilon$. Similarly, Figure 96B shows the potential locations for installing the sensors for measuring the longitudinal strains to detect the wear defect that will occur on the sleeper. The locations at the rail foot show potential for detecting the defect since they are away from the away from the switch toe and yet are yet able to capture the minimum required difference in the strain values. It can be seen that values of up to 80 $\mu\epsilon$ have been achieved. The colours indicated in the colour bar in the plots indicate the ranking of the locations.

It is noteworthy that the results that shown in Figure 96A were obtained whilst ignoring the first screening step. The results from the wear simulations were obtained in the absence of contact between the wheel and the switch rail because of the discontinuity in the rail profile. This loss of contact resulted in a value of less than $5 \mu\epsilon$ for the strains that were captured at most locations. As there was a risk of misrepresenting the locations for sensor placement, Step 1 of the screening step has been ignored in this case.

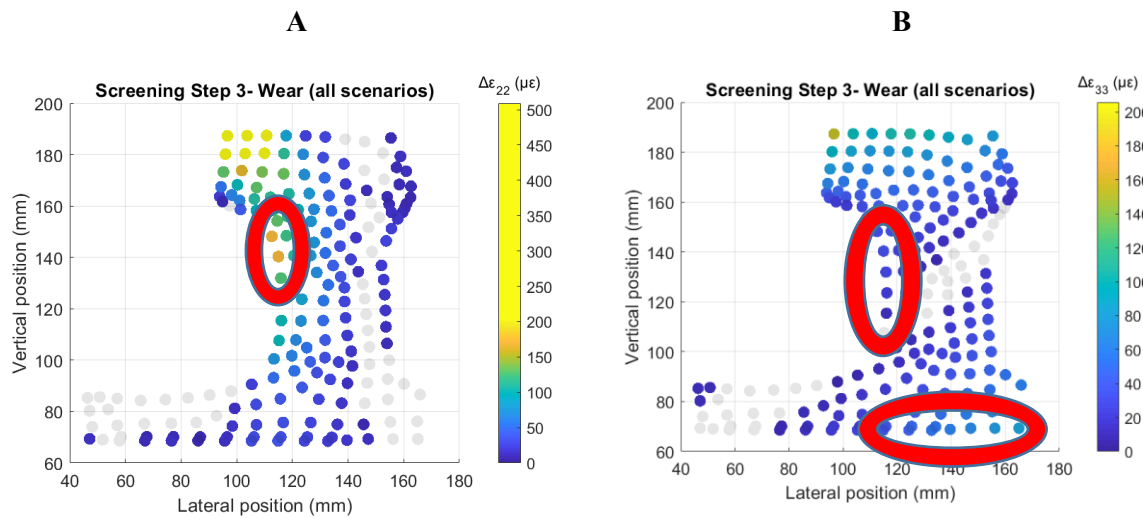


Figure 96: Results for the cross-sectional strains from the wear simulations- wheel-rail contact on the sleeper; (A) Vertical strains; (B) Longitudinal strains.

Figure 97 shows the ranked locations for installing the sensors for detecting the presence of the wear that would occur in between the sleeper spacing. Figure 97A shows the locations under the gauge corner of the rail on the field side (encircled) are ranked higher than the rest of the locations on the rail web and have output a strain change of up to $100 \mu\epsilon$. In this instance, the location of the contact patch had moved closer to the field side, because of the presence of the wear.

However, Figure 97B shows a similar strain distribution to Figure 96B, where the bottom portion of the rail foot is able to capture a change of up to $80 \mu\epsilon$ for the longitudinal strain. Moreover, the rail foot will experience strains that are tensile in nature and the sensor measurements will be less sensitive to the location of the contact patch than when measuring them on the rail web.

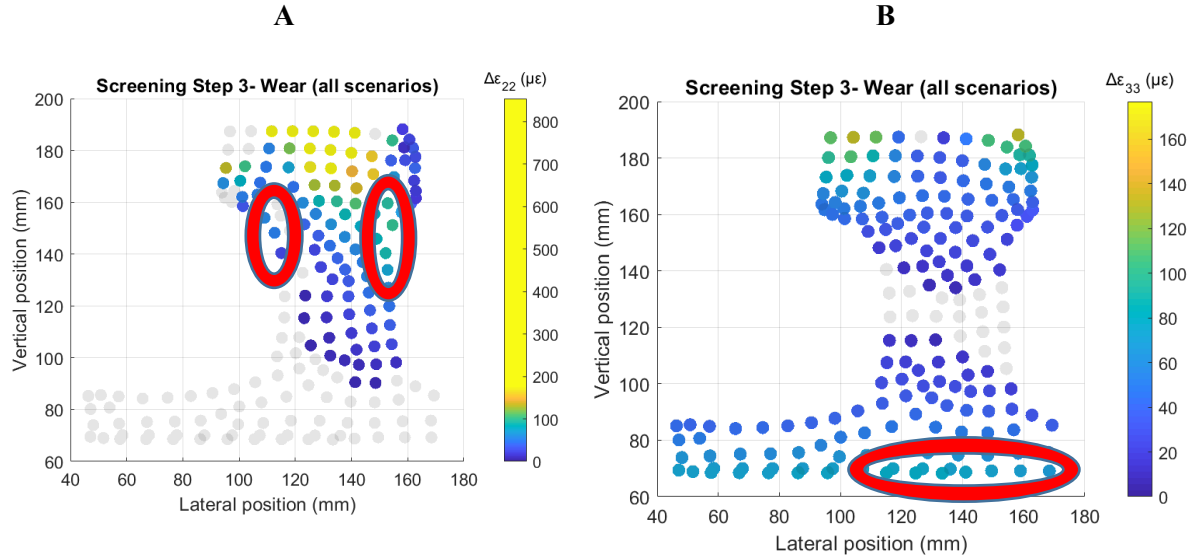


Figure 97: Results for the cross-sectional strains from the Wear simulations- wheel-rail contact in between the sleeper spacing; (A) Vertical strains; (B) Longitudinal strains.

The ranked locations for detecting the RCF defect on and in between the sleepers has been shown in Figure 98 and Figure 99 respectively. The stiffer support for the rail section that is supported by the sleeper would result in a higher overall amplitude and change in strains is higher than for the section in the sleeper spacing, going up to 100 $\mu\epsilon$ and 40 $\mu\epsilon$ for the vertical and longitudinal strains respectively. Therefore, the results from the section of the rail supported by the sleeper in Figure 98 show a larger number of candidate locations than the results that will be shown for the free section in Figure 99.

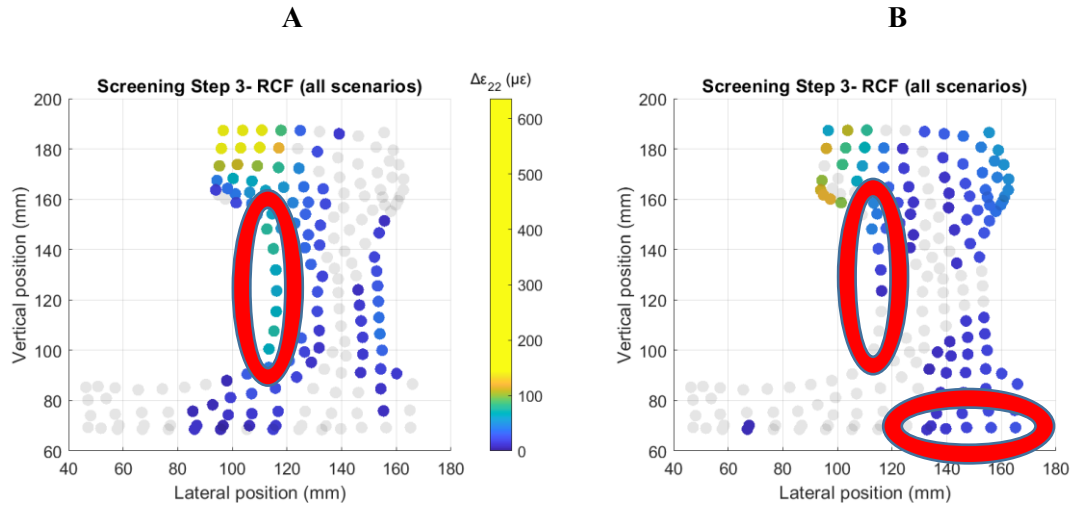


Figure 98: Results for the cross-sectional strains from the RCF simulations- wheel-rail contact in between the sleeper spacing; (A) Vertical strains; (B) Longitudinal strains.

The encircled locations on the rail web and the foot have shown potential for RCF detection in Figure 99. Values of up to $70 \mu\epsilon$ and $30 \mu\epsilon$ have been achieved for the average vertical and longitudinal strain change respectively.

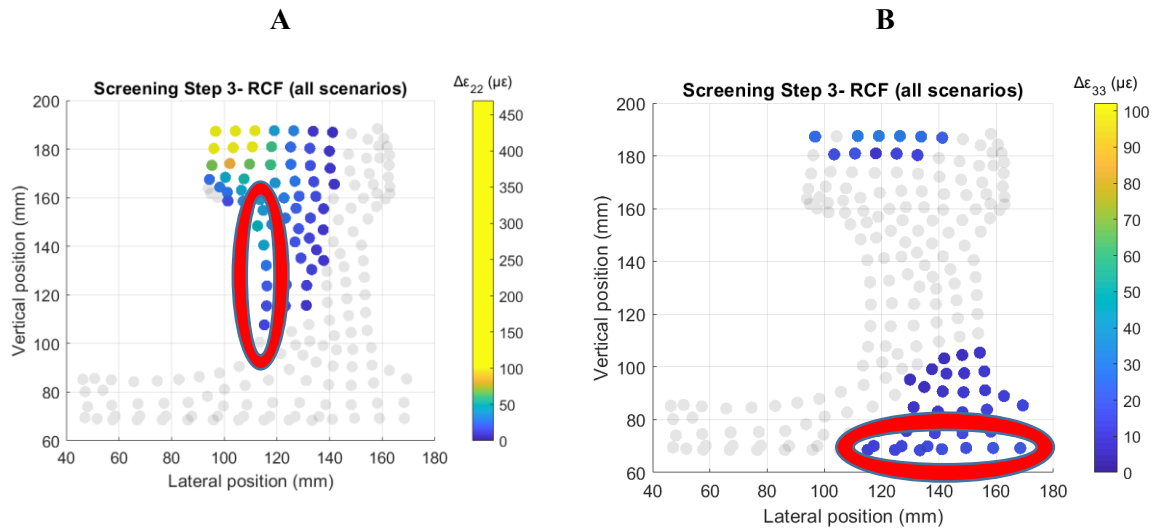


Figure 99: Results for the cross-sectional strains from the RCF simulations- wheel-rail contact on the sleeper. (A) Vertical strains; (B) Longitudinal strains.

The ranked locations for detecting the presence of the voiding defect on or in between the sleepers have been indicated in Figure 100 and Figure 101 respectively. Figure 100A,B show that the potential

for detecting the presence of the voiding defect on the sleeper is very low. For the vertical strains, this may be because a tie constraint has been implemented for connecting the rail to the baseplate and so forth. This would effectively clamp the rail to the sleeper and thus the deformation would be relatively smaller than the deformation that will be captured at the section that is not supported by the sleeper. Since the rail foot is clamped to the sleeper through the baseplate because of the tie constraint, the amplitude for the change in the deformation at lower portions of the rail such as the rail foot would be smaller than that on the rail web (Figure 100 B).

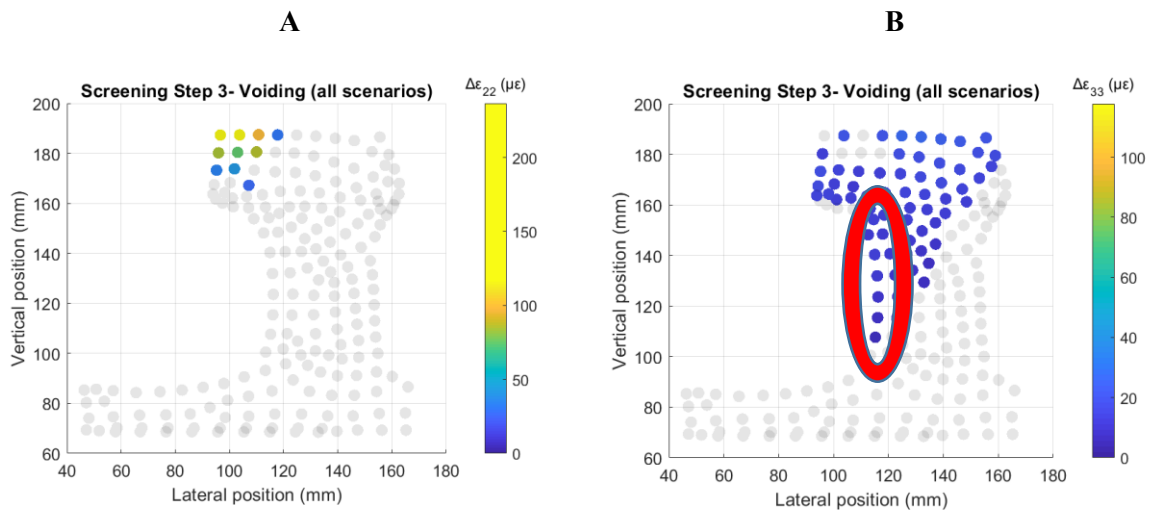


Figure 100: Results for the cross-sectional strains from the Voiding simulations- wheel-rail contact on the sleeper; (A) Vertical strains; (B) Longitudinal strains.

On the other hand, a sufficient change in the amplitude of the vertical and the longitudinal strains as a result of voiding can be captured for the rail section that is free. Figure 101A,B show that the placement of the sensors at the encircled locations on the rail web and the foot show potential for detecting the defect, achieving an average change in strain of up to 50 $\mu\epsilon$ at the encircled locations.

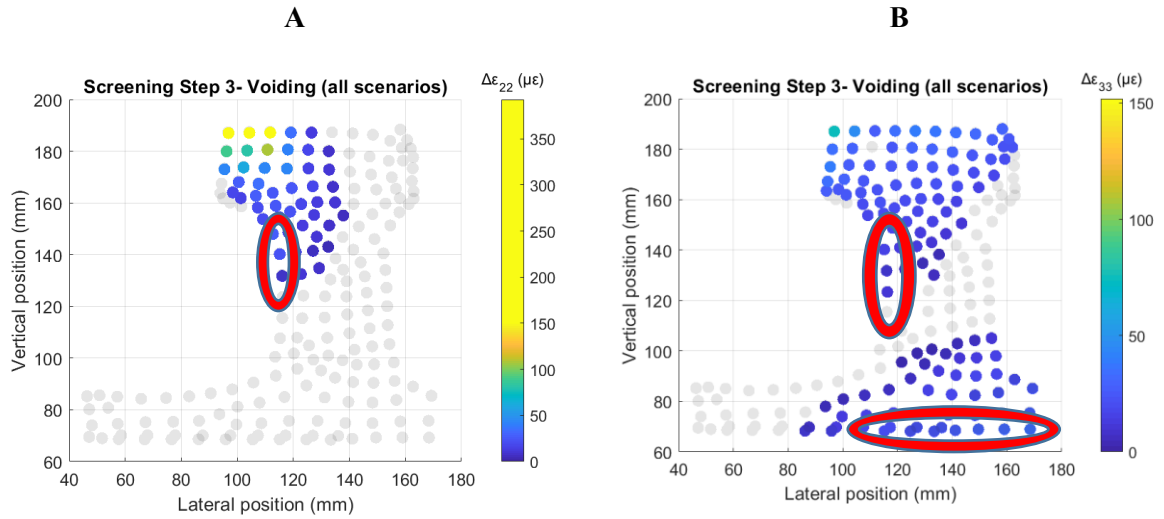


Figure 101: Results for the cross-sectional strains from the Voiding simulations- wheel-rail contact in between the sleeper spacing; (A) Vertical strains; (B) Longitudinal strains.

The locations for placing the sensors for detecting the surface defects, i.e. the wear and the RCF defects that would occur on the sleeper have been plotted in Figure 102A,B. The colourbar in Figure 102 shows the value for the mean amplitude of the change in strains. Figure 102A shows that for the presence of the surface defects a higher value for the mean change in the vertical strains has been captured at the encircled location (up to 120 $\mu\epsilon$) than the mean change in the longitudinal strains that is shown in the encircled location in Figure 102B (up to 60 $\mu\epsilon$).

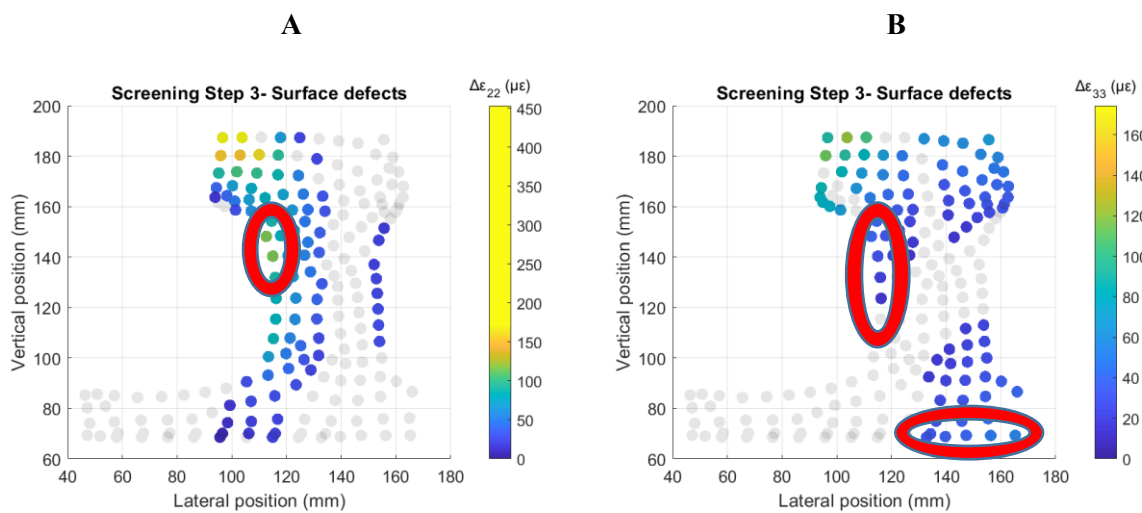


Figure 102: Results for the cross-sectional strains from all simulations with the surface defects- wheel-rail contact on the sleeper; (A) Vertical strains; (B) Longitudinal strains.

The locations where the sensors can be installed for detecting the surface defects that would occur in between the sleeper spacing have been shown in Figure 103A,B. Although, the number of candidate locations are less than those shown in Figure 102, the encircled locations in Figure 103 show a high probability for detecting the defect. An average value for the change in strain of $50 \mu\epsilon$ has been captured at these locations.

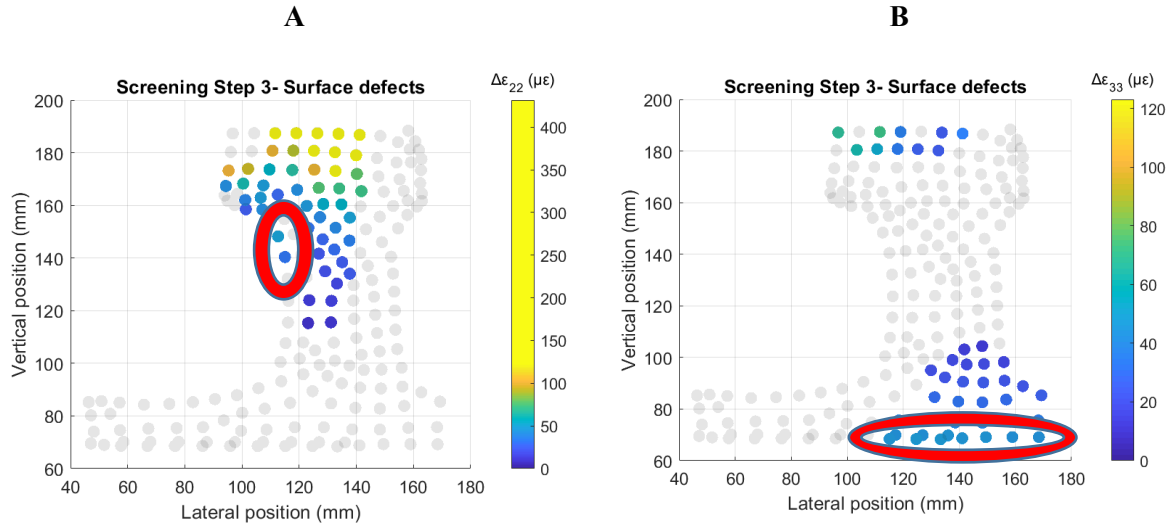


Figure 103: Results for the cross-sectional strains from all simulations with the surface defects- wheel-rail contact in between the sleeper spacing; (A) Vertical strains; (B) Longitudinal strains.

Figure 104 and Figure 105 show the locations that will be able to detect all the defects that have been modelled into the track. Figure 104 shows the locations that will be able to detect all the defects that are present on the sleeper. Unfortunately, as the locations that have been highlighted in the figure are an intersection of the results from the wear, RCF and the voiding defects, the poor potential for detecting the voiding defect in Figure 100 is reflected in the plots shown in Figure 104. Although there is a large pool of candidate locations for detecting the surface defects (Figure 102), the pool drastically reduces for picking the same location for detecting voiding along with the surface defects (Figure 104).

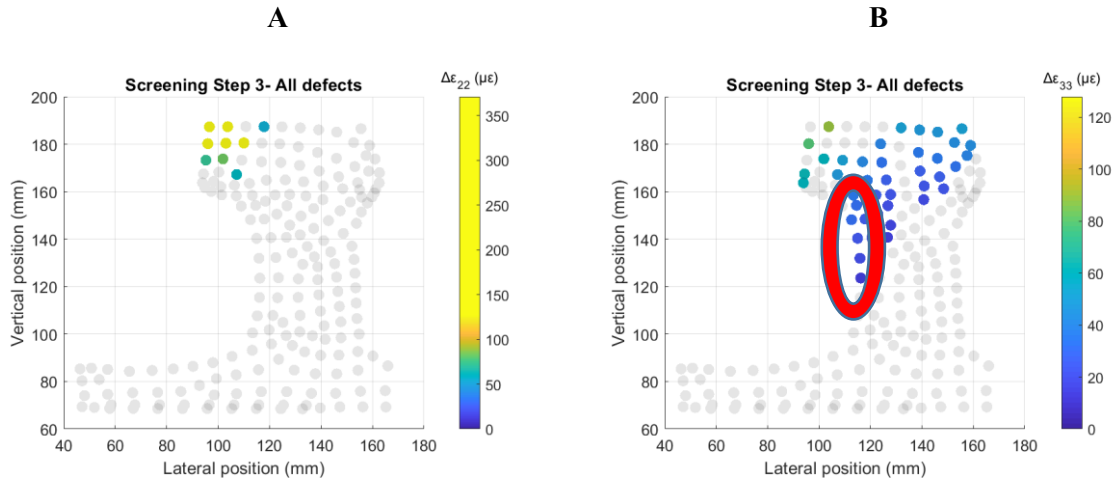


Figure 104: Results for the cross-sectional strains from the simulations with all defects- wheel-rail contact on the sleeper; (A) Vertical strains; (B) Longitudinal strains.

On the contrary, the encircled locations in Figure 105 show a good potential for detecting the wear, RCF defects in between the sleeper spacing as well as the voiding when the wheel would pass over the location in between the sleeper spacing. For the results of the average vertical and longitudinal strain change, an average value of 40 $\mu\epsilon$ and 30 $\mu\epsilon$ has been achieved respectively at the encircled locations.

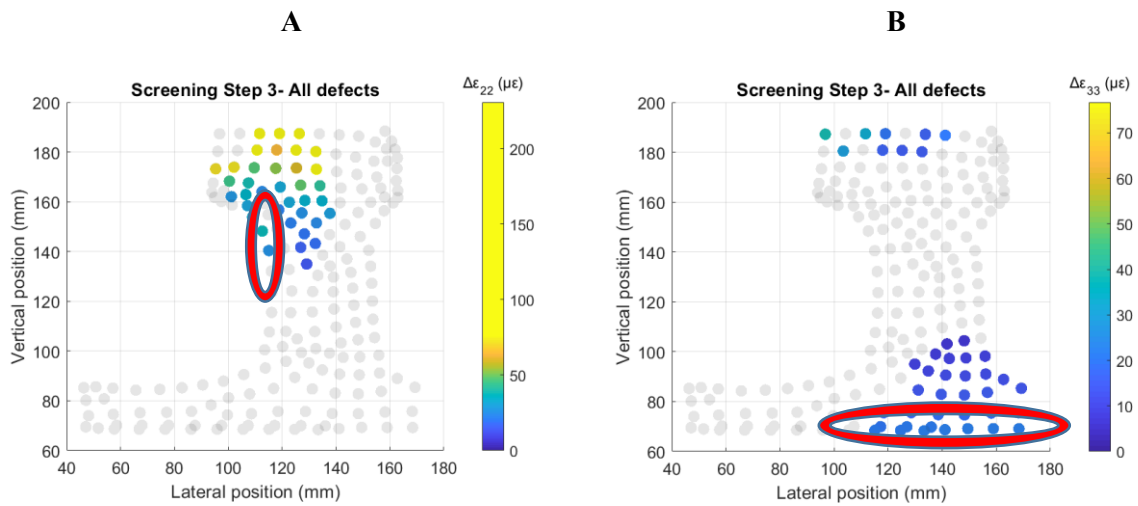


Figure 105: Results for the cross-sectional strains from the simulations with all defects- wheel-rail contact in between the sleeper spacing; (A) Vertical strains; (B) Longitudinal strains.

6.6 Testing the ability of the sensors installed at the proposed locations to detect the defects.

The ability of the sensors to detect the defects will be tested by determining the correlation between the impact force and the strain values. Essentially, the modelling results have been implemented for simulating the outputs that will be obtained from the sensor measurements.

The virtual sensor measurements or the modelling outputs have been analysed for the following scenarios:

1. Occurrence of the rail defect between sleeper spacing and sensor installed on the rail in sleeper spacing: This scenario has been presented in Figure 106, where the position of the sensors and the wheel during the time step at which the sensor results are to be analysed are shown. The vertical and the longitudinal strains can be measured by installing the sensor at the rail web and foot respectively at an approximate longitudinal distance of 9.45 m from the switch toe. It is noteworthy that the switch and the stock rail have been shown together in Figure 106, and the longitudinal sensor on the switch rail is actually installed at the bottom face of the rail foot, which corresponds to the location encircled in Figure 105B.

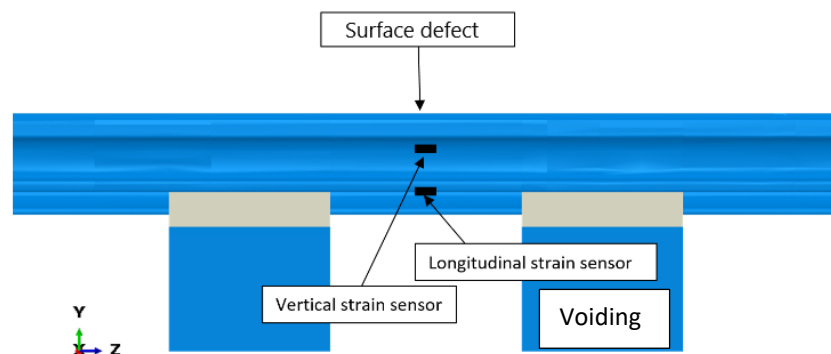


Figure 106: Occurrence of the rail defect between sleeper spacing and sensor installed on the rail in sleeper spacing.

2. Occurrence of the defect over sleeper-supported rail and sensor installed on sleeper supported rail: This scenario has been presented in Figure 107, where the position of the sensors and the

location of the passage of the wheel over the surface defect during the time step at which the sensor results will be analysed are shown. The strains are measured at an approximate longitudinal distance of 9.15 m from the switch toe.

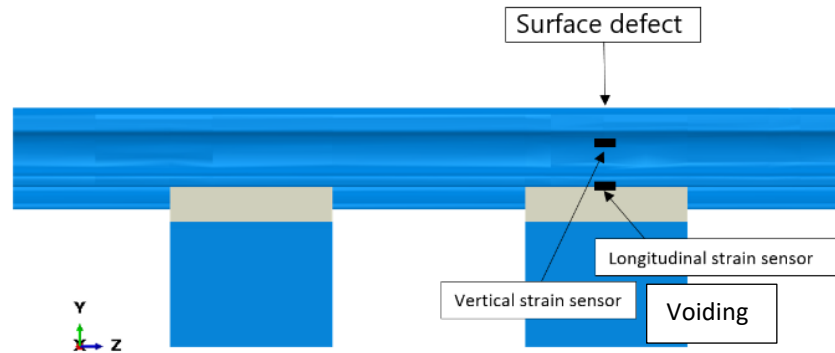


Figure 107: Occurrence of the rail defect between sleeper spacing and sensor installed on the rail in sleeper spacing.

3. Occurrence of the rail defect between the sleeper spacing and sensor installed on sleeper supported rail: This scenario has been presented in Figure 108, where the position of the sensors and the location of the passage of the wheel over the surface defect during the time step at which the sensor results will be analysed have been shown. The strains are measured at an approximate longitudinal distance of 9.15 m from the switch toe.

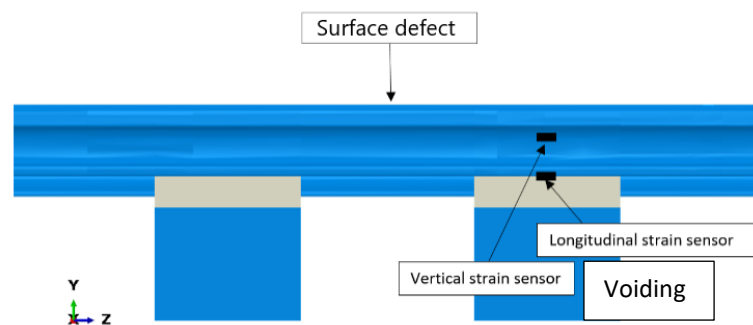


Figure 108: Occurrence of the rail defect between the sleeper spacing and sensor installed on sleeper supported rail.

4. Occurrence of the rail defect over sleeper supported rail and sensor installed on the rail in sleeper spacing: This scenario has been presented in Figure 109, where the position of the

sensors and passage of the wheel over the surface defect during the time step at which the sensor results were analysed have been shown. The strains are measured at an approximate longitudinal distance of 9.45 m from the switch toe.

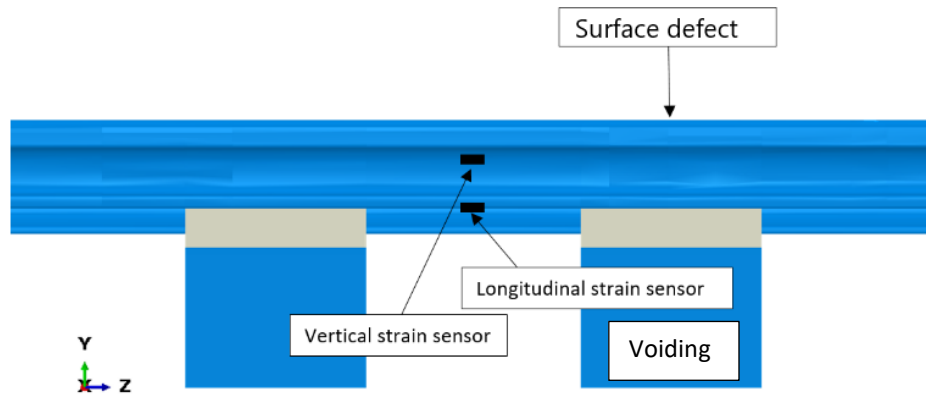


Figure 109: Occurrence of the rail defect over sleeper supported rail and sensor installed on the rail in sleeper spacing.

The sensor placement determination approach as well as the potential approach for fault detection were explained in Section 6.1. The potential sensor placement locations and the sensor orientations were determined in Section 6.5.

The impact load can be predicted from the sensor measurements if a high correlation exists between the measured strains and the wheel-rail contact force. It was described in Chapters 4 and 5 that the placement of sensors for measuring the vertical and longitudinal rail strains show a higher probability of fault detection than the measurement of the lateral rail strains. Hence, the Pearson's correlation coefficient between the vertical/lateral rail strains and the vertical wheel-rail contact force was first obtained from each of the simulations.

The outputs from the 30 numerical simulations were implemented for determining the possibility of a linear relationship between the strains and the vertical contact force for the four aforementioned scenarios from the result for the correlation coefficient. Finally, the possibility for obtaining this linear relationship was tested by deriving the contact force from the rail strains by performing linear

regression analysis and plotting the regression line and the data points that were extracted from the simulation on the same graph.

The ability to capture an accurate change in the vertical contact force from the sensor measurement is essential for performing the quantitative damage prediction studies that can be implemented for determining the health and condition of the switch by implementing traditional damage prediction models. However, even without obtaining a direct linear relationship between the strains and the wheel-rail impact force, it may be possible to detect and classify the defects if the results for the strains that are captured after introducing the different defects are distinctive. In essence, a linear relationship between the strains and the impact force would simplify the quantification of the presence of defects but is not a prerequisite for fault detection, as it will be shown in the next section.

6.6.1 Occurrence of the rail defect between sleeper spacing and sensor installed on the rail in sleeper spacing.

For this scenario that has been shown in Figure 106, the correlation between the vertical contact force/impact force and the vertical rail strains have been plotted in Figure 110 A,B.

The results for the wheel-rail impact force that were obtained from the FE simulations that were carried out with no defect, RCF between sleepers, wear and voiding have been plotted in Figure 110 A,B. The results from the simulations that were carried out with tare and laden loads have been plotted in Figure 110 A and B respectively.

When concentrating on the ordinate, it can be observed that a higher amplitude of negative compressive strains than the model with no defect are obtained in the presence of the RCF and voiding. Due to a considerable difference in the contact patch location, the results from the wear simulations show a reduction in the compressive strain amplitude when compared to the model with no defect. This also means that the wheel-rail contact patch has laterally moved away from the sensor location. An R value or a correlation coefficient of 0.61 is obtained between the vertical rail strains and the impact force. The influence of the wear simulations on the regression line can be clearly

observed. With the exception of the wear simulations, the results for the contact force can be predicted with a reasonably good accuracy from the vertical rail strains.

In the legend shown in Figure 110, the R value as well as the relationship between the values plotted on the X and Y axes can be seen.

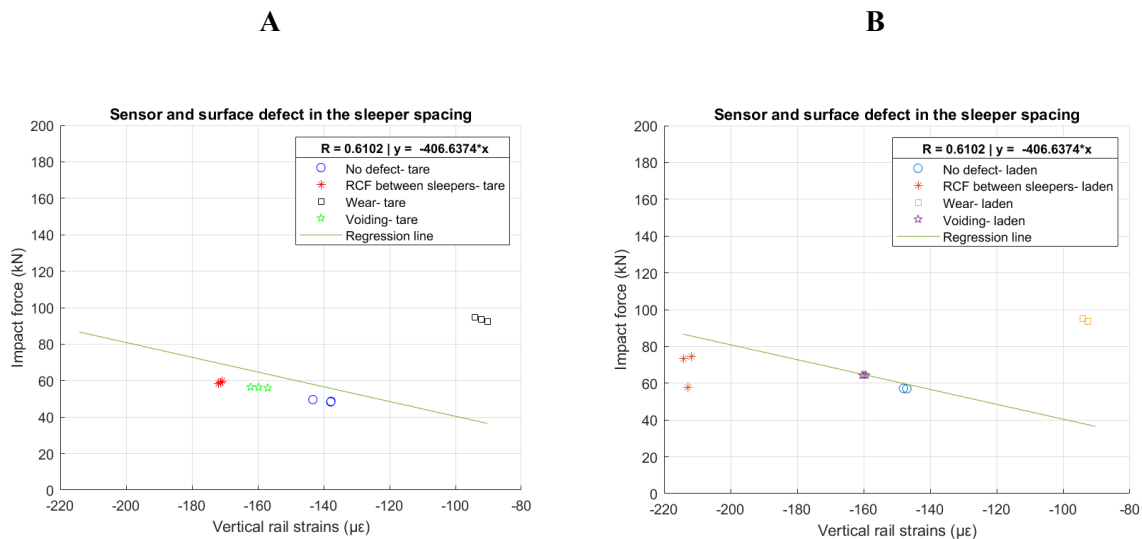


Figure 110: Correlation between the impact force and the vertical rail strains when both the sensor and the defect are in the sleeper spacing; (A) Tare load; (B) Laden/Heavier load.

The percentage difference between the strains that have been captured with and without the track defects have been highlighted in Table 39. The amplitude of the vertical strains is higher for the model with the RCF and the voiding defect than the model with no defect. A minimum difference of 20 % is captured when capturing the results with the wheel with the tare load, which demonstrates a good potential for condition monitoring. The amplitude of the strains for the worn rail is around 50% less, which also shows the potential for detecting the wear defect. From the values in Table 39, the potential for detecting the presence of RCF and Wear defects by placing the sensor in the vertical orientation at the proposed location is rather high. There is also some potential for detecting voiding, but the results show a higher probability of detecting RCF and Wear.

Table 39: Average change in the vertical strains when the sensor and the surface defect are in the sleeper spacing.

Defect type	Average change in the vertical strains (%)- Tare load	Average change in the vertical strains (%)- Laden load
RCF	31.73	65.58
Wear	-47.48	-53.76
Voiding	20.01	12.52

The histogram for the values for the vertical strains that were captured at the potential location for vertical sensor placement have been plotted in Figure 111. It can be observed that the absolute amplitude of the strains that have been captured would lie between 80 and 240 $\mu\epsilon$. The strain values that are captured from the majority of the simulations lie between are between 120 and 200 $\mu\epsilon$. The simulations where an amplitude that is greater than 200 $\mu\epsilon$ is captured has the presence of the RCF defect. The results that are obtained from the simulations with the wear defect lie between 80 and 100 $\mu\epsilon$. The results that are captured without any surface defects lie between 120 and 160 $\mu\epsilon$. Although the values for the vertical strains are highly dependent on the location of the contact patch, the defects can be classified based on the strain measurement range.

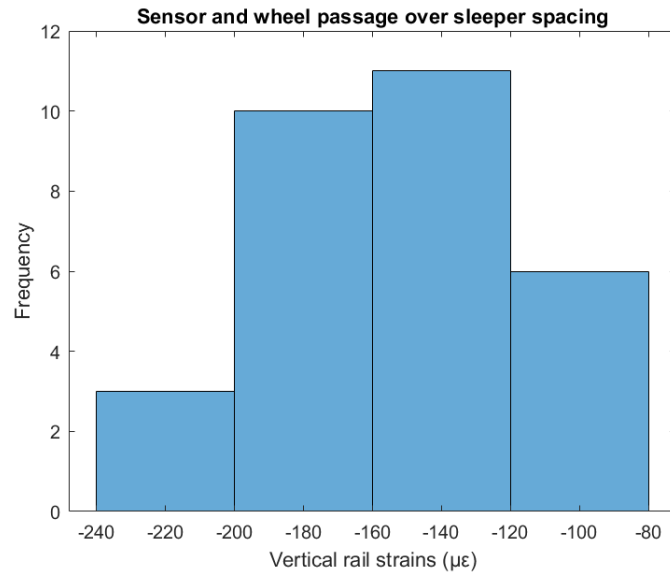


Figure 111: Histogram for the vertical strain values for determining the measurement range of the sensor when both the sensor and the defect are in the sleeper spacing.

For the same scenario, the correlation between the longitudinal strains that are measured at potential sensor placement location on the rail foot and the vertical impact force has been plotted in Figure 112. An R value of 0.97, which demonstrates a good correlation between the longitudinal strains and the vertical impact force has been obtained. Unlike Figure 110 where it is shown that the results for the vertical strains will not help obtain the accurate results for the vertical impact force for wear, the results for the longitudinal strains that have been shown in Figure 112 show an accurate estimate for the impact force for worn rail can be achieved. This demonstrates that the value for the longitudinal strains is therefore less sensitive to the lateral position of the contact patch. It can also be observed in Figure 112 that the longitudinal strain results are able to differentiate between the various defects and axle loads. The measurement of longitudinal strains at the proposed sensor placement location on the rail foot shows the potential for detecting the presence of surface defects in the sleeper spacing.

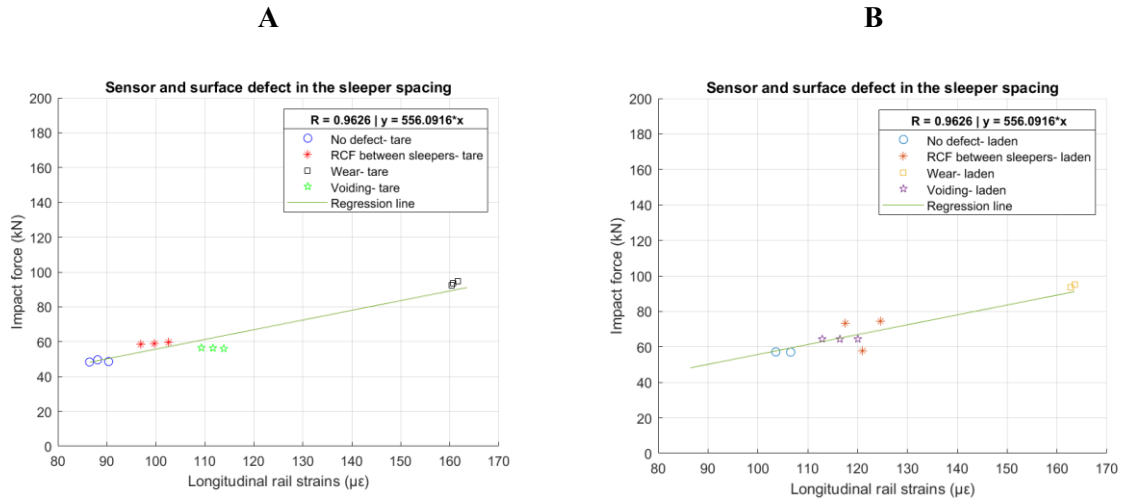


Figure 112: Correlation between the impact force and the longitudinal rail strains when both the sensor and the defect are in the sleeper spacing; (A) Tare load; (B) Laden/Heavier load.

The percentage difference between the strains that have been captured with and without the track defect have been highlighted in Table 40. The change in strains on introducing wear is much higher than RCF and voiding. The values for the percentage difference that have been included in Table 40 are positive, indicating that an overall average increase in the strain amplitude of at least 10 %.

Table 40: Average change in the longitudinal strains when the sensor and the surface defect are in the sleeper spacing.

Defect type	Average change in the longitudinal strains (%)- Tare load	Average change in the longitudinal strains (%)- Laden load
RCF	11.38	15.47
Wear	72.59	57.67
Voiding	23.29	10.87

The histogram that has been plotted in Figure 113 shows that the sensor will need to capture an absolute amplitude of the longitudinal strains between 80 and 170 $\mu\epsilon$. Classifying the defects based on

the amplitude of the strains is possible; however the influence of the axle load is also an important factor as the amplitude of the strain that is captured in the presence of the defect and lower axle load is similar to that which is captured in the absence of the defect and heavier axle load. Nevertheless, it should be easy to filter out the influence of the axle load for determining the condition of the track. A continuous measurement of the high amplitude of the strains by sensors that are located elsewhere on the infrastructure will be able to indicate the presence of heavier axle loads and thus be able to filter out its influence. It can be observed that the measurement range for capturing the longitudinal strains is lower than that for the vertical strains.

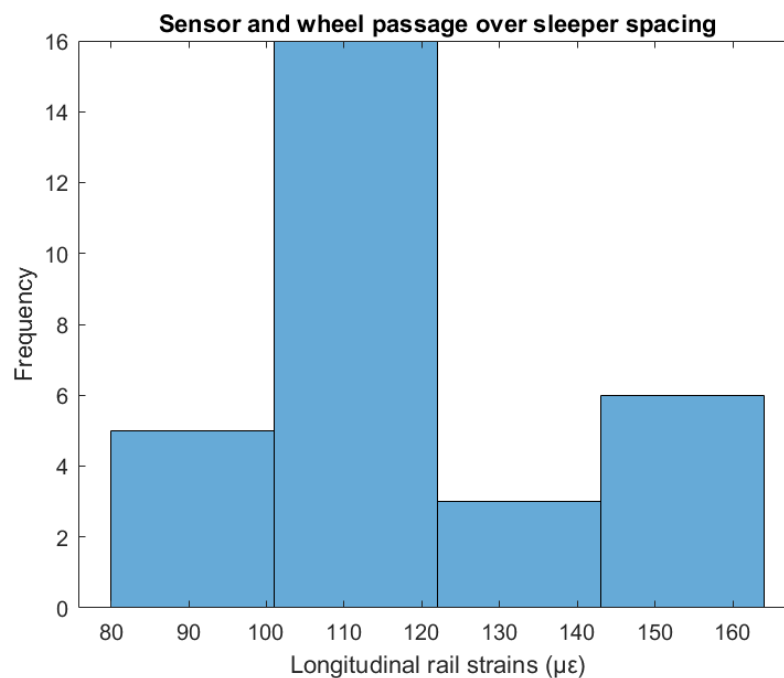


Figure 113: Histogram for the longitudinal strain values for determining the measurement range of the sensor when both the sensor and the defect are in the sleeper spacing.

6.6.2 Occurrence of the rail defect over supported sleeper and sensor installed on sleeper supported rail.

The installation of the sensor on the section of the rail that would lie on the sleeper as shown in Figure 107 has been investigated. The results for the correlation analysis between the vertical rail strains and the vertical impact force have been plotted in Figure 114. A correlation coefficient of -0.992 shows a

strong linear relationship between the vertical strains and the vertical impact force at this position. It can be observed in Figure 114 that the proposed location will be able to capture a higher amplitude of the vertical strains when the RCF is present on the sleeper-supported rail than in the absence of the defect. Similarly, Figure 114 shows that the loss of wheel-rail contact resulting from the presence of the wear defect would result in a value for the vertical strain that is close to zero. As there is a good correlation between the outputs of the strains and the impact force, the detection of the presence of the surface defects of wear and RCF on the sleeper by installing the sensor at this location and orientation could be achieved.

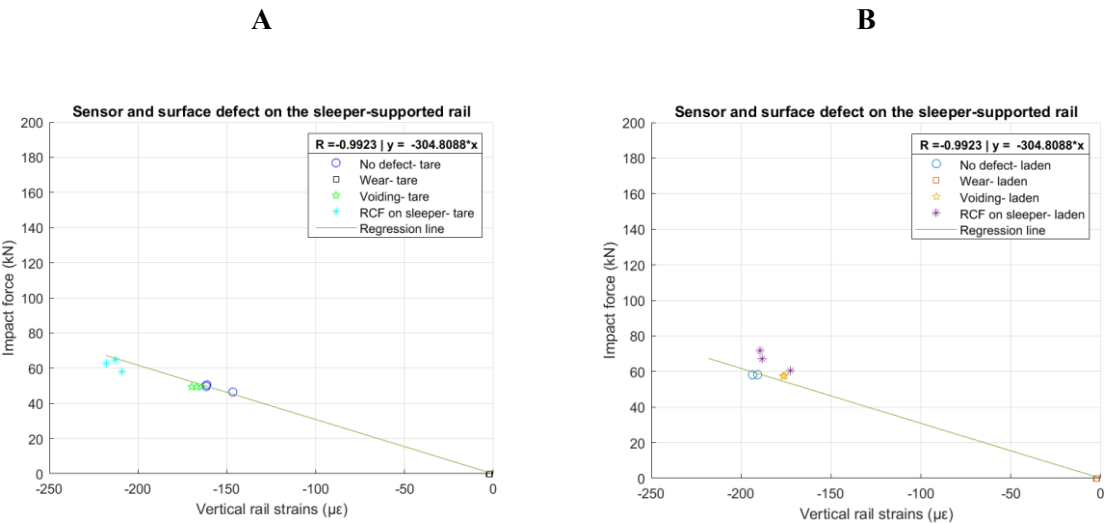


Figure 114: Correlation between the impact force and the vertical rail strains when both the sensor and the defect are on the sleeper-supported rail section; (A) Tare load; (B) Laden/Heavier load.

The percentage difference between the strains that have been captured with and without the track defect has been highlighted in Table 41. The change in strains on introducing wear is much higher than RCF and voiding. The results from the wear simulation have shown a reduction in the strain amplitude. The results from the RCF and voiding simulations with the tare load have shown an increase in the strain amplitude as expected. However, the results that have been obtained from the laden load have shown a decrease in the strain amplitude when compared with the results that were obtained from the simulation with no defect whilst implementing the laden load. As verified, this is because of the difference in the lateral contact position between the two models. Also, the correlation

between the strains and the impact force is better for the results that were obtained from the simulations with the tare load than the laden load.

Table 41: Average change in the vertical strains when the sensor and the surface defect are on the sleeper-supported rail section.

Defect type	Average change in the vertical strains (%)- Tare load	Average change in the vertical strains (%)- Laden load
RCF	56.88	-8.18
Wear	-154.38	-189.46
Voiding	10.44	-15.42

The histogram that has been plotted in Figure 115 shows that the absolute amplitude of the vertical strains that are captured when both the sensor is located and wheel passes over the sleeper-supported rail section lie between 0 and 250 $\mu\epsilon$. The loss of contact in the presence of the wear has resulted in the bin on the histogram that is closer to 0. The histogram bin after 200 $\mu\epsilon$ consists of the results from the simulations that had the presence of wear over the sleeper. The results with no defects and voiding lie in the bin with the highest frequency lie between 150 and 200 $\mu\epsilon$. This demonstrates that the classification of the defect based on the amplitude of the strain is clearly possible.

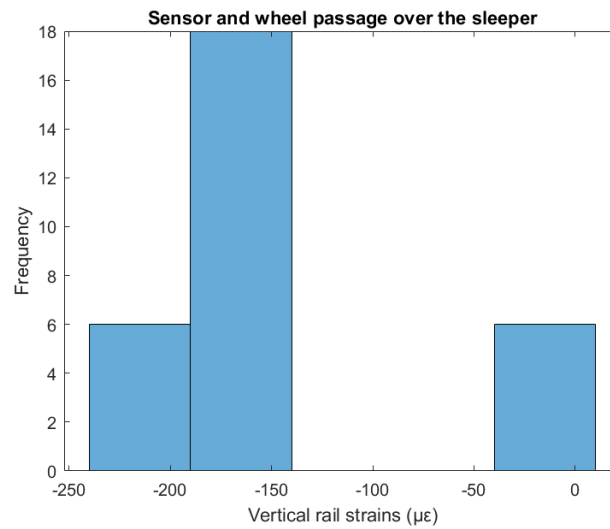


Figure 115: Histogram for the vertical strain values for determining the measurement range of the sensor when both the sensor and the defect are on the sleeper-supported rail section

At the same section of the sleeper-supported rail, the presence of a linear relationship between the vertical impact force and the longitudinal strains has been investigated in Figure 116. It can be observed that despite an increase in the contact force in the presence of the RCF on the sleeper, the amplitude of the longitudinal strains is either equal to or less than the results that are obtained from the simulations that were carried out without the RCF. However, a very low amplitude of longitudinal strains are obtained from this location for the results from the simulations with the wear defect. With the high value for the correlation coefficient of almost 0.87, although the installation of the sensor shows potential for detecting the loss of contact, it does not seem to capture the increased amplitude of the impact force that would result from the presence of the RCF on the sleeper and hence could possibly detect a defect on the loss of contact but not when there is an increase in the contact force. Similarly, Figure 116 shows that despite a good correlation between the strain and the impact force for the voiding simulations, the presence of voiding would not result in a much higher amplitude for the contact force.

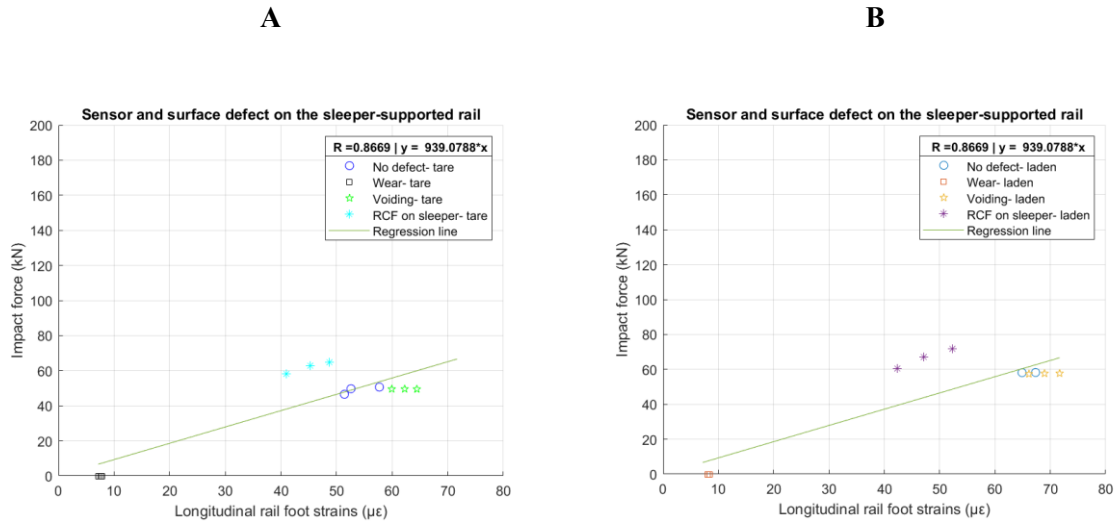


Figure 116: Correlation between the impact force and the longitudinal rail strains when both the sensor and the defect are on the sleeper-supported rail section; (A) Tare load; (B) Laden/Heavier load.

The tie constraint between the foot of the switch rail and the baseplate has influenced the amplitude of the strains. Due to the loss of the contact between the wheel and the switch rail in the presence of wear, the largest percentage for the change in the strains has been captured for this case as shown in Table 42. The results for the RCF show a reduction in the strain amplitude despite an increase in the contact force, indicating poor correlation. The results for the voiding show an increase in the strain amplitude as well as the contact force.

Table 42: Average change in the vertical strains when the sensor and the surface defect are on the sleeper-supported rail section.

Defect type	Average change in the longitudinal strains (%) - Tare load	Average change in the longitudinal strains (%) - Laden load
RCF	-8.95	-19.27
Wear	-46.40	-58.38
Voiding	8.30	2.40

The histogram shown in Figure 117 shows the low measurement range (0 to 80 $\mu\epsilon$) for the longitudinal strains on the rail foot on sleeper supported rail. Figure 116 and Figure 117 show that apart from the presence of wear, no other defect can be detected by measuring the longitudinal strains at the rail foot on the rail that is supported by the sleeper.

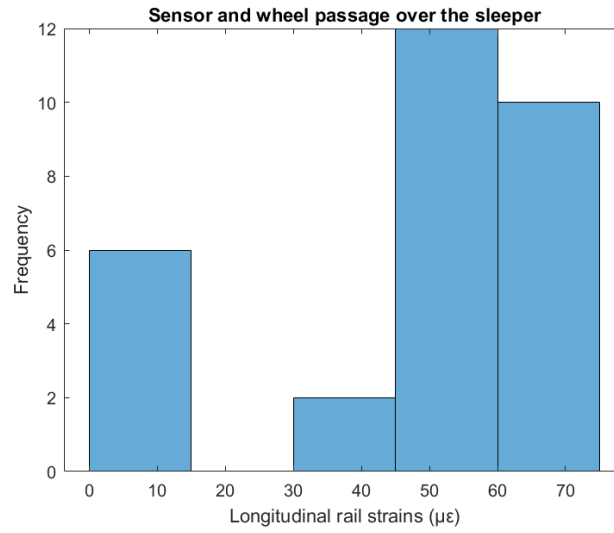


Figure 117: Histogram for the longitudinal strain values for determining the measurement range of the sensor when both the sensor and the defect are on the sleeper-supported rail section

6.6.3 Occurrence of the rail defect between the sleeper spacing and sensor installed on sleeper supported rail.

The ability of detecting the presence of the defect by installing the sensor at a distance away from the fault location has been investigated. As shown in Figure 108, the ability to detect the track defects when the wheel is positioned in between the sleeper spacing and the vertical and the longitudinal sensors are installed on the sleeper has been investigated. It can be observed in Figure 118 that when the vertical sensor is installed on the sleeper at the proposed location, a poor correlation is obtained with the impact force that is captured when the wheel passes over the location between the sleeper spacing. Moreover, Figure 118 shows that the amplitude of the strains that are captured is very less and there can be no differentiation between the different defects.

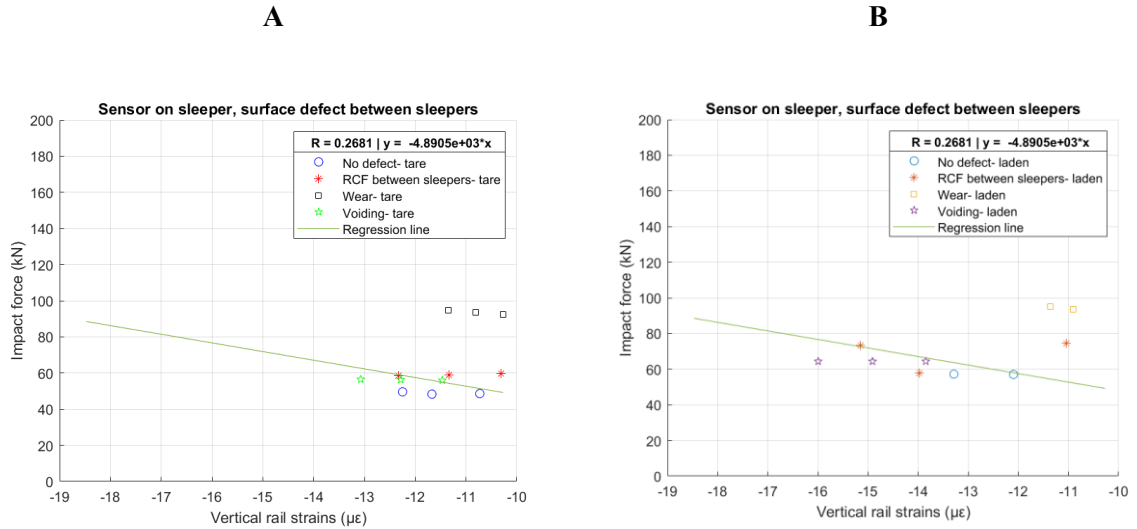


Figure 118: Correlation between the impact force and the vertical rail strains when the sensor is placed on the sleeper and the wheel passes over the defect between the sleepers; (A) Tare load; (B) Laden/Heavier load.

Similarly, a poor correlation is obtained between the longitudinal strains and the impact force when the sensor is installed on the sleeper-supported rail. Moreover, the amplitude of the strains that are captured is rather low and would lie between 2 and 14 $\mu\epsilon$, which demonstrates a rather low probability of detecting any defect by installing the sensor at this location.

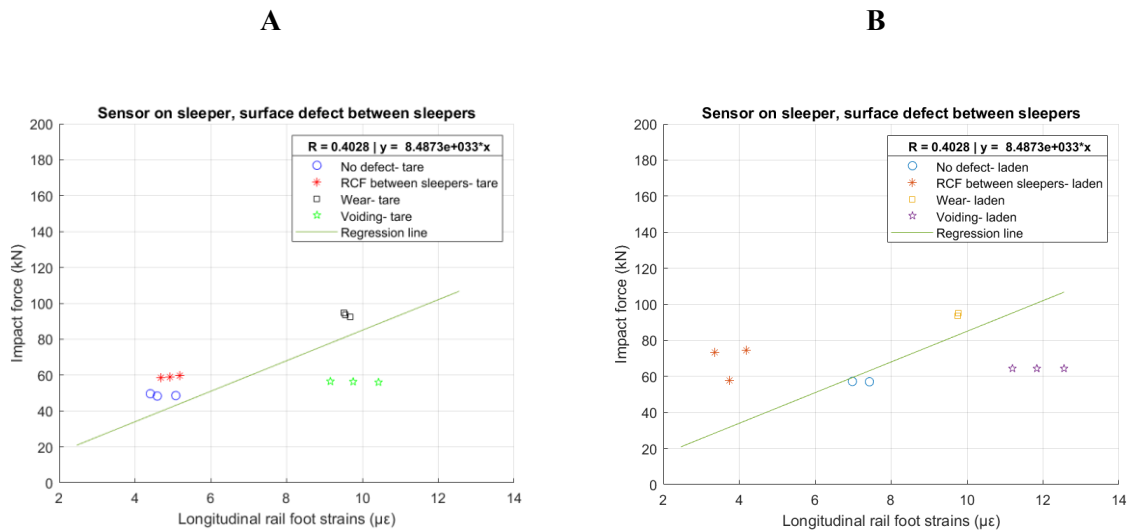


Figure 119: Correlation between the impact force and the longitudinal rail strains when the sensor is placed on the sleeper and the wheel passes over the defect between the sleepers; (A) Tare load; (B) Laden/Heavier load.

6.6.4 Occurrence of the rail defect over sleeper supported rail and sensor installed on the rail in sleeper spacing.

As shown in Figure 109, potential for detecting the occurrence of the track defects over the sleeper-supported rail when the sensor is installed in the sleeper spacing has been investigated. The correlation between the vertical rail strains and the vertical impact force, which has been plotted in Figure 120, shows that a high correlation between the strains and the impact force is obtained. However, barring some of the result points that are obtained from the simulations that were carried out in the presence of the RCF over the sleeper, the amplitude of the vertical strains are below the limit of $5 \mu\epsilon$ that was set for the sensor resolution. However, a sensor that is able to capture strain values with a very low resolution and error could potentially detect the presence of the surface defects on the sleeper.

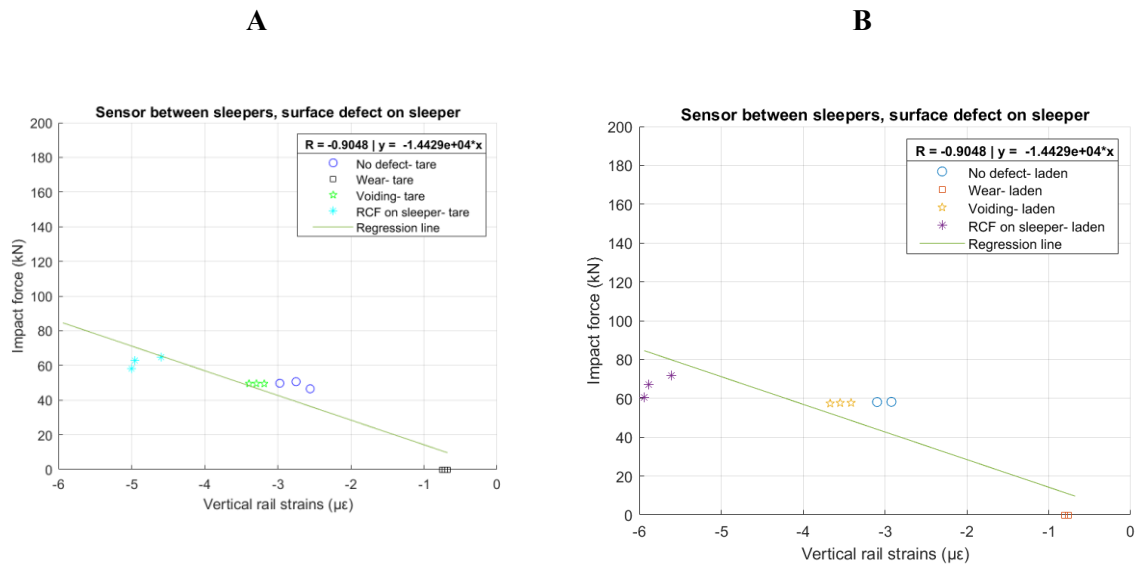


Figure 120: Correlation between the impact force and the vertical rail strains when the sensor is placed between the sleepers and the wheel passes over the defect on the sleeper; (A) Tare load; (B) Laden/Heavier load.

As shown in Figure 120, since the amplitude of the vertical strains that are captured by the sensor is very less, the location does not meet the screening requirement. However, the plots do show the clustering ability and repeatability of results from the simulations that were carried out with the same defect. The histogram for the results has not been plotted since it is fairly clear from Figure 120 that

capturing the strains up to $10 \mu\epsilon$ with a sensor that has a resolution that will be able to distinguish between the results will help differentiate between and thus detect the different defects.

Table 43 highlights the percentage difference between the results for the strains that were captured from the simulations that were carried out with and without the defect. The results for the vertical strains from the RCF and voiding simulations are higher than that from the simulations that were carried out with no track defects. Due to the loss of the wheel-rail contact, the results for the vertical strains that were captured from the wear simulations are much lower. The result for the vertical strain that is captured in the presence of the RCF defect is 43-50 % higher than the model with no defect. Those from the voiding simulations are 16% higher and the results from the wear simulations are 283-287% lower than the results from the model with no defect. If the resolution of the sensor is adequate and sensitive to changes at such low amplitudes, then the RCF and wear defects can be detected effectively. There is also potential for detecting voiding but this is lower than the potential for the detection of the wear and the RCF defects.

Table 43: Average change in the vertical strains when the sensor is placed between the sleepers and the wheel passes over the defect on the sleeper.

Defect type	Average change in the vertical strains (%) - Tare load	Average change in the vertical strains (%) - Laden load
RCF	43	50
Wear	-287	-283
Voiding	16	16

The linear relationship between the longitudinal rail foot strains and the vertical impact force when the sensor is installed on the foot of the rail that is supported by the sleeper and the wheel passes over the section of the rail lying in between the sleeper spacing has been shown in Figure 121. Although a

reasonably linear relationship with a correlation coefficient of 0.7 is obtained between the longitudinal strains and the vertical impact force, the higher contact forces that are present because of the presence of the RCF defect on the sleeper are not reflected in the results for the amplitude of the longitudinal strains. Figure 121 shows that there is a higher probability of capturing the wear and the voiding defects at this location than the presence of the RCF defect on the sleeper.

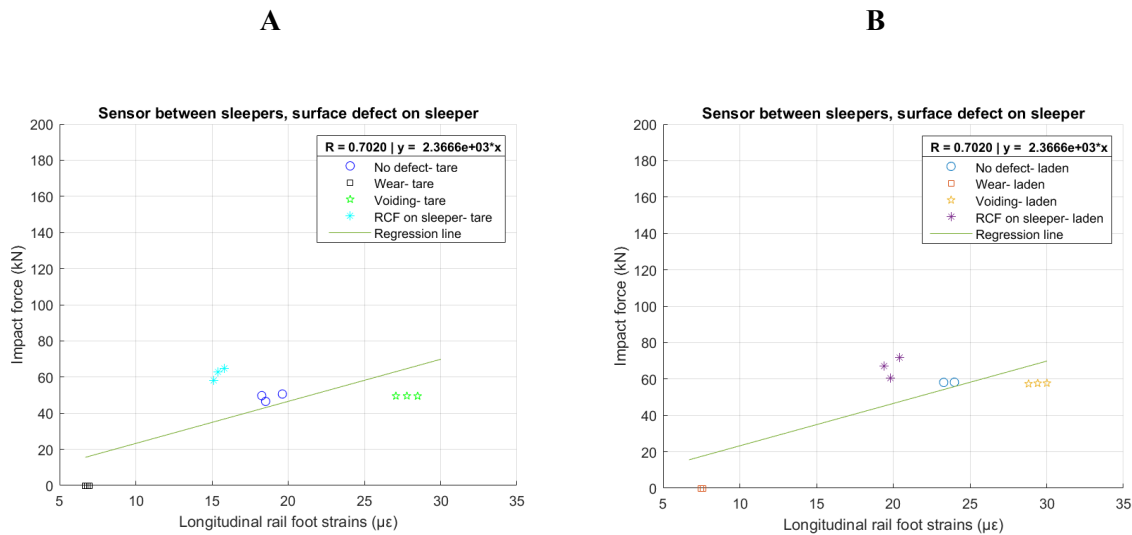


Figure 121: Correlation between the impact force and the longitudinal rail strains when the sensor is placed between the sleepers and the wheel passes over the defect on the sleeper; (A) Tare load; (B) Laden/Heavier load.

As shown in Table 44, the average amplitude for the longitudinal strains that are captured in the presence of wear and voiding are lower than that captured from the simulations that were carried out with no defects. There is an increase in the amplitude of the longitudinal strains because of the presence of voiding. A difference of 175-220% was captured from the simulations that were carried out in the presence of the wear defect. For RCF and voiding, the difference ranged between 19 and 42%, which is good enough for fault detection. The repeatability and clustering of results will be potentially able to detect the defect. However, it can be seen in Figure 121 that the amplitude of the strains that will be captured from the sensor will be lower than when placed somewhere closer to the defect location. With a sensor that is able to capture the results with a very less value for the resolution, this behaviour may be captured and thus there will be potential for fault detection.

Table 44: Average change in the longitudinal strains when the sensor is placed between the sleepers and the wheel passes over the defect on the sleeper.

Defect type	Average change in the longitudinal strains (%)- Tare load	Average change in the longitudinal strains (%)- Laden load
RCF	-22	-42
Wear	-176	-216
Voiding	32	19

The histogram for the longitudinal strain values when the sensor is installed on the rail foot in between the sleeper spacing has been plotted in Figure 122. It can be observed from Figure 121 and Figure 122 that the presence of the wear defect on the sleeper as well as the voiding defect can be classified based on the amplitude of the longitudinal strains. Moreover, the amplitude of the strain is higher than the minimum constraint on the sensor resolution of 5 $\mu\epsilon$. Therefore, those defects could be detected with a low probability by installing the sensor at this location.

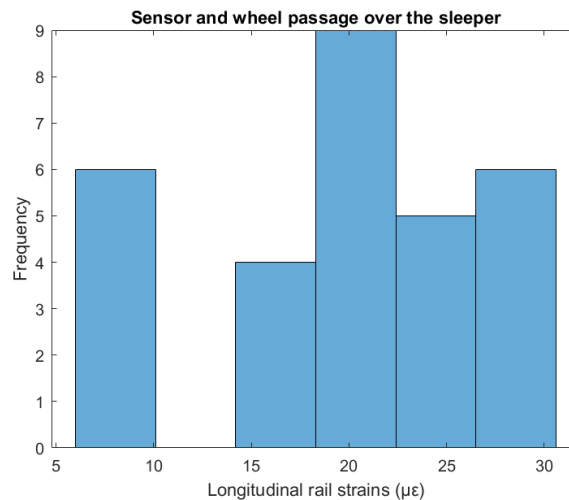


Figure 122: Histogram for the vertical strain values for determining the measurement range of the sensor when the sensor is placed between the sleepers and the wheel passes over the defect on the sleeper

It was discussed in section 6.1 that the assessment of the location for measuring the strains will be based on achieving a minimum difference of $\pm 10\%$ between the results for the value of the rail strains from the simulations with no defect and simulations with wear/RCF/voiding. This was decided because of the range of the reference strain sensor of $\pm 5\%$. The results that have been presented in sections 6.6.1 and 6.6.4 have shown that the measurement of both the vertical and longitudinal strains in the sleeper spacing has met this condition for the detection of defects that were introduced on the sleeper as well as in the sleeper spacing. The achievement of the criteria exceeding $\pm 10\%$ has been shown in Table 39, Table 40 for the detection of defects in the sleeper spacing and in Table 43, Table 44 for the detection of defects on the sleeper-supported section. However, the sensor resolution requirement ($> 5 \mu\epsilon$) has not been met for the measurement of the vertical strains in the sleeper spacing for detecting the presence of defects on the sleeper supported rail section in Figure 120 of section 6.6.4. In summary, these results hint at the possibility of fault detection by installing the sensor in the sleeper spacing. However, the recommendations will need to be validated against field experimentation in future work. The overarching objective of the research of implementing numerical simulations for structural health monitoring has been achieved through this chapter.

6.7 Summary and Conclusions from Chapter 6

The locations and orientation for installing the sensors for detecting the defects of wear, RCF and voiding that were introduced on the rail was discussed in this chapter. An approach to determining the sensor placement by screening and ranking the locations on the basis of the amplitude of the strains was presented. The correlation between the strain measurements and the wheel-rail impact force was investigated to check whether the impact force can be estimated from the strain for implementation in traditional damage prediction models. The constraints on sensor resolution and sensor range were implemented based on the properties of a reference strain sensor that was implemented in field experimentation for a railway crossing [39].

The best locations for installing the sensors on the sleeper and in between the sleeper spacing were investigated for detecting the modelled surface defects of wear and RCF, as well as voiding. The

locations where the change in the strain amplitude due to the presence of the defect were at least equal to the sensor resolution were retained during the screening step. Following the implementation of the screening process for each simulation where the defect was introduced, the intersection of the screening locations for different axle loads and defect types were obtained and the locations were ranked based on the mean change in the strain amplitude. Finally, based on the results from all the simulations, the best locations for detecting each individual defect, only the surface defects and all the defects together were determined.

The comparison of sensor placement for measuring the vertical, longitudinal and lateral strains showed that there are significantly more locations for installing the sensors for detecting the vertical and the longitudinal strains than the lateral strains. The highest overall strain amplitude as well as the amplitude for the change in the strains is obtained in the vertical direction followed by the longitudinal and lateral directions. The best sections of the rail for installing the sensors in the vertical and longitudinal orientations are the rail web and the foot respectively, despite the overall strain amplitude as well as the change in the strains being the highest on the rail head. Based on engineering judgement, it makes sense that the installation of the sensor away from the location of the wheel-rail interaction will improve sensor longevity.

It was shown that the surface defects on the sleeper can be best detected by measuring the vertical strains on the rail that is supported by the sleeper when the wheel passes over the defect on the sleeper. The foot of the switch rail is in contact with the baseplate at this section and thus can be seen to capture the change in the strains not as reliably. The surface defects on the sleeper show some probability of detection by vertical and longitudinal sensor installation on the free rail section in between the sleeper spacing when the wheel passes over the defect on the sleeper. The surface defects in between the sleeper spacing can be detected by installing the sensors for measuring the vertical and longitudinal strains in between the sleeper spacing with a lower probability by the vertical strains that are measured on the rail section that is supported by the sleeper. The probability of detecting voiding is higher by measuring the strains from the sensors that are installed on the section of the rail in between the sleeper spacing than on the sleeper.

The results for both the vertical and longitudinal strains at a distance of 9.45 m from the switch toe has shown the potential for sensor installation by demonstrating a good correlation with the contact force, achievement of the requirements around sensor range and in almost all cases the measurement of strain amplitude that is above the resolution of the reference sensor. The strain results from the numerical simulations have demonstrated the potential ability of detecting the specific defects that were introduced, regardless of whether the defect is on the sleeper supported rail section or in the sleeper spacing.

An aspect that will comprise important future work is the comparison of the strain results against the field measurements. The achievement of the modelling requirements through the comparison of the rail receptance and vertical wheel-rail interaction results against the reference were demonstrated in Chapters 3 and 4 respectively. Although the results of the strains have not yet been directly compared against a reference, the results in this chapter have been obtained whilst implementing the same simulation framework that was implemented for meeting the modelling assessment criteria in Chapters 3 and 4.

In summary, the numerical approach confirms the expected behaviour and also helps throw some light on the amplitude of the strains that would need to be captured by the strain sensors, thus helping determine the range of the strain sensor. In the future, detailed studies on testing the fault detection algorithms can be carried out by implementing the outputs that are obtained from these simulations. The model also helps carry out preliminary feasibility studies and thus reduces the time and cost of carrying out field experimentation for reaching similar conclusions.

CHAPTER 7. CONCLUSIONS AND FUTURE WORK

The contributions to the knowledge from the research that has been presented in this thesis will be summarised in this chapter. Moreover, the further work that would implement the outputs from this thesis will be suggested. The research that could not be carried out as it was beyond the scope of the research questions that were to be answered as well as the time and cost constraints will be suggested as further work.

7.1 Contributions from the thesis

Developing a numerical simulation framework that can be applied to studies on condition

monitoring of switches. The research has demonstrated the implementation of a numerical simulation approach for predicting the longitudinal positions along the switch that are susceptible to surface degradation as well as modelling the track for determining sensor placement.

In line with the recommendations from a literature evaluation, a holistic simulation of train-track dynamics in MBS was implemented for determining the crucial locations along the length of the switch that will experience rail damage by implementing the wear ($T\gamma$) number. This helped obtain a qualitative estimate of the locations that would need to be monitored for the development of surface damage. It must be emphasised that more detailed, quantitative predictions would have adopted the implementation of approaches such as models based on the Archard's wear law or the FI index, which have been explained in Chapter 2. The purpose of the degradation prediction model in this study was to provide quantitative estimates of the locations where damage will be expected on the passage of specific vehicle and for a specific grade of the rail steel and with good efficiency, which has been achieved by implementing the wear number.

Generally, the results from the model is as good as the level of detail of the vehicle and the track dynamics that is implemented in the damage prediction model. The simulations from which the results were analysed has been published and is a part of the S&C MBS benchmark project, which has been considered as the reference/standard.

The evaluation in Chapter 2 also emphasised the importance of considering the appropriate level of detail for the vehicle and the track dynamics and was reflected in the two-step MBS-FE simulation approach that was adopted for determining the sensor placement.

For the 60E1-760-1:15 switch layout, it was determined that the locations at an overall longitudinal distance of 9.5 to 10.5 m or 8.7 to 9.7 from the switch toe will be susceptible to high RCF and moderate Wear damage. Therefore, this location was chosen for detailed FE modelling for introducing the surface defects and determining sensor placement.

To this end, a representative FE model that would consider the vehicle and track dynamics was developed and was validated against the reference model that was adopted in the S&C benchmark project.

As the development of a Digital Twin model of a track model would necessitate the calibration of the track dynamics with a reference model, an approach to achieving this was demonstrated. This is a unique contribution that has not been demonstrated for the switch panel before.

To this end, a track model with the switch and stock rails, rail pads, baseplates, baseplate pads and the sleeper were modelled with solid elements. The vertical and lateral stiffness and damping representing the bedding were also incorporated into the model. The connections between the switch and the sleeper through the pads and the baseplate were important to model, as this interaction influences the amplitude and the direction of the strains, as discussed in Chapter 4. The appropriate mechanical properties of the materials, as dictated by the appropriate railway standards were included in the model.

For ensuring that the track dynamic behaviour was compatible between the MBS and the FEA models, the results for the rail receptance in the vertical and the lateral directions that were obtained from the FEA model was compared to another beam element FEA model that was based on the S&C benchmark project. Unlike the beam element FEA model, the 3D Solid element FEA model that has been developed can help analyse the element stresses and strains at various locations in the rail for

determining the sensor placement. It was shown in Chapter 3 that the modelling assessment criteria were achieved against the reference, thereby validating the track dynamics that has been implemented in the model.

The importance of modelling the track dynamics was also demonstrated in Chapter 4, when the results from the detailed FE model were compared with a model where the rail was directly fixed to the ground, i.e. had a very stiff support. The results showed that there is a significant difference in the strains as opposed to the contact forces that are captured between the two models. This has highlighted the importance of taking into account the impact of substructure dynamics along with the contact forces during condition monitoring. The results from the force-strain correlation analysis in Chapter 6 have shown that the measurement of the strains on the rail will potentially be able to deduce the contact force whilst considering the condition of the track support. If these outputs from trackside sensors are implemented along with the measurement of contact forces from on-board sensors on trains then a robust condition monitoring system can potentially be accomplished.

Mesh sensitivity analysis for modelling the wheel-rail interaction was carried out to determine the required element size for modelling the wheel-rail interaction with accuracy and efficiency. A converged result for the mesh size was obtained and has been implemented in the simulations.

The results for the vertical contact forces, vertical wheel displacement and the contact patch locations were compared between the MBS and the FEA models in Chapter 4. The results captured a good agreement between the MBS and the FEA models and have achieved the modelling assessment criteria. It was also commented that the adopted approach would vastly improve the accuracy and efficiency of the 3D FEA model when compared to another FEA model that was developed in-house.

The results for the Wear number and the comparison of the rail receptance helped determine the specific locations as well as the length of the track that would need to be modelled, thereby reducing the degrees of freedom and saving a significant amount of computational effort.

The implementation of the wheel movement and the forces acting on the wheel helped ensure that a representative amount of force was exerted through a reasonable contact patch that was placed reasonably. Past research has highlighted the difference that the lateral positioning of the contact patch would make on the result and therefore the indirect consideration of the holistic vehicle dynamics by implementing this approach would inspire more confidence in the results.

In a study that is one of its kind, the surface rail defects were introduced into the FE model of a switch and the interaction between the wheel and the rail was carried out. The influence of the change in the sleeper support was also modelled. The correlation between the vertical contact force and the rail strains were discussed in Chapter 6, highlighting the potential for monitoring the condition of the rail by measuring the rail strains.

An approach to determining sensor placement by implementing a model which is essentially a digital twin of a reference model has been demonstrated. The results for the mechanical strains that have been obtained from the model were implemented for determining sensor placement. This unique contribution involved screening the locations based on the resolution of a chosen strain sensor, followed by ranking the locations based on the amplitude of the strains.

The results from over 35 simulations that were carried out whilst implementing different inputs for the axle loads, coefficient of friction and rail defects were implemented for determining the sensor placement. The locations for installing the sensors for detecting the wear, RCF, voiding defects as well as the intersection of the locations for detecting the surface defects and all the defects were determined. The sensor placement for the occurrence of the defect at different locations, i.e. on the sleeper or in between the sleeper spacing were investigated.

It has been estimated that the measurement of the vertical and the longitudinal strains at the rail web and the foot respectively show a high potential for detecting the track defects whilst ensuring the longevity of the sensor. The amplitude of the strains that have been captured at the

recommended sensor placement locations have also been used for evaluating the strain measurement range for sensor selection.

Essentially, the main contribution of the research was to demonstrate an approach for developing a 3D FEA model of a switch that is calibrated against a reference model. A two-step MBS-FE simulation approach was adopted for incorporating a representative behaviour for the vehicle and the track dynamics. It was demonstrated through achieving the modelling assessment criteria that the results for the track dynamics as well as vertical wheel-rail interaction were compatible between the two models. The results for the mechanical behaviour of the track were then implemented for determining sensor placement and aiding sensor selection for monitoring the condition of switches.

7.2 Further work

The 3D FE model of the switch that was developed and calibrated against the reference model was applied to very specific parametric case studies due to efficiency and budget constraints, i.e. specific defect geometries, material properties, train speed and turnout layout. It is therefore acknowledged that the results that have been discussed in this thesis will be valid under very specific scenarios and more sensitivity studies will need to be carried out in the future. Essentially, a modelling framework that can be adopted for predicting defects and performing studies related to condition monitoring has been demonstrated through the original research that has been presented in this thesis.

Based on this framework, the actual application of this modelling approach to live, operating railways is the suggested next step. Moreover, a parallel field experimentation study that will help combine physics-based numerical simulations and sensor based, data driven condition monitoring is encouraged.

The following opportunities for further work have been recognised:

1. Comparing the results for the strains against field measurements.

The model that has been developed is actually based on a site in Sweden. There is also literature for the derivation of the track properties by implementing instrumentation on this site. The same track properties have been used in the reference models against which the results for the rail receptance and the wheel-rail interaction from this research have been compared. At present, the mesh convergence analysis has been adopted as an approach for inspiring confidence in the results for the strains that have been obtained from the model. However, further work would also need to include the comparison of the results for the strains that are obtained from the model and at the proposed sensor location in the field to help validate the results from the simulations.

2. Calibrating the model against an instrumented site and comparing the wheel-rail interaction results against the results that are obtained from field experiments.

A Digital Twin that is actually based on an instrumented site can be explored. The measurement for the track properties by implementing the approaches that have previously been demonstrated in the literature, such as rolling stiffness measurement vehicles can be adopted. A modelling catalogue for the different types of rolling stock that would pass over the site can be developed and the railway operation data for a particular site could be adopted for implementing a Digital Twin. Independent measurements for the wheel-rail contact force that are obtained from the sensors that are on board the vehicle can be compared against the measurements that are obtained from the sensors that are installed on the track. The numerical simulation models can be implemented for performing more detailed analysis based on the known operating conditions in the field.

3. Systems level Digital Twins, based on reduced order modelling approaches.

The efficiency of the model is a major factor that will influence its uptake as a Digital Twin. With the current figures for efficiency, a 3D FE simulation would take up to 24 hours for analysing the passage of a single wheelset. Reduced order modelling approaches, as highlighted in Chapter 2 will help achieve efficient systems level simulations with a sufficient accuracy. The fine tuning of track parameters with the field and the comparison of sensor measurement outputs with the results that are

obtained from the model will help validate the results from the model continuously. The reduced order simulations can then help estimate for the mechanical behaviour of the various track components and thereby provide insights on the possibility of maintenance intervention.

4. Testing fault detection algorithms and the potential for condition monitoring by implementing mechanics-based damage prediction models.

In Chapter 2, the various models that can be implemented for detecting the main types of surface failure mechanisms were explained. The possibility of obtaining the inputs that are needed for substitution in the damage prediction models can be investigated from the Digital twin. An example of this has been demonstrated in Chapter 6, where the possibility of accurately predicting the impact force from the strain sensor outputs was assessed for the different proposed locations for installing the sensors. Similarly, the data for signal processing for developing and testing condition monitoring algorithms can be generated from the model. Therefore, Digital Twins for the different switch layouts on railway networks can be modelled for testing the fault detection algorithms that will be able to detect, diagnose and predict switch damage [12].

LIST OF REFERENCES

1. Whitmore, S. *Understanding Track Engineering*; The Permanent Way Institution, 2014; ISBN 978-0-903489-04-1.
2. Wright, C. R. 1603 Turnouts Available online: <https://the-contact-patch.com/book/rail/r1603-turnouts> (accessed on May 14, 2022).
3. Morgan, J.C. *British Railway Track- Volume 1- Design Part 2- Switches and Crossings*; The Permanent Way Institution: Chesterfield, 2009.
4. Bezin, Y.; Pålsson, B.A.; Kik, W.; Schreiber, P.; Clarke, J.; Beuter, V.; Sebes, M.; Persson, I.; Magalhaes, H.; Wang, P.; et al. Multibody simulation benchmark for dynamic vehicle–track interaction in switches and crossings: results and method statements. *Veh. Syst. Dyn.* **2021**, 1–38, doi:10.1080/00423114.2021.1959038.
5. Dixon, R.; Gofton, N. Next generation switches and crossings: the outcomes of project S-CODE Available online: <https://www.globalrailwayreview.com/article/94357/switches-crossings-scode-outcomes/> (accessed on Nov 5, 2022).
6. Railway Signalling Switch & Crossing Components Available online: <https://www.railwaysignallingconcepts.in/railway-signalling-switch-crossing-components/> (accessed on Nov 5, 2022).
7. Cornish, A.; Smith, R.A.; Dear, J. Monitoring of strain of in-service railway switch rails through field experimentation. *Proc. Inst. Mech. Eng. Part F J. Rail Rapid Transit* **2016**, 230, 1429–1439, doi:10.1177/0954409715624723.
8. University of Birmingham *S&C Failure Analysis*; 2019;

9. Cornish, A. Life-time monitoring of in service switches and crossings through field experimentation, PhD thesis. Imperial College London. London. United Kingdom, 2014.
10. Grossoni, I.; Hughes, P.; Bezin, Y.; Bevan, A.; Jaiswal, J. Observed failures at railway turnouts: Failure analysis, possible causes and links to current and future research. *Eng. Fail. Anal.* **2021**, *119*, 104987, doi:10.1016/j.engfailanal.2020.104987.
11. Rail Accident Investigation Branch *Rail Accident Report- Derailment at Grayrigg 23 February 2007*; London, United Kingdom, 2011;
12. Pillai, N.; Shih, J.Y.; Roberts, C. Evaluation of numerical simulation approaches for simulating train–track interactions and predicting rail damage in railway switches and crossings (S&Cs). *Infrastructures* **2021**, *6*, doi:10.3390/infrastructures6050063.
13. Olofsson, U.; Zhu, Y.; Abbasi, S.; Lewis, R.; Lewis, S. Tribology of the wheel-rail contact-aspects of wear, particle emission and adhesion. *Veh. Syst. Dyn.* **2013**, *51*, 1091–1120, doi:10.1080/00423114.2013.800215.
14. Ekberg, A.; Åkesson, B.; Kabo, E. Wheel/rail rolling contact fatigue - Probe, predict, prevent. *Wear* **2014**, *314*, 2–12, doi:10.1016/j.wear.2013.12.004.
15. Yang, R.; Cao, S.; Kang, W.; Li, J.; Jiang, X. Mechanism Analysis of Spalling Defect on Rail Surface under Rolling Contact Conditions. *Math. Probl. Eng.* **2018**, *2018*, doi:10.1155/2018/7012710.
16. Ringsberg, J.W.; Bjarnehed, H.; Johansson, A.; Josefson, B.L. Rolling contact fatigue of rails - Finite element modelling of residual stresses, strains and crack initiation. *Proc. Inst. Mech. Eng. Part F J. Rail Rapid Transit* **2000**, *214*, 7–19,

doi:10.1243/0954409001531207.

17. Kaewunruen, S.; Ishida, M.; Marich, S. Dynamic wheel-rail interaction over rail squat defects. *Acoust. Aust.* **2015**, *43*, 97–107, doi:10.1007/s40857-014-0001-4.
18. Coleman, I. The Development of Modelling Tools for Railway Switches and Crossings, PhD thesis, Imperial College London, 2014.
19. Capacity4Rail *Deliverable D13.1: Operational failure modes of Switches and Crossings*; Brussels, Belgium, 2015;
20. Grassie, S.L.; Kalousek, J. Rail Corrugation: Characteristics, Causes and Treatments. *Proc. Inst. Mech. Eng. Part F J. Rail Rapid Transit* **1993**, doi:10.1243/PIME_PROC_1993_207_227_02.
21. Grassie, S.L. Rail corrugation: Characteristics, causes, and treatments. *Proc. Inst. Mech. Eng. Part F J. Rail Rapid Transit* **2009**, *223*, 581–596, doi:10.1243/09544097JRRT264.
22. Nielsen, J.C.O.; Pålsson, B.A.; Torstensson, P.T. Switch panel design based on simulation of accumulated rail damage in a railway turnout. *Wear* **2016**, *366–367*, 241–248, doi:10.1016/j.wear.2016.06.021.
23. Brouzoulis, J.; Torstensson, P.T.; Stock, R.; Ekh, M. Prediction of wear and plastic flow in rails-Test rig results, model calibration and numerical prediction. *Wear* **2011**, *271*, 92–99, doi:10.1016/j.wear.2010.10.021.
24. Xin, L.; Markine, V.L.; Shevtsov, I.Y. Numerical procedure for fatigue life prediction for railway turnout crossings using explicit finite element approach. *Wear* **2016**, *366–367*, 167–179, doi:10.1016/j.wear.2016.04.016.

25. Li, S.; Li, Z.; Núñez, A.; Dollevoet, R. New insights into the short pitch corrugation enigma based on 3D-FE coupled dynamic vehicle-track modeling of frictional rolling contact. *Appl. Sci.* **2017**, *7*, 1–23, doi:10.3390/app7080807.
26. Rail Accident Investigation Branch Rail Accident Report - Derailments at London Waterloo- 11 September and 24 October 2006. **2007**.
27. Rail Accident Investigation Branch *Rail Accident Report - Derailment near Exhibition Centre station, Glasgow- 3 September 2007; 2009;*
28. Rail Accident Investigation Branch *Rail Accident Report - Derailment at Princes Street Gardens, Edinburgh - 27 July 2011; 2012;*
29. Rail Accident Investigation Branch *Rail Accident Report - Derailment at Archway - 2 June 2006; 2006.*
30. Rail Accident Investigation Branch *Rail Accident Report - Derailment at Primrose Hill / Camden Road West Junction - 15 October 2013; 2014.*
31. Rusu, M.F. Automation of railway switch and crossing inspection, University of Birmingham, 2015.
32. Network Rail Track Engineering *The Measurement of Sidewear in Plain Rail and Rails with Full Head Section: Instructions for Use of the 'NR4' Stepped Sidewear Gauge;* 2005.
33. Moubray, J. *Reliability-centered maintenance;* Industrial Press Inc., 2001.
34. Buggy, S.J.; James, S.W.; Staines, S.; Carroll, R.; Kitson, P. V.; Farrington, D.; Drewett, L.; Jaiswal, J.; Tatam, R.P. Railway track component condition monitoring using optical fibre Bragg grating sensors. *Meas. Sci. Technol.* **2016**, *27*,

doi:10.1088/0957-0233/27/5/055201.

35. Oßberger, U.; Kollment, W.; Eck, S. Insights towards Condition Monitoring of Fixed Railway Crossings. *Procedia Struct. Integr.* **2017**, *4*, 106–114, doi:10.1016/j.prostr.2017.07.007.
36. Kerrouche, A.; Najeh, T.; Jaen-Sola, P. Experimental strain measurement approach using fiber bragg grating sensors for monitoring of railway switches and crossings. *Sensors* **2021**, *21*, doi:10.3390/s21113639.
37. Liu, X.; Markine, V.L. Train hunting related fast degradation of a railway crossing-condition monitoring and numerical verification. *Sensors (Switzerland)* **2020**, *20*, doi:10.3390/s20082278.
38. Liu, X.; Markine, V.L.; Wang, H.; Shevtsov, I.Y. Experimental tools for railway crossing condition monitoring (crossing condition monitoring tools). *Meas. J. Int. Meas. Confed.* **2018**, *129*, 424–435, doi:10.1016/J.MEASUREMENT.2018.07.062.
39. Shih, J.-Y.; Weston, P.; Entezami, M.; Roberts, C. Dynamic characteristics of a switch and crossing on the West Coast main line in the UK. *Railw. Eng. Sci.* **2022**, doi:10.1007/s40534-021-00269-4.
40. Hamarat, M.; Kaewunruen, S.; Papaelias, M.; Silvast, M. New insights from multibody dynamic analyses of a turnout system under impact loads. *Appl. Sci.* **2019**, *9*, doi:10.3390/app9194080.
41. Shih, J.-Y.; Ambur, R.; Dixon, R. Developing a detailed multi-body dynamic model of a turnout based on its finite element model. *Veh. Syst. Dyn.* **2021**, 1–14, doi:10.1080/00423114.2021.1981952.

42. Ansys Inc. Ansys Twin Builder- Create and Deploy Digital Twin Models Available online: <https://www.ansys.com/en-gb/products/digital-twin/ansys-twin-builder> (accessed on Oct 12, 2023).
43. Xu, J.; Wang, P.; Wang, L.; Chen, R. Effects of profile wear on wheel-rail contact conditions and dynamic interaction of vehicle and turnout. *Adv. Mech. Eng.* **2016**, *8*, 1–14, doi:10.1177/1687814015623696.
44. Kassa, E.; Nielsen, J.C.O. Dynamic train-turnout interaction in an extended frequency range using a detailed model of track dynamics. *J. Sound Vib.* **2009**, *320*, 893–914, doi:10.1016/j.jsv.2008.08.028.
45. Skrypnik, R.; Ekh, M.; Nielsen, J.C.O.; Pålsson, B.A. Prediction of plastic deformation and wear in railway crossings – Comparing the performance of two rail steel grades. *Wear* **2019**, *428–429*, 302–314, doi:10.1016/j.wear.2019.03.019.
46. Wang, P.; Xu, J.; Xie, K.; Chen, R. Numerical simulation of rail profiles evolution in the switch panel of a railway turnout. *Wear* **2016**, *366–367*, 105–115, doi:10.1016/j.wear.2016.04.014.
47. Ma, X.; Wang, P.; Xu, J.; Chen, R.; Wang, J. Assessment of non-Hertzian wheel-rail contact models for numerical simulation of rail damages in switch panel of railway turnout. *Wear* **2019**, *432–433*, 648–657, doi:10.1016/j.wear.2019.05.027.
48. Pålsson, B.A.; Nielsen, J.C.O. Wheel-rail interaction and damage in switches and crossings. *Veh. Syst. Dyn.* **2012**, *50*, 43–58, doi:10.1080/00423114.2011.560673.
49. Karttunen, K.; Kabo, E.; Ekberg, A. Estimation of gauge corner and flange root degradation from rail, wheel and track geometries. *Wear* **2016**, *366–367*, 294–302,

doi:10.1016/j.wear.2016.03.030.

50. Xu, J.; Wang, P.; Wang, J.; An, B.; Chen, R. Numerical analysis of the effect of track parameters on the wear of turnout rails in high-speed railways. *Proc. Inst. Mech. Eng. Part F J. Rail Rapid Transit* **2018**, *232*, 709–721, doi:10.1177/0954409716685188.
51. Hiensch, E.J.M.; Burgelman, N. Switch Panel wear loading—a parametric study regarding governing train operational factors. *Veh. Syst. Dyn.* **2017**, *55*, 1384–1404, doi:10.1080/00423114.2017.1313435.
52. Johansson, A.; Pålsson, B.; Ekh, M.; Nielsen, J.C.O.; Ander, M.K.A.; Brouzoulis, J.; Kassa, E. Simulation of wheel-rail contact and damage in switches & crossings. *Wear* **2011**, *271*, 472–481, doi:10.1016/j.wear.2010.10.014.
53. Ma, X.; Wang, P.; Xu, J.; Chen, R. Parameters studies on surface initiated rolling contact fatigue of turnout rails by three-level unreplicated saturated factorial design. *Appl. Sci.* **2018**, *8*, doi:10.3390/app8030461.
54. Burgelman, N.; Li, Z.; Dollevoet, R. A new rolling contact method applied to conformal contact and the train-turnout interaction. *Wear* **2014**, *321*, 94–105, doi:10.1016/j.wear.2014.10.008.
55. Kassa, E.; Andersson, C.; Nielsen, J.C.O. Simulation of dynamic interaction between train and railway turnout. *Veh. Syst. Dyn.* **2006**, *44*, 247–258, doi:10.1080/00423110500233487.
56. Lau, A.; Hoff, I. Simulation of Train-Turnout Coupled Dynamics Using a Multibody Simulation Software. *Model. Simul. Eng.* **2018**, *2018*, doi:10.1155/2018/8578272.
57. Bezin, Y.; Kostovasilis, D.; Sambo, B. *Relative Movement of Switch/Stock Rails and*

the Wheel/Rail Interaction Interface; 2020; ISBN 9783030380762.

58. Wang, P.; Ma, X.; Xu, J.; Wang, J.; Chen, R. Numerical investigation on effect of the relative motion of stock/switch rails on the load transfer distribution along the switch panel in high-speed railway turnout. *Veh. Syst. Dyn.* **2019**, *57*, 226–246, doi:10.1080/00423114.2018.1458992.
59. Pålsson, B.A. A linear wheel–crossing interaction model. *Proc. Inst. Mech. Eng. Part F J. Rail Rapid Transit* **2018**, *232*, 2431–2443, doi:10.1177/0954409718772984.
60. Bezin, Y.; Sarmiento-Carnevali, M.L.; Sichani, M.S.; Neves, S.; Kostovasilis, D.; Bemment, S.D.; Harrison, T.J.; Ward, C.P.; Dixon, R. Dynamic analysis and performance of a repoint track switch. *Veh. Syst. Dyn.* **2020**, *58*, 843–863, doi:10.1080/00423114.2019.1612925.
61. Lagos, R.F.; Alonso, A.; Vinolas, J.; Pérez, X. Rail vehicle passing through a turnout: Analysis of different turnout designs and wheel profiles. *Proc. Inst. Mech. Eng. Part F J. Rail Rapid Transit* **2012**, *226*, 587–602, doi:10.1177/0954409712445114.
62. Casanueva, C.; Doulgerakis, E.; Jönsson, P.A.; Stichel, S. Influence of switches and crossings on wheel profile evolution in freight vehicles. *Veh. Syst. Dyn.* **2014**, *52*, 317–337, doi:10.1080/00423114.2014.898779.
63. Sun, Y.Q.; Cole, C.; Boyd, P. A numerical method using VAMPIRE modelling for prediction of turnout curve wheel-rail wear. *Wear* **2011**, *271*, 482–491, doi:10.1016/j.wear.2010.10.010.
64. Nicklisch, D.; Kassa, E.; Nielsen, J.; Ekh, M.; Iwnicki, S. Geometry and stiffness optimization for switches and crossings, and simulation of material degradation. *Proc.*

- Inst. Mech. Eng. Part F J. Rail Rapid Transit* **2010**, 224, 279–292,
doi:10.1243/09544097JRRT348.
65. Pålsson, B.A. Design optimisation of switch rails in railway turnouts. *Veh. Syst. Dyn.* **2013**, 3114, 37–41, doi:10.1080/00423114.2013.807933.
66. Pålsson, B.A.; Nielsen, J.C.O. Track gauge optimisation of railway switches using a genetic algorithm. *Veh. Syst. Dyn.* **2012**, 50, 365–387,
doi:10.1080/00423114.2012.665167.
67. Pålsson, B.A. Optimisation of railway crossing geometry considering a representative set of wheel profiles. *Veh. Syst. Dyn.* **2015**, 53, 274–301,
doi:10.1080/00423114.2014.998242.
68. Pålsson, B.A.; Nielsen, J.C.O. Dynamic vehicle-track interaction in switches and crossings and the influence of rail pad stiffness - Field measurements and validation of a simulation model. *Veh. Syst. Dyn.* **2015**, 53, 734–755,
doi:10.1080/00423114.2015.1012213.
69. Jorge, P.; Bezin, Y.; Grossoni, I.; Neves, S. Modelling Track Flexibility in Turnouts Using MBS Approach. In Proceedings of the Advances in Dynamics of Vehicles on Roads and Tracks; Klomp, M., Bruzelius, F., Nielsen, J., Lillemyr, A., Eds.; Springer International Publishing: Cham, 2020; pp. 359–366.
70. Lu, C.; Rodríguez-Arana, B.; Prada, J.G.; Meléndez, J.; Martínez-Esnaola, J.M. A Full explicit finite element simulation for the study of interaction between wheelset and switch panel. *Veh. Syst. Dyn.* **2020**, 58, 229–248,
doi:10.1080/00423114.2019.1575425.

71. Pletz, M.; Daves, W.; Ossberger, H. A wheel set/crossing model regarding impact, sliding and deformation-Explicit finite element approach. *Wear* **2012**, *294–295*, 446–456, doi:10.1016/j.wear.2012.07.033.
72. Gao, Y.; Wang, P.; Liu, Y.; Xu, J.; Dong, Z.; Wang, K. Investigation on wheel-rail contact and damage behavior in a flange bearing frog with explicit finite element method. *Math. Probl. Eng.* **2019**, *2019*, doi:10.1155/2019/1209352.
73. Pålsson, B.A.; Nielsen, J.C.O. Wheel-rail interaction and damage in switches and crossings. *Veh. Syst. Dyn.* **2012**, *50*, 43–58, doi:10.1080/00423114.2011.560673.
74. Pletz, M.; Daves, W.; Yao, W.; Ossberger, H. Rolling contact fatigue of three crossing nose materials-Multiscale FE approach. *Wear* **2014**, *314*, 69–77, doi:10.1016/j.wear.2013.11.013.
75. Wiedorn, J.; Daves, W.; Ossberger, U.; Ossberger, H.; Pletz, M. Numerical assessment of materials used in railway crossings by predicting damage initiation – Validation and application. *Wear* **2018**, *414–415*, 136–150, doi:10.1016/j.wear.2018.08.011.
76. Skrypnik, R.; Nielsen, J.C.O.; Ekh, M.; Pålsson, B.A. Metamodelling of wheel–rail normal contact in railway crossings with elasto-plastic material behaviour. *Eng. Comput.* **2019**, *35*, 139–155, doi:10.1007/s00366-018-0589-3.
77. El-sayed, H.M.; Lotfy, M.; El-din Zohny, H.N.; Riad, H.S. Prediction of fatigue crack initiation life in railheads using finite element analysis. *Ain Shams Eng. J.* **2018**, *9*, 2329–2342, doi:10.1016/j.asej.2017.06.003.
78. Xin, L.; Markine, V.; Shevtsov, I. Analysis of the effect of repair welding/grinding on the performance of railway crossings using field measurements and finite element

- modeling. *Proc. Inst. Mech. Eng. Part F J. Rail Rapid Transit* **2018**, 232, 798–815, doi:10.1177/0954409717693960.
79. Ma, Y.; Markine, V.L.; Mashal, A.A. Rail surface crack initiation analysis using multi-scale coupling approach. In Proceedings of the The Dynamics of Vehicles on Roads and Tracks - Proceedings of the 24th Symposium of the International Association for Vehicle System Dynamics, IAVSD 2015; 2016; pp. 1611–1622.
 80. Wei, W.; Yuan, C.; Wu, R.; Chen, F.; Jiao, W. Wear of a crossing under dynamic wheel impact. *Wear* **2019**, 436–437, 202997, doi:10.1016/j.wear.2019.202997.
 81. Wiest, M.; Daves, W.; Fischer, F.D.; Ossberger, H. Deformation and damage of a crossing nose due to wheel passages. *Wear* **2008**, 265, 1431–1438, doi:10.1016/j.wear.2008.01.033.
 82. Gao, Y.; Xu, J.; Wang, P.; Dong, Z.; Liu, Y.; Wang, K. Numerical study of the transition characteristics and related degradation at the flange bearing frog. *Proc. Inst. Mech. Eng. Part F J. Rail Rapid Transit* **2020**, doi:10.1177/0954409720906636.
 83. Pletz, M.; Daves, W.; Ossberger, H. A wheel passing a crossing nose: Dynamic analysis under high axle loads using finite element modelling. *Proc. Inst. Mech. Eng. Part F J. Rail Rapid Transit* **2012**, 226, 603–611, doi:10.1177/0954409712448038.
 84. Xiao, J.; Zhang, F.; Qian, L. Numerical simulation of stress and deformation in a railway crossing. *Eng. Fail. Anal.* **2011**, 18, 2296–2304, doi:10.1016/j.engfailanal.2011.08.006.
 85. Wiedorn, J.; Daves, W.; Ossberger, U.; Ossberger, H.; Pletz, M. Simplified explicit finite element model for the impact of a wheel on a crossing – Validation and

- parameter study. *Tribol. Int.* **2017**, *111*, 254–264, doi:10.1016/j.triboint.2017.03.023.
86. Ma, Y.; Mashal, A.A.; Markine, V.L. Modelling and experimental validation of dynamic impact in 1:9 railway crossing panel. *Tribol. Int.* **2018**, *118*, 208–226, doi:10.1016/j.triboint.2017.09.036.
87. Guo, S.L.; Sun, D.Y.; Zhang, F.C.; Feng, X.Y.; Qian, L.H. Damage of a Hadfield steel crossing due to wheel rolling impact passages. *Wear* **2013**, *305*, 267–273, doi:10.1016/j.wear.2013.01.019.
88. Kovalchuk, V.; Bolzhelarskyi, Y.; Parneta, B.; Pentsak, A.; Petrenko, O.; Mudryy, I. Evaluation of the stressed-strained state of crossings of the 1/11 type turnouts by the finite element method. *Eastern-European J. Enterp. Technol.* **2017**, *4*, 10–16, doi:10.15587/1729-4061.2017.107024.
89. Li, Z.; Zhao, X.; Dollevoet, R.; Molodova, M. Differential wear and plastic deformation as causes of squat at track local stiffness change combined with other track short defects. *Veh. Syst. Dyn.* **2008**, *46*, 237–246, doi:10.1080/00423110801935855.
90. Xin, L.; Markine, V.L.; Shevtsov, I.Y. Analysis approach of turnout crossing performance by field measurements and finite element modeling. In Proceedings of the The Dynamics of Vehicles on Roads and Tracks - Proceedings of the 24th Symposium of the International Association for Vehicle System Dynamics, IAVSD 2015; 2016; pp. 1593–1600.
91. Xin, L.; Markine, V.L.; Shevtsov, I.Y. Numerical analysis of the dynamic interaction between wheel set and turnout crossing using the explicit finite element method. *Veh. Syst. Dyn.* **2016**, *54*, 301–327, doi:10.1080/00423114.2015.1136424.

92. Wei, Z.; Núñez, A.; Liu, X.; Dollevoet, R.; Li, Z. Multi-criteria evaluation of wheel/rail degradation at railway crossings. *Tribol. Int.* **2020**, *144*, doi:10.1016/j.triboint.2019.106107.
93. Wei, Z.; Núñez, A.; Boogaard, A.; Dollevoet, R.; Li, Z. Method for evaluating the performance of railway crossing rails after long-term service. *Tribol. Int.* **2018**, *123*, 337–348, doi:10.1016/j.triboint.2018.03.016.
94. Wei, Z.; Shen, C.; Li, Z.; Dollevoet, R. Wheel-Rail Impact at Crossings: Relating Dynamic Frictional Contact to Degradation. *J. Comput. Nonlinear Dyn.* **2017**, *12*, doi:10.1115/1.4035823.
95. Shih, J.Y.; Hemida, H.; Stewart, E.; Roberts, C. Understanding the impact of train run-throughs on railway switches using finite element analysis. *Proc. Inst. Mech. Eng. Part F J. Rail Rapid Transit* **2019**, *233*, 359–369, doi:10.1177/0954409718795759.
96. Sae Siew, J.; Mirza, O.; Kaewunruen, S. Nonlinear Finite Element Modelling of Railway Turnout System considering Bearer/Sleeper-Ballast Interaction. *J. Struct.* **2015**, *2015*, 1–11, doi:10.1155/2015/598562.
97. Salajka, V.; Smolka, M.; Kala, J.; Plášek, O. Dynamical response of railway switches and crossings. *MATEC Web Conf.* **2017**, *107*, 1–6, doi:10.1051/mateconf/201710700018.
98. Smith, M. ABAQUS/Standard User's Manual, Version 6.9; Dassault Systèmes Simulia Corp.: Providence, RI, USA, 2009.
99. Bezin, Y. An Integrated Flexible Track System Model for Railway Vehicle Dynamics, Manchester Metropolitan University, 2008.

100. AG, S. *Simpack Documentation*; 2018;
101. Kassa, E.; Johansson, G. Simulation of train-turnout interaction and plastic deformation of rail profiles. *Veh. Syst. Dyn.* **2006**, *44*, 349–359, doi:10.1080/00423110600871566.
102. Li, X.; Nielsen, J.C.O.; Pålsson, B.A. Simulation of track settlement in railway turnouts. *Veh. Syst. Dyn.* **2014**, *52*, 421–439, doi:10.1080/00423114.2014.904905.
103. Zhu, J.Y.; Thompson, D.J. Characterization of forces, dynamic response, and sound radiation from an articulated switch sleeper in a turnout system. *Proc. Inst. Mech. Eng. Part F J. Rail Rapid Transit* **2010**, *224*, 53–60, doi:10.1243/09544097JRRT302.
104. Markine, V.L.; Steenbergen, M.J.M.M.; Shevtsov, I.Y. Combatting RCF on switch points by tuning elastic track properties. *Wear* **2011**, *271*, 158–167, doi:10.1016/j.wear.2010.10.031.
105. Grossoni, I.; Bezin, Y.; Neves, S. Optimisation of support stiffness at railway crossings. *Veh. Syst. Dyn.* **2018**, *56*, 1072–1096, doi:10.1080/00423114.2017.1404617.
106. Grossoni, I.; Le Pen, L.M.; Jorge, P.; Bezin, Y.; Watson, G.V.R.; Kostovasilis, D.; Powrie, W. The role of stiffness variation in switches and crossings: Comparison of vehicle–track interaction models with field measurements. *Proc. Inst. Mech. Eng. Part F J. Rail Rapid Transit* **2019**, *0*, 1–14, doi:10.1177/0954409719892146.
107. Hamarat, M.; Papaelias, M.; Silvast, M.; Kaewunruen, S. The effect of unsupported sleepers/bearers on dynamic phenomena of a railway turnout system under impact loads. *Appl. Sci.* **2020**, *10*, doi:10.3390/app10072320.
108. Ren, Z.; Sun, S.; Zhai, W. Study on lateral dynamic characteristics of vehicle/turnout system. *Veh. Syst. Dyn.* **2005**, *43*, 285–303, doi:10.1080/00423110500083262.

109. Xu, J.; Wang, P.; Ma, X.; Gao, Y.; Chen, R. Stiffness characteristics of high-speed railway turnout and the effect on the dynamic train-Turnout interaction. *Shock Vib.* **2016**, *2016*, doi:10.1155/2016/1258681.
110. Wan, C.; Markine, V.L.; Shevtsov, I.Y. Analysis of train / turnout vertical interaction using a fast numerical model and validation of that model. **2014**, *228*, 730–743, doi:10.1177/0954409713489118.
111. Wiest, M.; Kassa, E.; Daves, W.; Nielsen, J.C.O.; Ossberger, H. Assessment of methods for calculating contact pressure in wheel-rail/switch contact. *Wear* **2008**, *265*, 1439–1445, doi:10.1016/j.wear.2008.02.039.
112. Andersson, C.; Dahlberg, T. Wheel/rail impacts at a railway turnout crossing. *Proc. Inst. Mech. Eng. Part F J. Rail Rapid Transit* **1998**, *212*, 123–134, doi:10.1243/0954409981530733.
113. Xu, J.; Wang, J.; Wang, P.; Chen, J.; Gao, Y.; Chen, R.; Xie, K. Study on the derailment behaviour of a railway wheelset with solid axles in a railway turnout. *Veh. Syst. Dyn.* **2020**, *58*, 123–143, doi:10.1080/00423114.2019.1566558.
114. Li, X.; Torstensson, P.T.; Nielsen, J.C.O. Simulation of vertical dynamic vehicle–track interaction in a railway crossing using Green’s functions. *J. Sound Vib.* **2017**, *410*, 318–329, doi:10.1016/j.jsv.2017.08.037.
115. Chen, R.; Chen, J.; Wang, P.; Fang, J.; Xu, J. Impact of wheel profile evolution on wheel-rail dynamic interaction and surface initiated rolling contact fatigue in turnouts. *Wear* **2019**, *438–439*, doi:10.1016/j.wear.2019.203109.
116. Qian, Y.; Wang, P.; Chen, J.; Bethel Lulu, G.; Xu, J.; An, B. Numerical investigation

- of the influence of the creep curve on the wheel–rail contact damage in high-speed railway turnouts. *Proc. Inst. Mech. Eng. Part F J. Rail Rapid Transit* **2018**, *0*, 1–11, doi:10.1177/0954409718819574.
117. Shu, X.; Wilson, N.; Sasaoka, C.; Elkins, J. Development of a real-time wheel/rail contact model in NUCARS® 1 and application to diamond crossing and turnout design simulations. *Veh. Syst. Dyn.* **2006**, *44*, 251–260, doi:10.1080/00423110600870378.
 118. Alfi, S.; Bruni, S. Mathematical modelling of train – turnout interaction. **2009**, *3114*, doi:10.1080/00423110802245015.
 119. Li, X.; Nielsen, J.C.O.; Torstensson, P.T. Simulation of wheel–rail impact load and sleeper–ballast contact pressure in railway crossings using a Green’s function approach. *J. Sound Vib.* **2019**, *463*, doi:10.1016/j.jsv.2019.114949.
 120. Torstensson, P.T.; Squicciarini, G.; Krüger, M.; Pålsson, B.A.; Nielsen, J.C.O.; Thompson, D.J. Wheel–rail impact loads and noise generated at railway crossings – Influence of vehicle speed and crossing dip angle. *J. Sound Vib.* **2019**, *456*, 119–136, doi:10.1016/j.jsv.2019.04.034.
 121. Hertz, H. Über die Berührung fester elastischer Körper. *J. für die reine und Angew. Math.* **1881**, *319*, 156–171.
 122. Piotrowski, J.; Kik, W. A simplified model of wheel/rail contact mechanics for non-Hertzian problems and its application in rail vehicle dynamic simulations. *Veh. Syst. Dyn.* **2008**, *46*, 27–48, doi:10.1080/00423110701586444.
 123. Ayasse, J.B.; Chollet, H. Determination of the wheel rail contact patch in semi-Hertzian conditions. *Veh. Syst. Dyn.* **2005**, *43*, 161–172,

doi:10.1080/00423110412331327193.

124. Sichani, M.S.; Enblom, R.; Berg, M. A novel method to model wheel-rail normal contact in vehicle dynamics simulation. *Veh. Syst. Dyn.* **2014**, *52*, 1752–1764, doi:10.1080/00423114.2014.961932.
125. Kalker, J.J. Wheel-rail rolling contact theory. *Wear* **1991**, *144*, 243–261, doi:10.1016/0043-1648(91)90018-P.
126. Sebès, M.; Chevalier, L.; Ayasse, J.B.; Chollet, H. A fast-simplified wheel-rail contact model consistent with perfect plastic materials. *Veh. Syst. Dyn.* **2012**, *50*, 1453–1471, doi:10.1080/00423114.2012.669483.
127. Zhao, X.; Li, Z. The solution of frictional wheel – rail rolling contact with a 3D transient finite element model : Validation and error analysis. *Wear* **2011**, *271*, 444–452, doi:10.1016/j.wear.2010.10.007.
128. Iwnicki, S. *Handbook of railway vehicle dynamics*; 1st Editio.; CRC Press: Boca Raton, USA, 2006; ISBN 9781420004892.
129. Sh. Sichani, M.; Enblom, R.; Berg, M. An alternative to FASTSIM for tangential solution of the wheel–rail contact. *Veh. Syst. Dyn.* **2016**, *54*, 748–764, doi:10.1080/00423114.2016.1156135.
130. Shen, Z.Y.; Hedrick, J.K.; Elkins, J.A. Comparison of Alternative Creep Force Models for Rail Vehicle Dynamic Analysis. *Dyn. Veh. Roads Tracks, Proc. IAVSD Symp. (International Assoc.* **1984**, 591–605.
131. Vermeulen, P.J.; Johnson, K.L. Contact of nonspherical elastic bodies transmitting tangential forces. *J. Appl. Mech. Trans. ASME* **1964**, *31*, 338–340,

doi:10.1115/1.3629610.

132. Sebès, M.; Chollet, H.; Ayasse, J.B.; Chevalier, L. A multi-Hertzian contact model considering plasticity. *Wear* **2014**, *314*, 118–124, doi:10.1016/j.wear.2013.11.036.
133. Evans, J.R.; Burstow, M.C. Vehicle / track interaction and rolling contact fatigue in rails in the UK. **2007**, *3114*, doi:10.1080/00423110600883652.
134. Burstow, M. *Whole Life Rail Model application and development: Development of a rolling contact fatigue damage parameter (Burstow report)*; 2003.
135. Evans, J.R.; Lee, T.K.Y.; Hon, C.C. Optimising the wheel/rail interface on a modern urban rail system. In Proceedings of the Vehicle System Dynamics; 2008; Vol. 46, pp. 119–127.
136. Harvey, R.F.; McEwen, I.J. *The Relationship between Wear Number and Wheel/Rail Wear in the Laboratory and the Field. British Rail Research Report TM-VDY-001*; 1986;
137. Archard, J.F. Contact and rubbing of flat surfaces. *J. Appl. Phys.* **1953**, *24*, 981–988, doi:10.1063/1.1721448.
138. Peng, B.; Iwnicki, S.; Shackleton, P.; Crosbee, D. Comparison of wear models for simulation of railway wheel polygonization. *Wear* **2019**, *436–437*, 203010, doi:10.1016/j.wear.2019.203010.
139. Meghoo, A.; Loendersloot, R.; Tinga, T. Rail wear and remaining life prediction using meta-models. *Int. J. Rail Transp.* **2020**, *8*, 1–26, doi:10.1080/23248378.2019.1621780.
140. Jiang, Y.; Sehitoglu, H. A model for rolling contact failure. *Wear* **1999**, *224*, 38–49, doi:10.1016/S0043-1648(98)00311-1.

141. Johnson, K.L. The Strength of Surfaces in Rolling Contact. *Proc. Inst. Mech. Eng. Part C Mech. Eng. Sci.* **1989**, *203*, 151–163, doi:10.1243/PIME_PROC_1989_203_100_02.
142. Sun, Y.Q.; Spiryagin, M.; Cole, C.; Nielsen, D. Wheel-rail wear investigation on a heavy haul balloon loop track through simulations of slow speed wagon dynamics. *Transport* **2018**, *33*, 843–852, doi:10.3846/16484142.2017.1355843.
143. Dang Van, K.; Maitournam, M.H.; Moumni, Z.; Roger, F. A comprehensive approach for modeling fatigue and fracture of rails. *Eng. Fract. Mech.* **2009**, *76*, 2626–2636, doi:10.1016/j.engfracmech.2008.12.020.
144. Ohno, N.; Wang, J.D. Kinematic hardening rules with critical state of dynamic recovery, part I: formulation and basic features for ratchetting behavior. *Int. J. Plast.* **1993**, *9*, 375–390, doi:10.1016/0749-6419(93)90042-O.
145. Lemaitre, J.; Chaboche, J.-L. *Mechanics of Solid Materials*; Cambridge University Press: Cambridge, UK, 1990; ISBN 9780521328531.
146. Johansson, G.; Ahlström, J.; Ekh, M. Parameter identification and modeling of large ratcheting strains in carbon steel. *Comput. Struct.* **2006**, *84*, 1002–1011, doi:10.1016/j.compstruc.2006.02.016.
147. Shih, J.Y.; Kostovasilis, D.; Bezin, Y.; Thompson, D.J. Modelling options for ballast track dynamics. In Proceedings of the 24th International Congress on Sound and Vibration, ICSV 2017; 2017; pp. 1–15.
148. Kassa, E.; Nielsen, J.C.O. Dynamic interaction between train and railway turnout: Full-scale field test and validation of simulation models. *Veh. Syst. Dyn.* **2008**, *46*, 521–534, doi:10.1080/00423110801993144.

149. David, F.N. *Tables of the ordinates and probability integral of the distribution of the correlation coefficient in small samples.*; Cambridge University Press: Cambridge, UK, 1938.
150. Bonett, D.G.; Cruz, S. Sample size requirements for Pearson , Kendall , and Spearman correlations. *Psychometrika* **2000**, *65*, 23–28, doi:10.1007/BF02294183.
151. Bezin, Y.; Pålsson, B.A. Multibody simulation benchmark for dynamic vehicle-track interaction in switches and crossings: modelling description and simulation tasks. *Veh. Syst. Dyn.* **2021**, 1–16, doi:10.1080/00423114.2021.1942079.
152. Pålsson, B.A.; Ambur, R.; Sebès, M.; Wang, P.; Shih, J.-Y.; Fan, D.; Xu, J.; Chen, J. A comparison of track model formulations for simulation of dynamic vehicle–track interaction in switches and crossings. *Veh. Syst. Dyn.* **2021**, 1–27, doi:10.1080/00423114.2021.1983183.
153. Iwnicki, S. Manchester benchmarks for rail vehicle simulation. *Veh. Syst. Dyn.* **1998**, *30*, 295–313, doi:10.1080/00423119808969454.
154. Pålsson, B.A.; Ambur, R.; Sebès, M.; Wang, P.; Shih, J.Y.; Fan, D.; Xu, J.; Chen, J. A comparison of track model formulations for simulation of dynamic vehicle–track interaction in switches and crossings. *Veh. Syst. Dyn.* **2023**, *61*, 698–724, doi:10.1080/00423114.2021.1983183.
155. Kalker, J.J. A Fast Algorithm for the Simplified Theory of Rolling Contact. *Veh. Syst. Dyn.* **1982**, doi:10.1080/00423118208968684.
156. Molyneux-berry, P.; Bevan, A. *T775-01 Further Development of the WLRM Damage Parameter : Integration Report [# 110/41]*; 2011.

157. British Standards Institution *BS EN 13674-2:2019 Railway applications — Track — Rail*; 2011.
158. Schwihaag-AG Fastening systems for turnouts Available online:
<https://schwihaag.com/en/products-track-technology-railway/fastening-systems-turnouts/> (accessed on Oct 13, 2021).
159. Network Rail *Track Design Handbook*; London, United Kingdom, 2010.
160. British Standards Institution *BS EN 13715 : 2020 Railway applications — Wheelsets and bogies — Wheels — Tread profile*; 2020.
161. Zhao, X.; Li, Z. The solution of frictional wheel-rail rolling contact with a 3D transient finite element model: Validation and error analysis. *Wear* **2011**, 271, 444–452, doi:10.1016/j.wear.2010.10.007.
162. Thompson, D. *Railway noise and vibration: mechanisms, modelling and means of control*; Elsevier, 2008.
163. Jenkins, H.H.; Stephenson, J.E.; Clayton, G.A.; Morland, G.W.; Lyon, D. The effect of track and vehicle parameters on wheel/rail vertical dynamic forces. *Railw. Eng. J.* **1974**, 3, 2–16.
164. Shih, J.; Weston, P.; Pillai, N.; Entezami, M.; Stewart, E.; Roberts, C. Potential condition monitoring system for switch and crossings using accelerometers. In *Proceedings of the Proceedings of the 13th International Workshop on Railway Noise*; Ghent, Belgium, 2019.
165. Cope, G.H. *British railway track: design, construction and maintenance*; 6th ed.; Permanent Way Institution, 1993; ISBN 0903489031.

166. Bogdański, S.; Olzak, M.; Stupnicki, J. Numerical modelling of a 3D rail RCF 'squat'-type crack under operating load. *Fatigue Fract. Eng. Mater. Struct.* **1998**, *21*, 923–935, doi:10.1046/j.1460-2695.1998.00082.x.
167. Bogdański, S.; Brown, M.W. Modelling the three-dimensional behaviour of shallow rolling contact fatigue cracks in rails. *Wear* **2002**, *253*, 17–25, doi:10.1016/S0043-1648(02)00078-9.